Contract No:

This document was prepared in conjunction with work accomplished under Contract No. 89303321CEM000080 with the U.S. Department of Energy (DOE) Office of Environmental Management (EM).

Disclaimer:

Project Title:	Solar Receiver with Integrated Thermal Storage for a Supercritical Carbon Dioxide Power Cycle
Project Period:	10/01/15 – 3/31/22
Project Budget:	$3,249,949
Submission Date:	7/6/2022
Recipient:	Brayton Energy LLC
Address:	75 Lafayette Rd Hampton, NH 03842-2624
Award Number:	DE-EE0007118

Principal Investigator: Jacob Hinze, Mechanical Engineer
Phone: 603-601-0450
Email: jack.hinze@braytonenergy.com

Business Contact: Shaun Sullivan, President
Phone: 603-601-0450
Email: sullivan@braytonenergy.com

Technology Manager: Kamala Raghavan

Project Officer: Christine Carter

Grant Specialist: Clay Pfrangle

Contracting Officer: Diana Bobo

Agency to which Report is Submitted:	DOE/EERE Solar Technologies Office
FOA Name:	CONCENTRATING SOLAR POWER: ADVANCED PROJECTS OFFERING LOW LCOE OPPORTUNITIES (CSP: APOLLO)
FOA Number:	DE-FOA-0001186
Report:	Final Scientific/Technical Report
Award Type:	Cooperative Agreement

Award Number:	DE-EE0007118	
Prime Recipient:	Brayton Energy LLC	
Prime Recipient Type:	For-Profit	
Project Title:	Solar Receiver with Integrated Thermal Storage for a Supercritical Carbon Dioxide Power Cycle	
Principal Investigator (PI):	Jacob Hinze; Mechanical Engineer; jack.hinze@braytonenergy.com; 603-601-0450	
DOE Technology Manager (TM):	Kamala Raghavan	
DOE Technical Project Officer (TPO):	Christine Carter	
DOE Grants Management Specialist (GMS):	Clay Pfrangle	
DOE Contracting Officer (CO):	Diana Bobo	
Prime Recipient DUNS Number:	142905376	
Award Period of Performance (POP):	Start: 09/01/2015	End: 03/31/2022
Award Budget Period (BP):	Start: 04/01/2019	End: 03/31/2022
Date of Report:	7/6/2022	
Reporting Period (covered by this report):	09/01/2015 to 03/31/2022	

Acknowledgement: "This material is based upon work supported by the Department of Energy, Office of Energy Efficiency and Renewable Energy, Solar Energy Technologies Office, Tech to Market Sub-program, under Award Number DE-EE0007118.

Solar Receiver with Integrated Thermal Storage for a Supercritical Carbon Dioxide Power Cycle

Final report for DE-EE0007118

7/18/2022

PI: Jacob Hinze, Brayton Energy LLC

Other Contributors:

Shaun Sullivan, Brayton Energy

Patrick Ward, Savanah River National Laboratory

Ragaiy Zidan, Savanah River National Laboratory

Executive Summary:

This project endeavors to design and demonstrate an integrated CSP system that meets the Department of Energy's 6¢/kW-hr LCOE goal [1]. This design is based on the 10 MW_e Supercritical Transformational Electric Power (STEP) engine specifications, but adaptable to any sCO_2 power module up to 10 MW_e. The enabling technology to be tested is a new class of metal hydride based thermal energy storage materials which can store thermal energy in the hydrogen bonds between the metal hydride and hydrogen. This thermochemical energy storage solution provides a much greater energy density than sensible and latent energy storage enabling an integrated system design that closely linked the metal hydride to the power block. This allows the entire system to be mounted up tower to provide cost reductions. The following components were developed in the course of this project:

- A solar receiver design capable of operating at high temperatures (>760°C) while maintaining efficiency greater than 90%
- A novel metal hydride material capable of operating at up to 760°C
- A metal hydride to CO_2 heat exchanger capable of storing and discharging heat from the metal hydride while operating at high temperature (760°C) and pressure (25MPa) was developed
- Designs for an integrated up-tower installation with close-coupled receiver, engine, and energy storage subsystems

A solar receiver was designed that uses Inconel 740H tubes to capture energy from the sun and transport it to the metal hydride for storage. This receiver can reach temperatures in excess of 760°C and efficiencies of ~80% were demonstrated through modeling.

A novel metal hydride, capable of operating above 760 °C, was developed during the course of this project and thoroughly tested at a lab scale. The material's hydrogen capacity, reaction enthalpy, thermal conductivity, and cyclic stability were measured. Additionally, lower cost manufacturing methodologies for the new material were demonstrated and the materials evaluated to confirm that it met required specifications.

A metal hydride to CO_2 heat exchanger was developed which can store heat from the solar receiver, and discharge heat to the power block while keeping the metal hydride under pressure. This heat exchanger employs Brayton's cellular design, which uses folded fin to create brazed cells which are capable of withstanding high temperature and pressure while utilizing low-cost sheet and plate material.

A demonstration test article was built that can store 2kW_h of thermal energy and was coupled to Brayton Energy's CO_2 loop where the performance of the metal hydride under commercial conditions was measured. Difficulties with measuring a small heat release with a relatively large test article meant that tests showed that only 59.1% of the thermal energy of the laboratory material was released. Changes such as larger thermal duty, more insulation, lower

pressures/longer duration discharging would likely increase the measured heat release and bring it in line with the lab tested material.

An integrated model was created that uses the inputs from all the different sub-models in order to return an overall system LCOE using SAM [2]. A LCOE of 8.56 ¢/kWh$_e$ was calculated which is greater than the DOE SunShot goal for baseload power, however it is lower than the 10 ¢/kWh$_e$ identified for peaker applications. The higher-than-expected LCOE came from several sources:

- Initial cost estimates of the metal hydride slightly exceeded \$15/kWh$_{th}$ (DOEs goal for TES) due to the high cost of precursor materials, but a synthetic methodology was demonstrated late in the project to reduce the cost well below the \$15/kWh$_{th}$ target
- The necessity of nickel-based alloys for high temperature operation and containment of both hydrogen and carbon dioxide substantially increase the cost of the storage containment and heat exchangers used for heat storage and transfer.
- Although the incorporation of additives enhanced the metal hydride's thermal conductivity above that of molten salts, the need for many heat exchange cells results in higher heat exchanger costs. This is largely due to the solid state nature of the material since the thermal storage material cannot be pumped through the heat exchanger system to reduced the total number of heat exchangers required.
- A hydrogen control loop is required, to store hydrogen when it is not being used in the TES system which adds cost to the overall storage system.

This project greatly advanced metal hydride based thermochemical energy storage technology and demonstrated its use. Previously there were no metal hydrides which were capable of operating at the proposed temperature limits (760°C), there is now a high temperature metal hydride with documented performance/stability and a path for low-cost production. Additionally, the metal hydride was tested at a scale >650x larger than what had previously been done in the lab. While not at commercial scale, it was an excellent demonstration of the technology and provided knowledge that can be leveraged for other applications. Areas where volume reduction and long-term storage is desired could benefit from metal hydride TES. Results from the project will allow for further exploration of these areas.

Table of Contents

Background:

The integrated nature of this project builds on developing technologies in a number of key areas. While not specifically within the scope of this work, ongoing research and development in supercritical carbon dioxide power cycles – including the work performed at General Electric, SouthWest Research Institute, Echogen, Sandia National Labs [3], NETL[4], NREL[5], [6], and many other industrial, government [7], and academic institutions [8] – informs the overall system integration and is critical to determining its performance. The findings of these programs are incorporated directly.

Brayton's receiver technologies are responsive to the aforementioned specifications, while employing different technology elements tested under previous DOE programs. Alkali metal heat pipe solar absorbers have been analyzed and tested by DOE contractors under the ASCS[9] program, Sandia National Labs, NASA, Argonne National Labs, Los Alamos National Labs[10], and other institutions[11] over a three decade period. Gas-heating solar receivers have likewise received significant attention over past decades for Brayton, Stirling, and indirect cycles, and recently have been identified by the DOE as one of the three likely technology paths towards the next generation receiver for use with high efficiency CSP systems. Recent work by Brayton Energy[12], [13], Sandia National Labs, NREL[14], [15], and other institutions[16] have all demonstrated the viability of the technology, especially in an application with gas pressures in the range being considered here. These results are leveraged heavily and, where applicable, existing models are applied for the specific operating conditions of this program.

Metal hydride materials, because of their high degree of reversibility, have shown the most promise of the thermochemical storage media currently under consideration. The amount of thermal energy that can be stored per kilogram of metal hydride is comparatively large—often 15 to 20 times more than what can be stored in traditional molten-salt systems. The higher energy density provided by the use of metal hydride systems also can reduce CSP TES system size and cost.

Recently, Sheppard *et al* [17] assessed the performance of the perovskite-type hydride, $NaMgH_3$ under high temperature CSP plant conditions. The authors suggest the use of $NaMgH_3$ hydride at temperatures between 580-600 °C; however, material cycling stability and other issues have limited the current potential for this material. Renewed interest is directed at Ca-based hydride due to its very high heat of formation and energy storage capacity and stability up to 800°C. A CSP plant using calcium hydride as the storage material with a continuous output of 100 kWe system coupled to a Stirling engine has recently been investigated in Australia [18]. Despite their favorable high temperature and thermal storage capacity, calcium systems, which need to

operate under molten conditions, have aggressive corrosion issues in the molten state and typically operate at very low pressures.

An array of candidate materials based on Ca were patented by SRNL for this application and shown to operate at very high temperatures (>650°C) and still be low cost.[19] The engineering properties of this material were obtained and then employed in a series of screening, transport and system models to evaluate the performance and cost of this new

Material for solar applications. [20] A bench-scale metal hydride TES system was built, tested and used to characterize key performance parameters. [21], [22] With its partner CU, SRNL initiated an International Energy Agency (IEA) working group for MH TES technology to expand collaborative research in the evolving field.

Also fundamental to the success of this program is a variety of low-cost, high-performance, long-life heat exchangers suitable for operation at high temperatures and very high pressures. The development work performed by Brayton Energy during its 2012-2016 SunShot program[13] has been applied to these units to great effect. Validated performance, durability, weight, and cost models based on testing and commercial production are central to this program's success.

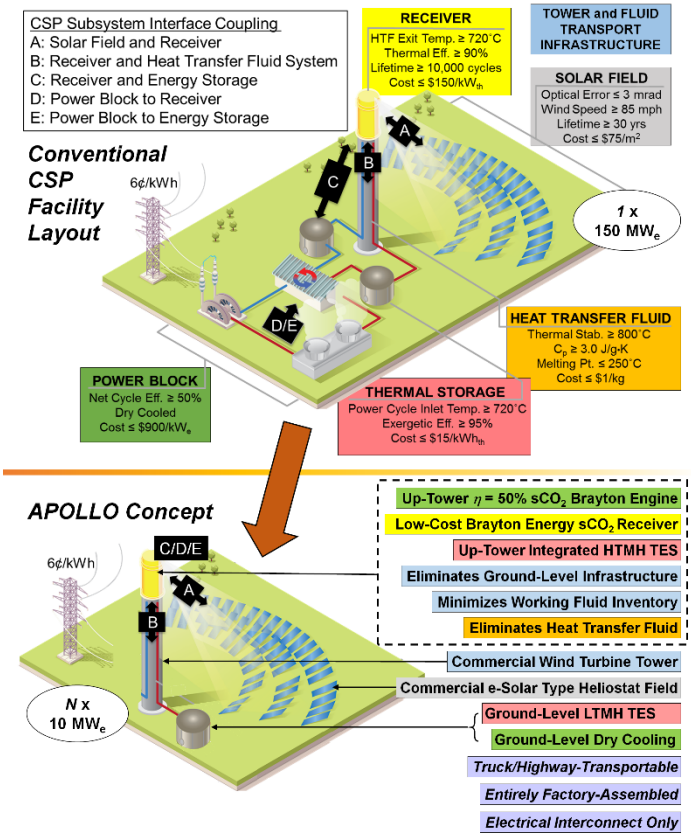

Figure 1 – Vision for the APOLLO Modular CSP layout, wherein the power block and thermal energy storage are mounted up-tower and close-coupled to the absorber.

Project Objectives:

Brayton Energy's APOLLO project is an ambitious 4-year $3M undertaking to:

- Develop, model, and validate via testing a set of metal hydride formulations for a CSP applications
- Specify a cost-effective CSP system integrating a metal hydrides TES solution using these media
- Design the receiver architecture and layout suitable for integration in the aforementioned system

- Design the TES metal hydride heat exchanger modules for use in the aforementioned system
- Specify and/or design the ancillary systems required to enable the aforementioned system (including tower, heliostats, valves, piping, regenerator, operating profile and control schema, etc.)
- Model the integrated system to determine its fully integrated annual/diurnal operating performance
- Evaluate the capital and operating costs, electrical production, and LCOE in commercial scenarios
- Design, build, commission, and operate a test system capable of demonstrating operation and performance of the core integrated technologies developed under the scope of this program

Successful completion of this project will reduce the cost for thermal energy storage and allow for a more compact, low cost CSP plant to be built. This in turn will reduce the LCOE from CSP plants encouraging their adoption. Greater use of CSP will displace demand for fossil fuels and allow for more stable operation of the energy grid.

Budget Period 1

Task 1.1: Develop the engineering models needed to simulate the critical subcomponents of the proposed integrated solution (specifically: the absorber, the sCO_2/high temperature metal hydride (HTMH) thermal transport, metal hydride thermal energy storage, and the low temperature metal hydride (LTMH)/sCO_2 thermal transport), the fully-integrated system model incorporating the individual subcomponent models, and perform the preliminary performance, cost, and operability studies.

SubTask 1.1.1: Establish a Commercialization Advisory Board (CAB) consisting of multiple potential stakeholders in the project to act as a source of feedback and guidance with respect to programmatic decisions.

SubTask 1.1.2: With input from the Commercialization Advisory Board, compile a suitable selection of representative surface flux profiles on potential absorber surface geometries.

Milestone 1.1.2.1: As an initial deliverable from the CAB, representative and documented field layouts that project ~37 MW_{th} of concentrated solar energy onto the top of the tower at design point conditions will be identified and approved.

SubTask 1.1.3: Generate and exercise a thermo-hydraulic absorber model that will interface with the overall system thermo-hydraulic model.

Milestone 1.1.3.1: An absorber architecture that, at design point, maintains a metal temperature ≤ 800^0C while receiving the specified ~37 MW_{th} of incoming solar energy and conveying it to the sCO_2 working fluid and the HTMH media.

SubTask 1.1.4: Identify candidate options for conveying the required rate of thermal energy from sCO_2 working fluid to the HTMH – including but not limited to primary surface contact, extended surfaces (fins, pins, etc.), heat pipe-type designs, convective fluid circulation, etc. – and evaluating the options on the basis of performance, cost, risk, and complexity.

Milestone 1.1.4.1: Identification of a Thermal Communication System for conveying 20 MW_{th} thermal energy between the sCO_2 working fluid and the HTMH media.

Milestone 1.1.4.2: Identification of a Thermal Communication System that does not exceed an HTMH temperature of 780 °C anywhere within the media.

SubTask 1.1.5: Identify the specific and unique HTMH and LTMH formulations – hereafter referred to as the "selected formulation" for each – based on their cost, their chemical kinetics, and their performance in conjunction with the entire system.

Milestone 1.1.5.1: The selected HTMH formulation can achieve the required thermochemical energy storage and transfer rates in a mass compatible with mounting the entire integrated system up-tower – initially estimated at 150 tons by the manufacturer, with provisions that that might be increased to 204 tons with structural enhancement work to the tower.

Milestone 1.1.5.2: The selected HTMH will associate/dissociate hydrogen at its operating pressure at an operating reaction temperature ≥ 750^0C.

Milestone 1.1.5.3: The selected HTMH formulation will operate reversibly for 150 cycles with prediction of low material degradation (≤2%) commensurate with longer cycling (10,000 cycles).

Milestone 1.1.5.4: The selected LTMH formulation will associate/dissociate hydrogen at its operating pressure at an operating reaction temperature ≤ 60^0C.

Milestone 1.1.5.5: The selected LTMH formulation will operate reversibly with prediction of low material degradation (<2%) commensurate with longer cycling (10,000 cycles).

Milestone 1.1.5.6: A preliminary integrated receiver, tower, and thermal energy storage system designed for a 10 MW_e modular tower-based CSP sCO_2 Brayton Power Plant with Integrated TES that has a capital cost of \$210/kW_{th} or less (corresponding to the DoE goal of \$150/kW_{th} for the receiver/tower system + [\$15/$kWhr_{th}$ x4 hrs. storage] for the TES), within an uncertainty of ±50%, over the full range of input variability.

SubTask 1.1.6: Generate a complete metal hydride thermal energy storage system model to interface with the overall system thermo-hydraulic model; in addition to the MH formulations, this will include vessels and hydrogen transport piping designed for the appropriate pressures, temperatures, material compatibility, and flow pressure drop.

SubTask 1.1.7: Generate a suitable model to evaluate the heat exchange between the LTMH and Cycle Low-Temperature-Recuperator discharge flow (engine exhaust).

Milestone 1.1.7.1: The design of an LTMH heat exchange system capable of charging/discharging at a rate of ≥ 10 MW_{th} at 50% power cycle efficiency to accommodate TES operation over the selected storage time (nominally 4 hours) at full power sCO_2 power cycle conditions (flow rate, low temperature recuperator flow temperature, etc.); furthermore the discharge rate must be capable of operating at lower discharge rates corresponding to 20% cycle power (2 MW_e)

conditions (required input power, mass flow rate, low temperature recuperator discharge temperature, etc.).

SubTask 1.1.8: Integrate all of the constituent sub-models into a cohesive whole and exercise that model to define the system architecture and predict its design point performance.

SubTask 1.1.9: Apply rigorous thermodynamic, conjugate transport, and chemical kinetic models to fully define and specify the subsystems such that they achieve the target overall system performance. The following key pieces will come out of this task:

An absorber cell geometry and receiver configuration appropriate for the needs of the sCO_2 Brayton power cycle and the MH thermal energy storage system

A validated means of conveying the absorbed thermal energy from the receiver cells into the bulk HTMH volume

Final formulations for both the HTMH and the LTMH materials

Milestone 1.1.9.1: An integrated, reversible, end-to-end thermal model that spans from the solar input during charging (location, time of day, day of year) to the LTMH heat addition/rejection, including interactions with the sCO_2 working fluid and thermal losses to the environment, which predicts a Thermal Energy Storage design point efficiency ≥ 99%.

Milestone 1.1.9.2: An integrated, reversible, end-to-end thermal model that spans from the solar input during charging (location, time of day, day of year) to the LTMH heat addition/rejection, including interactions with the sCO_2 working fluid and thermal losses to the environment, and which predicts a design point exergetic efficiency ≥ 95%.

Milestone 1.1.9.3: An absorber design that, with its performance integrated over all time-weighted modes of operation, exhibits a thermal efficiency of 90% in accordance with the DOE SunShot target.

Milestone 1.1.9.4: Determine limits of system operability and desirable modes of operation, including:

the maximum flux that may be absorbed by the receiver during a zero-sCO_2-flow scenario, corresponding to charging-only operation

the peak storage rate achievable by the system in conjunction with sCO_2 flow

the maximum flux that may be accommodated with elevated sCO_2 flow rate

the sCO_2 flow and resulting pressure drop required to operate in no-storage mode

Go/No-Go Decision Point 1: Design Point Integrated System Design that meets the performance targets outlined in the Budget Period 1 Milestone tables.

Budget Period 2

Task 2: A full comparative evaluation of the two candidate absorber technology paths – namely, (1) a heat pipe absorber design and (2) an intermediate gas path absorber design – must be performed in order to identify which of the two layouts will be pursued in depth in Budget Phases 2 and 3.

SubTask 2.1: Perform a comprehensive comparative analysis between two viable absorber systems (both of which were outlined in detail in the Budget Period 1 final report):

An absorber comprised of multiple parallel heat pipes, each of which communicates with a corresponding volume of high temperature metal hydride; absorbed heat is conveyed to the metal hydride directly via the heat pipe working fluid.

An absorber surface comprised of multiple parallel tube-based sections, through which an intermediate heat transfer fluid is being circulated. Absorbed heat is conveyed to the metal hydride via a heat exchanger configuration

Task 3: Exercise the integrated model will be exercised to determine the annualized system performance.

SubTask 3.1: Apply the range of solar inputs representing the diurnal and annual variations to the model developed in Task 1.1.3 for the absorber layout down-selected in Task 1.1.5.

Milestone 3.1.1: The full-scale system is predicted to have an annualized system energetic efficiency ≥ 99%.

Milestone 3.1.2: The full-scale system is predicted to have an annualized system exergetic efficiency ≥ 95%.

SubTask 3.2: Further characterize the selected HTMH and LTMH metal hydride media properties, specifically with respect to their internal thermal transport properties – how effectively thermal energy can be conveyed through the media and the resulting intermedia temperature gradients – and any performance degradation or material breakdown over time.

SubTask 3.2.1: Perform an analysis to identify the relative impact of metal hydride material properties (thermal conductivity, gravimetric density, cost, operating temperature, kinetic rate, temperature variation) on the potential to improve the LCOE of the overall system.

SubTask 3.2.2: Evaluate variations on the additives and formulations for the MH media to modify the greatest-effect material property(-ies) identified in SubTask 4.1. Fully characterize the selected HTMH and LTMH formulations based on their inter-material thermal transport rates and their operational degradation and life. Evaluate the availability and scale up of the new enhanced material formulation.

Milestone 3.2.2.1: The enhanced HTMH and/or LTMH formulations applicable for scale up to commercial production, will reduce the calculated LCOE by >$0.01/kWh. The revised HTMH formulation will be available at a price at or below $1.10/kg in quantities of 40,725,000 kg annually, while the revised LTMH formulation will be available at a price at or below $5.20/kg in quantities of 52,575,000 kg annually.

Milestone 3.2.2.2: Material properties for commercial versions of the HTMH and LTMH formulations identified in Milestone 3.2.2.1 will be experimentally measured at a commercial level. The thermodynamic and cycling properties of the material will be tested and compared with the lab scale material properties.

SubTask 3.3: The system layout will be specified, capital costs (detailed for the engineered components, generalized for the balance of the system) will be calculated, and the results will be used to generate a full Power Plant LCOE. Detailed capital costs for the full scale system will be generated for the absorber cells, metal hydride TES system, and the LTMH thermal communication heat exchanger cells.

SubTask 3.3.1: Define the layout of the system components and address any identified thermo-mechanical concerns.

Milestone 3.3.1.1: An integrated receiver and thermal energy storage system layout that is shown to have a predicted operation life of 90,000 hours considering creep, fatigue, corrosion, strength, and appropriate environmental factors (wind loads, etc.).

SubTask 3.3.2: Generate detailed costs for the engineered components in the system (e.g., absorber cells and the metal hydride TES), and general costs for the balance of the system

SubTask 3.3.3: Apply the capital costs and annualized receiver/TES performance profile to generate a system LCOE.

Milestone 3.3.3: An integrated receiver, tower, and thermal energy storage system designed for a 10 MW_e modular tower-based CSP sCO_2 Brayton Power Plant with Integrated TES that has a capital cost of \$210/kW_{th} or less (corresponding to the DoE goal of \$150/kW_{th} for the receiver/tower system + [\$15/$kWhr_{th}$ x4 hrs. storage] for the TES), within an uncertainty of ±35%, over the full range of input variability.

SubTask 3.4: Design a prototype article to evaluate its performance and validate the predictions for the full-scale system. A sub-scale test article will be specified which captures all of the important operational characteristics of the full-scale system and incorporates all of the engineered innovations in this proposal.

SubTask 3.4.1: A prototype article that embodies the innovative and functional elements of the proposed receiver and thermal energy storage system will be designed.

SubTask 3.4.2: Successfully demonstrate the manufacture of any new, untested, innovative, or different design elements critical to the operation of the proposed integrated receiver design. Any novel absorber brazed-cell architectures will be manufactured and quality tested to ensure adequate strength and performance in accordance with program requirements.

SubTask 3.4.3: A test loop will be designed for use of prototype testing.

Milestone 3.4.3.1: Design of a 5 kW_{th} test article and test setup – with a 10 kWh_{th} storage capacity – to be used for simulated on-sun operation, the article itself consisting the absorber architecture, flowing working fluid, and integrated thermal energy storage.

Milestone 3.4.3.2: Analytically supported predictions that the test setup has a creep life of at least 1,000 hours in order to ensure safe operation throughout the testing program.

SubTask 3.4.4: A test plan will be generated to document the equipment, procedures, and calculations needed to operate a prototype system to demonstrate that the proposed receiver/TES system will meet the performance predictions.

Milestone 3.4.4.1: A test plan describing the full range of tests to be performed, and demonstrating an experimental uncertainty for the TES energetic efficiency that will be ≤ 0.5 pts.

Milestone 3.4.4.2: A test plan describing the full range of tests to be performed, and demonstrating an experimental uncertainty for the TES exergetic efficiency that will be ≤ 0.5 pts.

Go/No-Go Decision Point 2: Successful delivery of an integrated receiver/thermal transport/metal hydride system design that meets the annualized performance targets, a comprehensive capital cost and LCOE model, detailed test article and test rig designs, and a detailed test article test plan, all of which meet the corresponding requirements as defined in the Budget Period 2 Milestone tables.

Budget Period 3

Task 4.1: Build and test a prototype article to evaluate its performance and validate the predictions for the full scale system.

SubTask 4.1.1: Sourcing, Purchasing, Fabrication, and Assembly of Test System

SubTask 4.1.2: The prototype article will be tested in accordance with the test plan, with the data being used to validate the predicted performance of the full scale system. The system performance will be demonstrated in each of the operational modes and at the operational limits identified in Milestone 1.1.8.3.

Milestone 4.1.2.1: A difference between experimental data and numerical operating data of ≤ 15% will be shown at the selected measurement points.

Milestone 4.1.2.2: Applying the data and learnings from the test article testing, the full scale system is predicted to have an annualized system energetic efficiency ≥ 99%.

Milestone 4.1.2.3: Applying the data and learnings from the test article testing, the full scale system is predicted to have an annualized system exergetic efficiency ≥ 95%.

SubTask 4.1.3: Apply the capital costs and annualized receiver/TES performance profile to generate a system LCOE.

Milestone 4.1.3.1: An integrated receiver, tower, and thermal energy storage system designed for a 10 MW_e modular tower-based CSP sCO_2 Brayton Power Plant with Integrated TES that has a capital cost of \$210/kW_{th} or less (corresponding to the DoE goal of \$150/kW_{th} for the receiver/tower system + [\$15/$kWhr_{th}$ x 4 hrs. storage] for the TES), within an uncertainty of ±10%, over the full range of input variability.

Project Results and Discussion:

Budget Period 1

A successful solution to the challenge of integrating the thermal energy storage (TES) system up-tower is dependent on multiple interconnected subsystems. Each subsystem must be modeled appropriately to allow inputs and outputs relative to the other subsystems, as the interplay between these subsystems is critical to a fully realizable solution. Defining this interaction will also be necessary in order to down-select the thermal transport options to a single identified solution.

Problem Statement: Incident concentrated solar energy must be absorbed and conveyed into both the supercritical carbon dioxide (sCO_2) working fluid and into the TES without violating any material temperature limits; conversely the system must work in reverse, with energy being discharged from the TES at twice the rate of charging into the working fluid.

Task 1.1:

Develop the engineering models needed to simulate the critical subcomponents of the proposed integrated solution (specifically: the absorber, the sCO_2/high temperature metal hydride (HTMH) thermal transport, metal hydride thermal energy storage, and the low temperature metal hydride (LTMH)/sCO_2 thermal transport), the fully-integrated system model incorporating the individual subcomponent models, and perform the preliminary performance, cost, and operability studies.

General Schematic

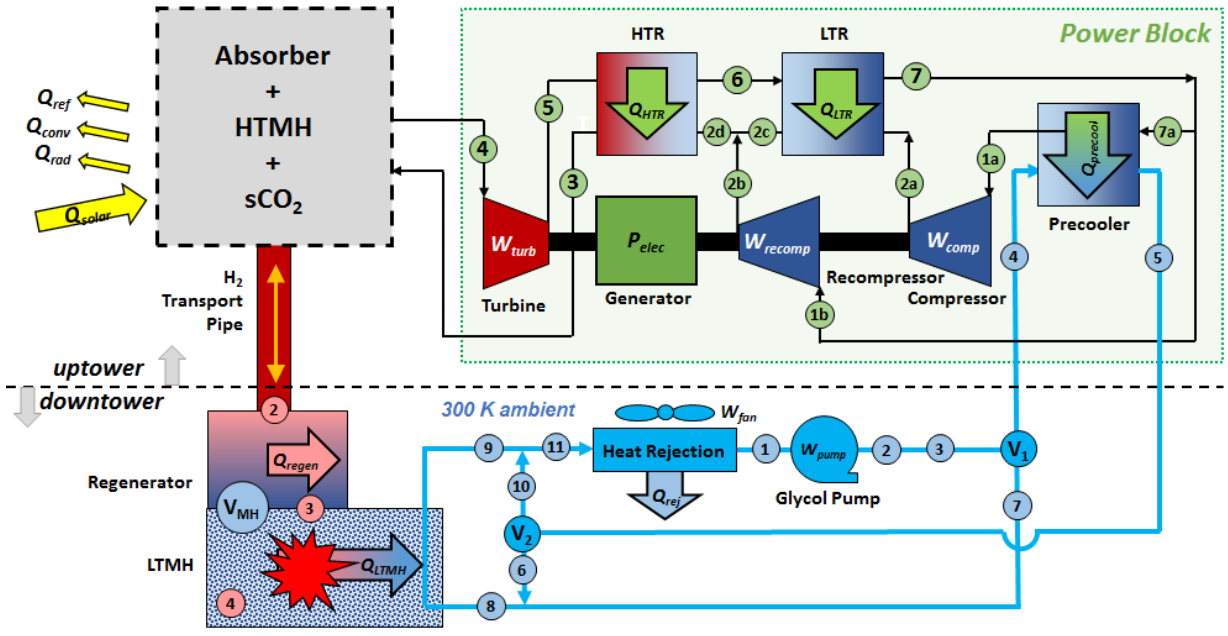

Figure 2 – General schematic for the proposed integrated system. The details of the Absorber, HTMH Media Bed, and interconnecting thermal transport of the sCO_2 cycle working fluid are presented as a "black box" in this schematic. Two competing configurations were developed during this program.

An overall schematic of the proposed system is shown in Figure 2; depicted are all of the major systems critical to the integrated system performance and cost. These include:

- A tower upon which the absorber, the HTMH and the sCO_2 power cycle are mounted. In an effort to minimize the cost of the system, the proposed solution utilizes commercial wind turbine industry components for the receiver tower.
- The sCO_2 Recompression Brayton Cycle power block; for the purposes of this program this is a 10 MW_e power cycle – mounted up-tower – operating at a 50% conversion efficiency. The working fluid is at 545 ^oC and 25 MPa when it enters the heat addition section, and the turbine inlet conditions are nominally 720 ^oC and 25 MPa. Note that the main compressor precooling is performed via a compact sCO_2-to-glycol heat exchanger, which transports the 30% glycol mixtures down to a dry-cooling waste heat rejection heat exchanger at ground level.
- A hydrogen transport pipe for conveying the gaseous hydrogen between the HTMH and LTMH during operation.
- A regenerator; this passive component is required as the hydrogen leaving the HTMH during TES charging is at high temperature (745 ^oC); if the sensible heat of the high temperature hydrogen were simply discarded it would be a significant thermal inefficiency (approximately 20%); the regenerator instead captures this sensible heat during charging, retains it during storage intervals, and then returns it to the hydrogen during TES discharge.
- A LTMH system, situated at ground level; this bed is where the energy is actually stored, in the form of hydrogen bonds. As heat must be either liberated or absorbed during TES charging and discharging, respectively, the LTMH bed is in close communication with the glycol waste heat rejection system; with relatively simple valving the inlet conditions of the glycol into the LTMH media bed may be controlled, allowing it to either absorb or release the required heat.
- The waste heat rejection from the sCO2 engine is used to energize the LTMH during TES discharge. This subsystem circulates a glycol-water mixture (30%) through the LTMH bed, and in some configurations through the up-tower thermal transport system. Low grade excess heat is rejected to ambient via a typical radiator-type heat exchanger. Note that this heat exchanger must be upsized from the baseline sCO_2 cycle heat rejection requirements in order to provide the capacity to accommodate the additional thermal duty of the LTMH heat transfer.
- An up-tower "Absorber + HTMH + sCO_2" system is shown here as a "black box" In two competing configurations, solar energy is absorbed and conveyed in the HTMH media (for the purposes of TES) and into the sCO_2 cycle working fluid. Additionally, there must be thermal communication between the HTMH and the sCO_2 cycle working fluid for the purposes of generating electricity from the TES during off-sun operation. The two configurations analyzed by Brayton will be discussed in detail below.

- Also note that the proposed systems all utilize sCO_2 heat exchangers capable of operating under very high pressures and temperatures. Where these are required, the Brayton sCO_2 heat exchanger design developed under its SunShot program are being employed; to date, these have been shown to be among the most compact, highest performing, and lowest cost option available.

SubTask 1.1.1:

Establish a Commercialization Advisory Board (CAB) consisting of multiple potential stakeholders in the project to act as a source of feedback and guidance with respect to programmatic decisions. Stakeholders may include, but are not limited to, the Department of Energy/governmental organization, engine/tower/heliostat original equipment manufacturers (OEMs), installation integrators, and/or utility representatives.

Feedback for various design decisions for the project were obtained from three outside entities; NREL, Sandia, and Solar Dynamics. A questionnaire was sent out to these organizations and feedback was organized into useful data. The feedback obtained from these entities has been reported in the subtask they are most relevant to.

SubTask 1.1.2:

With input from the Commercialization Advisory Board, compile a suitable selection of representative surface flux profiles on potential absorber surface geometries. These flux profiles may represent multiple field configurations, multiple absorber surface geometries, and/or multiple operational strategies.

Flux Profiling

Conveying the concentrated solar power from the heliostat field throughout the HTMH media is of critical important to the success of this program; fundamental to this and the evaluation of the potential system configurations is the flux distribution imposed by the heliostat field upon the defined absorber geometry. An understanding of the distribution of that power over the surface is essential.

A Monte Carlo ray-tracing flux model was developed, benchmarked, and used to study the absorber flux profiles. Heliostat surface slope error, reflectivity, aiming error and sun arc angle are all used to determine deviations from ideal ray reflection angle.

Two field configurations were studied in detail: the surround field (and cylindrical receiver) that was the default layout for the program, and a North field (with planar receiver) that leverages advantageous cosine angles to maximize the heliostat usage. For both analyses the following assumptions were applied:

- 40,000 heliostats
- Specularity + Aiming Error = 3 mrad (DoE spec)

- Equinox Noon, Barstow, CA
- e-solar type flat heliostats
- 60 m tower
- 93% reflectivity

- Initial Absorber Surface Geometries:
- 6m x 6m panel for the north field
- 6m diameter x 6 meter height cylinder for the Surround Field

The resulting field layouts and flux profiles for the two layouts are shown in Figure 3, Figure 4, Figure 5, and Figure 6.

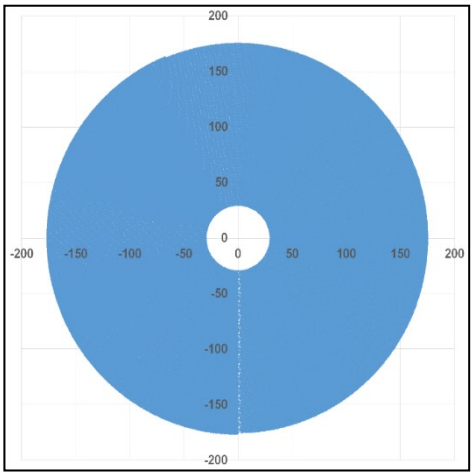

Figure 3 – Surround field heliostat layout

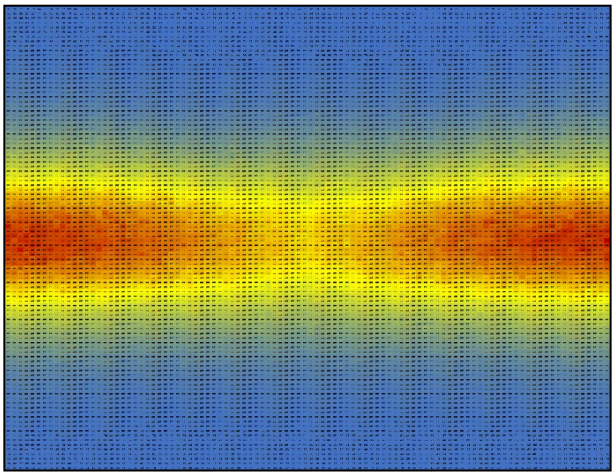

Figure 4 – Mercator projection of the surround field power incident on the cylindrical absorber surface

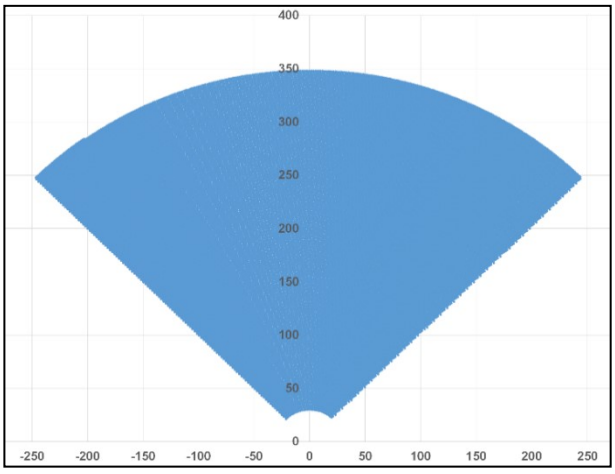

Figure 5 – North field heliostat layout

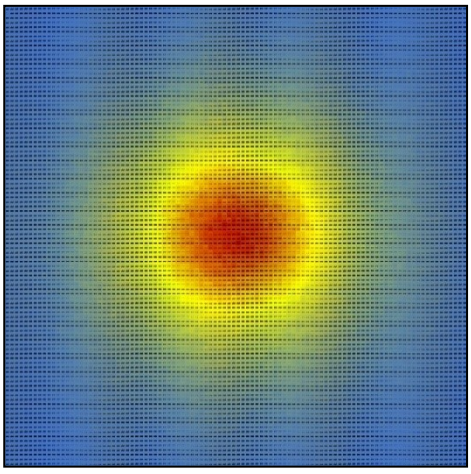

Figure 6 – Projection of the north field power incident on the planar absorber surface

SURROUND FIELD

- Cylindrical Absorber Area = 113 m^2
- Accumulated power = 31.4 MW_{th}

NORTH FIELD

- Panel Absorber Area = 36 m^2
- Accumulated power = 32.8 MW_{th}

- Spilled Power = 0.029 MW_{th} (99.9% Capture)
- Peak Flux = 118 W/cm^2
- Field Layout (175 m from absorber to farthest heliostat)

- Spilled Power = 2.45 MW_{th} (93.1% Capture)
- Peak Flux = 515 W/cm^2
- Field Layout (350 m from absorber to farthest heliostat)

These designs are normalized to the power absorbed at the receiver; therefore each design is suitable to operate the proposed APOLLO system of electrical generation and thermal energy storage.

For a given power (in the range of interest), the north field will use less heliostats (slightly) and have a smaller absorber surface (by a factor of ~π – which both increases efficiency and reduces cost by that factor), but a much higher spillage (about 100x). The peak flux will be about 436% higher in the North field. Also note that with center aiming, the flux distribution on the north field absorber should look pretty much the same regardless of the time of day or year, whereas the peak flux will move around on the surround field absorber. These results are summarized in Table 1.

Given these findings, the north field looks better for the APOLLO application if:

- The significant spillage can be accommodated. Note that the peak flux at the panel edge is ~258 kW/m^2 (or 25.8 W/cm^2), with an average ~142 kW/m^2 (14.2 W/cm^2).
- The peak flux (515 W/cm^2) is acceptable
- Significant power variations among heat pipes can be handled (note that a horizontal or vertical 6 cm pipe passing through the middle peak flux region of the panel absorber will absorb 700 kW, while one along an edge will only absorb 50 kW. The range for heat pipes arranged vertically in the surround field absorber is 365 kW to 250 kW).

Table 1 – Absorber performances.

PARAMETR	UNITS	SURROUND	NORTH
Accumulated Power	kW	31,412	32,798
Spilled Power	kW	29	2449
Captured Fraction	%	99.9%	93.1%
Peak Flux	kW/m^2	1,184	5,153
	W/cm^2	118	515

A rule of thumb for the maximum allowable flux on a heat pipe is about 300 W/cm^2. As defined above, the North field design demonstrates a prohibitively high peak flux. To mitigate this affect, a simple aiming algorithm was applied to leverage the large variations in focal distance between the nearest and farthest heliostats in the

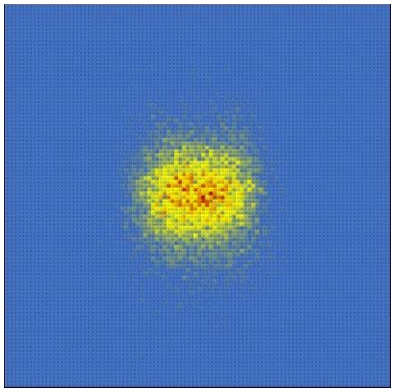

Figure 7 – Projected power on the planar absorber from a central heliostat at 50 m

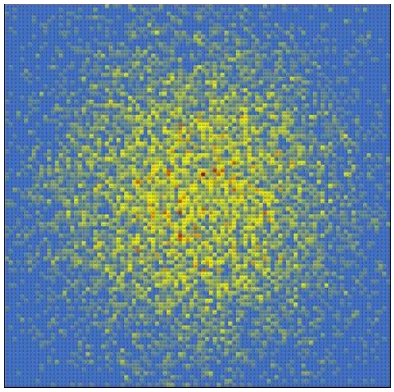

Figure 8 – Projected power on the planar absorber from a central heliostat at 300m

North field. The projected sun spot with center aiming on the planar absorber from a near heliostat and a far heliostat is shown in Figure 7 and Figure 8.

As can be seen, there is significant margin to relocate the near-heliostat aim points without increasing spillage significantly. This can be used to redistribute the flux somewhat, and reduce the peak flux to an acceptable level. An aiming algorithm used to

evaluate this possibility followed a set of simple rules:

- Heliostats are aimed along the vertical centerline
- Heliostats alternate between aiming above and below the horizontal centerline
- The aim offset above or below the horizontal centerline is derived from a polynomial relationship for the projected sunspot size as a function of distance from the tower. This imposes the greatest aim offset to the nearest heliostat, and a zero aim offset to the farthest heliostat. The result bifurcates and diffuses the flux profile, reducing the peak flux under the 300 W/cm^2 limit. The resulting flux profile is shown in Figure 9, and results in Table 2.

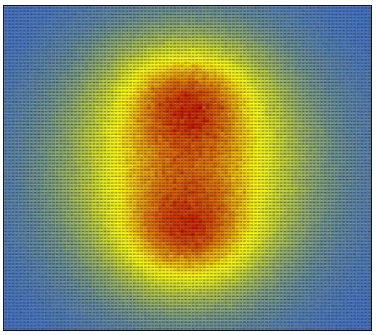

Figure 9 – Adjusted power profile incident on absorber with the described aiming algorithm

The aiming offset results in a marginal increase in spillage and a consequently lower power capture. To compensate for this and enable comparison to the surround field, the

vertical height of the panel receiver is increased to 6.55m so the prior spillage (and power capture) was achieved.

Table 2 – Adjusted north field absorber performance

PARAMETER	UNITS	NORTH
Accumulated Power	kW	32,278
Spilled Power	kW	2969
Captured Fraction	%	91.6%
Peak Nose Flux	kW/m^2	2,897
	W/cm^2	290

The resulting North field configuration is very attractive. The planar configuration is a less complex layout for packaging and assembly, and does not constrain the volume of space on the backside of the absorber. Furthermore, even with the vertical growth to match the power capture, the receiver that is still 65% smaller than the original surround field cylindrical receiver layout. This represent a significant cost savings:

- Assuming 3” heat pipes, the North field has 156 heat pipes, as compared to 456 for the surround receiver.
- The North field heat pipes won’t require complex downcomer shelves (full of welds and holes and complex wick tacking)
- The cost of the quartz window will be reduced proportionally
- The North field heat pipes may have shorter condensers

Note that while these results are presented in terms of the Heat Pipe absorber configuration, the results are equally applicable to the HTF-based Receiver System.

A downward facing planar absorber was also evaluated; in this configuration the panel is oriented horizontally, with all heliostats aimed at the center of the flat absorber. While this appears to be an attractive option due to reduced convection losses and shorter reflected ray distances, it has not been adopted due to its unconventional nature.

Heat Pipe System Overview

A schematic of the heat pipe system is shown in Figure 10, with conditions at each statepoint given in Table 3. Missing values are not necessary to calculate the pertinent design point performance results, but will be established for off-design studies.

Figure 11 depicts a single module consisting of a heat pipe and an HTMH module. Incident concentrated solar energy is absorbed on the evaporator section of the heat pipe; the condenser section of the heat pipe is embedded in a prescribed volume of HTMH media corresponding to the design point power incident on the heat pipe in question.

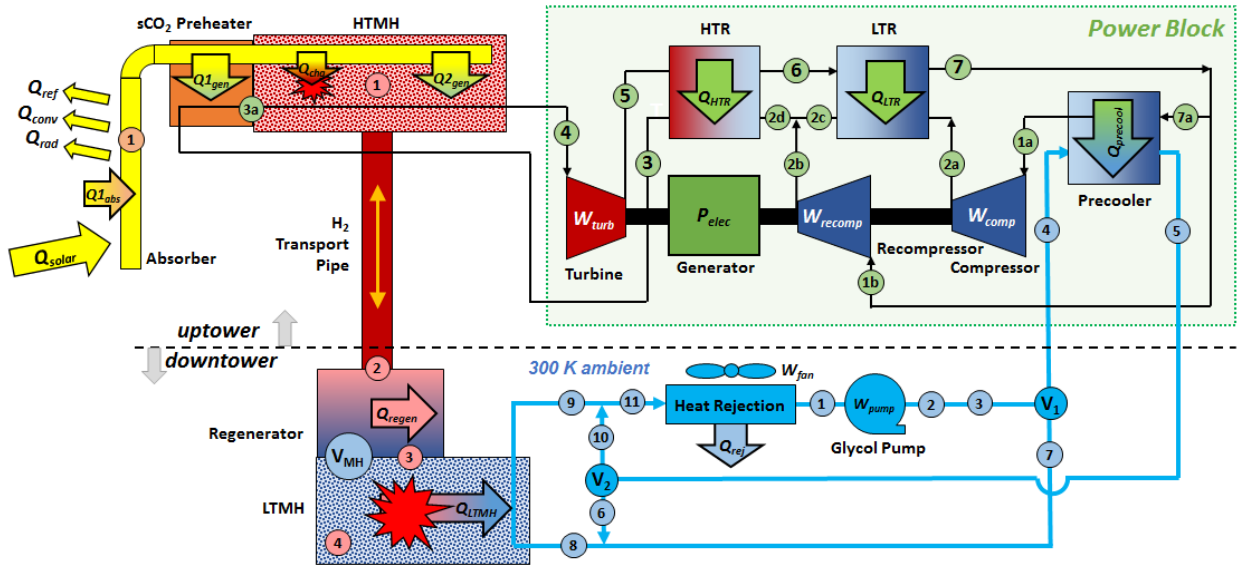

Figure 10 – Schematic of fully integrated heat pipe absorber system (1 out of 144 heat pipes shown).

Table 3 – Heat Pipe Statepoints. Missing values are not required for design point analyses.

HTF LOOP CONFIG., SEPARATE HTMH HEX		CHARGING + GENERATING				GENERATING ONLY				CHARGING ONLY				DISCHARGING + GENERATING				STORAGE ONLY			
ID	DESCRIPTION	FLOW (kg/s)	TEMP (C)	PRESS (MPa)	DUTY (kW)	FLOW (kg/s)	TEMP. (C)	PRESS. (MPa)	DUTY (kW)	FLOW (kg/s)	TEMP. (C)	PRESS. (MPa)	DUTY (kW)	FLOW (kg/s)	TEMP. (C)	PRESS. (MPa)	DUTY (kW)	FLOW (kg/s)	TEMP. (C)	PRESS. (MPa)	DUTY (kW)
SOLAR PARAMETERS																					
Q_{solar}	*- Incident Solar Energy -*	-	-	-	33,378	-	-	-	23,341	-	-	-	13,442	-	-	-	0	-	-	-	0
Q_{ref}	*- Reflection Loss to Ambient -*	-	-	-	1,548	-	-	-	1,548	-	-	-	1,548	-	-	-	0	-	-	-	0
Q_{rad}	*- Radiation Loss to Ambient -*	-	-	-	1,395	-	-	-	1,457	-	-	-	1,457	-	-	-	0	-	-	-	0
Q_{conv}	*- Convection Loss to Ambient -*	-	-	-	334	-	-	-	337	-	-	-	337	-	-	-	0	-	-	-	0
Q_{abs}	*- Solar Energy Absorbed -*	-	-	-	30,101	-	-	-	20,000	-	-	-	10,101	-	-	-	0	-	-	-	0
HEAT PIPE																					
1	Heat Pipe Conditions (Cumulative)	7.56	775	0.0349	30,101	5.02	775	0.0349	-	2.5204	775	4.92	-	0.00	730	0.0207	-	0	n/a	n/a	-
METAL HYDRIDE THERMAL ENERGY STORAGE																					
1	HTMH Media	-	745	1.45	-	-	745	1.45	-	-	745	1.45	-	-	730	1.19	-	-	745	1.45	-
Q_{chg}	*- HTMH Storage Duty -*	-	-	-	10,101	-	-	-	0	-	-	-	10,101	-	-	-	-20,000	-	-	-	0
2	Regenerator, HTMH Side	0.185	745	1.42	-	0	= f(t)	1.45	-	0.185	745	1.45	-	0.37		1.24	-	0	= f(t)	1.45	-
Q_{regen}	*- Regenerator Thermal Duty -*	-	-	-	1,950	-	-	-	0	-	-	-	1,950	-	-	-	3,900	-	-	-	0
3	Regenerator, LTMH Side	0.185		1.42	-	0	= f(t)	1.45	-	0.185		1.42	-	0.37	34.8	1.24	-	0	= f(t)	1.42	-
4	LTMH Media	-	38.7	1.42	-	-	38.7	1.42	-	-	38.7	1.42	-	-	34.8	1.24	-	-	38.7	1.42	-
Q_{LTMH}	*- LTMH Storage Duty -*	-	-	-	2,620	-	-	-	0	-	-	-	2,620	-	-	-	5,250	-	-	-	0
sCO_2 BRAYTON POWER CYCLE																					
1a	Precooler Outlet/Main Compressor Inlet	54.1	37	8	-	54.1	37	8	-	0	n/a	n/a	-	54.1	37	8	-	0	n/a	n/a	-
1b	Recompressor Inlet	36.1	60	8	-	36.1	60	8	-	0	n/a	n/a	-	36.1	60	8	-	0	n/a	n/a	-
W_{comp}	*- Main Compressor Work -*	-	-	-		-	-	-		-	-	-	0	-	-	-		-	-	-	0
2a	Main Comp. Outlet/LTR HP Inlet	54.1		25	-	54.1		25	-	0	n/a	n/a	-	54.1		25	-	0	n/a	n/a	-
W_{recomp}	*- Recompressor Work -*	-	-	-		-	-	-		-	-	-	0	-	-	-		-	-	-	0
2b	Recompressor Outlet	36.1		25	-	36.1		25	-	0	n/a	n/a	-	36.1		25	-	0	n/a	n/a	-
Q_{LTR}	*- LTR Thermal Duty -*	-	-	-	19,100	-	-	-	19,100	-	-	-	0	-	-	-	19,100	-	-	-	0
2c	LTR HP Outlet	54.1		25	-	54.1		25	-	0	n/a	n/a	-	54.1		25	-	0	n/a	n/a	-
2d	HTR HP Inlet	90.25		25	-	90.25		25	-	0	n/a	n/a	-	90.25		25	-	0	n/a	n/a	-
Q_{HTR}	*- HTR Thermal Duty -*	-	-	-	47,000	-	-	-	47,000	-	-	-	0	-	-	-	47,000	-	-	-	0
3	HTR HP Outlet/sCO_2 Preheater Inlet	90.25	545	25	-	90.25	545	25	-	0	n/a	n/a	-	90.25	545	25	-	0	n/a	n/a	-
$Q1_{Gen}$	*- sCO_2 Preheater Generating Duty -*	-	-	-	20,000	-	-	-	20,000	-	-	-	0	-	-	-	0	-	-	-	0
3a	sCO_2 Preheater Outlet/HTMH HEX Inlet	90.25	720	25	-	90.25	720	25	-	0	n/a	n/a	-	90.25	545	25	-	0	n/a	n/a	-
$Q2_{Gen}$	*- HTMH Generating Duty -*	-	-	-	0	-	-	-	0	-	-	-	0	-	-	-	20,000	-	-	-	0
4	HTMH HEX Outlet/Turbine Inlet	90.25	720	25	-	90.25	720	25	-	0	n/a	n/a	-	90.25	720	25	-	0	n/a	n/a	-
W_{turb}	*- Turbine Work -*	-	-	-		-	-	-		-	-	-	0	-	-	-		-	-	-	0
P_{elec}	*- Generator Electrical Power -*	-	-	-	10,000	-	-	-	10,000	-	-	-	0	-	-	-	10,000	-	-	-	0
5	Turbine Outlet/HTR LP Inlet	90.25		8	-	90.25		8	-	0	n/a	n/a	-	90.25		8	-	0	n/a	n/a	-
6	HTR LP Outlet/LTR LP Inlet	90.25		8	-	90.25		8	-	0	n/a	n/a	-	90.25		8	-	0	n/a	n/a	-
7	LTR LP Outlet	90.25	60	8	-	90.25	60	8	-	0	n/a	n/a	-	90.25	60	8	-	0	n/a	n/a	-
7a	sCO2 Precooler Inlet	54.1	60	8	-	54.15	60	8	-	0	n/a	n/a	-	54.15	60	8	-	0	n/a	n/a	-
$Q_{precool}$	*- sCO_2 Precooler Thermal Duty -*	-	-	-	4,200	-	-	-	4,200	-	-	-	0	-	-	-	4,200	-	-	-	0
GLYCOL HEAT TRANSFER LOOP																					
1	Heat Rejection HEX Outlet/Pump Inlet	272	32		-	100	32		-	172	32		-	136	45		-	0	n/a	n/a	-
W_{pump}	*- Glycol Loop Pump Power -*	-	-	-	15	-	-	-	5	-	-	-	9	-	-	-	7	-	-	-	0
2	Pump Outlet	272	32		-	100	32		-	172	32		-	136	45		-	0	n/a	n/a	-
3	Valve 1 Inlet	272	32		-	100	32		-	172	32		-	136	42		-	0	n/a	n/a	-
4	sCO_2 Precooler Inlet	100	32		-	100	32		-	0	n/a	n/a	-	136	42		-	0	n/a	n/a	-
$Q_{precool}$	*- sCO_2 Precooler Thermal Duty -*	-	-	-	4,200	-	-	-	4,200	-	-	-	0	-	-	-	4,200	-	-	-	0
5	sCO_2 Precooler Outlet/Valve 2 Inlet	100	43		-	100	43		-	0	n/a	n/a	-	136	50		-	0	n/a	n/a	-
6	Valve 1 Outlet to LTMH	172	32		-	0	n/a	n/a	-	172	32		-	0	n/a	n/a	-	0	n/a	n/a	-
7	Valve 2 Outlet to LTMH	0	n/a		-	0	n/a	n/a	-	0	n/a	n/a	-	136	50		-	0	n/a	n/a	-
8	LTMH Inlet	172	32		-	0	n/a	n/a	-	172	32		-	136	50		-	0	n/a	n/a	-
Q_{LTMH}	*- LTMH Thermal Duty -*	-	-	-	2,620	-	-	-	0	-	-	-	2,620	-	-	-	-5,250	-	-	-	0
9	LTMH Outlet	172	36		-	0	n/a	n/a	-	172	36		-	136	40		-	0	n/a	n/a	-
10	Valve 2 Outlet to Heat Rejection HEX	100	43		-	100	43		-	0	n/a	n/a	-	0	n/a	n/a	-	0	n/a	n/a	-
11	Heat Rejection HEX Inlet	272	39		-	100	43		-	172	36		-	136	45		-	0	n/a	n/a	-
W_{fan}	*- Heat Rejection Fan Power*	-	-	-	1,598	-	-	-	984	-	-	-	307	-	-	-	0	-	-	-	0
Q_{rej}	*- Heat Rejection HEX Thermal Duty -*	-	-	-	6,820	-	-	-	4,200	-	-	-		-	-	-	0	-	-	-	0

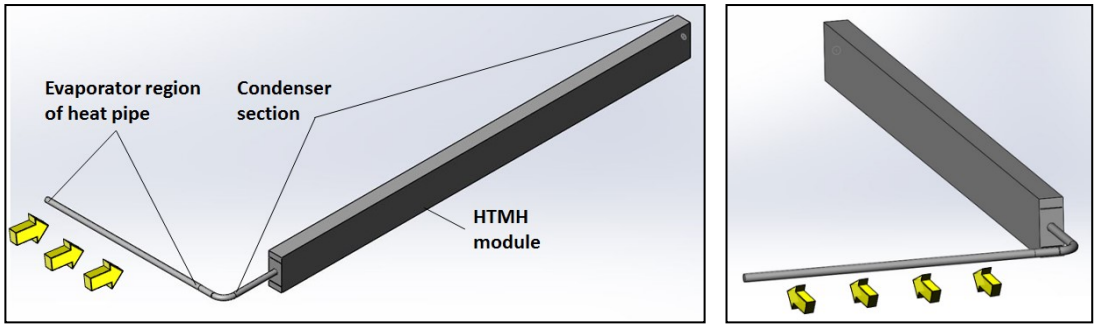

Figure 11 – Layout mages of a single absorber heat pipe and its corresponding TES module.

The full system consists of multiple instances of this same general layout, arranged such that the evaporator sections of the heat pipes form a full absorber surface. An example layout is shown in Figure 12, where half of the full absorber surface is formed via a vertical stack of horizontal heat pipes; a top-down view of this assembly is shown in Figure 13. A mirror image of this assembly – with the ends of the heat pipes butted up against each other – would form a complete absorber surface with the HTMH modules situated behind the absorber and insulation.

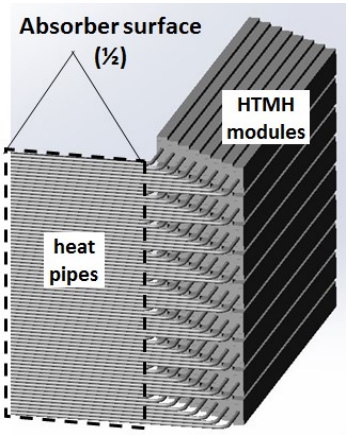

Figure 12 – Full heat pipe absorber and TSM layout.

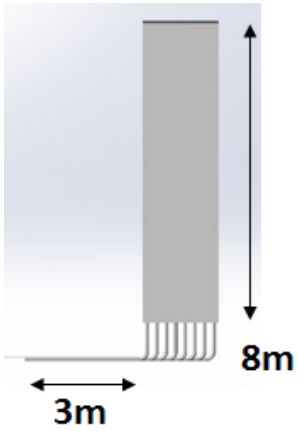

Figure 13 – Top view of full absorber and TES layout.

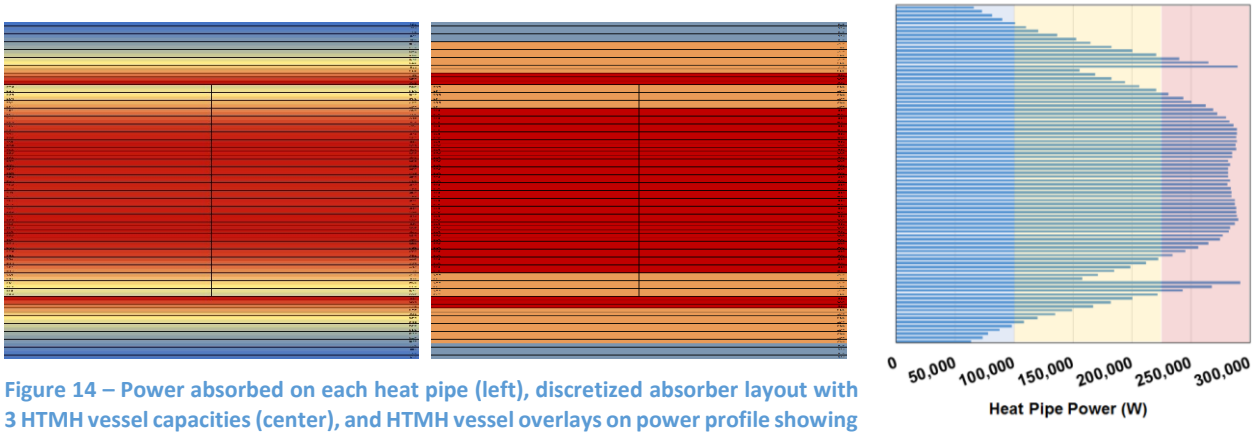

Figure 14 – Power absorbed on each heat pipe (left), discretized absorber layout with 3 HTMH vessel capacities (center), and HTMH vessel overlays on power profile showing the excess storage capacity for each pipe (right).

Due to the nature of the flux profile projected on the flat panel receiver, the flux incident on a given horizontal cross section of the absorber varies with the absorber's height (Figure 14). Trade studies were performed, indicating that with two different heat pipe geometries (a full absorber width and a half absorber width design) and three different HTMH vessel media capacities (100 kW (blue), 225 kW (orange), and 300 kW (red)), the full system can be constructed with a reasonably small finite number of heat pipe and vessel variations with only 13% excess HTMH media.

Note that a guiding principle of the heat pipe system is that the section of heat pipe inserted into the HTMH vessel is to be straight (no bends or curves). Adhering to this allows the heat pipe to be removed by sliding it out along its longitudinal axis; this allows to the possibility of replacing a single heat pipe should the need arise.

Milestone 1.1.2.1:

As an initial deliverable from the CAB, representative and documented field layouts that project ~37 MW_{th} of concentrated solar energy onto the top of the tower at design point conditions will be identified and approved.

Two different heliostat fields were proposed to meet the required thermal input, a north field and a surround field. These were both optimized around 32 MW_{th} thermal load, as the required heat input was updated throughout the project. In addition to specifying the field, modeling was also completed to determine the flux profile on the receiver for each of the different fields. It was determined that the north field would be a better solution as it requires a smaller receiver and results in a more efficient field.

SubTask 1.1.3:

Generate and exercise a thermo-hydraulic absorber model that will interface with the overall system thermo-hydraulic model. The model's enabling assumptions, operability range, and limitations will all be described and documented.

Up-tower Absorber + HTMH + sCO2 Heat Transfer

The predominant technical challenge to the success of this program is the development of an effective means of transferring the thermal energy absorbed in the solar receiver to both the HTMH media bed but also the power cycle sCO_2 working fluid. Ideally this is accomplished in such a way that both can happen in parallel, enabling concurrent electrical generation and TES charging.

Much of the first phase of this program focused on defining a design capable of accomplishing these challenging requirements. At present, there are two potential configurations that have been identified and analyzed, either of which are suitable for use in the system. Down selection to a final configuration will be performed on the basis of further performance studies, further refinement of their LCOEs, and any other pertinent consideration (such as safety, reliability, industry acceptance, etc.)

Table 4 provides an overview of the configuration options currently deemed viable from a technical perspective. Analyses have demonstrated that these options will meet the thermal performance requirements dictated by the program; further investigations will refine the performance differentiation as well as the LCOE associated with each design, allowing a final down-selection in Phase 2 of the program. The candidate designs are as follows:

Table 4 – Table of viable Absorber + HTMH + sCO_2 Thermal Transport options.

THERMAL TRANSPORT:	HEAT PIPE	HEAT TRANSFER FLUID	
Absorber Configuration	Heat Pipe	Gas Tube	
Thermal transport to sCO_2 via:	1. Preheat Section, and 2. Cells/Tubes Embedded in HTMH	1. Nested Cell HEX Design, and 2. HTF-sCO_2 HEX	Single Cell (Conventional) Heat Exchanger Design
Parasitic During TES Charge	No	Yes	Yes
Parasitic During TES Discharge	No	No	Yes
Concurrent Generate + Charge	Yes	Yes	Yes

- **A heat pipe absorber design**. In this configuration, concentrated solar energy is absorbed by the evaporator section of sodium heat pipes. The condenser end of the heat pipe has two distinct regions; a section that conveys heat into the sCO_2 cycle working fluid, and a section embedded in the HTMH.
- **A heat transfer fluid loop design**. This design, pursued in light of the promising technical evaluation performed at the Gen 3 Receiver Roadmapping Workshop, utilizes a gas receiver design circulating a heat transfer fluid. The heat transfer fluid conveys the thermal energy to the HTMH and to the cycle sCO_2 working fluid. Two configuration variants of this concept are being considered in parallel; layout and operational differences exist between the two variants, but the analyses have thus far not clearly identified the preferable design.

These configurations are discussed in detail below.

Heat Pipe Architecture

Figure 15 shows the heat pipe and HTMH vessel module described above, with labels indicating where along the heat pipe length evaporating and condensing is occurring during on-sun operation. Speaking broadly, liquid sodium returning from the condenser flows into the evaporator (the entire assembly may be tilted slightly to provide gravity drainage), where it is wicked around the inner perimeter. The liquid boils off the heated surface with the addition of the concentrated thermal energy, and the vapor flows in the direction of the pressure gradient towards the condenser. In the condensing section heat rejection into the HTMH removes heat and cools the local vapor, causing it to condense on the heat pipe walls. Liquid sodium collects and flows back to the evaporating section so the loop can be repeated.

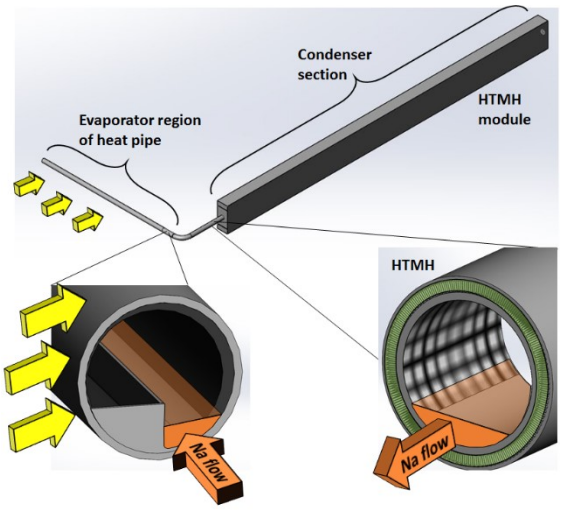

Figure 15 – Evaporator and condensor sections of the heat pipe absorber tube.

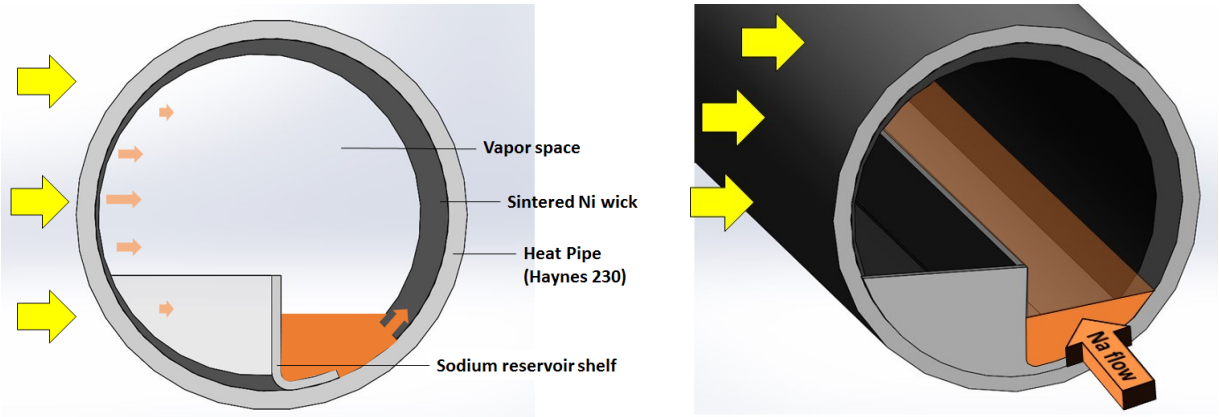

Figure 16 – Cutaway details of the evaporator section of the heat pipe absorber. An internal feature guides return flow along tube axis, while a sintered Ni wick transports fluid over the entire irradiated surface.

Figure 16 depicts the evaporating section of the heat pipe – where the concentrated solar energy is absorbed – in detail. Inside the heat pipe is a sintered Ni wick, which ensures that liquid sodium is transported around the inner circumference of the pipe and maintains a fluid presence at every point. The incoming energy is incident on one half of the heat pipe, where it is absorbed by the metal and boils the liquid sodium in local proximity. As the liquid is boiled off, the wick ensures that more liquid sodium replaces it so that all heated surfaces have a ready supply of available liquid. A feature along the bottom of the heat pipe provides a path for liquid sodium returning from the condenser to flow freely, wetting the wick along the entire evaporator length.

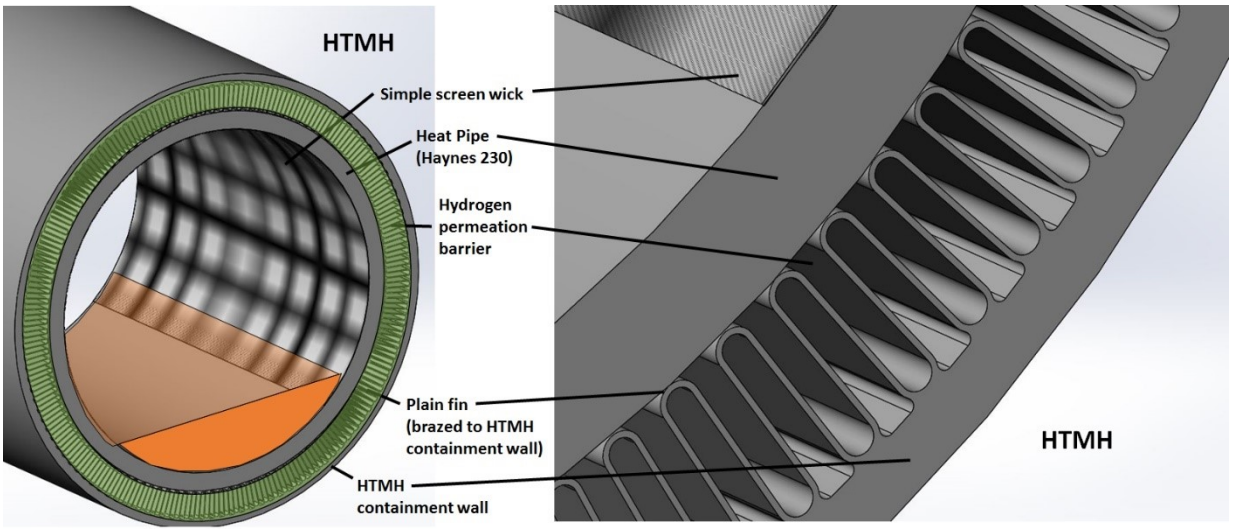

Figure 17 – Cutaway details of the condenser section of the heat pipe absorber. A simple screen wick collects condensed sodium and conveys it to the return channel. A permeation barrier – shown here as a finned structure, but likely to be a porous media fill – surrounds the heat pipe to prevent hydrogen ingress.

Figure 17 shows a close-up of the condensing section of the heat pipe. The internal structure is somewhat simpler, as there is a simple mesh wish designed to ensure that condensation can occur everywhere along the surface easily. Again, the condensed fluid is allowed to flow freely back along the gravity gradient towards the condenser. External to the heat pipe, however, there is an additional structure consisting of a finned annulus. This finned annulus acts as a permeation barrier, preventing the ingress of hydrogen into the heat pipe.

Heat Pipe sCO2 Heater

It is critical to note that when the heat pipe absorber is not illuminated, the heat pipes passively become nonoperational. Without heat addition sodium boiling ceases, and condensed sodium remains in its liquid state; this "shuts off" the heat pipes. The advantage of this feature is that during off-sun hours, there is no heat transfer from the rest of the system back to the absorber. As a result, there is no ongoing absorber heat loss to ambient once there is no solar input into the system.

It is desirable to have the ability to convey heat directly from the heat pipe into the sCO_2 working fluid, for two reasons:

1. For the system to operate in generation-only mode – in which heat is to be added to the sCO_2 working fluid but not to the HTMH media
2. To preheat the sCO_2 entering the HTMH vessel during combined generation/charging mode; if the sCO_2 were to enter the HTMH vessel at its receiver inlet temperature of 545°C temperature, it would locally depress the media temperature and prevent it from reaching its operating temperature.

Two options for enabling upstream heat transfer from the heat pipe into the sCO_2 are:

1. Where the cold sCO_2 enters the HTMH vessel at its inlet temperature, the vessel is filled with a conductive medium instead of the HTMH media. This media allows heat from the heat pipe to conduct directly into the sCO_2 channels without passing through intervening HTMH media. The sCO_2 can be heated to the HTMH operating temperature before it reaches the HTMH, ensuring that the full volume of HTMH will be thermochemically usable.

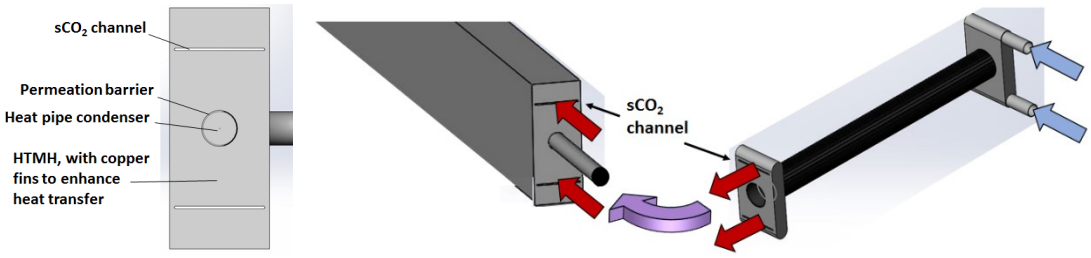

Figure 18 – sCO_2 preheater consisting of an annular heat transfer channel outboard of the heat pipe.

2. An upstream annular heat exchanger section – shown in Figure 18 – preheats the sCO_2 prior to entering the HTMH vessel. This preheater may consist of an annular folded fin construction that enhances the heat transfer and provides structural support to the sCO_2 flowpath. The tolerances of the system are designed such that the heat pipe may be inserted directly through the central core of the annulus, preserving the ability to remove and repair/replace any heat pipe if necessary. A potential construction is shown in Figure 19.

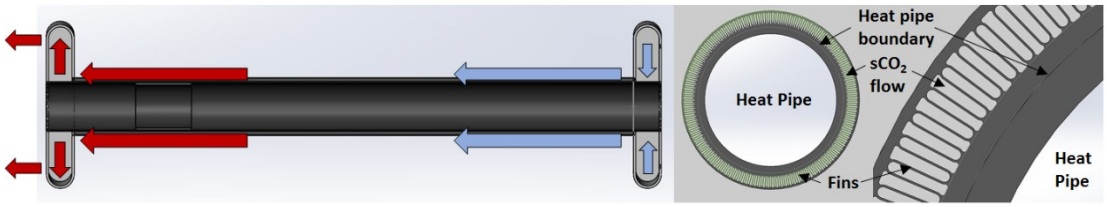

Figure 19 – Cutaway views of the sCO2 preheater mounted on the heat pipe.

Figure 20 and Figure 21 show sketches of possible sCO_2 channel architectures within the HTMH vessel; these allow the HTMH to heat the working fluid during TES discharge mode; the geometry and spacing of the sCO_2 paths is critical to ensure an acceptable temperature gradient limit within the HTMH and the required heat transfer between the media and the sCO_2 is achieved.

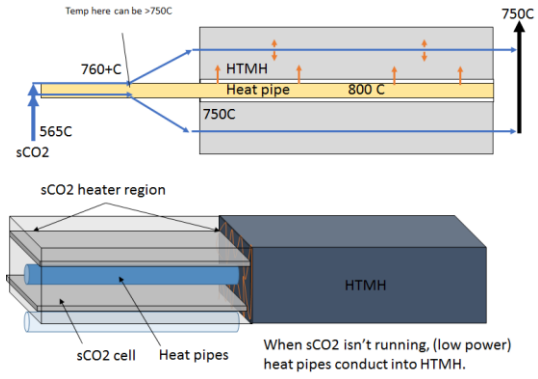

Figure 20 – Alternative preheater configuration for use with internally-supported sCO_2 cells.

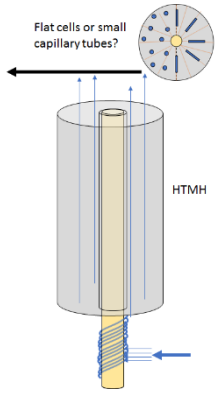

Figure 21 – Vessel-based HTMH module

Hydrogen Permeation and Recovery

Due to the elevated operating temperature and the ample availability of hydrogen within the metal hydride media, hydrogen permeation will occur; the prevailing concerns with respect to this system are:

- Ingress of hydrogen into a heat pipe will compromise its performance, ultimately resulting the system ceasing to operate as intended
- The loss of hydrogen from the metal hydride system will, over time, compromise the performance of the TES; removing hydrogen reduces the capacity of the system to transport and storage energy.

In accordance with advice from Thermacore, a thin porous media layer will be employed between the outside of a heat pipe and a pressure boundary sleeve in the HTMH tank. While permeation out of the system is still a concern, the permeation through the porous media into the heat pipe can be controlled to the point that it becomes negligible.

For the heat pipe design, two remediation strategies would be employed to protect the heat pipes from contamination. These are:

- **Porous media layer** – An annular channel around the heat pipe is filled with a porous media (spherical media, loose pack, porosity = 0.4, material = Al_2O_3), as

shown in Figure 22. The porous media provides good thermal contact between the inner wall (the heat pipe wall) and the outer wall (the HTMH shell) of the annulus, minimizing the thermal resistance and the corresponding temperature gradient across the annulus. The low-H_2-partial-pressure gas voids within the porous media provide a sink for permeating hydrogen, such that the hydrogen will preferentially diffuse into the gas rather than continue to permeate through the media towards the heat pipe. Circulation of gas ensures that the local H_2 partial pressure remains low for continued hydrogen capture; while this hydrogen-laden gas may be vented to atmosphere, reclamation methods for the captured H_2 are being considered.

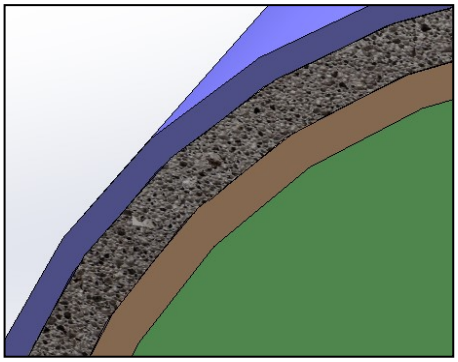

Figure 22 – Heat pipe annulus with porous media permeation barrier. The heat pipe wall is shown in brown, with the sodium vapor in green. The HTMH is in the white region, with the grey porous media protecting the heat pipe from hydrogen ingress.

- **Coatings** – A thin ceramic or oxide layer may impede the permeation of hydrogen – though the high temperatures and pressures suggest limits to the efficacy of this method. This technique requires more research, but newer sources suggest that coatings may reduce permeation rates by 4-5x as compared to uncoated surfaces.

In addition to the porous media solution described above, a folded finned solution – whereby the annular gap contained IN625 extended surfaces that were brazed to the HTMH sleeve and contact-fit to the heat pipe, as shown in Figure 23 and Figure 24 – were evaluated. Wall thickness requirements were specified using a Hoop Stress (s_t) model and Creep characteristics of material at maximum operating temperature and differential pressure, with an additional 15% safety margin imposed. For calculating the performance of the configuration radiation was included as parallel resistance to the extended surface conduction/convection term.

A thermal resistance analysis was conducted for the various annular permeation barrier methods considered to determine which would be most advantageous in the system with regards to thermal performance and pressure drop (which is an indicator of pumping parasitic). The results indicated that the optimal permeation barrier architecture consists of a porous media fill in the annular gap, and a flow loop that enables natural convection cells to establish. This gaseous circulation can carry any permeated hydrogen out of the annulus, while still ensuring that the thermal resistance across the barrier remains low; the thermal resistance across from the sodium vapor to the HTMH with the porous media fill annular barrier (0.10 K/W-m) is only twice that of the coated pipe alone (0.05 K/W-m). With

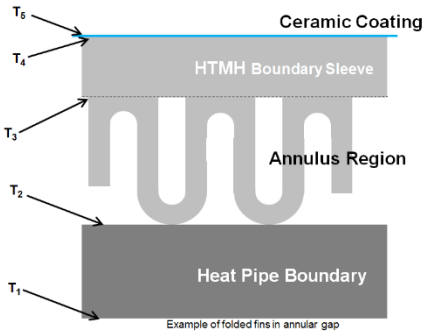

Figure 23 – Schematic of a folded-fin heat pipe annulus permeation barrier

twice the thermal resistance the temperature gradient across the system is only a few degrees, which is acceptable. Note that the annular gap permeation barrier – which has been strongly encouraged by Thermacore – has additional benefits:

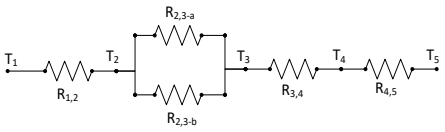

Figure 24 – Thermal circuit for the folded-fin heat pipe annulus permeation barrier

- The permeation barrier may be designed such
- That the heat pipes are inserted straight into the sleeves; this enables the simple removal and replacement of individual heat pipes within the system without having to breach the MH system
- The hydrogen collected within the annular gap may be recaptured and reclaimed periodically. This may be accomplished via several methods:
    - The gap may be evacuated such that its internal pressure is very low. A pump may be set to engage when the partial pressure within that evacuated gap reaches a predefined threshold, indicating that the partial pressure of permeated hydrogen has exceeded its allowable level. The pump discharges the captured hydrogen back into the dehydrogenated HTMH bed, evacuating the annular gap once again. This scheme is shown schematically in Figure 25.

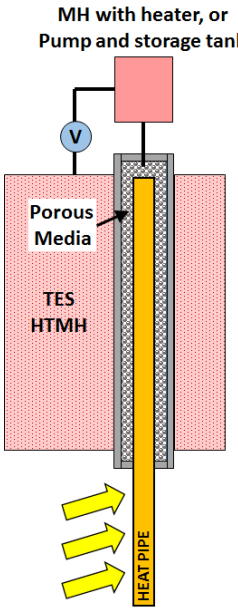

Figure 25 – Schematic of H_2 recovery system

    - A chemical getter may be incorporated into the annular porous media flow loop (for example a small HTMH bed, possibly of a different formulation, will absorb available permeated hydrogen). Periodically and in accordance with favorable conditions the captured hydrogen may be re-introduced into the HTMH bed; if done when the HTMH is hydrogen depleted and at low pressure, the reintroduction of hydrogen may even be performed passively, necessitating no additional pumping parasitic; alternatively the chemical capture bed may be reheated to facilitate the transfer of hydrogen back into the main TES.

The rate of hydrogen loss due to permeation is extremely temperature dependent.

Because of this, the majority of loss will occur at the heat pipes where temperature is highest. Table 5 shows losses for uncoated pipes.

Table 5 – Uncoated pipe hydrogen loss rates

		HEAT PIPE OPERATING TEMP. (°C)		
HYDROGEN LOSS		700	800	900
per heat pipe	g/hr	0.455	1.182	2.61
per 150 heat pipes	g/hr	68.25	177.3	391.5
per 150 heat pipes per day	g/day	546	1418.4	3132
% of total system H2 lost	%/day	0.013%	0.034%	0.075%

If a coating is applied, these losses are expected to decrease by a factor of 4-5. Using a different high temperature alloy (IN-800) may also reduce permeation by a factor of 2.

Adding fins in the HTMH is necessary to dissipate heat and keep the temperature down. The increased surface area from adding fins within the HTMH increases permeation out of the vessel. The required fins are expected to increase permeation by a factor of 2-3.

Milestone 1.1.3.1:

An absorber architecture that, at design point, maintains a metal temperature ≤ 800^0C while receiving the specified ~37 MW_{th} of incoming solar energy and conveying it to the sCO_2 working fluid and the HTMH media.

A heat pipe receiver architecture which operates at a nominal 775°C temperature was developed. The duty for the receiver was reduced to 30MW_{th} to better match the energy requirement of the power cycle instead of the 37MW_{th} initially specified. Results from design point modeling are given in Table 3.

SubTask 1.1.4:

Identify candidate options for conveying the required rate of thermal energy from sCO_2 working fluid to the HTMH – including but not limited to primary surface contact, extended surfaces (fins, pins, etc.), heat pipe-type designs, convective fluid circulation, etc. – and evaluating the options on the basis of performance, cost, risk, and complexity. Viable options will be rank-ordered using a weighted concept scoring matrix according to the operational priorities and weighted established by the Commercial Advisory Board in M 1.1.8.3, and generate a corresponding thermo-hydraulic model.

Indirect Heat Transfer Fluid Loop System Overview

An alternative receiver design scheme – the intermediate heat transfer fluid loop concept – has received significant attention lately. In this design, the concentrated solar energy from the heliostat field is absorbed by a heat transfer fluid circulating through the receiver. This HTF then flows to the intended thermal sink; in this application that may be either the HTMH media bed – in which case the energy will be used to charge the TES – or the power cycle sCO_2 working fluid, in which case the energy will be used to generate electricity. In an ideal system, the disbursement of the incoming energy may be apportioned in any split between the two sinks.

A schematic of the HTF loop system configuration is shown in Figure 26. Note that in this schematic there are only two Absorber + HTMH + sCO_2HEX modules depicted; in actuality there would be considerably more modules. A total of 60 modules have been used in the systemic analysis, though this quantity may be optimized further later in the program. The two modules are representative of the entirety of the system, though: the first absorber module may be slightly larger to overcome the ineffectiveness of the HTF recuperator, but all subsequent modules will be identical in their statepoints.

The conditions at each of the statepoints shown in Figure 26 are shown in Table 6. Note that missing values are not necessary to calculate the pertinent performance results.

An extensive analysis was performed to evaluate the best working fluid for this system; air, carbon dioxide, hydrogen, helium, and argon were all considered. Of those, the optimal selection based on a combination of heat transfer properties, pressure drop characteristics, and associated pumping power requirements turned out to be carbon dioxide; however, the carbon dioxide does

not need to be in a supercritical state, which eliminates the need to accommodate extremely high pressures.

Based on these temperature, flows, and parasitics, the design point conversion efficiency (incident solar to electric) for this design is calculated to be 42.1%.

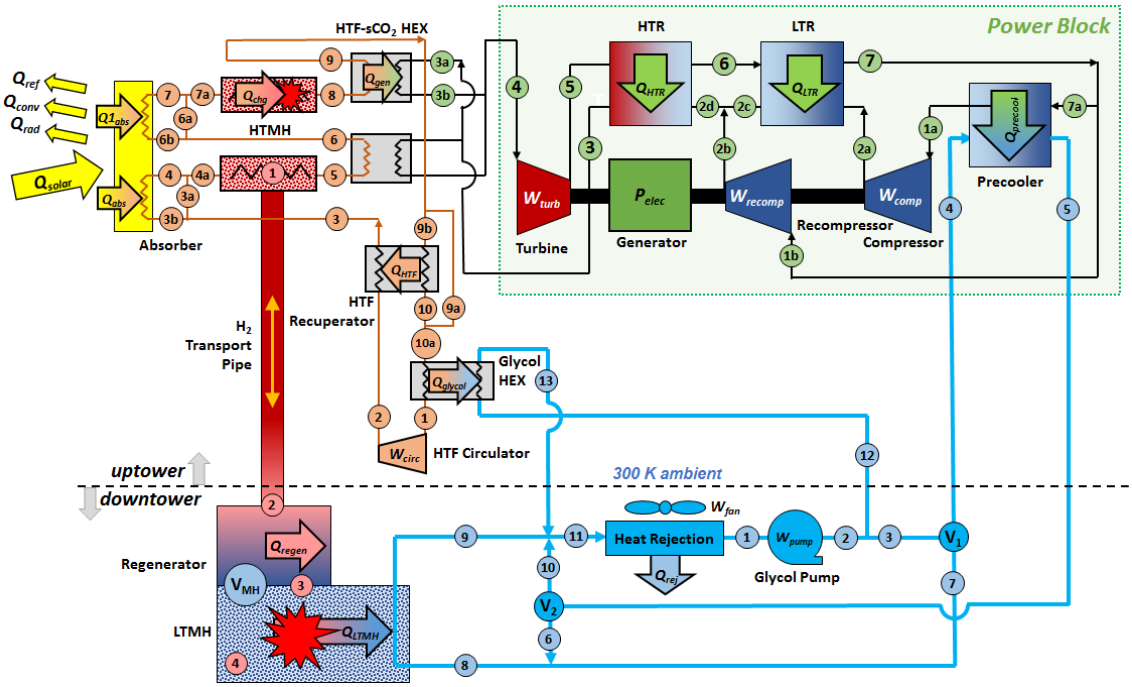

Figure 26 – Schematic for the Indirect HTF Loop system (2 of 60 Absorber+HTMH+HEX modules shown).

Table 6 – Conditions for each of the statepoints identified in Figure 26. Note that missing values are not required to calculate pertinent system performance metrics.

HTF LOOP CONFIG., SEPARATE HTMH HEX		CHARGING + GENERATING				GENERATING ONLY				CHARGING ONLY				DISCHARGING + GENERATING				STORAGE ONLY			
ID	DESCRIPTION	FLOW (kg/s)	TEMP. (C)	PRESS. (MPa)	DUTY (kW)	FLOW (kg/s)	TEMP. (C)	PRESS. (MPa)	DUTY (kW)	FLOW (kg/s)	TEMP. (C)	PRESS. (MPa)	DUTY (kW)	FLOW (kg/s)	TEMP. (C)	PRESS. (MPa)	DUTY (kW)	FLOW (kg/s)	TEMP. (C)	PRESS. (MPa)	DUTY (kW)
SOLAR PARAMETERS																					
Q_{solar}	- Incident Solar Energy -	-	-	-	33,753	-	-	-	23,341	-	-	-	13,442	-	-	-	0	-	-	-	0
Q_{ref}	- Reflection Loss to Ambient -	-	-	-	1,548	-	-	-	1,548	-	-	-	1,548	-	-	-	0	-	-	-	0
Q_{rad}	- Radiation Loss to Ambient -	-	-	-	1,457	-	-	-	1,457	-	-	-	1,457	-	-	-	0	-	-	-	0
Q_{conv}	- Convection Loss to Ambient -	-	-	-	337	-	-	-	337	-	-	-	337	-	-	-	0	-	-	-	0
Q_{abs}	- Solar Energy Absorbed -	-	-	-	30,101	-	-	-	20,000	-	-	-	10,101	-	-	-	0	-	-	-	0
ABSORBER																					
1	Tube Absorber Surface (Cumulative)	-	784	-	30,101	-	784	-	-	-	784	-	-	-	n/a	-	-	0	n/a	n/a	-
HEAT TRANSFER FLUID INTERMEDIATE LOOP																					
1	HTF Glycol HEX Outlet/Circulator Inlet	10.62	141	4.24	-	7.28	141	4.86	-	3.64	141	4.62	-	0	n/a	n/a	-	0	n/a	n/a	-
W_{circ}	- Circulator Electrical Power -	-	-	-	296	-	-	-	198	-	-	-	99	-	-	-	0	-	-	-	0
2	Circulator Outlet/HTF Recup HP Inlet	10.62	161	5	-	7.28	161	5	-	3.64	161	5	-	0	n/a	n/a	-	0	n/a	n/a	-
Q_{HTF}	- HTF Recuperator Thermal Duty -	-	-	-	6,865	-	-	-	4,577	-	-	-	2,288	-	-	-	0	-	-	-	0
3	HTF Recup HP Outlet	10.62	709	5	-	7.28	709	5	-	3.64	709	5	-	0	n/a	n/a	-	0	n/a	n/a	-
3a	First Absorber Bypass	0	n/a	n/a	-	0	n/a	n/a	-	0	n/a	n/a	-	0	n/a	n/a	-	0	n/a	n/a	-
3b	First Absorber Inlet	10.62	709	5	-	7.28	709	5	-	3.64	709	5	-	0	n/a	n/a	-	0	n/a	n/a	-
Q_{abs}	- First Pass HTF Thermal Heating Duty -	-	-	-	502	-	-	-	20,000	-	-	-	10,101	-	-	-	0	-	-	-	0
4	First Absorber Outlet	10.62	780	4.998	-	7.28	745	4.998	-	3.64	750	5.000	-	0	n/a	n/a	-	0	n/a	n/a	-
4a	First MTMH HEX Inlet	10.62	780	4.998	-	7.28	725	4.998	-	3.64	750	5.000	-	0	n/a	n/a	-	0	n/a	n/a	-
Qf_{gen}	- MTMH Generating Duty -	-	-	-	0	-	725	-	0	-	-	-	10,101	-	-	-	0	-	-	-	0
5	First MTMH HEX Outlet/First HTF-sCO$_2$ HEX Inlet	10.62	745	4.992	-	7.28	745	4.997	-	3.64	745	4.999	-	0	n/a	n/a	-	0	n/a	n/a	-
$Q2_{gen}$	- HTF Generating Duty -	-	-	-	333	-	-	-	20,000	-	-	-	0	-	-	-	0	-	-	-	0
6	First HTF-sCO$_2$ HEX Outlet	10.62	721	4.987	-	7.28	721	4.994	-	3.64	745	4.999	-	0	n/a	n/a	-	0	n/a	n/a	-
6a	Last Absorber Bypass	0	n/a	n/a	-	0	n/a	n/a	-	0	n/a	n/a	-	0	n/a	n/a	-	0	n/a	n/a	-
6a	Last Absorber Inlet	10.62	709	4.26	-	7.28	709	4.87	-	3.64		4.62	-	0	n/a	n/a	-	0	n/a	n/a	-
Q_{chg}	- HTF Charging Duty -	-	-	-	167	-	-	-	20,000	-	-	-	10,101	-	-	-	0	-	-	-	0
7	Last Absorber Outlet	10.62	780	4.25	-	7.28	780	4.87	-	3.64	750	4.62	-	0	n/a	n/a	-	0	n/a	n/a	-
7a	Last HTMH HEX Inlet	10.62	780	4.25	-	7.28	780	4.87	-	3.64	750	4.62	-	0	n/a	n/a	-	0	n/a	n/a	-
8	Last HTMH HEX Outlet/Last HTF-sCO$_2$ HEX Inlet	10.62	721	4.25	-	7.28	721	4.87	-	3.64	745	4.62	-	0	n/a	n/a	-	0	n/a	n/a	-
9	Last HTF-sCO$_2$ HEX Outlet	10.62	709	4.24	-	7.28	709	4.86	-	3.64	745	4.62	-	0	n/a	n/a	-	0	n/a	n/a	-
9a	HTF Recuperator Bypass	0	n/a	n/a	-	0	n/a	n/a	-	0	n/a	n/a	-	0	n/a	n/a	-	0	n/a	n/a	-
9b	HTF Recup LP Inlet	10.62	709	4.24	-	7.28	709	4.86	-	3.64	745	4.62	-	0	n/a	n/a	-	0	n/a	n/a	-
10	HTF Recup LP Outlet	10.62	709	4.24	-	7.28	709	4.86	-	3.64	745	4.62	-	0	n/a	n/a	-	0	n/a	n/a	-
10a	HTF Glycol HEX Inlet	10.62	174	4.24	-	7.28	174	4.86	-	3.64	174	4.62	-	0	n/a	n/a	-	0	n/a	n/a	-
Q_{glycol}	- HTF Glycol HEX Thermal Duty -	-	-	-	59	-	-	-	39	-	-	-	20	-	-	-	0	-	-	-	0
METAL HYDRIDE THERMAL ENERGY STORAGE																					
1	HTMH Media	-	745	1.45	-	-	745	1.45	-	-	745	1.45	-	-	730	1.19	-	-	745	1.45	-
Q_{chg}	- HTMH Storage Duty -	-	-	-	0	-	-	-	0	-	-	-	0	-	-	-	0	-	-	-	0
2	Regenerator, HTMH Side	0.185	745	1.42	-	0	= f(t)	1.45	-	0.185	745	1.45	-	0.37		1.24	-	0	= f(t)	1.45	-
Q_{regen}	- Regenerator Thermal Duty -	-	-	-	1,850	-	-	-	0	-	-	-	1,950	-	-	-	3,900	-	-	-	0
3	Regenerator, LTMH Side	0.185		1.42	-	0	= f(t)	1.45	-	0.185		1.42	-	0.37	34.8	1.24	-	0	= f(t)	1.42	-
4	LTMH Media	-	38.7	1.42	-	-	38.7	1.42	-	-	38.7	1.42	-	-	34.8	1.24	-	-	38.7	1.42	-
Q_{LTMH}	- LTMH Storage Duty -	-	-	-	2,620	-	-	-	0	-	-	-	2,620	-	-	-	5,250	-	-	-	0
sCO$_2$ BRAYTON POWER CYCLE																					
1a	Precooler Outlet/Main Compressor Inlet	45.0	37	8	-	45.0	37	8	-	0	n/a	n/a	-	52.6	37	8	-	0	n/a	n/a	-
1b	Recompressor Inlet	30.0	60	8	-	30.0	60	8	-	0	n/a	n/a	-	35.1	80	8	-	0	n/a	n/a	-
W_{comp}	- Main Compressor Work -	-	-	-		-	-	-		-	-	-	0	-	-	-		-	-	-	0
2a	Main Comp. Outlet/LTR HP Inlet	45.0		25	-	45.0		25	-	0	n/a	n/a	-	52.6		25	-	0	n/a	n/a	-
W_{recomp}	- Recompressor Work -	-	-	-		-	-	-		-	-	-	0	-	-	-		-	-	-	0
2b	Recompressor Outlet	30.0		25	-	30.0		25	-	0	n/a	n/a	-	35.1		25	-	0	n/a	n/a	-
Q_{LTR}	- LTR Thermal Duty -	-	-	-	19,100	-	-	-	19,100	-	-	-	0	-	-	-	19,100	-	-	-	0
2c	LTR HP Outlet	45.0		25	-	45.0		25	-	0	n/a	n/a	-	52.6		25	-	0	n/a	n/a	-
2d	HTR HP Inlet	75.05		25	-	75.05		25	-	0	n/a	n/a	-	87.71		25	-	0	n/a	n/a	-
Q_{HTR}	- HTR Thermal Duty -	-	-	-	47,000	-	-	-	47,000	-	-	-	0	-	-	-	47,000	-	-	-	0
3	HTR HP Outlet	75.05	545	25	-	75.05	545	25	-	0	n/a	n/a	-	87.71	545	25	-	0	n/a	n/a	-
3a	HTF-sCO$_2$ HEX Inlet	1.25	545	25	-	1.25	545	25	-	0	n/a	n/a	-	1.46	545	25	-	0	n/a	n/a	-
$Q2_{gen}$	- HTF Generating Duty -	-	-	-	20,000	-	-	-	20,000	-	-	-	0	-	-	-	0	-	-	-	0
3b	HTF-sCO$_2$ HEX Outlet/HTMH HEX Inlet	1.25	725	25	-	1.25	725	25	-	0	n/a	n/a	-	1.46	545	545	-	0	n/a	n/a	-
Qf_{gen}	- HTMH Generating Duty -	-	-	-	0	-	-	-	0	-	-	-	0	-	-	-	20,000	-	-	-	0
3c	HTMH HEX Outlet	1.25	755	25	-	1.25	755	25	-	0	n/a	n/a	-	1.46	725	25	-	0	n/a	n/a	-
4	Turbine Inlet	75.05	755	25	-	75.05	755	25	-	0	n/a	n/a	-	87.71	725	25	-	0	n/a	n/a	-
W_{turb}	- Turbine Work -	-	-	-		-	-	-		-	-	-	0	-	-	-		-	-	-	0
P_{elec}	- Generator Electrical Power -	-	-	-	10,000	-	-	-	10,000	-	-	-	0	-	-	-	10,000	-	-	-	0
5	Turbine Outlet/HTR LP Inlet	75.05		8	-	75.05		8	-	0	n/a	n/a	-	87.71		8	-	0	n/a	n/a	-
6	HTR LP Outlet/LTR LP Inlet	75.05		8	-	75.05		8	-	0	n/a	n/a	-	87.71		8	-	0	n/a	n/a	-
7	LTR LP Outlet	75.05	60	8	-	75.05	60	8	-	0	n/a	n/a	-	87.71	80	8	-	0	n/a	n/a	-
7a	sCO2 Precooler Inlet	45.0	60	8	-	45.0	60	8	-	0	n/a	n/a	-	52.6	80	8	-	0	n/a	n/a	-
$Q_{precool}$	- sCO$_2$ Precooler Thermal Duty -	-	-	-	4,200	-	-	-	4,200	-	-	-	0	-	-	-	4,200	-	-	-	0
GLYCOL HEAT TRANSFER LOOP																45.03	0.00				
1	Heat Rejection HEX Outlet/Pump Inlet	282	32		-	107	32		-	175	32		-	148	45		-	0	n/a	n/a	-
W_{pump}	- Glycol Loop Pump Power -	-	-	-	15	-	-	-	6	-	-	-	10	-	-	-	8	-	-	-	0
2	Pump Outlet	282	32		-	107	32		-	175	32		-	148	45		-	0	n/a	n/a	-
3	Valve 1 Inlet	272	32		-	100	32		-	172	32		-	136	42		-	0	n/a	n/a	-
4	sCO$_2$ Precooler Inlet	100	32		-	100	32		-	0	n/a	n/a	-	136	42		-	0	n/a	n/a	-
$Q_{precool}$	- sCO$_2$ Precooler Thermal Duty -	-	-	-	4,200	-	-	-	4,200	-	-	-	0	-	-	-	4,200	0	n/a	n/a	0
5	sCO$_2$ Precooler Outlet/Valve 2 Inlet	100	43		-	100	43		-	0	n/a	n/a	-	136	50		-	0	n/a	n/a	-
6	Valve 1 Outlet to LTMH	172	32		-	0	n/a	n/a	-	172	32		-	0	n/a	n/a	-	0	n/a	n/a	-
7	Valve 2 Outlet to LTMH	0	n/a		-	0	n/a	n/a	-	0	n/a	n/a	-	136	50		-	0	n/a	n/a	-
8	LTMH Inlet	172	32		-	0	n/a	n/a	-	172	32		-	136	50		-	0	n/a	n/a	-
Q_{LTMH}	- LTMH Thermal Duty -	-	-	-	2,620	-	-	-	0	-	-	-	2,620	-	-	-	-5,250	-	-	-	0
9	LTMH Outlet	172	36		-	0	n/a	n/a	-	172	36		-	136	40		-	0	n/a	n/a	-
10	Valve 2 Outlet to Heat Rejection HEX	100	43		-	100	43		-	0	n/a	n/a	-	0	n/a	n/a	-	0	n/a	n/a	-
11	Heat Rejection HEX Inlet	282	36		-	107	42		-	175	36		-	148	45		-	0	n/a	n/a	-
W_{fan}	- Heat Rejection Fan Power	-	-	-	1,776	-	-	-	1,095	-	-	-	341	-	-	-	0	-	-	-	0
Q_{rej}	- Heat Rejection HEX Thermal Duty -	-	-	-	6,879	-	-	-	4,239	-	-	-	0	-	-	-	0	-	-	-	0
12	HTF Glycol HEX Inlet	10	32		-	7	32		-	3	32		-	10	45		-	0	n/a	n/a	-
Q_{glycol}	- HTF Glycol HEX Thermal Duty -	-	-	-	59	-	-	-	39	-	-	-	20	-	-	-	1,050	-	-	-	0
13	HTF Glycol HEX Outlet	10	34		-	7	34		-	3	34		-	10	45		-	0	n/a	n/a	-

By evaluating potential layouts an efficient and flexible configuration was identified, with the following flow scheme:

- The HTF circulates through multiple modules in series; each module consists of an absorber section, an HTMH media block, and an HTF-to-sCO$_2$ heat exchanger. Each module represents only a fraction of the entire power rating of the system – corresponding to the total power divided by the number of modules. This design selection ensures that the HTF flow rate can be small. From $Q = \dot{m}\, c_p \Delta T$ the flow rate is proportional to the heat rate for a given temperature rise. By reducing the mass flow, the parasitic can be reduced, increasing the overall system efficiency.
- The cycle sCO$_2$ working fluid is distributed among all of the modules in parallel; each module therefore raises its sCO$_2$ flow over the full temperature range, from its 545 ^{o}C inlet to its 745 ^{o}C outlet. Furthermore, by dividing the flow amongst many parallel units, the pressure drop across each unit can be very small, ensuring that the performance impact on the sCO$_2$ cycle is minimal.

Note that a small waste heat rejection heat exchanger must be incorporated into the HTF loop; this is required to overcome the pump and heat exchanger inefficiencies that would otherwise

cause the HTF temperature to rise continuously. Fortunately, integration with the existing glycol system is trivial.

During the April 2016 Department of Energy Gen 3 Receiver Roadmap workshop, the merits of the HTF loop were evaluated and presented. These benefits include:

- Systemic flexibility: Incorporating an independent flow loop between the solar absorber, the HTMH, and the sCO_2 working fluid provides a means of controlling the rate of heat transfer amongst any of them. This flexibility ensures that the greatest possible range of operating conditions – i.e. charging, discharging, generating, etc. – may be accommodated.
- User familiarity: while heat pipes are a proven and deployed technology, they have not to date seen wide application in the power generation or utility industries. As a result, the end users for this application are not familiar with their fundamentals or operation. By contrast, the circulation of a heat transfer fluid is a common and familiar element of most power plants, so the barrier to entry and acceptance for a design of this nature is commensurately lower.

Absorber Architecture

Initially the intention was to modify Brayton's SunShot sCO_2 receiver cells for use with the low(er) pressure CO_2 heat transfer fluid. However, important considerations quickly suggested that this solution was problematic:

1. In order to reduce the HTF circulation parasitic, a large number of modules are desirable (as described previously). As these modules must all be plumbed in series, the pressure drop through each module must be very small. A failure to abide by this principle results in either a prohibitively high pressure rise (and therefore parasitic) across the circulator pump, or a very high pressure requirement that imposes design challenges and cost implications similar to the sCO_2 power cycle through the entire HTF loop.
2. The actual absorber surface needs to be as small as practically possible; ideally, it needs to be the larger of (a) the size needed to capture the requisite reflected power from the heliostat field and (b) the size that distributes the requisite power over enough area to achieve acceptable peak flux levels. With that in mind, requiring the absorber to be as small as possible suggests that there is a limit to the cross sectional flow area that can be apportioned to each module.

Given that each module is nominally $1/60^{th}$ of the entire absorber area, that the absorber area needs to be as small as possible, and that the pressure drop through each module needs be very small, a large number of parallel paths per module is required. Preliminary analyses indicated that it is not feasible to achieve these competing objectives with Brayton's SunShot absorber cells; because these have high pressure drops per unit length a very large number of short parallel cells would be needed in each module. The cost and complexity of such a design, with its integral headering exposed to the

concentrated sunlight and the profound challenge of balancing the incident power on each module, suggested that another design would be preferable.

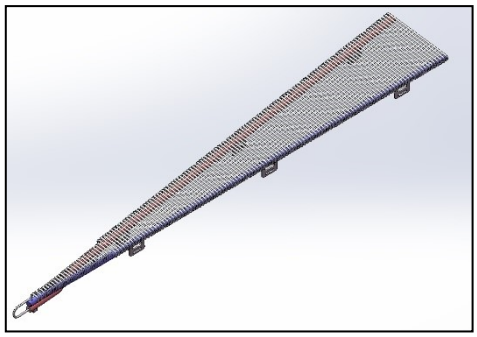

Figure 27 – An example tubular absorber section for a single Intermediate HTF loop module. Flow enters one of the two large manifold pipes, distributes through the large number of small parallel tubes, and collects in the other manifold. In the case of a 60-module system, each absorber section would consist of a 6° arc to collect 1/60th of the total incident power.

Because the HTF loop has a moderate fluid pressure of 5 MPa a tube-based design is feasible. Whereas the 25 MPa sCO_2 power cycle pressure would require thick-walled tubes that ultimately imposed deleterious through-wall temperature gradients and associated stresses, the lower pressure HTF loop uses tubes with reasonable wall thicknesses and consequently acceptable stresses. Recognizing that the flux profile on the planar absorber will have the same general form as that depicted in Figure 6, it is possible to define equal-power absorber sections that represent arc sections of a circular surface. For a system with 60 modules, each absorber section would be a radial 6 ° arc wedge of the entire circular absorber. An example absorber section architecture is shown in Figure 27. In this design the HTF flow enters one of the large manifolds and distributes in parallel through each of the myriad small absorber tubes before being collected in the other large manifold.

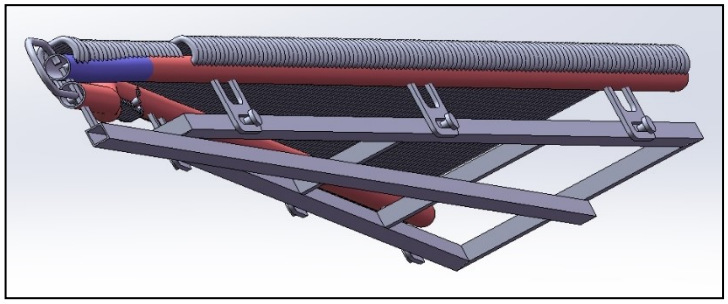

Figure 28 – View of absorber section support frame

Due to the proposed geometry, the shortest (and therefore highest flow) tubes are located in the highest flux region of the absorber. A thermal analysis shows that with 1.0 cm OD tubes and the tube wall thickness iteratively defined such that the worst case tube stress

ensures a 90,000 hour creep life, the design point HTF outlet temperatures across the full absorber section varies from 722 to 752 ^{o}C, with a peak wall temperature of 767 ^{o}C. Upon mixing at the outlet, the mass-averaged discharge temperature of the HTF is 741 ^{o}C. The pressure drop for the worst case HTF flow rate is 4.8 kPa, or < 0.1% DP/P per module on the nominal 5 MPa HTF pressure.

Note that there is a space between each of the parallel absorber tubes in the module; this gap is used to accommodate the quartz tubes that comprise Brayton's patented low-cost quartz window design to increase the efficiency by reducing the radiation and convection losses from the absorber to ambient. Figure 29 depicts a full absorber comprised of 60 instances of the tube-based module just described.

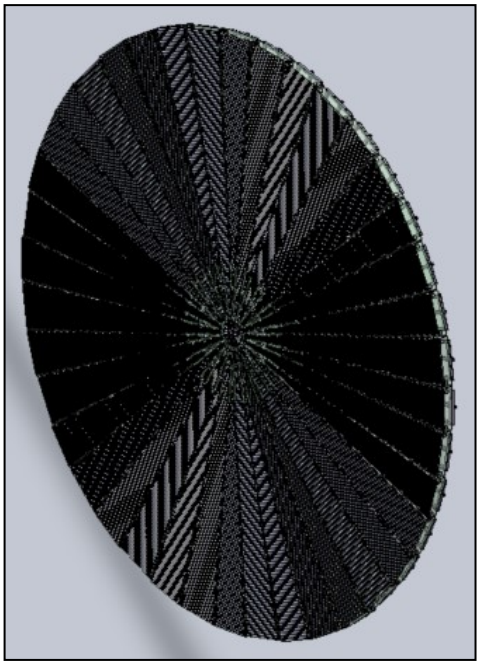

Figure 29 – Full HTF absorber layout, consisting of 60 modules arranged in radial arcs from the central hub.

HTMH Module

Having absorbed the prescribed fraction of the concentrated solar energy in the tube-based absorber module, the heat transfer fluid is conveyed into the HTMH module. This module is based on the Brayton heat exchanger architecture derived from its 2012-2016 SunShot sCO_2 Receiver program. However, whereas the standard fluid-to-fluid heat exchanger configuration shown in Figure 54 has the LP fluid flowing in the finned gaps between adjacent shells, the HTMH heat exchanger replaces this finned region with packed and enhanced HTMH media – this is shown graphically in Figure 30. The inter-cell spacing is determined based on design specifications, namely: a maximum 15 ^{o}C temperature gradient across the HTMH during operation, the worst case TES power (which corresponds to 20 MW_{th} during TES discharge), and the unit cell geometry (width, length, and number of cells) required to achieve not only the requisite heat transfer between the fluid and the HTMH but also the strict pressure drop requirement. For the nominal design point case defined in this Phase, that spacing is approximately 6 cm; that is, at the full discharge power conditions the HTMH module geometry is such that there will be no more than a 15 ^{o}C temperature gradient through the media. This geometry results in a 3 kPa pressure drop through each module at worst case HTF flow, or under 0.065% DP/P per module on the nominal 5 MPa HTF pressure.

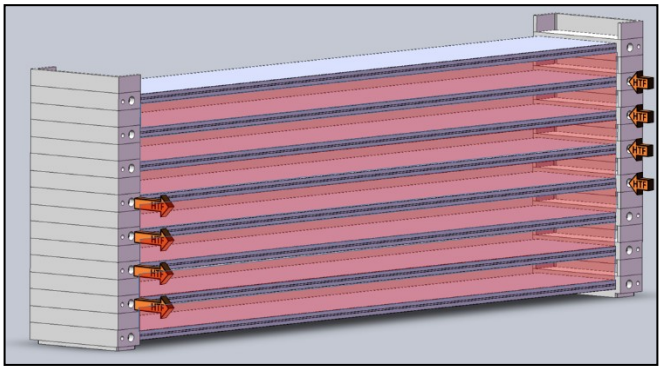

Figure 30 – Representative section of the HTMH heat exchanger module; internally-supported finned cells are sandwiched between HTMH media volumes, shown in red.

HTF-to-sCO2 Heat Exchanger Module

After passing through the HTMH module, the HTF enters a HTF-to-sCO_2 Heat Exchanger module, shown in Figure 31. This module is an ultra-high-pressure plate-fin heat exchanger design of the type developed during the course of Brayton's 2012-2016 SunShot sCO_2 Receiver program. This is a well-developed architecture that is a commercial offering, and represents little to no program risk. The pressure drop through each HTF-to-sCO_2 Heat Exchanger Module is 0.06%, or about 3.1 kPa per unit.

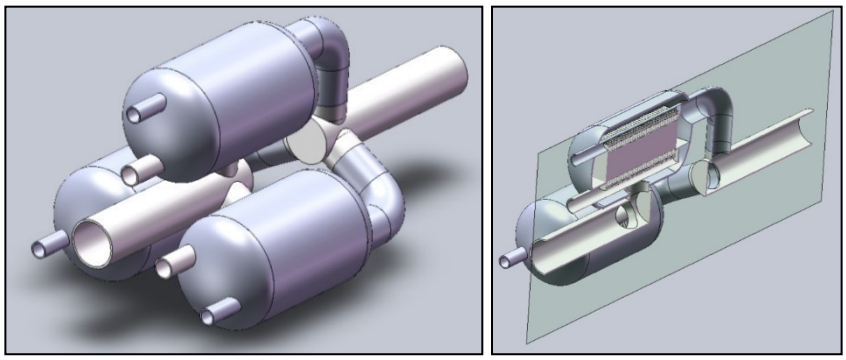

Figure 31 – HTF-to-sCO_2 Heat Exchanger Module

Integrated HTF Module

Figure 32 depicts 1 of the 60 integrated HTF modules, consisting of the absorber section, a HTMH heat exchanger pack corresponding to 1.3 MW_{th} of storage, and HTF-to-sCO_2 heat exchanger. This design provides a great deal of operational flexibility, and accommodates all of the operating profiles described in Table 6 specifically:

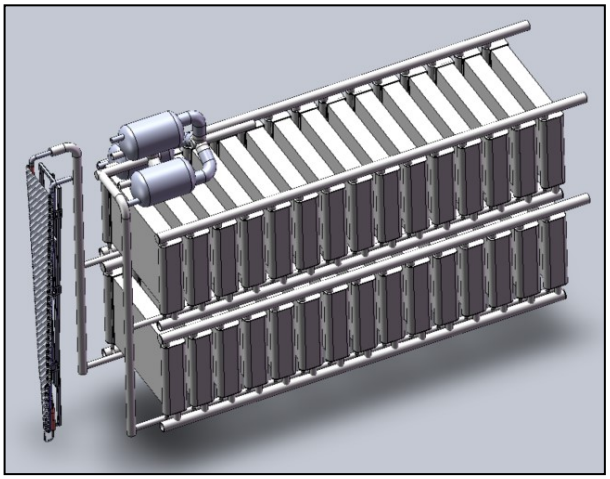

Figure 32 – One Receiver Module, consisting of an absorber arc, an HTMH Heat Exchanger pack, and an HTF-to-sCO_2 heat exchanger. Each HTMH heat exchanger stack depicted contains 10 HTF cells

- **To charge the TES and generate electricity concurrently**: solar input is absorbed to raise the full HTF flow to (10 MW_{th}) above the HTMH operating temperature at the absorber section discharge. That 10 MW_{th} worth of temperature is conveyed into the HTMH in the HTMH module, and the HTF leaves the HTMH module at its operating temperature (which is above the nominal sCO_2 power cycle TIT). The HTF then donates heat in counterflow heat transfer to the sCO_2 flow fraction in the HTF-to-sCO_2 heat exchanger module before returning to the absorber to enter the next module.
- **To charge the TES only**: solar input is absorbed to raise the HTF flow to [10 MW_{th}] above the HTMH operating temperature at the absorber section discharge. That 10 MW_{th} worth of temperature is conveyed into the HTMH in the HTMH module, and the HTF leaves the HTMH module at its operating temperature (which is above the nominal sCO_2 power cycle TIT). The HTF then passes through the HTF-to-sCO_2 heat exchanger module, but without

sCO_2 flow no additional heat transfer occurs. Finally, the HTF returns to the absorber to enter the next module.

- **To generate electricity only**: solar input is absorbed to raise the HTF flow to approximately the HTMH operating temperature at the absorber section discharge. Without a driving temperature difference no heat is conveyed into the HTMH in the HTMH module, and the HTF leaves the HTMH module with its temperature unchanged. The HTF then donates heat in counterflow heat transfer to the sCO_2 flow fraction in the HTF-to-sCO_2 heat exchanger module. Finally, the HTF returns to the absorber to enter the next module.
- **To discharge the TES and generate electricity**: the HTF flow bypasses the absorber altogether; this prevents heat loss from the absorber to ambient when there is no solar input into the system. The HTF enters the HTMH module at its warm inlet temperature, which is below the HTMH operating temperature. The HTMH proceeds to heat the HTF flow such that the HTF leaves the HTMH at approximately the HTMH operating temperature. . The HTF then donates heat in counterflow heat transfer to the sCO_2 flow fraction in the HTF-to-sCO_2 heat exchanger module. The HTF then bypasses the next absorber section to absorber to enter the next HTMH module.
- **During periods of storage**: there is no HTF flow; without flow through the absorber there is no heat loss to ambient. The well-insulated HTMH modules remain at high temperature, and there is no sCO_2 flow through the HTF-to-sCO_2

heat exchanger module.

HTF Circulation Loop

Incorporating an intermediate loop of heat transfer fluid necessitates supporting hardware. In addition to piping and valving this consists of three main components:

- **CIRCULATOR**: a gas circulator (of the type shown in Figure 33) is needed to induce the HTF

flow. In the specified case – which has not been optimized – the inlet fluid (CO_2 gas) enters at 4.1 MPa and 141 C and discharges at 5 MPa. This combination of temperature and pressure does not require development work by potential vendors. Table 7 shows the pressure losses through the full HTF loop.

- **RECUPERATOR**: Without the recuperator the pump would need to accommodate a 545 C fluid inlet temperature, which would dramatically increase both the capital cost and operating parasitic of the pump.

Table 7 – Pressure loss budget through the HTF loop.

PARAMETER	UNITS	VALUE	NOTES
Circulator Discharge Pressure	kPa	5,000	
DP, Circulator Recuperator HP	kPa	2.9	
DP, 60x HTF Modules	kPa	772.9	
DP, HTF Module	kPa	12.9	
Tube Absorber Section	kPa	4.8	1 cm OD tubes
HTMH HEX Pack	kPa	3.1	nested cell
sCO_2/HTF Recup HEX	kPa	4.9	
DP, Circulator Recuperator LP	kPa	1.3	
DP, Circulator Glycol HEX	kPa	4.5	
DP, Additional Losses	kPa	100.0	2% piping loss
Circulator Inlet Pressure	kPa	4,118	

Figure 33 – Example gas circulator

Instead, the heat is transferred into the circulator discharge flow, bypassing the circulator altogether.

- **GLYCOL HEAT EXCHANGER**: A small heat rejection heat exchanger is located between the recuperator and the circulator inlet. This unit is required to compensate for the inefficiencies of the heat exchangers and the pump; without some means of rejecting excess heat the temperature of the fluid loop would continue to rise during operation. The glycol loop may also, in conjunction with a bypass valve around the circulator recuperator, add extra heat to the LTMH to accelerate the discharge rate beyond that which can be sustained by the power

  cycle waste heat rejection alone.

Hydrogen Permeation and Recovery

As with the heat pipe configuration described previously, hydrogen egress out of the HTMH media is still a concern with the Intermediate HTF Loop layout. Therefore a chemical getter – such as a small HTMH bed – must be in intimate contact with the circulating HTF fluid. Permeated hydrogen can be absorbed in the getter bed, and then reinjected back into the HTMH periodically.

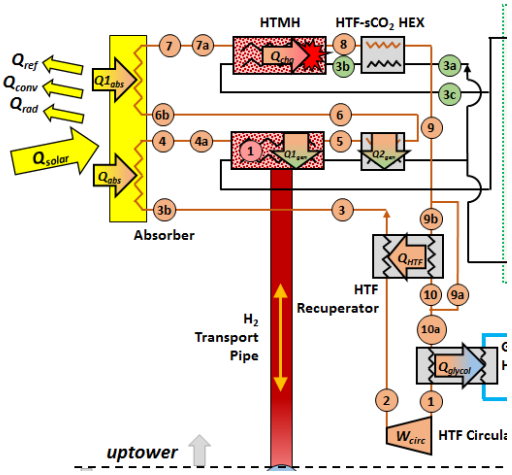

Figure 34 – Schematic of the nested cell HTMH design, which eliminates the need to circulate the HTF during TES discharge. It also eliminates the need for bypass valves around the absorber.

Alternative Configurations

As indicated in Table 4 the intermediate HTF loop configuration described above has a pumping parasitic even during TES discharge. An alternative configuration transfers heat directly from the HTMH into the power cycle sCO_2 working fluid (Figure 34), eliminating the need to circulate HTF during TES discharge and thereby eliminating a parasitic during off-sun generation. This also eliminates the need for bypass valves at the absorber as there would be no HTF flow during TES discharge. Brayton has identified potential HTMH heat exchanger architectures that achieve this; however, further details on this system are not reported here as most of the pertinent system details are identical to those reported for the HTF loop previously.

Milestone 1.1.4.1:

Identification of a Thermal Communication System for conveying 20 MW_{th} thermal energy between the sCO_2 working fluid and the HTMH media. Note that this full thermal transport requirement must be met for all cases over the full range of input variability.

A thermal transport system was designed using an intermediate heat transfer fluid (CO_2) to remove heat from the HTMH and convey it to the sCO_2 cycle. A moderate pressure of 5MPa is used in the intermediate heat transfer loop as a compromise between high density (low pumping power) and low pressure (low material costs). Table 6 shows that 20MW_{th} of heat transfer is

possible while in charging only mode, while generate only mode results in a heat transfer rate of $10MW_{th}$. This system is capable of supplying sufficient heat for all required state points.

Milestone 1.1.4.2:

Identification of a Thermal Communication System that does not exceed an HTMH temperature of 780 °C anywhere within the media.

A maximum fluid temperature is specified as 780°C out of the receiver which limits the temperature of the HTMH during the charging process. The HTMH to HTF heat exchanger is designed to have a maximum approach temperature of 15°C between the HTMH and HTF. With a design exit temperature from the HTMH HX of 745°C, this means the maximum HTMH temperature is 760°C as illustrated in Table 6.

SubTask 1.1.5:

Identify the specific and unique HTMH and LTMH formulations – hereafter referred to as the "selected formulation" for each – based on their cost, their chemical kinetics, and their performance in conjunction with the entire system. Furthermore, the selected formulations must be suitable for commercial scale-up, in that they may be readily acquired in suitable quantitates for full production.

Other elements critical to the success of this program are the material properties and chemical behavior of the selected MH formulations. Based on documented properties of the LTMH (TiMn1.5) and the preliminary modeled HTMH (CaSi) properties, a fully integrated system has been fully defined for design point operation. Figure 35 shows the charging and discharging interactions for the two materials, with the corresponding pressure gradient inducing the flow of released hydrogen from one MH bed to the other.

HTMH-LTMH Formulation Modeling

Results obtained from the first year of this project highlighted several important aspects related to the performance of the integrated HTMH-LTMH system configurations and to the LTMH formulations. An extensive literature review for possible LTMH materials was carried out during the first two quarters with several simulations carried out for some preliminary LTMH formulations. In particular, two materials were identified as possible LTMHs to be paired with the HTMH. In particular, a LTMH formulation (referred to as

LTMH2) was considered to be a very promising candidate LTMH. The material demonstrated excellent performance during system discharging (i.e. with hydrogen absorbed by the HTMH) but required operating temperatures on the order of 8-10 °C to achieve a good performance during system charging (hydrogen absorbed in the LTMH).

This makes the HTMH matching with the previously selected LTMH2 unfeasible under the dry-cooling power plant schematic. Three possible candidate LTMHs were down selected to operate under dry-cooling conditions; their properties and performance are reported and discussed herein.

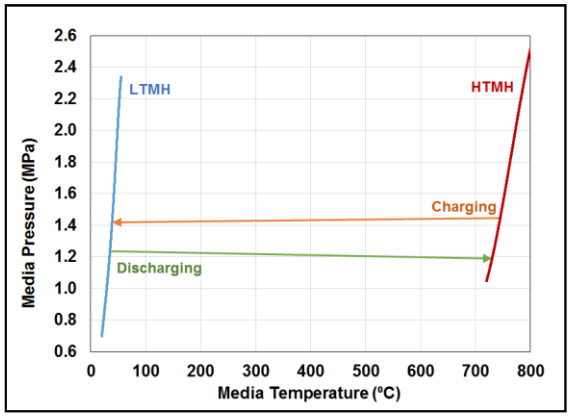

Figure 35 – The pressure gradients between the HTMH and LTMH during TES charging and discharging conditions.

A detailed transport phenomena model was developed during Quarter 2 and several HTMH-LTMH paired system configurations were examined and simulated. Initially the HTMH system was simulated as a separate unit to evaluate the performance of the system (in terms of actual charging/discharging capacity) and to find the best configuration. After that the coupled HTMH-LTMH system was examined and simulated. Many cases have been analyzed, mainly considering: (1) different configurations for the sCO_2 channel pairing with the HTMH material and the heat pipe system; (2) different finned structures to enhance the heat transfer properties of the HTMH system; (3) different LTMH material formulations included in the model. The details relative to the initial configurations as well as to the improved material and configurations can be found in the Quarters 2-4 reports and presentations. The current continuation document describes the final HTMH-LTMH configuration identified as the baseline configuration at the current status of the material development. Results of the charging/discharging process (in a continuous operation mode) are reported and discussed in the document.

A simplified 1-D steady state model has also been developed to assess the thermal distance of the enhanced thermal conductivity material to achieve a maximum temperature variation during hydrogen charging/discharging in the material.

LTMH Formulation

The dry-cooling power plant concept results in the heat transfer system operating conditions reported in Table 8 (with ethylene glycol mixture as the heat transfer fluid). After extensive literature data review, three LTMH material formulations were identified for coupling with the HTMH and the interfaced sCO_2 power plant. The three materials have been identified on the basis of the constraints given in Table 8, also paying particular attention at the thermal power required to absorb and release the hydrogen (i.e. material reaction enthalpy) and to material cost. The three materials (LTMHn1, LTMHn2 and LTMHn3) are shown in Table 9 with their thermodynamic and physical properties.

LTMHn1 was extensively examined during the Quarter 3. The material has an equilibrium

Table 8 – LTMH operating conditions for charging/discharging

pressure of 13.3 bar at about 30 °C, resulting in a low performance during system charging scenario, with reduced hydrogen flowing from the HTMH to the LTMH.

Scenario	Glycol mixture T (°C)	Required LTMH Pressure (bar)
System charging (i.e. hydrogen flowing from HTMH to LTMH)	≥ 30	≤ 10-15 (equilibrium pressure of HTMH at 720-770 °C)
System discharging (i.e. hydrogen flowing from LTMH to HTMH)	≤ 41	≥ 10-15 (equilibrium pressure of HTMH at 720-770 °C)

Simulations show low H_2 concentrations in the LTMHn1 during TES charging. The LTMHn2 ($TiMn_{1.5}$) and LTMHn3 ($(Ti_{0.8}Zr_{0.2})_{1.1}CrMn$) have similar characteristics in terms of operating equilibrium temperatures and pressures. Equilibrium T-P profiles for the two materials are reported in Figure 36 showing the pairing with the HTMH conditions.

Table 9 – Thermodynamic and thermo-physical properties of LTMHn1 ($Ti_{0.9}Zr_{0.1}Mn_{1.4}Cr_{0.35}V_{0.2}Fe_{0.05}$), LTMHn2 ($TiMn_{1.5}$) and LTMHn3 ($(Ti_{0.85}Zr_{0.15})_{1.1}CrMn$). References are: [23]–[26]

	LTMHn1	LTMHn2	LTMHn3	NOTES
ΔH (kJ/molH_2)	25.89	28.7	28.3	Literature data [1,2,4]
ΔS (J/molH_2-K)	106.9	114	111.8	Literature data [1,2,4]
Bulk density (kg/m^3)	3200	3129	3840	Estimated, with void fraction of about 50%
Thermal conductivity, bare (W/m-K)	0.35	0.35	0.35	Assumed values based on conservative assumptions for less conductive materials [3]
Thermal conductivity enhanced (W/m-K), 8-10wt% ENG added	7	7	7	Typical values achieved with ENG inclusion range between 7 W/mK to 10 W/mK [3]
Weight capacity (kg_{H2}/kg_{MH})	0.015-0.016	0.0153	0.015-0.016	Literature data [1,2,4]
Specific heat (J/kg-K)	500	500	500	Assumed, typical Ti based LTMH values

While these two LTMH materials (LTMHn2 and LTMHn3) have been selected, many similar materials exist with slightly different chemical element ratios or addition of small amounts of other elements (e.g. Zr, Al) that would result in other favorable thermodynamic properties (equilibrium pressure and temperature).

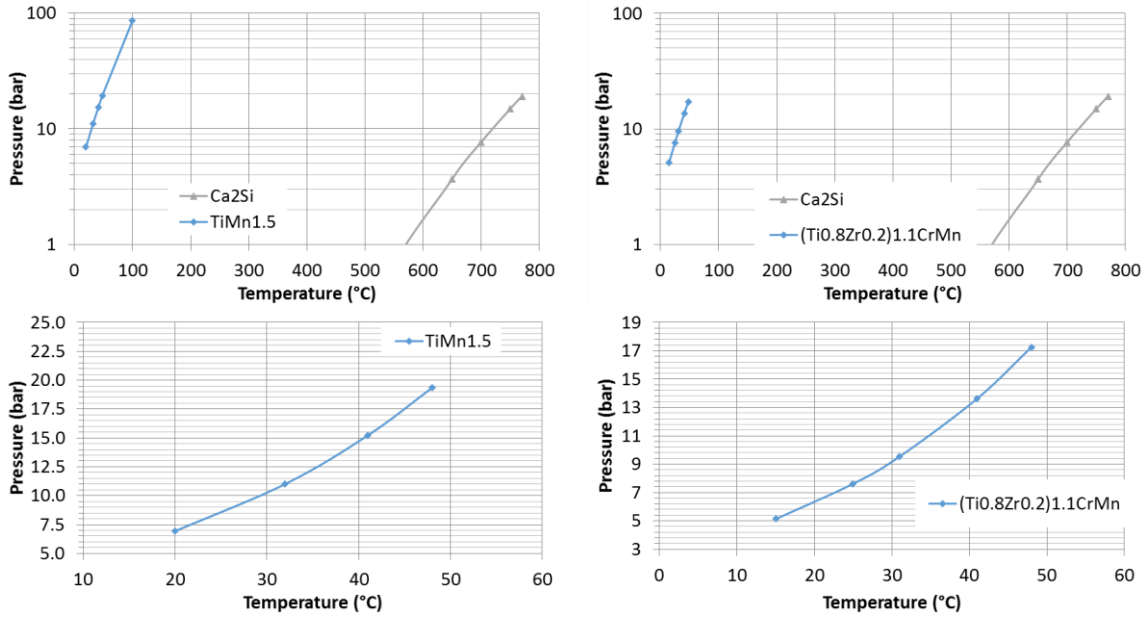

Figure 36 – Equilibrium temperature, pressure profiles for LTMHn2 and LTMHn3 paired with HTMH (Ca_2Si).

Preliminary cost calculations have been carried out for the two materials resulting in a raw material cost of 5.2 $/$kg_{Matl}$ for the LTMHn2 and 6.9 $/$kg_{Matl}$ for the LTMHn3. Based on the results obtained and on the data available in the literature, the LTMHn2 ($TiMn_{1.5}H_{2.47}$) has been selected

as the baseline material to be paired with the Ca_2Si HTMH. Kinetics expressions for the down selected LTMH have been established based on previously reported experimental data. [27] Figure 37 show LTMHn2 State of Charge (SOC) profiles during hydrogen charging (T=30 °C and P=11, 12.5 and 15 bar) and hydrogen discharging (T=41 °C and P= 11, 12.5 and 15 bar). Results reported in Figure 37 show that the LTMHn2 can be suitably paired with the HTMH in the operating pressure range of 10-15 bar and with the interfaced power plant equipment (glycol heat exchanger) in a temperature range of 30-41 °C.

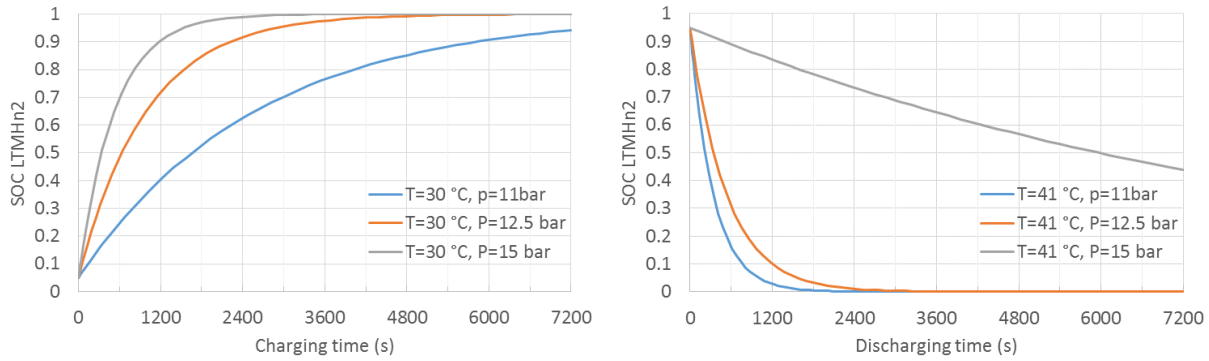

Figure 37 – LTMHn2 ($TiMn_{1.5}H_{2.47}$) State of Charge (SOC) profiles during hydrogen charging (T=281 K and P= 10, 15, 20 bar) and hydrogen discharging (T=318 K and P= 20, 25 bar)

The three LTMH materials can transfer the required hydrogen flow rate to the HTMH material during the system discharging (to drive the sCO2 power plant) at temperatures below 60 °C, as required in the Milestone 1.1.5.4. The conditions reported in Table 8 indicate operating conditions with temperature range between 30 °C and 41 °C. The materials also assure a reaction rate (multiplied by the material reaction enthalpy and material volume) lower than the corresponding thermal power available from the power plant as required by the Milestone 1.1.5.4. This will be shown in the Continuation Presentation, based on power plant configuration schemes, integrating the power plant, glycol loop and MH-TES system, developed by Brayton Energy in conjunction with SRNL.

The selected materials, part of the Ti-based AB2 class of MHs, showed excellent cycling performances with available cycling data showing no degradation for a number of cycles higher than 10,000 as required by the Milestone 1.1.5.5. This is documented by extensive data reported in the literature. An extensive cycling campaign for this class of materials was carried out at BNL by Johnson and Reilly in the late 1970's.[28] They paid attention in particular to Ti-Mn compounds with Fe inclusion. Their report shows the results obtained for long term cycling, showing that no degradation was observed as a function of time over a large number of cycles between 20,000 and 30,000 at temperatures between -1 °C and 100 °C. In addition there was no evidence for the formation of TiH_2 in the alloys as determined by x-ray diffraction analysis. Another long term cycling for AB2 class of MHs was carried out at University of Stuttgart in the mid 1990's by Friedlmeier et al [29] examining the long term cycling properties of different AB2 materials, in comparison with AB5 and MgNi materials. They specifically reported results for the following AB2 material: $Ti_{0.98}Zr_{0.02}V_{0.43}Fe_{0.09}Cr_{0.05}Mn_{1.5}$. A total of 42,400 cycles were carried out for this material by Friedlmeier et al at temperatures between 45 °C and 120 °C with pressures

between 2.6 MPa and 3.2 MPa. The authors showed this to be the only material which did not show any degradation for more than 40,000 cycles.

High Temperature Metal Hydride Material Properties

A critical aspect of the project, but easily overlooked, are the planned operational conditions of the system, specifically for the high temperature metal hydride bed, which present unique challenges to overcome when designing a vessel to conduct experiments. Due to the high temperatures involved (~750 °C), hydrogen gas permeation and embrittlement has to be considered. In addition, due to the heat involved, reliable sealing mechanisms are not trivial. Several iterations of designs with outside vendors were evaluated for the lab scale analysis of the new HTMH materials. The vessels purchased by outside vendors began to exhibit slow leaks after operation of the vessel at high temperatures and several assembly and disassembly steps. In order to circumvent this limitation, custom sample vessels were designed by SRNL staff and constructed. These reaction vessels have proven suitable for materials testing at these conditions.

To provide experimental densities of the HTMH material, several pellets were prepared over a range of applied pressures. For comparison, the tap density of the hydride was also measured. The dehydrogenated metal hydride showed signs of a plastic nature when pelletized. Once the necessary force was applied, the pellet press gauge almost immediately began to decrease implying the material was slowly conforming to the space in which it was confined. To maintain consistency across all pellets, the force was slowly maintained for a period of one minute. Table 10 displays density values for several pellets prepared as well as the tap density for dehydrogenated Ca_2Si.

Table 10 – Tap and pellet densities of dehydrogenated-Ca_2Si

APPLIED PRESSURE	SAMPLE #1 (g/cc)	SAMPLE #2 (g/cc)	SAMPLE #3 (g/cc)	AVERAGE (g/cc)	STD. DEV.	STD. ERROR
Tap	0.7683	0.7831	0.7752	0.7755	0.0074	0.0042
10 kPSI	1.3035	1.276	1.2764	1.2853	0.0157	0.0091
20 kPSI	1.3722	1.3378	1.3203	1.3434	0.0264	0.0153
40 kPSI	1.5164	1.5484	1.4958	1.5202	0.0265	0.0153

Thermal conductivity measurements were carried out on HTMH samples up to 200 °C (temperature limitation of this instrument) in an inert atmosphere glovebox. Because of the temperature limitations of this instrument, it was utilized as a means to screen potential thermal conductive enhancers for the HTMH, which were required due to its naturally low thermal conductivity. The additives considered were iron powder, copper power, flakes and fibers as well as expanded natural graphite (ENG). These measurements were performed using the TCi Thermal Conductivity Analyzer by C-Therm Technologies™. The instrument employs a one-sided, interfacial heat reflectance sensor that applies a momentary constant heat source to the sample. A typical measurement pulse is 1 to 3 seconds. Thermal conductivity is measured directly, providing a detailed overview of the heat transfer properties of the sample material. A total of 36 samples were prepared. The 36 samples are broken down into two sets, hydrogenated Ca_2Si and dehydrogenated Ca_2Si. Each set contained a pure sample

in order to establish a baseline.

The remaining 15 samples from each set consist of the 5 different additives as potential thermal enhancers at 3 loading amounts (10, 15 and 20 wt. %). From the 36 samples an initial screening set was chosen. Figure 38 shows the thermal conductivity of the three enhancers along with baseline Ca_2Si. As can be seen, the iron powder and copper flakes do not show a significant increase, whereas, ENG shows a 100% increase at 30 °C with a 350% increase at 180 °C compared to the baseline Ca_2Si.

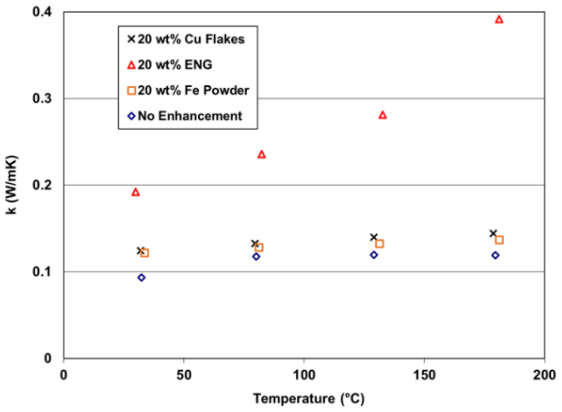

Figure 38 – Thermal conductivity of dehydrogenated Ca_2Si without enhancement and with the enhancers iron powder, copper flakes and expanded natural graphite over a temperature range of 30 to 180 °C

From the low temperature measurements, ENG was determined to be more effective at enhancing thermal conductivity than copper or iron powder. To determine thermal conductivities at operational temperature (750 °C) a Netzsch LFA 457 Microflash® that measures thermal diffusivity (α) was employed by our collaborators at Clemson University. Thermal conductivity can then be calculated directly from thermal diffusivity, heat capacity and sample density via $\kappa = \alpha \cdot \rho \cdot c_p$, where κ = thermal conductivity (W/m·K), α = thermal diffusivity (m^2/s), ρ = density (kg/m^3), and c_p = specific heat capacity (kJ/kg·K).

Sample insertion into the instrument without air exposure was not possible on this instrument, so a technique to avoid oxidation was developed. To prevent oxidation of the pellets during sample insertion, the samples were gold sputtered (~40 nm) under vacuum followed by thin layer graphite coating to reduce reflectivity. Gold sputtering prevented sample oxidation, while the graphite coating reduced the reflectivity of the samples to allow for accurate measurements during the laser flash analysis. Graphite coating is a common technique used to measure thermal diffusivities of reflective materials.

In order to calculate the thermal conductivity, the specific heat was measured on a Setaram Sensys evo Differential Scanning Calorimeter (DSC). Each component (Ca_2Si and ENG) were measured independently up to the instruments maximum temperature of 600 °C and the data was extrapolated to 750 °C. The final Cp for Ca_2Si + 10% ENG was determined by the addition of 90% of the Ca_2Si value with 10 wt. % of the ENG value at a given temperature based on the calculation for heat capacity of mixtures. A complete table of the Cp is given in Table 11.

Table 11 – Specific heat capacities of Ca_2Si, ENG and composites up to 750 °C

TEMP. (°C)	Ca_2Si c_p (kJ/kg·K)	ENG c_p (kJ/kg·K)	90% Ca_2Si + 10% ENG c_p (kJ/kg·K)
30	0.7644	1.1988	0.8078
50	0.7704	1.2468	0.8180
100	0.7854	1.3668	0.8435
150	0.8004	1.4868	0.8690
200	0.8154	1.6068	0.8945
250	0.8304	1.7268	0.9200
300	0.8454	1.8468	0.9455
350	0.8604	1.9668	0.9710
400	0.8754	2.0868	0.9965
450	0.8904	2.2068	1.0220
500	0.9054	2.3268	1.0475
550	0.9204	2.4468	1.0730
600	0.9354	2.5668	1.0985
650	0.9504	2.6868	1.1240
700	0.9654	2.8068	1.1495
750	0.9804	2.9268	1.1750

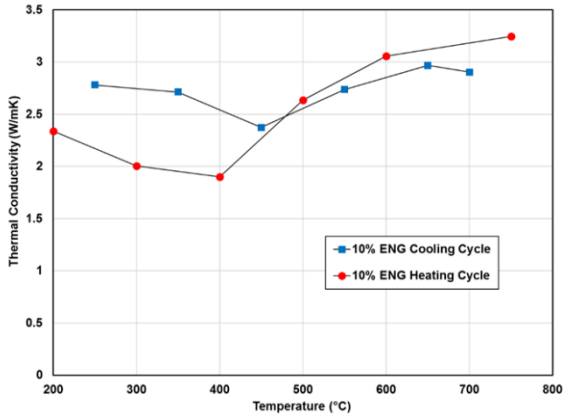

Figure 39 – Thermal conductivity of Ca2Si with 10 wt. % ENG from 200 °C to 750 °C

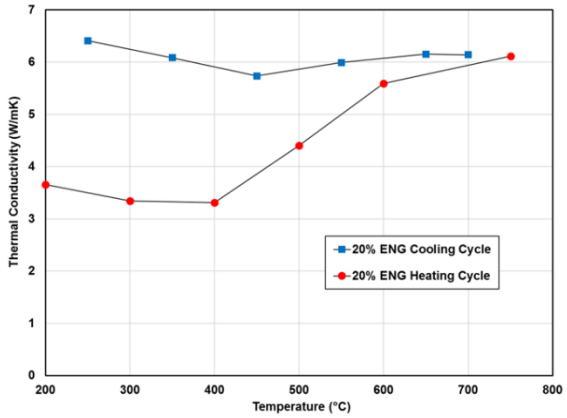

Figure 40 – Thermal conductivity of Ca2Si with 20% ENG from 200 °C to 750 °C

Figure 39 and Figure 40 show the thermal conductivity of pelletized Ca_2Si with 10 wt. % ENG and 20 wt. % ENG, respectively, up to 750 °C. The thermal diffusivity measurements taken while the sample temperature was being increased are given in red circles. The thermal diffusivity measurements taken after cooling down from 750 °C are represented by blue squares. This approach was employed to determine if any materials changes may have occurred during the heating process. As can be seen in Figure 40, the thermal conductivity measurements during the cool down are higher than would be expected compared to those of the heat ramp measurements. This is indicative of a sintering effect or growth of larger particle sizes during the temperature ramp and cool down. It should be noted that thermal conductivity measurements of the hydrogenated material will not be possible at temperatures above 500 °C without the construction of a pressurized cell and the use of a specialized instrument due to the release of hydrogen at these temperatures without hydrogen back pressure. With the incorporation of 10 wt. % ENG thermal conductivities of ~ 3 W/mK are achievable and ~ 6 W/mK is realized with the inclusion of 20 wt. % ENG.

Figure 41 shows scanning electron microscopy (SEM) micrographs of dehydrogenated Ca_2Si powder and loose ENG. The particle size for the ENG is very dispersed ranging from 50-500+ microns. The ENG forms "ribbon-like" sheets including some larger

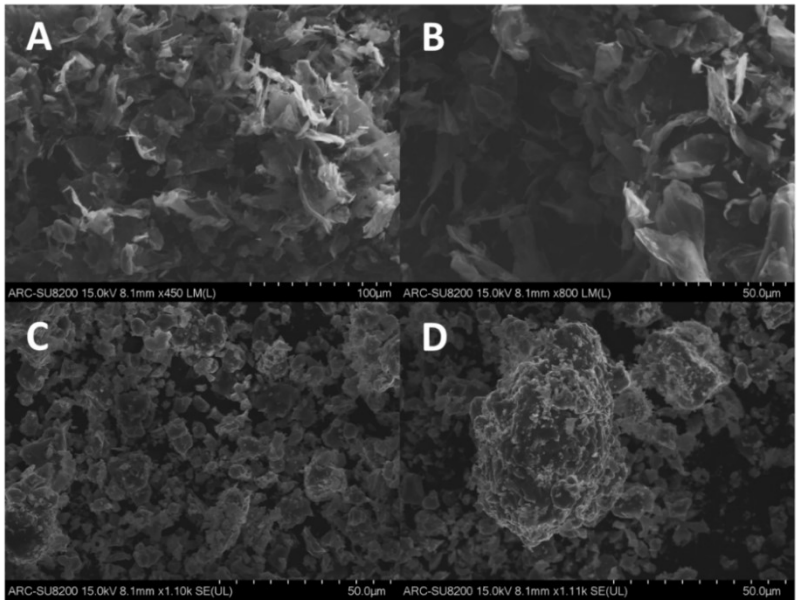

Figure 41 – SEM micrographs of ENG (a and b) and dehydrogenated Ca_2Si powder (c and d)

particles with many "ribbon-like" sheets coming off of the particle. The Ca_2Si has a size distribution as well, with a range of 5-50 microns.

Metal Hydride Capacity and Cycling

Ca_2Si was hydrogenated without the presence of a catalyst achieving a capacity of 1.7 wt. % as shown by Thermal Gravimetric Analysis (TGA) in Figure 42. Ca2Si doped with TiCl3 and Al was found to increase the kinetics of hydrogenation to achieve 2.2 wt. % H2 capacity (total composite) over 6 hours at 750 °C and 100 bar H2. (Figure 43). While pressures of this magnitude are not required for the regeneration of this material, these pressures were used to provide insight into achievable hydrogen capacities of this material over a six hour timeframe. Considering the formation of $CaCl_2$ and the dead weight of the additives Al and Ti, the hydrogen capacity of Ca_2Si would be 2.44 wt. %. Furthermore, the incorporation of Al is expected to enhance the thermal conductivity of the material. The hydrogen capacity shown by Thermal Gravimetric Analysis (TGA) below is from the second cycle of the material.

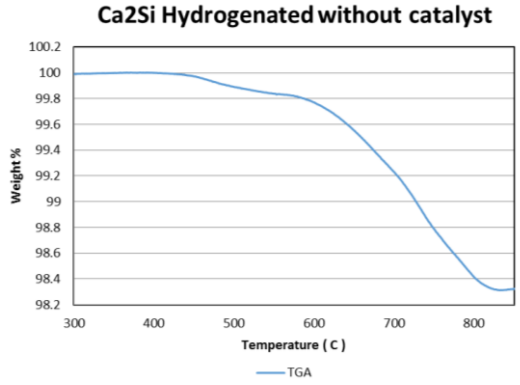

Figure 42 – Ca_2Si hydrogenated at 750 °C without a catalyst

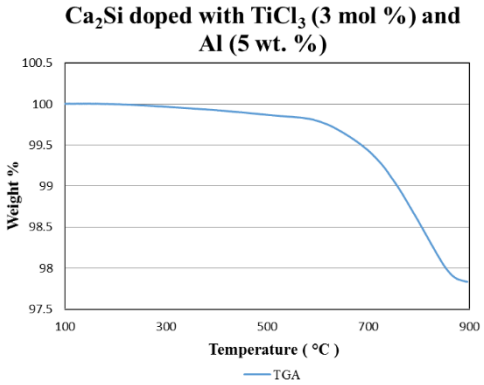

Figure 43 – TGA of Ca_2Si doped with $TiCl_3$ and Al and hydrogenated at 750 °C for 6 hours, 100 bar H_2

The "overall" hydrogen capacity of Ca_2Si without a catalyst was previously shown to be 1.7 wt. % by Thermal Gravimetric Analysis (TGA) as shown in Figure 44, reaching a hydrogen weight capacity of 2.4 wt. % with the addition of the enhancers $TiCl_3$ and Al. Isothermal absorption measurements shown in Figure 45 demonstrate an "accessible" hydrogen capacity of 1.4 wt. % at 750 °C and 14.3 bar H_2 starting pressure without inclusion of any catalyst. The initial kinetics of absorption in the Ca_2Si material are very rapid even at relatively low pressures (below 15 bar H2) and the hydrogenation is completed after 13 minutes. The sharp transition to a plateau at 11.5 bar H_2 suggests that this is the equilibrium pressure of this material at 750 °C with this H_2 concentration.

The full desorption of hydrogen from the hydrogenated Ca_2Si material is sluggish in comparison to the hydrogen uptake kinetics. Figure 46 displays a typical desorption profile carried out over 4 hours. The initial hydrogen release occurs quite quickly and 1.3 wt. % is released after 1 hour, but the remaining 0.1 wt. % requires another 3 hours to remove. This is believed to be due to the low mobility of silicone at these temperature and the lower probability of close proximity of CaH_2 and Si once most of the materials has desorbed. Temperature measurements of the sample during

absorption (Figure 47) allude to a multistep absorption mechanism. This is evident due to the separate temperature spike which are observed.

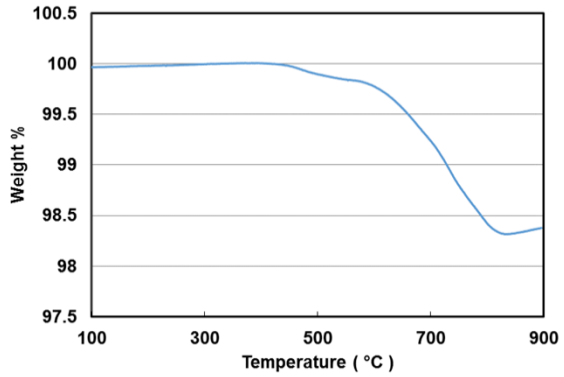

Figure 44 – Thermal Gravimetric Analysis (TGA) of hydrogenated Ca_2Si

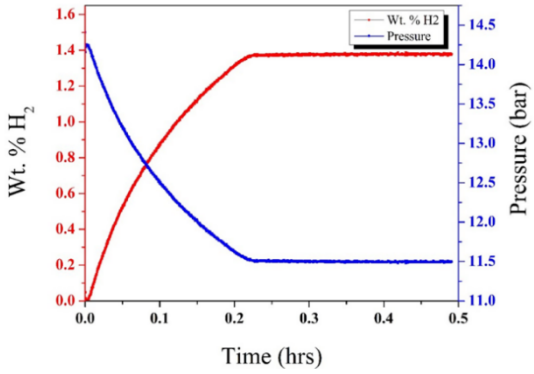

Figure 45 – Isothermal absorption in Ca2Si at 750 °C starting at 14.3 bar

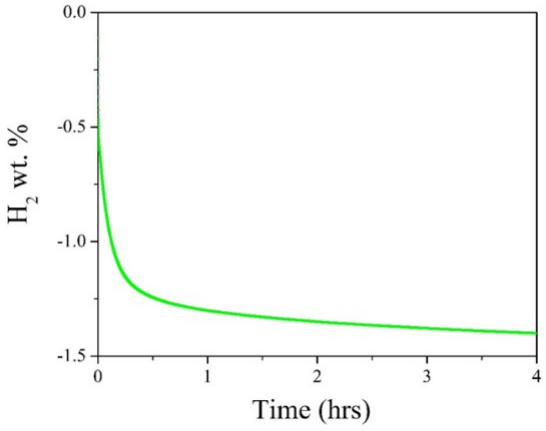

Figure 46 – Isothermal desorption of hydrogenated Ca2Si at 750 °C

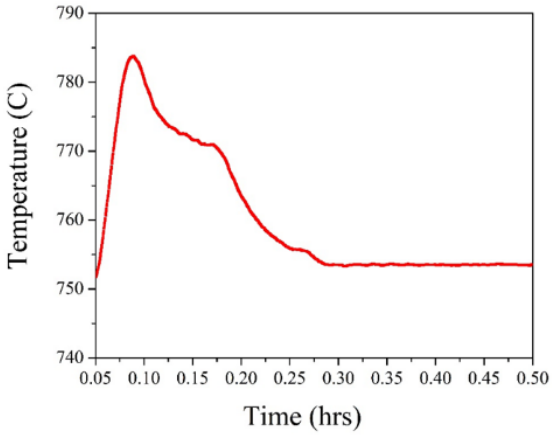

Figure 47 – Sample temperature during hydrogen absorption at 14.3 bar (starting pressure) and 750 °C

Previous thermal conductivity measurements, carried out by SRNL, have shown thermal conductivities greater than 10 W/mK for $CaAl_2$. [30] This is not all that surprising considering aluminum has a thermal conductivity greater than 200 W/mK at 30 °C. Inspired by previous work, the enhancement of the Ca_2Si material was pursued to enhance thermal conductivity and kinetics.

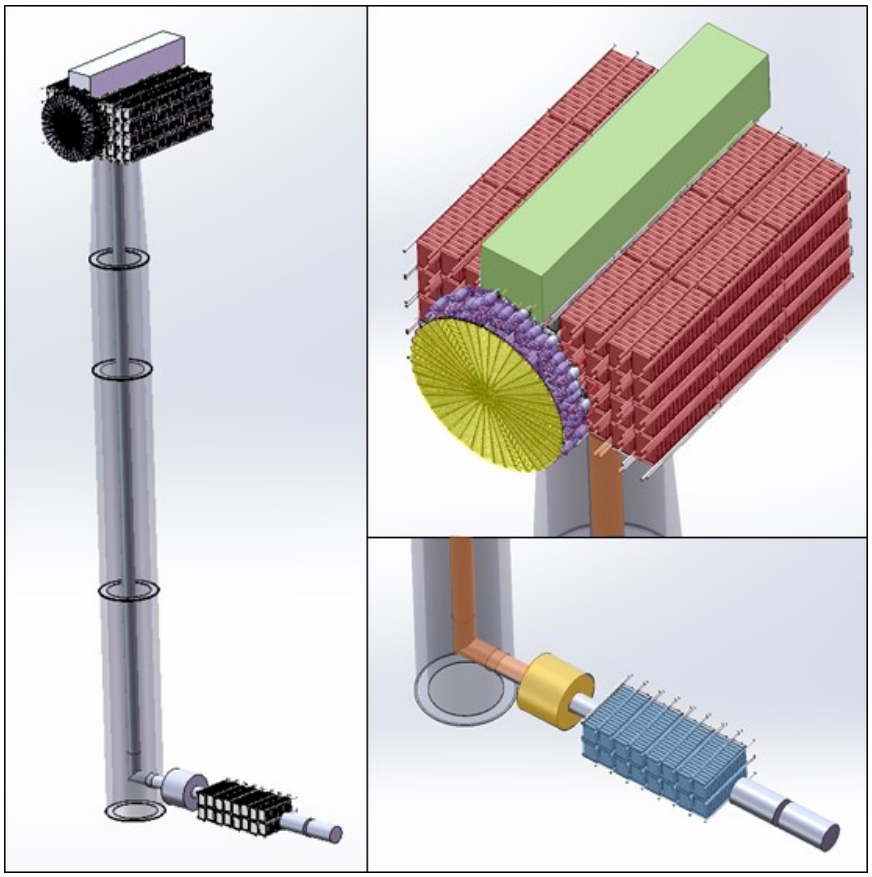

Figure 48 – Full system layout with a 60 m wind turbine tower. Shown (from top to bottom are) the sCO_2 power block (green), 60 x 1.3 MWh_{th} HTMH heat exchanger packs (red), 60 x sCO_2-to-HTF heat exchangers (purple), 60 arc sections comprising the full absorber (yellow), H_2 transport pipe (dark orange), regenerator (light orange), and LTMH bed (blue).

Integrated System

A representative layout of the full HTF-loop system – integrated with a 60 m wind turbine tower – is shown in Figure 48. The waste heat rejection heat exchanger is not shown.

Quartz Window

Inherent in all of the solar absorber designs is the assumption that Brayton Energy's patented low-cost quartz tube window will be incorporated. This window – which consists of commodity quartz tubes mounted between absorber surfaces and extending beyond them towards the heliostats, as shown in Figure 49 – are transparent to the incoming concentrated solar energy but opaque to a fraction of the infrared energy emitted by the hot metal absorber surfaces. The tubes therefore act as a radiation shield, eliminating a significant fraction (40-50%) of the radiation loss that would otherwise occur to ambient. Furthermore, the tubes may be mounted by design such that they form a flow obstruction, which further reduces receiver inefficiency by

reducing convection losses to ambient. In Brayton's prior SunShot project, receiver testing with the quartz tube window installed showed a 5.5 point

receiver efficiency gain as compared to the same design without the window. This significant benefit justifies the additional cost of the quartz window; therefore both the heat pipe and tube-based gas absorber designs will have this quartz window incorporated.

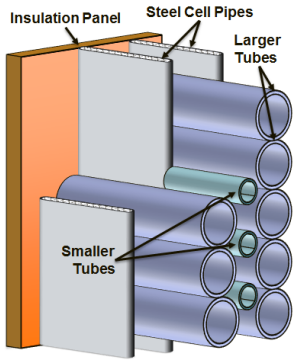

Figure 49 – Schematic of quartz tube window

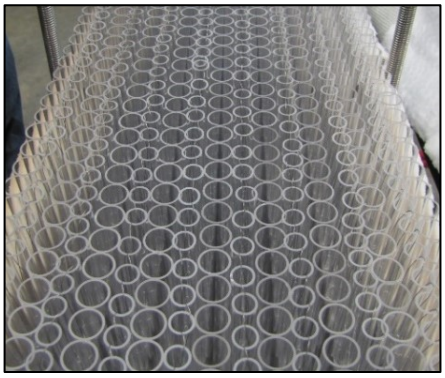

Figure 50 – Quartz tube window test section

System Cost and Mass

Table 12 gives a detailed cost and mass rollup for each of the two proposed system configurations. At this point the costs and masses are quite similar between the two, though the additional components needed for the HTF loop configuration suggests that it may ultimately be somewhat more expensive and heavier than its heat pipe counterpart. Note that the items highlighted in dark blue are those components and assemblies which reside up-tower and are therefore incorporated in the weight rollup.

Some notes regarding the costs and weight estimates:

- Rough cost estimates for the tower are from GE.
- Tower installation estimates costs were provided by Reed & Reed, a contractor specializing in New England wind tower installations.
- Critical components have not yet been optimized; the system was specified with high-confidence solutions that may be more than what is strictly necessary (e.g. Brayton-style heat exchanger for the LTMH unit, when it may be possible to use simple glycol tubes throughout the media).
- Only those components highlighted in dark blue are mounted up-tower.
- Wind turbine power heads range in size from small land-based ones weighing 190,000 kg up to large off-shore units over 636,000 kg. These load ratings are for dynamic loads as the blade loading and overturning moment during operation is quite high. The proposed design is considered dead load; Brayton has obtained verbal confirmation from a reputable wind installation contractor (Reed & Reed) and GE that the tower rating could be increased between 2 and 3 times.
- The crane Reed & Reed uses for nacelle installation has a nameplate rating of 440,000 lb, de-rated to a limit of 200,000 lb at 90m extension. Total up-tower installed weight exceeds the crane lift rating. Some assembly will be required up-tower to allow the machinery to be installed in multiple lifts, unless the economics justify the use of a larger-capacity crane.

Table 12 – Cost and Mass Estimates for the integrated system.

	HEAT PIPE SYSTEM		HTF LOOP SYSTEM	
	COST ($)	WEIGHT (kg)	COST ($)	WEIGHT (kg)
TOWER				
65m tower	350,000	-	350,000	-
Foundation prep. and pour	200,000	-	200,000	-
Tower Assembly	250,000	-	250,000	-
Crane mobilization	150,000	-	150,000	-
TURBOMACHINERY	-	36,364	-	36,364
HTR/LTR	-	18,182	-	18,182
ABSORBER	2,811,600	12,402	1,239,302	4,243
sCO_2 PREHEATER		1,094	-	-
PERMEATION BARRIERS	103,445		-	-
QUARTZ TUBE WINDOW	138,666	738	93,350	497
HTMH CaSi MEDIA	372,694	246,817	372,694	246,817
HTMH HEAT EXCHANGER	7,270,006	60,881	7,270,006	60,881
HTMH HEX FRAMING				
sCO_2 PIPING				
sCO_2 TEE FITTINGS				
sCO_2 LINE INSULATION				
HTF-sCO_2 HEX	-	-	770,927	3,490
HTF-sCO_2 HEX FRAMING	-	-		
HTF INVENTORY	-	-		
HTF RECUPERATOR	-	-	1,006,388	9,194
HTF RECUP FRAMING	-	-		
HTF RECUP BYPASS VALVE	-	-		
HTF RECUP BYPASS TEES	-	-		
HTF-GLYCOL HEX	-	-	5,569	16
HTF-GLYCOL FRAMING	-	-		
HTF CIRCULATOR	-	-	300,000	
HTF CIRCULATOR FRAMING	-	-		
HTF TRANSPORT PIPING	-	-		
HTF ABS. BYPASS VALVES	-	-		
HTF ABS. BYPASS TEES	-	-		
HTF LOOP INSULATION	-	-		
PERMEATION RECOVERY				
H_2 MANIFOLDING				
H_2 TRANSPORT PIPE	-	-	-	-
IN625 Liner	9,157	-	9,157	-
Containment Pipe	4,476	-	4,476	-
Insulation	20,360	-	20,360	-
Convection Barrier	7,377	-	7,377	-
H2 Isolation Valve	5,000	-	5,000	-
REGENERATOR	1,538,880	-	1,538,880	-
LTMH TiMn1.5 MEDIA	1,480,904	-	1,480,904	-
LTMH HEAT EXCHANGER	635,301	-	635,301	-
LTMH HEX INSULATION		-		-
Δ HEAT REJECTION HEX		-		-
GLYCOL PUMP		-		-
GLYCOL PIPING		-		-
GLYCOL TEE FITTINGS		-		-
GLYCOL METERING VALVES		-		-
GLYCOL INSULATION		-		-
TRUCK TRANSPORTATION		-		-
SYSTEM INSTALLATION		-		-
TOTALS	15,347,866	376,478	15,709,690	379,684

These costs and operating parasitics have been applied to a preliminary LCOE model, assuming an installation in Barstow, CA. With the associated assumptions and the known costs, the calculated LCOE is 12.8¢/kW-hr. The normalized cost of the receiver, tower, and thermal energy storage is $425/$kW_{th}$. There is significant opportunity to reduce this cost further, as the current design has not yet been optimized and some components (e.g. the LTMH heat exchanger, for which embedded glycol tubing may be a more cost effective design than a plate-fin heat exchanger) may be excessive.

Based on preliminary up-tower component weights (380,000 kg) and the rated load capacity of the tower (380,000 to 570,000 kg or more), the commercial wind-turbine tower is adequate for mounting the proposed system.

Milestone 1.1.5.1:

The selected HTMH formulation can achieve the required thermochemical energy storage and transfer rates in a mass compatible with mounting the entire integrated system up-tower – initially estimated at 150 tons by the manufacturer, with provisions that that might be increased to 204 tons with structural enhancement work to the tower.

Phase 1 modeling shows 246,817 kg (272 tons) of HTMH is required to store the required amount of heat in the thermal energy storage system. This is greater than the desired weight specified in the milestone, however, it was found that the tower with reinforcement would be able to handle the increased weight. A summary of the weights located up-tower is given in Table 12.

Milestone 1.1.5.2:

The selected HTMH will associate/dissociate hydrogen at its operating pressure at an operating reaction temperature ≥ 750^0C. To meet this target, the HTMH material needs to be able to exchange the thermal power required by the power plant. Thus the thermal power related to the exothermic reaction needs to be equal to the thermal power required by the CO_2 power plant. This implies that the HTMH material reaction rate ($r_{rxnHTMH}$) needs to satisfy the following relationship: $r_{rxnHTMH} \geq Q_{PP}/(\Delta H_{HTMH} \bullet V_{HTMH})$, with $r_{rxnHTMH}$ being the reaction rate (identified as the time variation of the reacted hydrogen moles per unit of HTMH volume), Q_{PP} being the maximum power plant inlet thermal power (equal to 20 MW_{th}), ΔH_{HTMH} being the reaction enthalpy (in terms of energy per mole of hydrogen) and V_{HTMH} being the HTMH volume. A system model based on mass and energy balance, including the kinetics of the material will be developed and used to evaluate the behavior of the TES system under the operating conditions dictated by the power plant requirements. Three different scenarios will be examined with the power plant requiring: (1) maximum (nominal) power, (2) half the max power, and (3) ¼ of the maximum power.

Testing of the HTMH shows that it can operate at 750°C as shown in Figure 45 and Figure 46. Initial reaction rate calculations showed that full absorption took longer than 4 hours. This would indicate that the reaction rate would be insufficient for operating in this cycle. Future work was planned to add an adsorption catalyst which would allow for faster adsorption of the hydrogen into the metal hydride.

Milestone 1.1.5.3:

The selected HTMH formulation will operate reversibly for 150 cycles with prediction of low material degradation (≤2%) commensurate with longer cycling (10,000 cycles).

Initial cycling trials did not show a significant degradation of HTMH performance over the tested number of cycles (see **Error! Reference source not found.**). This milestone was finalized in phase 2.

Milestone 1.1.5.4:

The selected LTMH formulation will associate/dissociate hydrogen at its operating pressure at an operating reaction temperature ≤ 60^0C.

$TiMn_{1.5}H_{2.47}$ was selected as the LTMH of choice for the cycle. It has good performance characteristics during both the charging (30°C) and discharging (41°C) temperatures. For equilibrium temperature/pressure plots and reaction rates please see Figure 36 and Figure 37.

Milestone 1.1.5.5:

The selected LTMH formulation will operate reversibly with prediction of low material degradation (<2%) commensurate with longer cycling (10,000 cycles).

Prior literature search has revealed that there is little risk of degradation even in up to 30,000 cycles. See LTMH formulation section above.

Milestone 1.1.5.6:

A preliminary integrated receiver, tower, and thermal energy storage system designed for a 10 MW_e modular tower-based CSP sCO_2 Brayton Power Plant with Integrated TES that has a capital cost of \$210/kW_{th} or less (corresponding to the DoE goal of \$150/kW_{th} for the receiver/tower system + [\$15/$kWhr_{th}$ x4 hrs. storage] for the TES), within an uncertainty of ±50%, over the full range of input variability.

Costs are listed in Table 12 for the system which assumes 20MW_{th} of energy storage for four hours or 80MWh_{th}. A total cost of \$196/kWh_{th} for the system is reported. The uncertainty in the cost estimate is assumed to be ±50% based on the level of effort that went into specifying the costs.

SubTask 1.1.6:

Generate a complete metal hydride thermal energy storage system model to interface with the overall system thermo-hydraulic model; in addition to the MH formulations, this will include vessels and hydrogen transport piping designed for the appropriate pressures, temperatures, material compatibility, and flow pressure drop.

sCO2 Heat Exchangers

Wherever appropriate, the APOLLO system employs the high pressure plate-fin heat exchanger designs developed by Brayton Energy under its 2012-2016 SunShot program. These heat exchangers utilize a unit-cell construction that enables qualification testing throughout the manufacturing process. The unit cells themselves consist of thin-walled shells internally

supported by a network of brazed fins; these fins not only enhance the heat transfer with the high-pressure working fluid within the shell, but they also provide a network of structural cross members that may react the internal pressure load. This design eliminates the need for thick walled structures.

Individual cells are then brazed in header blocks (Figure 51), which both collect and distribute the internal pass of the working fluid as well as provide structural support the ends of the cells. The cell may also have a network of fins brazed to the outside of the shell, enhancing the heat transfer on the fluid flowing between the unit cells. Examples of completed unit cells – with both internal and external fins, along with brazed header blocks – are shown in Figure 52.

Multiple unit cells may then be stacked atop each other and welded at their header blocks. This produces a full core, with the characteristic that the individual cells are free to relieve their thermal strain independent of their neighbors.

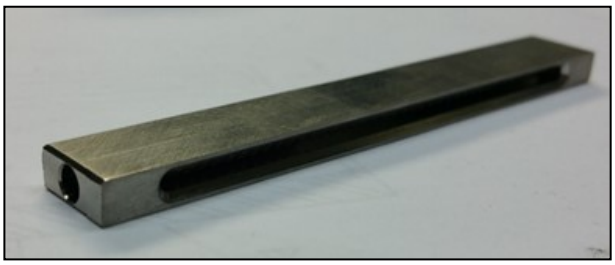

Figure 51 – Example header block

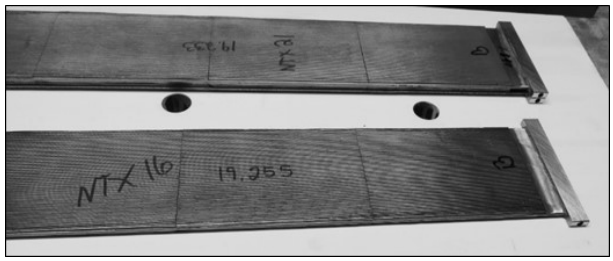

Figure 52 – A pair of headered cells.

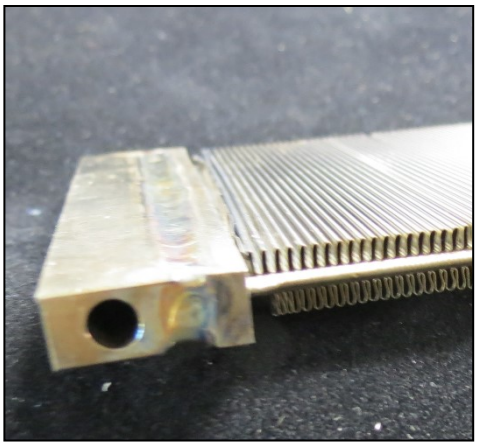

Figure 53 – Full cell and manifold assembly, showing the welded 2-piece manifold assembly (left) with its mated brazed cell (right).

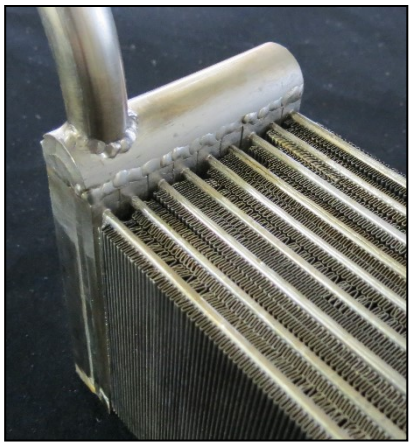

Figure 54 – Full heat exchanger core assembly, showing multiple cells welded together and capped with a semicircular flow channel.

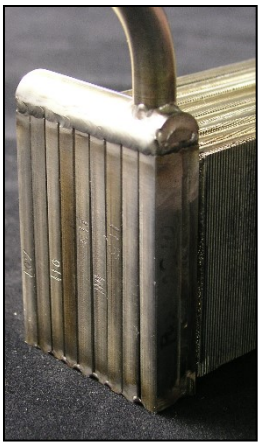

Figure 55 – Assembled core consisting of multiple cell sub-assemblies.

This relative freedom reduces stresses within the core, ensuring that the assemblies are capable of enduring many cycles (i.e. exhibiting long fatigue lives) and accommodating the fast transients associated with gas turbine operation.

An example of a full manufactured cross-flow configuration core – manufactured for and delivered to a commercial client – is shown in Figure 53 through Figure 56.

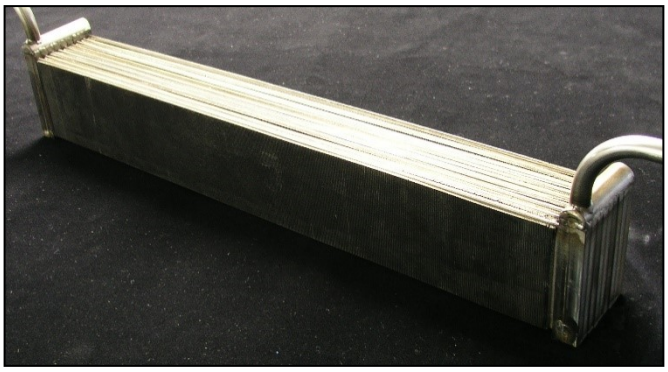

Figure 56 – View of a fully assembled heat exchanger core manifolded as described in this section.

SubTask 1.1.7:

Generate a suitable model to evaluate the heat exchange between the LTMH and Cycle Low-Temperature-Recuperator discharge flow (engine exhaust).

Hydrogen Transport Pipe

The APOLLO CSP tower is currently specified to be about 60 m tall. The HTMH vessel resides at the top of the tower, while the LTMH will be at ground level. The temperature-dependent equilibrium pressure drives the flow from one MH to the other depending on charge/discharge state. While the hydrogen does not incur pumping losses, the pressure drop through the transfer pipe will affect overall system efficiency. It is also important to minimize heat losses to atmosphere.

For conservative analysis, the pipe loss model assumes a straight pipe 100 m long. Minimizing dP/P allows room in the pressure loss budget for additional elbows and pipe runs; the pipe is internally insulated to avoid expensive alloys (Figure 57).

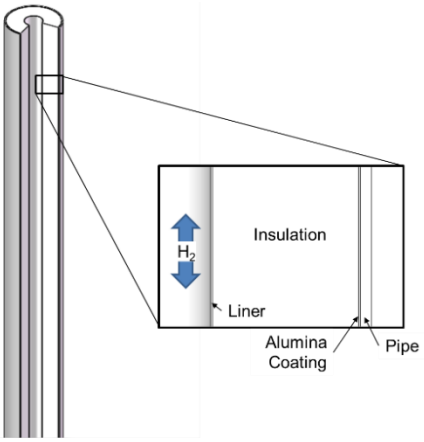

Figure 57 – Hydrogen transport pipe concept.

Pipe loss calculations are straightforward using pipe geometry, operating conditions, and hydrogen properties. For the low dP/P assumed (<2 %), incompressible flow assumptions are valid. It is also important to limit the heat losses from the pipe to minimize cycle efficiency losses. Brayton uses an iterative calculation to determine the heat loss from a piping system using alternating layers of insulation and metal. Calculations accounts for conduction, convection, and radiation (the latter necessitates an iterative solution). For the proposed piping system there is no external insulation. Pipe diameter and insulation thickness are varied to arrive at a solution that

achieves the desired heat loss and pressure drop.

Hydrogen gas has a high thermal conductivity relative to air; therefore the thermal conductivity implications of insulation saturated with hydrogen must be considered. As a baseline study, a low-cost easy-to-install UNIFRAX insulation was considered: Durablanket S (ρ = 128 kg/m^3). The manufacturer supplied thermal conductivity for this material in a hydrogen environment, via testing performed in accordance with ASTM C-177. The results, shown in Figure 58, indicates that the thermal conductivity of the material increases by a factor of ~3 with hydrogen infiltration. Figure 59 shows the results for losses manageable 0.25% during attention to hydrogen enough to justify Additionally, permeability of natural annulus filled with considered. The goal of the study was to determine the critical height (H) for vertical annulus segment which limits development of natural convection; that is, where Nu = 1 such that heat transfer is dominated by conduction only. The results of the study – shown in Figure 60– suggest that incorporating one convective barrier (such as an annular ring or a solid barrier) every meter is sufficient to impede convection effects within the insulation.

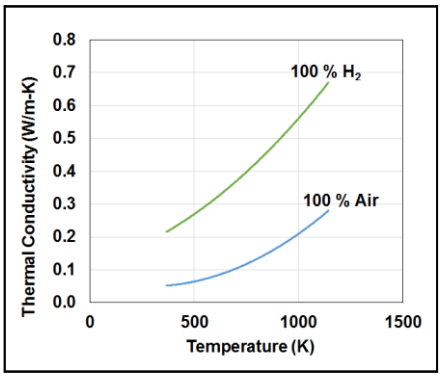

Figure 58 – Insulation conductivity under hydrogen-saturated conditions.

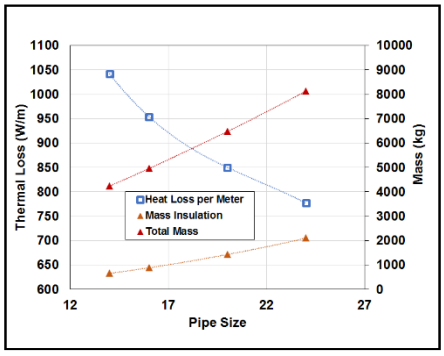

Figure 59 – Hydrogen transport pipe thermal loss study for hydrogen-saturated insulation

systemic implications of this; while the from the hydrogen transport pipe are (0.50% thermal loss during charging, discharging), the study suggests that mitigating the thermal losses from the transport pipe may benefit the system the additional effort.

because of the extremely high gaseous hydrogen, the effect of convection in the vertically-oriented porous media (i.e. insulation) was also

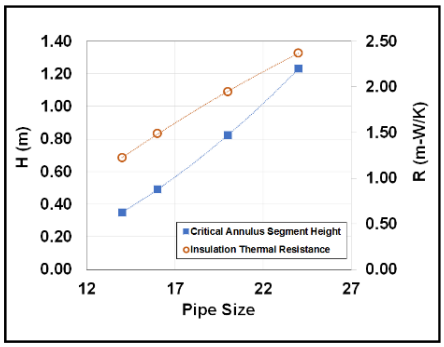

Figure 60 – Convection-limiting critical H_2 transport pipe lengths

Hydrogen Regenerator

During TES charging, heat from the solar input is being absorbed by the HTMH, which causes an endothermic reaction that releases gaseous hydrogen. The hydrogen gas exits the HTMH at its operating temperature, specified in the proposed system as 745 °C; conversely, the match LTMH media into which the liberated hydrogen will be absorbed has an operating temperature of 38.7 °C. The heat from the hydrogen gas must therefore be rejected, or it will raise the LTMH temperature and the system will re-establish equilibrium at an undesirably higher pressure and temperature.

At the specified charge rate, the mass flow of hydrogen from the HTMH to the LTMH is 0.185 kg/s. Calculating the sensible heat associated with the required cooling from $Q_{H_2} = \dot{m}_{H_2} * \Delta h_{H_2}$ gives 1,832 kW_{th}, or 18% of target 10,000 kW_{th} storage power. Rejecting this in the LTMH via the glycol loop would introduce a thermal inefficiency far in excess of the desired 1% round-trip loss. The proposed solution to address this is to capture the sensible heat of the hydrogen during LTMH charging, and then re-introduce the heat when the system is operating in reverse (during TES discharging).

Thermocline storage provides a straightforward method for storing the hydrogen sensible heat. The hydrogen flows through a vessel containing porous thermal storage media (TSM). During tank charging the TSM extracts heat from the hydrogen and retains it until tank discharging. The vessel temperature varies along its length, from 745 °C at the end nearest the HTMH, to 38.7 °C at the LTMH end (Figure 65). At some point between the two ends, the TSM experiences a temperature gradient (Figure 66). The location of the temperature transition depends on charge/discharge state and time. The "sharpness" of the gradient is measured in length, and depends on the hydrogen residence time, heat transfer coefficient, TSM heat capacity, and TSM thermal conductivity. A shorter transition length (sharper transition) is preferred as it results in higher thermocline effectiveness and better round-trip efficiency.

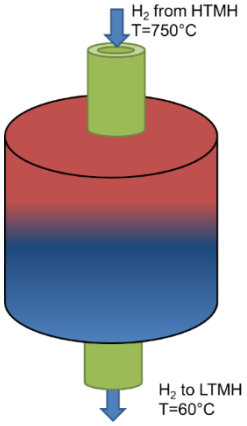

Figure 61 – Thermocline Storage Concept

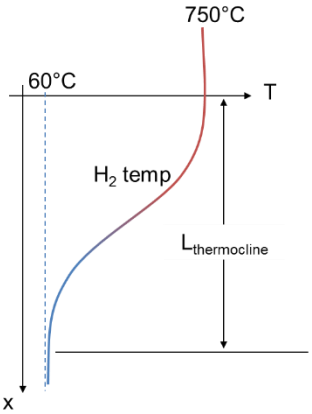

Figure 62 – Thermocline gradient

Several materials are under consideration for the TSM:

- Ceramics can have quite high heat capacity and very high temperature capabilities. Their downside is typically high cost and sometimes low conductivity.
- Some metals may be quite inexpensive and exhibit good conductivity, but lower heat capacity and temperature capability. In this case, the temperature is low enough that steel is an option. The temperature is too high to consider aluminum, and copper is far too expensive.

Material can be sold either by mass or volume; for consistency all costs are reported by mass. The required storage volume is driven by density, heat capacity, and void fraction of the material. The storage volume was over-sized by a safety factor to ensure effective

thermocline storage. The ideal material to minimize storage volume is highly dense with a large specific heat capacity. Minimizing storage volume is important because the vessel cost can be greater than that of the TSM itself.

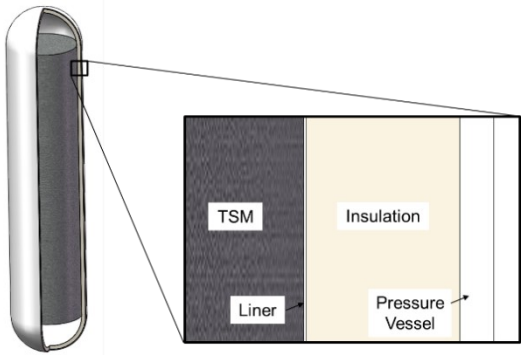

Figure 63 – Thermal storage media system

The proposed vessel design consists of an internally-insulated pressure vessel with an internal metal liner to protect the TSM from insulation and vice versa, shown in Figure 67. The vessel thickness is sized using ASME B31.3 – Process Piping. The vessel is modeled with hemispherical endcaps. This may be slightly inaccurate depending on the manufacturer's preference, but it a good approximation and is mathematically straightforward. It also avoids stress concentrations caused by tighter curvature.

For a given pipe diameter and internal pressure, the required tank length and minimum wall thickness were calculated via geometry and ASM B31.3-2002, Eq (3a), respectively.

Pressure drop through the storage media is geometry- and time-dependent. As the media heats up, pressure drop increases due to lower fluid density and increased viscosity. Assuming the media is entirely at 745°C gives the worst-case pressure drop. There are two TSM flow geometries under consideration: honeycomb matrix and packed (pebble) bed. The honeycomb matrix uses many linear passages to give a high wetted surface area and enhance heat transfer. The packed bed has roughly uniform particles randomly arranged to provide high flow tortuosity. Appropriate correlations reported in prior quarters were used to evaluate the pressure drop and heat transfer associated with each material and configuration.

Table 13 – TSM candidate comparison

	UNITS	STEEL	CORDIERITE	ALUMINA (ZIRCAR PELLETS)	DENSTONE 99
Cp	kJ/kg-K	0.45	0.5	0.75	1.04
Mass	kg	88,154	79,339	52,892	38,090
Density	kg/m^3	8,050	2,200	590	1,998
Solid Volume	m^3	16.43	54.09	134.47	28.60
Void Fraction		0.40	0.40	0.40	0.40
Total volume	m^3	41.07	135.24	336.18	71.49
Vol. Heat Capacity	kJ/m^3-K	3,623	1,100	443	2,081
Permeability	m2	5.00E-11	4.15E-10		
Flow diameter	mm	6	6	6	--
Hydraulic Diameter	mm	4.71		4.71	
Thermal Conductivity	W/m-K	53.7	20	25	16.6
Particle Diameter	mm	6	--	3	6
Cost	$/$m^3$	$ 17,750	$ 61,024		$ 7,155
Total cost	$	$ 291,569	$ 3,301,049	$ -	$ 204,616

The materials considered for TSM are shown in Table 13. Note that pricing was not obtained for Zircar pellets, although the price is expected to be similar to the Denstone 99 since their intended market and formulation are similar. The cordierite pricing is for low-volume honeycomb matrix, pricing obtained by David Wilson. Steel pricing is commodity $2.21/kg ($1/lb). Denstone 99 is pelletized alumina manufactured by Saint-Gobain, and pricing is direct from Saint-Gobain for 100,000 kg.

Figure 68 shows normalized cost of the thermocline storage and tank heat loss plotted as a function of tank diameter. The TSM volume (and therefore cost) is held constant, so the driver on normalized cost is the vessel and insulation. Heat loss declines as tank diameter increases because the surface area is dropping. The heat loss eventually bottoms out at the minimum tank

surface area, beyond the plotted chart limit. The thermocline storage cost includes inner metal liner, insulation, pressure vessel, and TSM. Metal costs include estimates for welding and assembly. Figure 69 shows a comparison of pressure drop for the two options. At reasonable tank dimensions for the application (>2 m) the pressure drops are nearly identical, and so low as to be of no consequence.

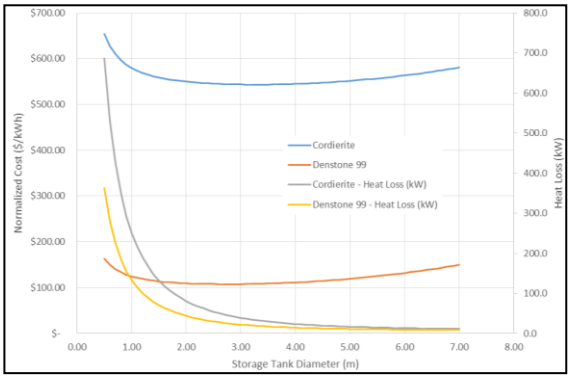

Figure 64 – Comparison of cordierite honeycomb matrix to Denstone 99 (Saint-Gobain) packed bed. Price for cordierite from David Wilson, price for Denstone 99 from Saint-Gobain.

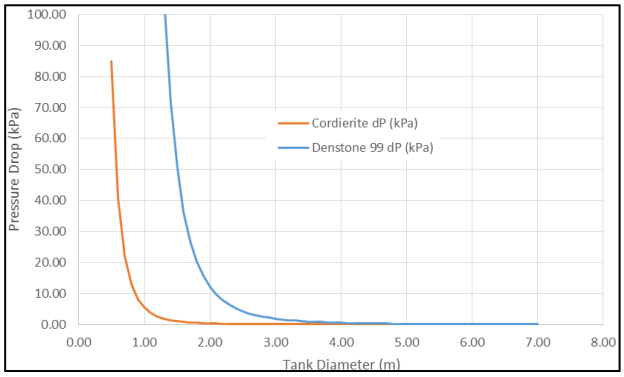

Figure 65 – Comparison of pressure drop for cordierite honeycomb matrix to Denstone 99 (Saint-Gobain) packed bed.

The packed bed exhibits increased pressure drop compared to the honeycomb matrix, but only at small tank diameters that do not make practical sense (i.e. result in tank lengths of hundreds of meters). Within the range of manageable tank size (tank diameter > 2 m), the pressure drop is very low for both options, and the price of the packed bed is much lower than the honeycomb. Some of the price difference comes from choice of materials, but the honeycomb manufacturing process is assuredly more expensive than the pellet forming. Additional care and cost must be taken during handling and assembly of the honeycomb to prevent damage and undue pressure loss. Consequently, the proposed regenerator is a Denstone-99 pebble-bed design; this configuration is used for cost and efficiency calculations.

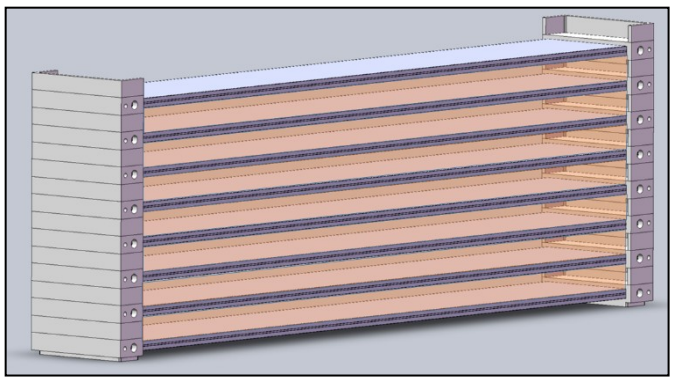

Figure 66 – Representative LTMH heat exchanger architecture; media is depicted in orange between cells.

LTMH System

The LTMH system consists of the required volume of media and an effective means of removing or adding heat throughout the volume – for TES charging and discharging, respectively – without imposing an undesirably large temperature gradient. The conventional means of accomplishing this is to employ a large number of tubes embedded throughout the media; analysis performed at SRNL and Brayton indicate the radial conduction paths from tube through media make it difficult to utilize all of the media effectively. Therefore an alternative design is being proposed, which leverages Brayton's

low-cost unit-cell design developed in the SunShot program. By running glycol through flat channels, bounded on either side by appropriate volumes of LTMH, large conduction areas and linear conduction paths are achieved. The unit is compact, manufacture is highly automatable, and the resulting units are relatively low cost (with numbers that are defensible and well-benchmarked through Brayton's experience). Because the LTMH operates at low temperature, hydrogen permeation – a significant issue in the HTMH, and discussed later – is not a concern in this unit.

Glycol System

In its non-integrated configuration, the closed sCO_2 Brayton cycle achieves its maximum efficiency via a waste heat rejection precooler located upstream of the main compressor. This allows the majority of the working fluid (nominally the 60% flow split that goes through the main compressor) to be cooled near its critical point, increasing its density and specific heat dramatically and thereby greatly reducing the compression workload needed to pressurize the cycle.

The precooler would typically take one of two forms; the first and simplest is a sCO_2-to-air crossflow (radiator) style dry cooling heat exchanger, in which the working fluid rejects its heat directly to ambient. This minimizes the number of heat exchangers employed and eliminates an intermediate heat exchanger inefficiency, but it is not without disadvantages; the heat exchanger itself is necessarily very large to achieve the requisite heat transfer, and there is considerable cost associated with the flow length between the cycle and the precooler is critical due to the high pressure of the working fluid.

The alternative configuration is to use a sCO_2-to-glycol heat exchanger in the power cycles, and then circulate the glycol to a conventional air-cooled radiator to reject the excess heat to ambient. Although this introduces a second heat exchanger in the thermal network, the bulk of the heat exchanger volume – i.e. the air cooled unit – does not need to be intimately collocated with the cycle as it is inexpensive to pump the glycol around. Furthermore, the cost of the heat rejection heat exchangers may be less than the single sCO_2-air unit; because of the high capacitance achievable on the glycol side the cycle unit may be much more compact, and because the very high pressure of the sCO_2 is not present in the air cooler that unit may be a low-cost commercial design.

In the proposed APOLLO configuration, the latter waste glycol-loop heat rejection system is employed; beyond the advantages just mentioned, this configuration is critical to the overall integration of the system as it links the waste heat from the cycle to be the LTMH heat requirement during TES discharge. Furthermore, the glycol system works well in conjunction with the intermediate heat transfer fluid loop designs discussed in the indirect heat transfer fluid receiver section. The flexibility of the glycol heat rejection loop enables the elegant integration that is the hallmark of the proposed receiver/TES/sCO_2 cycle design.

Because a glycol cooling system is a conventional heat transfer design, its inclusion in the system is low risk. In its entirety, the glycol loop consists of:

- A glycol-to-air radiator style air cooler (commercially available, commodity pricing)
- A sCO_2-to-glycol heat exchanger (low cost high-pressure Brayton unit cell heat exchanger design)
- A glycol-to-LTMH heat exchanger design (although there may be a commercially-available commodity-priced option for this component, current pricing and modeling utilizes a low-cost Brayton unit cell heat exchanger design with well-vetted performance and price indices)
- A liquid pump (commercially available, commodity pricing)
- Standard 2-way or 3-way valves for liquid service (commercially available, commodity pricing)
- Standard insulated piping and connections/fittings (commercially available, commodity pricing)
- A glycol-to-CO_2 heat exchanger design - if the intermediate heat transfer fluid receiver loop design is employed (although there may be a commercially-available commodity-priced option for this component, current pricing and modeling utilizes a low-cost Brayton unit cell heat exchanger design with well-vetted performance and price indices)

sCO2 Power Cycle

The power cycle being employed in this program is a Recompression Brayton Cycle, described in detail in the seminal work by Dostal[31]. The driving motivation behind this selection is the size and cost of the recuperator; in a standard recuperated configuration, the physical properties of supercritical carbon dioxide lead to a "pinch point" within the recuperator, where the two fluids approach the same temperature before the full thermal duty is achieved; this results in a recuperator that must be extremely large – and therefore expensive – to fabricate. By splitting the working fluid between two compressors and employing two distinct recuperators, the fluid capacitances may be tailored to achieve the desired thermal duty in a more economical fashion, with minimal penalty to the overall cycle efficiency.

The scope of this program does not include a detailed cycle analysis. The statepoints specified by General Electric as part of its SunShot program (listed above) are being applied directly.

Milestone 1.1.7.1:

The design of an LTMH heat exchange system capable of charging/discharging at a rate of ≥ 10 MW_{th} at 50% power cycle efficiency to accommodate TES operation over the selected storage time (nominally 4 hours) at full power sCO_2 power cycle conditions (flow rate, low temperature recuperator flow temperature, etc.); furthermore the discharge rate must be capable of operating at lower discharge rates corresponding to 20% cycle power (2 MW_e) conditions (required input power, mass flow rate, low temperature recuperator discharge temperature, etc.).

A LTMH to glycol heat exchanger was designed that was capable of providing or removing the necessary heat from the LTMH through all operating modes of the system defined in Table 6. This heat exchanger uses the same brazed plate geometry as the high temperature metal hydride heat exchanger as it is a low-cost option, however commercially available products may also suffice.

SubTask 1.1.8:

Integrate all of the constituent sub-models into a cohesive whole and exercise that model to define the system architecture and predict its design point performance.

The definition of the overall system model is given in Subtask 1.1.4.

SubTask 1.1.9:

Apply rigorous thermodynamic, conjugate transport, and chemical kinetic models to fully define and specify the subsystems such that they achieve the target overall system performance. Develop the full design point model for the receiver and thermal energy system for the 10 MW_e modular tower-based CSP sCO_2 Brayton Power Cycle with integrated TES identified as the case study for the program. The inputs and outputs for each module of the model are listed in the descriptions below; note, however, that the models must also be reversible in order to reflect the discharging of the thermal energy storage system during off-sun operation. The following key pieces will come out of this task:

1. An absorber cell geometry and receiver configuration appropriate for the needs of the sCO_2 Brayton power cycle and the MH thermal energy storage system
2. A validated means of conveying the absorbed thermal energy from the receiver cells into the bulk HTMH volume
3. Final formulations for both the HTMH and the LTMH materials

The definition of the overall system model is given in Subtask 1.1.4.

Milestone 1.1.9.1:

An integrated, reversible, end-to-end thermal model that spans from the solar input during charging (location, time of day, day of year) to the LTMH heat addition/rejection, including interactions with the sCO_2 working fluid and thermal losses to the environment, and which predicts a Thermal Energy Storage design point efficiency ≥ 99%.

State points for the integrated system model are provided in Table 6. Losses from the thermal system include thermal losses from the HTMH vessel, hydrogen piping, and hydrogen regenerator as well as inefficiencies in the regenerator. These were minimized, however a total round-trip efficiency was not reported in this phase, however this value was reported in phase 2 and 3.

Milestone 1.1.9.2:

An integrated, reversible, end-to-end thermal model that spans from the solar input during charging (location, time of day, day of year) to the LTMH heat addition/rejection, including interactions with the sCO_2 working fluid and thermal losses to the environment, and which predicts a design point exergetic efficiency ≥ 95%.

Like the round-trip efficiency milestone (1.1.9.1) the round trip exergetic efficiency was not reported in phase 1, however it was reported in phase 2 and 3.

Milestone 1.1.9.3:

An absorber design that, with its performance integrated over all time-weighted modes of operation, exhibits a thermal efficiency of 90% in accordance with the DOE SunShot target.

Two absorber architectures were proposed in this project, one based on heat pipes conveying heat to the metal hydride, and the other using a secondary heat transfer loop of CO_2. It was found that the heat pipe solution would provide an efficiency on the order of 45% solar to thermal, however the receiver utilizing the secondary heat transfer loop (in this case CO_2) was able to achieve efficiencies of 89.1% as shown in Table 6.

Milestone 1.1.9.4:

Determine limits of system operability and desirable modes of operation, including:

- the maximum flux that may be absorbed by the receiver during a zero-sCO_2-flow scenario, corresponding to charging-only operation
- the peak storage rate achievable by the system in conjunction with sCO_2 flow
- the maximum flux that may be accommodated with elevated sCO_2 flow rate
- the sCO_2 flow and resulting pressure drop required to operate in no-storage mode

This information is critical to the analyses in SubTasks 2.1.2, 2.3.3 in Budget Period 2 and SubTasks 3.1.2 and 3.1.3 in Budget Period 3. In each of these case, understanding the probable operating modes will inform the results.

An integrated system model was created which models the following operating modes: charging + generating, generating only, charging only, discharging + generating, storage only. A state point diagram is provided for each of these operating conditions in Table 6. This table in turn describes the limits of operation for the system.

Go/No-Go Decision Point 1:

Design Point Integrated System Design that meets the performance targets outlined in the Budget Period 1 Milestone tables.

The design point integrated system design was determined to meet sufficient milestones in order to progress to budget period 2.

Budget Period 2

A down-selection from the two viable alternatives developed in Budget Period 1 is required to focus the efforts in the direction of the most promising technology path. It is necessary to establish the off-design performance of the proposed system, which enables a full annualized evaluation of the integrated solution. Further characterization of the metal hydride media is important, including its internal thermal behavior during charging and discharging, and its long-term operational life. The fully specified solution will also be laid out in the context of the up-tower components and the ground-level components to a level of detail appropriate to establish a detailed capital cost and operating cost roll-up of the integrated system, providing the comparative data needed to demonstrate its ability to achieve the SunShot 6¢/kW_e target. A test article and test loop will be designed for the purposes of evaluating functionality of the integrated system.

Problem Statement:

A rigorous evaluation of the two proposed candidate absorber technology paths must be performed in order to identify the preferred direction for further development. Off-design conditions must be considered in order to identify any potential areas of concern arising from annual and/or diurnal variations; long-term viability of the metal hydride media must be evaluated in order to validate the cost effectiveness of the system; the mechanical layout identifies any regions of thermo-mechanical concern, and informs the cost model to generate a comprehensive LCOE; the sub-scale test article and test setup, along with a detailed test plan, also need to be specified and reviewed prior to any substantial purchases.

Task 2:

A full comparative evaluation of the two candidate absorber technology paths – namely, (1) a heat pipe absorber design and (2) an intermediate gas path absorber design – must be performed in order to identify which of the two layouts will be pursued in depth in Budget Phases 2 and 3. The two proposed concepts will be evaluated on cost, maintenance, efficiency, operability limits, safety, barriers to adoption, controllability, tolerance to systemic deviations, manufacturability, etc. The optimal architecture will be identified and down-selected, and will be the subject of the ongoing development efforts in Budget Periods 2 and 3.

SubTask 2.1:

Perform a comprehensive comparative analysis between two viable absorber systems (both of which were outlined in detail in the Budget Period 1 final report):

1. An absorber comprised of multiple parallel heat pipes, each of which communicates with a corresponding volume of high temperature metal hydride; absorbed heat is conveyed to the metal hydride directly via the heat pipe working fluid.
2. An absorber surface comprised of multiple parallel tube-based sections, through which an intermediate heat transfer fluid is being circulated. Absorbed heat is conveyed to the metal hydride via a heat exchanger configuration

These two candidate technologies were:

- A Heat Pipe receiver (shown in Figure 67), wherein sodium heat pipes absorb incident solar flux and convey the energy into parallel beds of HTMH media. Each heat pipe is designed to effectively transport the heat along its entire length (approximately 11-12 meters) and return the condensed sodium vapor back to the absorber section.
- An intermediate gas-phase heat transfer loop receiver, wherein an inert gas is circulated between the absorber section and the HTMH media bed (shown in Figure 68).

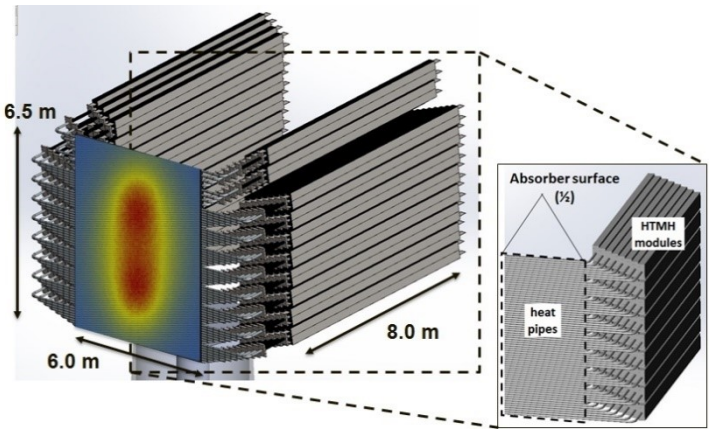

Figure 67 – Heat-pipe receiver concept, wherein an array of heat pipe absorb concentrated solar energy and convey it into an array of HTMH vessels.

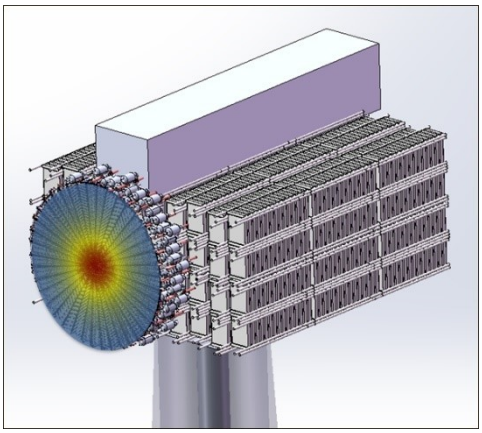

Figure 68 – Heat Transfer Fluid (HTF) Loop receiver, with ah an inert gas is circulating between the absorber and HTMH media.

As described previously, there are a number of competing advantages and challenges associated with each design. Advantages for heat pipes include:

- Heat pipes are extremely flux-tolerant and operate at low pressure, eliminating the high-temperature and/or peak flux stress concerns that are paramount in high-pressure gas-receiver cells
- The heat pipe operate passively, and do not require any additional components to convey the heat transfer or actively control it
- Because the surface of the heat pipe remains isothermal, heat transfer into the metal hydride will be at a constant temperature.
- The system may be designed to thermally isolate the HTMH media from the absorber when solar input ceases (e.g. during TES discharge mode and storage periods).
    - If the evaporator (solar absorber) is located below the level of the condenser (HTMH), liquid return will be driven by gravity. When the solar heat input is removed the liquid in the absorber section will not boil and will pool there
    - Even when heat is added to the condenser section during TES discharge, without a constant supply of liquid to sustain boiling there will be no heat transfer to the

absorber; the system will be stable with a static temperature gradient from the hot HTMH end (top) to the cold absorber end (bottom)

- Note that this thermal isolation is passive, and does not rely on active control.

Heat Pipe challenges include:

- Because the system is passive, there is less flexibility or inherent responsiveness that may be employed for off-design or unexpected conditions
- On the basis of previous experience, the inclusion of sodium within a solar power system is an area of general unease; additional safety measures and compelling justification will be needed to overcome this barrier to adoption
- At the high temperatures at which the HTMH will be operating, the released hydrogen will be able to permeate through the metals and materials of construction. The heat pipes themselves are extremely sensitive to contamination and would undergo severe performance degradation in the presence of permeated hydrogen. Very robust measures need to be taken to ensure that permeated hydrogen does not compromise heat pipe performance.

For the Heat Transfer Loop system, compelling advantages include:

- The overall system architecture is familiar to the end-user, who is familiar with the concept of using intermediate heat transfer fluids to convey energy between components
- The fundamental research and development required to implement an HTF system is predominantly complete (including receiver designs, circulator technology, heat exchanger architecture, etc); the remaining challenges are fundamentally engineering in nature

Challenges associated with the Heat Transfer Loop system include:

- A somewhat lower system efficiency may be expected, as there is an additional heat exchanger (with its associated ineffectiveness) in the thermal loop.
- There will be an operating parasitic associated with the operation of this system, as there needs to be a means of circulating the heat transfer fluid. This parasitic will reduce the net power generation of the integrated power system
- The initial estimate suggests that the HTF system – which includes a circulator, heat exchangers, intermediate fluid connections – may have a higher initial capital cost than the heat pipe system. That said, the estimates are close enough to be within the margins of uncertainty.

The candidate designs will be evaluated on multiple criteria, including cost, maintenance, efficiency, operability limits, safety, barriers to adoption, controllability, tolerance to systemic

deviations, and manufacturability. Each criteria will be weighted for criticality and importance on the basis of team and advisory committee input. Each candidate system will then be scored in each criteria, which will provide a full weighted score for each criteria, and the sum of all scores will be used to quantitatively compare the candidate systems. On the basis of this Concept Scoring matrix (or Selection Matrix) a single go-forward technology path will be identified and selected.

To accomplish this SubTask, Brayton Energy solicited feedback from industry, research, and end user institutions to determine their perceived weighting of the various parameters identified as critical elements of the receiver designs. The questionnaire is shown in Table 14.

Table 14 – Questionnaire submitted to government research labs, industry OEMs and integrators, end-users, and R&D institutions soliciting feedback on the relative criticality of various receiver parameters; these ratings are used to compare and evalute the two proposed design and down-select to a single go-forward technology path.

CATEGORY	WEIGHTING/SCORE OF CRITICALITY	DESCRIPTION/EXPLANATION
Receiver Efficiency		The overall efficiency of the system, which has a direct bearing on the overall system efficiency. Assume that the receiver has at least a comparable efficiency to state of the art designs; how critical is increasing this efficiency?
Control Complexity		The intricacy of the control system needed to maintain efficient, safe, or long-life operation of the system. Is a complex control scheme acceptable if it is not apparent to the end user, or is logical understanding of the system's operational control critical?
System Safety		Overall safety of the system; assume that the system as design is inherently safe, but how critical is safety in the scope of unexpected failures or issues?
Initial Capital Cost		Assume that the LCOE of the proposed integrated system is acceptable and aligns with current DoE targets; given that assumption, how critical is the capital cost of the system?
Ease of Manufacture		More complex manufacturing techniquies may imply longer lead times, single-source vendors, and/or limitedleverage for negotiating cost reductions. How critical is this in comparison to the other categories?
Technical Risk		A technically risky system may have been adequately demonstrated appropriately in the lab and small scale prototypes, but may represent a first-of-its-kind at utility scale. Assume that all technical demonstrations at subscale have been successfully achieved.
System Complexity		The intricacy of the overall system needed to maintain efficient, safe, or long-life operation of the system. Is a complex system acceptable if it achieves all of the operational objectives of the end user, or is an intuitive understanding of the system's operation, feedback repsonses, and sensitivity to changes critical?
User Familiarity with Technology		How critical is it for the new technology to be of a form familiar to the end user? E.g.: a molten salt heat transfer fluid system looks, in many ways, like a thermal oil heat transfer fluid system, making it more intuitively familiar to the end user. Phase change thermal energy storage, however, may be very unfamiliar to a user accustomed to a molten salt sensible thermal energy storage system.
Tolerance to Peak Flux Deviations		How critical is it that any receiver design be tolerant to incident flux distributions that may result from heliostat misalingment, meteorological effects, etc?
Tolerance to Power Deviations		How critical is it that a receiver design be tolerant to power variations during operation? Is a system that operates at a constant incident power or not at all viable, or is a large range of operating powers imperative?
Tolerance to Cycle Flow Deviations		How critical is it that a receiver design be tolerant to variations on the thermal energy storage/power cycle end? Are conjoined TES/power blocks envisioned to run at constant input power, or is it critical that there be variable input power ratings depending on the instantaneous storage and load requirements?
Tolerance to Peak Temperature Deviations		How critical is it that the receiver be tolerant of surface temperature excursions or unexpected temperature spikes? Does the industry see heliostat response delays that may result in significant short-terms spikes in incident power/flux that produces transient hot spots?
Tolerance to Overall Temp Profile Deviations		How critical is it that the receiver be tolerant of surface temperature profile deviations; that is, is the overall system sensitive to the distribution of temperature along the receiver surface, or fast variations/gradients in temperature, assuming that overall receiver performance remains acceptable? Does the industry see effects that may result in significant short-terms temperature profile changes?
Ease of Repair/ Maintenance		How critical is it that the receiver be easy to repair or maintain? Assume that the design maintenance interval is reasonable - but how critical is it that the scheduled maintenance or unexpected repairs be easy or quick, as opposed to time-consuming. Once the system is off-line, how critical is it that the unit be restarted quickly, or do these opportunities ofter allow other maintenance/upkeep that tends to limit the time to-restart regardless of the receiver maintenece/repair duration?
		Score Each Criteria 1 to 10 Please score each category with a value between 1 and 10 to describe its criticality (1 = not critical at all, 10 = extremely critical)

5 sets of responses have been compiled and evaluated. The parameter ratings, the parameter weights (grouped cumulatively and by sector) and the weighted scores are shown for the Heat Pipe receiver and the HTF Loop Receiver in Table 15 and Table 16, respectively. A bar chart showing the results along with error bars representing single standard deviations is shown in Figure 69.

Table 15 – Compiled Heat Pipe receiver results, with collated weightings applied to the specific technology ratings to generate weighted scores; results are presented for all sectors, and for each sector independently.

CATEGORY	HEAT PIPE RATING	ALL SECTORS		GOVERNMENT SECTOR		INDUSTRY SECTOR		R&D SECTOR	
		MEAN WEIGHT	WEIGHTED SCORE	MEAN WEIGHT	WEIGHTED SCORE	MEAN WEIGHT	WEIGHTED SCORE	MEAN WEIGHT	WEIGHTED SCORE
Receiver Efficiency	4	5.6	22.4	7.0	28.0	5.0	20.0	4.5	18.0
Control Complexity	2	7.0	14.0	6.5	13.0	10.0	20.0	6.0	12.0
System Safety	2	7.8	15.6	7.0	14.0	10.0	20.0	7.5	15.0
Initial Capital Cost	3	5.2	15.6	3.0	9.0	8.0	24.0	6.0	18.0
Ease of Manufacture	2	5.6	11.2	5.5	11.0	8.0	16.0	4.5	9.0
Technical Risk	2	6.0	12.0	6.0	12.0	8.0	16.0	4.0	8.0
System Complexity	2	6.8	13.5	7.0	14.0	7.0	14.0	6.0	12.0
End-User Familiarity	2	3.6	7.2	3.5	7.0	2.0	4.0	4.5	9.0
Ease of Repair/ Maintenance	2	7.8	15.5	8.0	16.0	7.0	14.0	8.0	16.0
Tolerance to Deviations									
Peak Flux Deviations	5	7.2	36.0	7.0	35.0	5.0	25.0	8.5	42.5
Power Deviations	5	7.2	36.0	6.5	32.5	7.0	35.0	8.0	40.0
Cycle Flow Deviations	4	7.6	30.4	6.5	26.0	10.0	40.0	7.5	30.0
Peak Temp. Deviations	4	7.0	28.0	7.0	28.0	5.0	20.0	8.0	32.0
Overall Temp. Profile Dev.'s	3	7.0	21.0	7.0	21.0	6.0	18.0	7.5	22.5
WEIGHTED TOTAL			257.4		245.5		268.0		261.5

Table 16 – Compiled Heat Transfer Loop receiver results, with collated weightings applied to the specific technology ratings to generate weighted scores; results are presented for all sectors, and for each sector independently.

CATEGORY	HTF LOOP RATING	ALL SECTORS		GOVERNMENT SECTOR		INDUSTRY SECTOR		R&D SECTOR	
		MEAN WEIGHT	WEIGHTED SCORE	MEAN WEIGHT	WEIGHTED SCORE	MEAN WEIGHT	WEIGHTED SCORE	MEAN WEIGHT	WEIGHTED SCORE
Receiver Efficiency	3	5.6	16.8	7.0	21.0	5.0	15.0	4.5	13.5
Control Complexity	4	7.0	28.0	6.5	26.0	10.0	40.0	6.0	24.0
System Safety	4	7.8	31.2	7.0	28.0	10.0	40.0	7.5	30.0
Initial Capital Cost	2	5.2	10.4	3.0	6.0	8.0	16.0	6.0	12.0
Ease of Manufacture	4	5.6	22.4	5.5	22.0	8.0	32.0	4.5	18.0
Technical Risk	4	6.0	24.0	6.0	24.0	8.0	32.0	4.0	16.0
System Complexity	4	6.8	27.0	7.0	28.0	7.0	28.0	6.0	24.0
End-User Familiarity	5	3.6	18.0	3.5	17.5	2.0	10.0	4.5	22.5
Ease of Repair/ Maintenance	4	7.8	31.0	8.0	32.0	7.0	28.0	8.0	32.0
Tolerance to Deviations			**0.0**		**0.0**		**0.0**		**0.0**
Peak Flux Deviations	3	7.2	21.6	7.0	21.0	5.0	15.0	8.5	25.5
Power Deviations	4	7.2	28.8	6.5	26.0	7.0	28.0	8.0	32.0
Cycle Flow Deviations	4	7.6	30.4	6.5	26.0	10.0	40.0	7.5	30.0
Peak Temp. Deviations	4	7.0	28.0	7.0	28.0	5.0	20.0	8.0	32.0
Overall Temp. Profile Dev.'s	4	7.0	28.0	7.0	28.0	6.0	24.0	7.5	30.0
WEIGHTED TOTAL			317.6		305.5		344.0		311.5

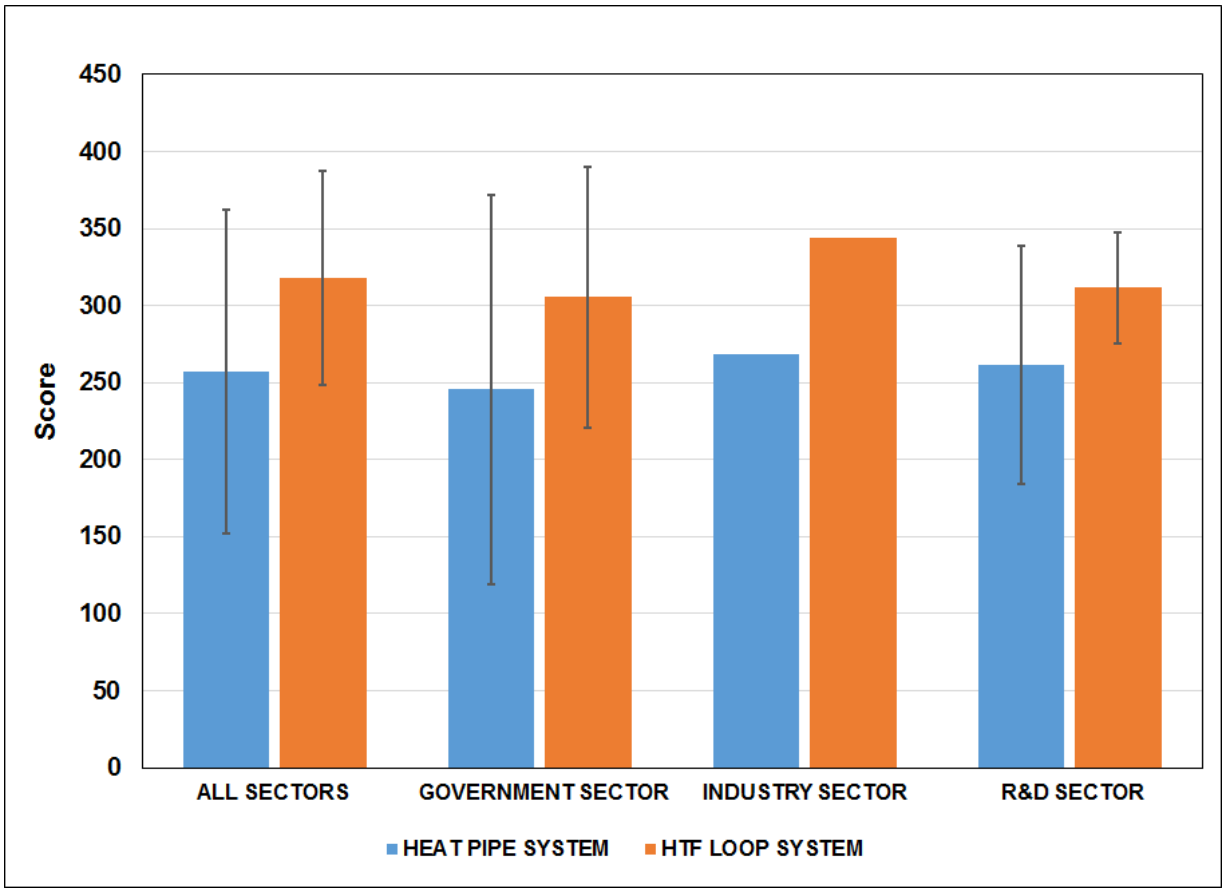

Figure 69 – Bar chart showing the compiled average weighted score for the two proposed receiver technologies, presented by sector and for all sectors combined. Error bars indicate ±1 standard deviation on each category.

The responses show a higher overall weighted score across all sectors for the Heat Transfer Loop design. In order to evaluate the strength of this conclusion, a one-sided test of hypotheses on the equality of two means with the variances known is performed. The null and alternative hypotheses are:

H_0: HTF = HeatPipe

H_1: HTF > HeatPipe

Equation 1

And the test statistic, assuming H_0 is true, is:

$$Z_0 = \frac{\bar{X}_1 - \bar{X}_2}{\sqrt{\frac{\sigma_1^2}{n_1} + \frac{\sigma_2^2}{n_2}}}$$

Equation 2

Table 17 – Results from one-sided test of hypotheses on the equality of means with known variances. Cells shaded red represent those categories in which the heat pipe receiver is statistically "better" than the heat transfer loop design.

CATEGORY	ALL SECTORS		GOV'T SECTOR		INDUSTRY SECTOR		R&D SECTOR	
	z_0	P-value	z_0	P-value	z_0	P-value	z_0	P-value
Receiver Efficiency	-3.53	0.9998	-1.65	0.9505	*n/a*	*n/a*	-7.61	1.0000
Control Complexity	10.43	0.0000	6.13	0.0000	*n/a*	*n/a*	10.14	0.0000
System Safety	13.79	0.0000	9.90	0.0000	*n/a*	*n/a*	8.45	0.0000
Initial Capital Cost	-3.06	0.9989	-2.12	0.9831	*n/a*	*n/a*	-2.54	0.9944
Ease of Manufacture	11.68	0.0000	15.56	0.0000	*n/a*	*n/a*	15.21	0.0000
Technical Risk	8.22	0.0000	4.24	0.0000	*n/a*	*n/a*		0.5000
System Complexity	22.29	0.0000	9.90	0.0000	*n/a*	*n/a*		0.5000
End-User Familiarity	7.42	0.0000	4.95	0.0000	*n/a*	*n/a*	4.56	0.0000
Ease of Repair/ Maintenance	49.02	0.0000		0.5000	*n/a*	*n/a*		0.5000
Tolerance to Deviations								
Peak Flux Deviations	-8.21	1.0000	-3.30	0.9995	*n/a*	*n/a*	-9.58	1.0000
Power Deviations	-5.55	1.0000	-1.84	0.9670	*n/a*	*n/a*	-6.76	1.0000
Cycle Flow Deviations	0.00	0.5000	0.00	0.5000	*n/a*	*n/a*	0.00	0.5000
Peak Temp. Deviations	0.00	0.5000	0.00	0.5000	*n/a*	*n/a*		0.5000
Overall Temp. Profile Dev.'s	11.07	0.0000	4.95	0.0000	*n/a*	*n/a*	12.68	0.0000

The results of this analysis are given on a per-parameter basis in Table 17, with conditions that meet the alternative hypothesis H_1 highlighted in red. To summarize the findings, the heat pipe receiver is statistically more efficient, has a lower initial capital cost (based on preliminary data, though there may be significant room for this to change), and is more tolerant to peak flux and power deviations at a confidence level of >99.8%. In all other categories the HTF loop receiver design is the statistically favorable design.

A secondary analysis that endeavors to compile all of the results into a statistically defensible case, a paired t-test was also applied to the data. For the same hypotheses, the test statistic is:

$$t_0 = \frac{\bar{d}}{s_d/\sqrt{n}} \qquad \text{Equation 3}$$

Where

$$\bar{d} = \frac{\sum_{j=1}^{n} d_j}{n} \quad \text{and} \quad s_d^2 = \frac{\sum_{j=1}^{n} d_j^2 - \left[\left(\sum_{j=1}^{n} d_j\right)^2/n\right]}{n-1} \qquad \text{Equation 4}$$

The calculated test statistic for the compiled data is given in Table 18. The conclusion is that the alternative hypothesis is true – i.e., the HTF loop receiver design is the preferred technology to pursue – with a 91.8% confidence level (all sectors being considered).

Table 18 – Results from the paired t-test of compiled data.

CATEGORY	ALL SECTORS		GOV'T SECTOR		INDUSTRY SECTOR		R&D SECTOR	
	D_j	D_j^2	Dj	D_j^2	Dj	D_j^2	Dj	D_j^2
Receiver Efficiency	-5.60	31.36	-7.00	49.00	-5.00	25.00	-4.50	20.25
Control Complexity	14.00	196.00	13.00	169.00	20.00	400.00	12.00	144.00
System Safety	15.60	243.36	14.00	196.00	20.00	400.00	15.00	225.00
Initial Capital Cost	-5.20	27.04	-3.00	9.00	-8.00	64.00	-6.00	36.00
Ease of Manufacture	11.20	125.44	11.00	121.00	16.00	256.00	9.00	81.00
Technical Risk	12.00	144.00	12.00	144.00	16.00	256.00	8.00	64.00
System Complexity	13.50	182.25	14.00	196.00	14.00	196.00	12.00	144.00
End-User Familiarity	10.80	116.64	10.50	110.25	6.00	36.00	13.50	182.25
Ease of Repair/ Maintenance	15.50	240.25	16.00	256.00	14.00	196.00	16.00	256.00
Tolerance to Deviations								
Peak Flux Deviations	-14.40	207.36	-14.00	196.00	-10.00	100.00	-17.00	289.00
Power Deviations	-7.20	51.84	-6.50	42.25	-7.00	49.00	-8.00	64.00
Cycle Flow Deviations	0.00	0.00	0.00	0.00	0.00	0.00	0.00	0.00
Peak Temp. Deviations	0.00	0.00	0.00	0.00	0.00	0.00	0.00	0.00
Overall Temp. Profile Dev.'s	7.00	49.00	7.00	49.00	6.00	36.00	7.50	56.25
SUMS	67.20	1614.54	67.00	1537.50	82.00	2014.00	57.50	1561.75
Dbar	4.80		4.79		5.86		4.11	
S_D^2	99.38		93.60		117.98		101.97	
t_0	1.80		1.85		2.02		1.52	
P-Value	0.0820		0.0759		0.0578		0.1243	

Based on the results presented above, **there is a strong and statistically-defensible community perspective that favors the development of the intermediate gas-phase heat transfer loop system design for the receiver**. Although there are challenges associated with this design, they are engineering in nature, and Brayton is dedicated to successfully demonstrating a design that will de-risk the full-scale system design.

Task 3:

Further investigations needed to validate the system designed in Budget Period 1 will be performed. During these investigations the integrated model will be exercised to determine the annualized system performance.

HTMH and LTMH HEX Design

The HTMH and LTMH HX consist of many of Brayton's internally finned cells headered together inside of an outer shell containing the hydrogen gas. The gaps between the cells is packed with MH. Because of the high permeability of hydrogen, there is no need to provide flow paths through the MH. The spacing of the cells determined based on the desired temperature drop over the MH. At the maximum charging rate, the temperature drop over the MH should be limited to 30 °C.

Another limiting factor for the HX

is the length of the cells, using current manufacturing techniques, the maximum cell length is two meters. There are three separate TES modules in the system, each of which operates identically. During discharge, the HTMH HX experiences its maximum discharge rate of 6.6 MW per module. The LTMH discharges at a lower rate because of its composition and only experiences 1.9 MW of maximum heat transfer. Using the maximum allowable temperature drop, the mass of MH required, MH conductivity, and maximum heat transfer rate, the number of cells can be calculated for the HTMH, and LTMH, this is listed in Table 19.

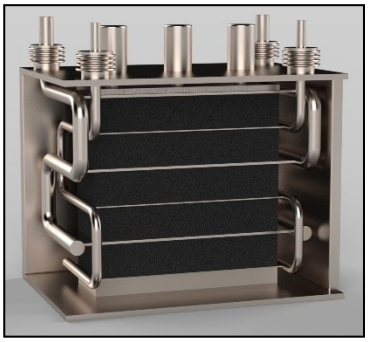

Figure 71 – Representative MH heat exchanger layout, with MH media sandwiched between alternating charge- and discharge-pass cells.

Figure 70 – HTMH PV cutaway to show layout of cells.

Once the number of cells are known, the pressure vessel size can be calculated. The pressure vessel is sized to hold all of the MH while including space for the volume filled by the cells, as well as an additional 10-15% volume to account for the rectangular packing inside of a circular pressure vessel. A proposed HTMH core is shown in Figure 71; a rendering of the HTMH and LMTH PVs filled with cells is shown in Figure 70.

Pressure vessel wall thickness are sized using ASME BPVC Section VIII design by rule [32]. Because of the low pressure of the hydrogen, 316 stainless steel can be used for the shell of the PV, which reduces costs compared to nickel alloys. The cost of the pressure vessel is calculated using correlations for vertical pressure vessels presented in [33]. Inflation and material corrections were obtained from [34], [35]. It was determined that this method of costing would provide adequate accuracy for this project.

The costs of the cells are determined from a rigorous costing exercise studying labor costs, capital cost requirements, material costs, and processing costs. Costs presented in Table 20 correspond to the situation where at least four complete systems are produced per year. Costs for the LTMH cells are scaled by 0.13 to account for differences in required material, as stainless steel can be used in the LTMH HX [35].

An alternative to the high cost 316 stainless steel HTMH pressure vessels is an internally insulated design. Internal insulation is commonly used for hydrogen gas plants to keep the steel temperature low. Hydrogen passing through the lines can reach 870°C which is much greater than the maximum temperature of the HTMH vessel (760°C) [36]. Because of the low flow rates of hydrogen, and vast industrial experience of internal insulation for hydrogen transfer lines, it is assumed that internal insulation can be safely used. The goal of the internal insulation is to reduce the wall temperature of the pressure vessel shell so a lower grade, lower cost steel can be used. In this case P91 was specified because of

Table 19 – Internally insulated pressure vessel

its high allowable stress, and frequent use in steam power plants [32]. The allowable stress of P91 starts to fall off at temperatures greater than 400°C, so the internal insulation was designed to keep the shell below that temperature. Higher allowable stress means a larger vessel can be specified with a reasonable wall thickness. It was assumed that the vessel would operate with 2 sets of cells in series. The large flow area means there is minimal pressure drop through each cell, placing the cells in series results in a pressure drop increase from 27kPa to 293kPa. While this is a 10x increase in pressure drop, the total pressure drop is still barely more than 1% of the absolute pressure. Having a larger pressure drop will allow for a more even flow distribution and a lower cost pressure vessel. A summary of the internally insulated pressure vessel design is given in Table 19.

specifications.

PARAMETER	UNITS	HTMH HX
Number of Pressure Vessels per Module	#	2
PV Outer Diameter	m	4.882
PV Thickness	mm	25.8
PV Length	m	4
PV Material	-	P91
Insulation Thickness	mm	200
Insulation Material	-	Greentherm 23 LI
Insulation Conductivity	W/m-K	0.26
Number of Modules	#	3
Total PV Cost	$	$1,119,000
Total Cost Insulation	$	$322,000

Pressure vessel costs are determined using the same method as the 316 pressure vessels with a different cost factor for P91 construction [37]–[39]. The insulation chosen was listed as one of those used in hydrogen gas plants, and it is assumed that it will perform well in this application [36]. A cost of the insulation material is also needed to ensure that the cost savings of the pressure vessel is not lost to the additional cost of the insulation. The volume of insulation needed is calculated and, using available pricing, the cost of the insulation was calculated [40]. This cost does not include any discounts for bulk ordering, and represents a conservative cost estimate.

Another potential cost savings for the system is changing the allowable temperature drop through the MH. The current specification calls for a maximum temperature drop of 30°C through the MH during discharge when the bed is under the highest load. This assumes that all of the power going to the cell is coming from the MH at the furthest limit of the MH bed. In reality this will never be the case, at the start of the charge or discharge cycle the temperature difference between the MH and CO_2 will be very small, and as the MH is discharged the temperature difference will grow larger as a temperature profile develops in the MH. Limiting the maximum temperature drop across the MH to 30°C means the HTMH HX will perform much better than the cycle model predicts. Specifying the average temperature drop through the MH to be 30°C would more closely represent the performance model. To fully understand the behavior of the HTMH HX a full numerical model of the regenerator is required that takes into account conduction, reaction rate, and heat transfer. However, this model is difficult to create and has not been produced. Instead we will have to assume that the maximum temperature difference across the MH corresponds to twice the average temperature difference. For a 30°C average temperature drop over the MH a maximum temperature drop of 60°C is specified. This reduces the number of cells from 4,420 to 3,125. It might be expected that doubling the allowable temperature drop would halve the cell count; however, as the cell count is decreased the specific heat transfer rate

increases, resulting in a 30% reduction. Using the 60°C maximum temperature drop, the new cost for all HTMH cells is $8,044,000.

System Performance

Thermal performance of the TES module is measured by taking the ratio of the amount of energy recovered from TES divided by the amount of energy provided to the TES module. Energy passed to and from the TES is assumed to be equal to the heat transfer to the CO_2, i.e. no losses in the CO_2 before or after the model are considered. Because these losses are likely to be constant for any CO_2 cycle, they are not necessary for this analysis. To calculate the round-trip efficiency, all of the loss mechanisms must be identified. First, there are no losses in the MH hydration reaction, it is assumed that this reaction is reversible, so the same amount of energy is needed to free the hydrogen as is released when the H_2 is re-bonded. Next, the thermal losses from the exterior of the shell need to be calculated. These losses are expected to be small because low cost, low conductivity insulation can be liberally applied to the exterior of the vessels. Additionally, at large sizes, the ratio of surface area to volume is small making it much easier to prevent heat loss. Next there are the thermal losses associated with the hydrogen transport system. There is a heat loss associated with the hydrogen transport pipe, which takes hydrogen released from the TES module on the tower and brings it to the regenerator and LTMH HX at the base of the tower. Again, adequate insulation can be applied to keep the thermal losses low. Finally, there are losses in the hydrogen regenerator which is used to recover the thermal energy from the hydrogen before it is stored in the LTMH HX. The regenerator is not perfectly effective, and there is some heat loss associated with

that ineffectiveness.

Additionally, when the regenerator sits idle for long periods of time there is a degradation in the thermocline (bed axial temperature profile) which results in the hydrogen exiting the hot side of the regenerator cooler than it would have been if the flow was immediately switched. Each of these losses has been calculated, and where applicable a yearly average value is reported in Table 20.

Table 20 – TES round trip energetic efficiency for design day.

PARAMETER	UNITS	VALUE
Heat Transfer Rate	MW_t	19.8
Vessel Thermal Loss	kW_t	81
H_2 Pipe Thermal Loss	kW_t	32
H_2 Regenerator Thermal Loss	kW_t	17.6
H_2 Regenerator Ineffectiveness	kW_t	55.5
H_2 Regenerator Thermocline	kW_t	6.6
Total TES Loss	kW_t	192.7
Energetic Round Trip Eff.	%	99.00%

The HTMH HX, H_2 pipe thermal loss, and regenerator thermal loss are all calculated using the same 1-d resistance network model. In the case of the H_2 pipe and regenerator the model calculates a heat transfer coefficient based on the flow conditions. In the vessel the temperature at the inner wall is assumed to be a constant 730°C. In addition to calculating heat transfer through the wall, it is also assumed that 15mm of microtherm insulation is applied to the outside of the component. Microtherm is a silica aerogel product that has been formed into sheets. It has a very low conductivity (0.025 W/m-K) and can be used at over 1050°C [41]. It is assumed that the H_2 pipe and regenerator have 15mm of insulation while the HTMH vessels have 40mm. The ambient conditions are variable according to the weather file provided in SAM for Daggett,

CA. The thermal loss was calculated for each hour and averaged throughout the year for each component. The outside of the component is allowed to convect at the specified air speed and dry bulb temperature. Additionally, the exterior experiences radiation with the surrounding at the dry bulb temperature, the outside of the insulation is assumed to have an emissivity of 0.85.

The HTMH HX is separated into many smaller pressure vessels to maintain reasonable wall thicknesses. These pressure vessels can be mounted in close proximity so they behave like a single vessel when calculating heat loss. Instead of modeling the heat loss for one vessel and multiplying it by the number of vessels, the heat loss per module of 9 pressure vessels are calculated together to capture the close mounted heat loss effects.

The regenerator model described above is also used to determine the ineffectiveness of the regenerator. Ineffectiveness is a measure of how much additional heat needs to be added in the HTMH HX to make up for imperfect heat transfer in the regenerator. Because the cost of the regenerator is small compared to the total plant size, the ineffectiveness should be specified as a fairly low value. An ineffectiveness of 1.6% was desired in order to keep the round trip energetic efficiency high. There is not expected to be any annular variation in regenerator ineffectiveness.

Degradation in the regenerator thermocline is something that is normally not considered in the design of a regenerator. Normally regenerators are design to always be in either the charging or discharging state. Allowing a regenerator to dwell in a charged state will result in a flattening of the temperature profile in the regenerator which means the temperature of the H_2 leaving the hot side of the regenerator and returning to the HTMH HX will be lower than if the thermocline had not degraded. In order to quantify this effect a model is created in python that discretizes the regenerator into a 1-D array of nodes and numerically solves for the thermocline degradation. An important part of this model is the conductivity assumed for the packed bed. The packed bed is specified as a randomly packed bed of spheres which have a much lower conductivity compared to a solid material. The air gaps in the bed are too small to set up natural convection cells, and point contact between the spheres mean the conductivity of the bed is low. 0.3 W/m-K was used as the effective conductivity of the bed, which was obtained from [42]. Stainless steel spheres with a diameter of 3 mm are used for the packing, the small diameter means the packing has a large surface area, increasing effectiveness. Figure 72 shows the temperature at the hot side of the regenerator as a function of an 8hr dwell.

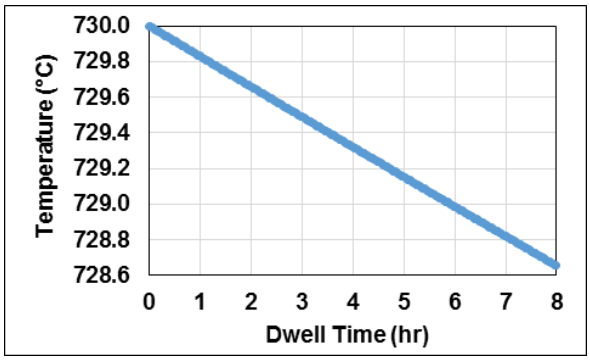

Figure 72 – Temperature at hot end of H_2 regenerator as a function of dwell time.

The target energetic efficiency uncertainty is under 2% of the 99% round trip efficiency. Because of the high efficiency, having an uncertainty of -2% means having a round trip efficiency of 97%. To realize a 97% round trip efficiency losses in the system would need to be tripled. Since this is such a large increase in losses, it is impossible that changing any of the parameters by some amount of uncertainty will cause the energetic efficiency to move below 97%. For this reason, it is assumed that the design meets milestone 3.1.1

It is also desirable to measure the exergetic efficiency of the TES system, as exergy is a better measure of how well the available energy is being utilized. The exergetic efficiency of the TES module is defined according to Equation 5.

$$\eta_X = \frac{\dot{X}_{Discharge}\, t_{Discharge}}{\dot{X}_{Charge}\, t_{Charge}} \qquad \text{Equation 5}$$

where $t_{Discharge}$ is the amount of time spent discharging, t_{Charge} is the time spent charging, $X_{Discharge}$ is the exergy transfer rate out of the TES module during discharge, and X_{Charge} is the exergy storage rate into the TES module during charge. X_{Charge} is defined in Equation 6.

$$\dot{X}_{Charge} = \dot{Q}_{Charge}\left(1 - \frac{T_0}{T}\right) \qquad \text{Equation 6}$$

where $\dot{Q}_{Charge}$ is the heat transfer rate while charging calculated based on the temperature difference and mass flow rate into and out of the TES module during charge. T_0 is the heat rejection temperature, in this case it is assumed to be 32 °C. And T is the temperature at the boarder over which heat transfer occurs, for the case of charging this is taken to be 730 °C. Because there is a ratio of temperatures, T_0 and T must be converted to K in Equation 6. A similar equation can be used to calculate the discharge exergy flow rate except the energetic efficiency must be taken into account. The discharge exergy flow rate is given in Equation 7.

$$\dot{X}_{Discharge} = \dot{Q}_{Discharge}\eta_{Energetic}\left(1 - \frac{T_0}{T}\right) \qquad \text{Equation 7}$$

In this case T is defined as 700 °C because the heat transfer into the fluid occurs at a lower temperature. The energetic efficiency ($\eta_{Energetic}$) is added to account for the losses that occur between charging and discharging. The lower heat transfer boundary temperature and energetic efficiency results in a lower exergy transfer rate during discharge than charging. The resulting exergetic efficiency is 97.7%. An uncertainty

analysis was also conducted, the temperature at the heat transfer boundary was allowed to vary by 30 °C which is the maximum expected variation in temperature of the heat transfer boundary. The energetic efficiency will be allowed to vary by 2%, which is the limit from milestone 3.1.1. The resulting uncertainty is ±2.7%, which means that at the low end of the range, the exergetic efficiency is 95% which meets the milestone goal.

SubTask 3.1:

Apply the range of solar inputs representing the diurnal and annual variations to the model developed in Task 1.1.3 for the absorber layout down-selected in Task 2.1. Evaluate the proposed system, which was defined at design point, across these anticipated variations in operating conditions to understand how the proposed system performs throughout the full year.

Solar Field Modeling

Heliostats

The solar field was designed using the heliostats specified for the GEN3 project. Each heliostat has a small surface area, yielding more accurate aiming but requiring more rigorous cleaning procedures. Since the heliostats are so small, the focusing strategy is not as important. A field created using flat mirrors is only 1.5% more expensive than a field created using individually-focused heliostats. Individually-focused mirrors were utilized for the field design discussed in subsequent sections. The heliostat dimensions and properties are listed in Table 21.

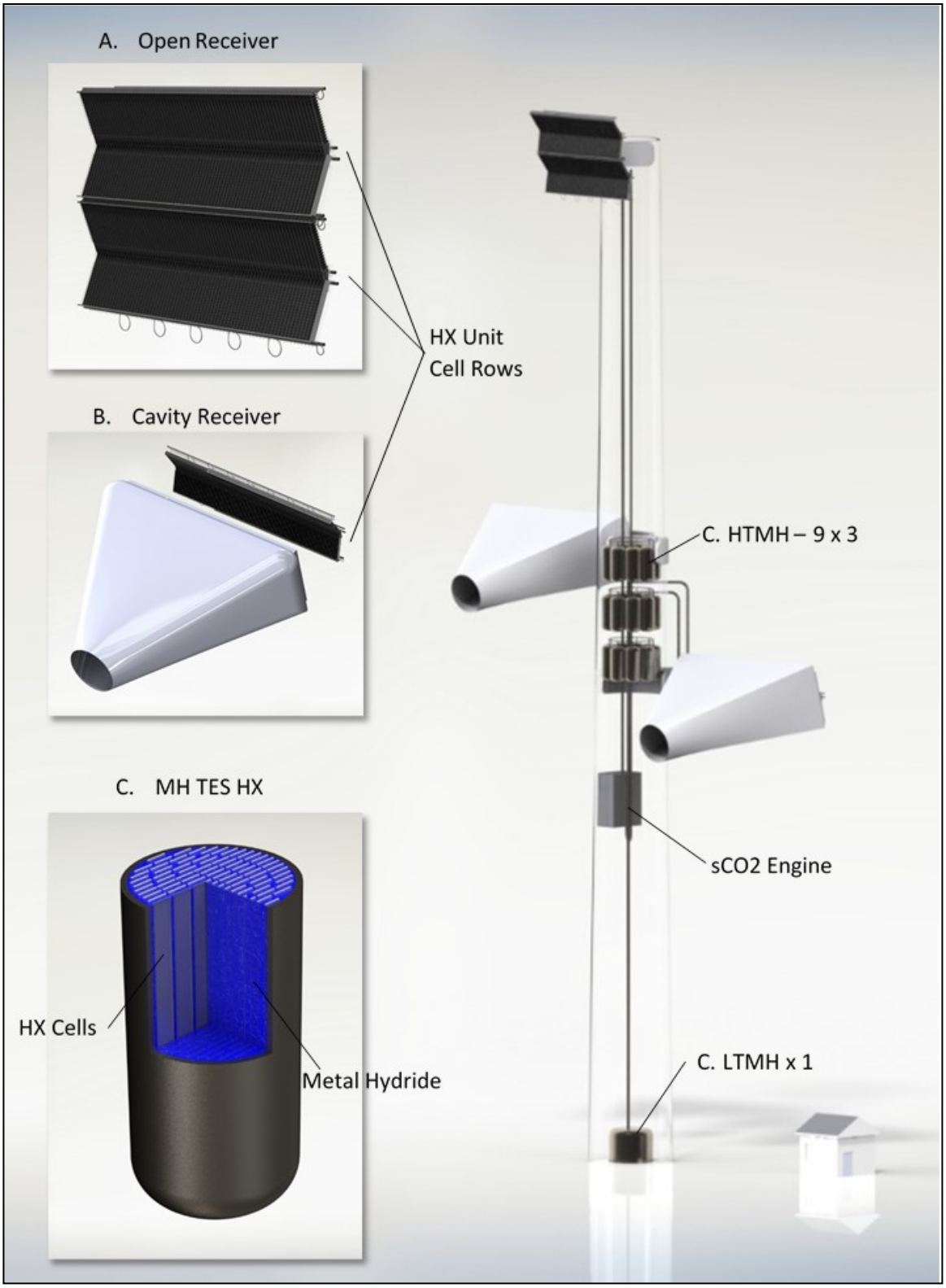

Figure 73 – Integrated System Architecture: (A.) Open Receiver: two rows of heat exchanger unit cells (B.) Cavity Receiver: single row of heat exchanger unit cells (C.) MH TES HX: HX Cell array and metal hydride packing, applicable to both LT and HT heat exchangers.

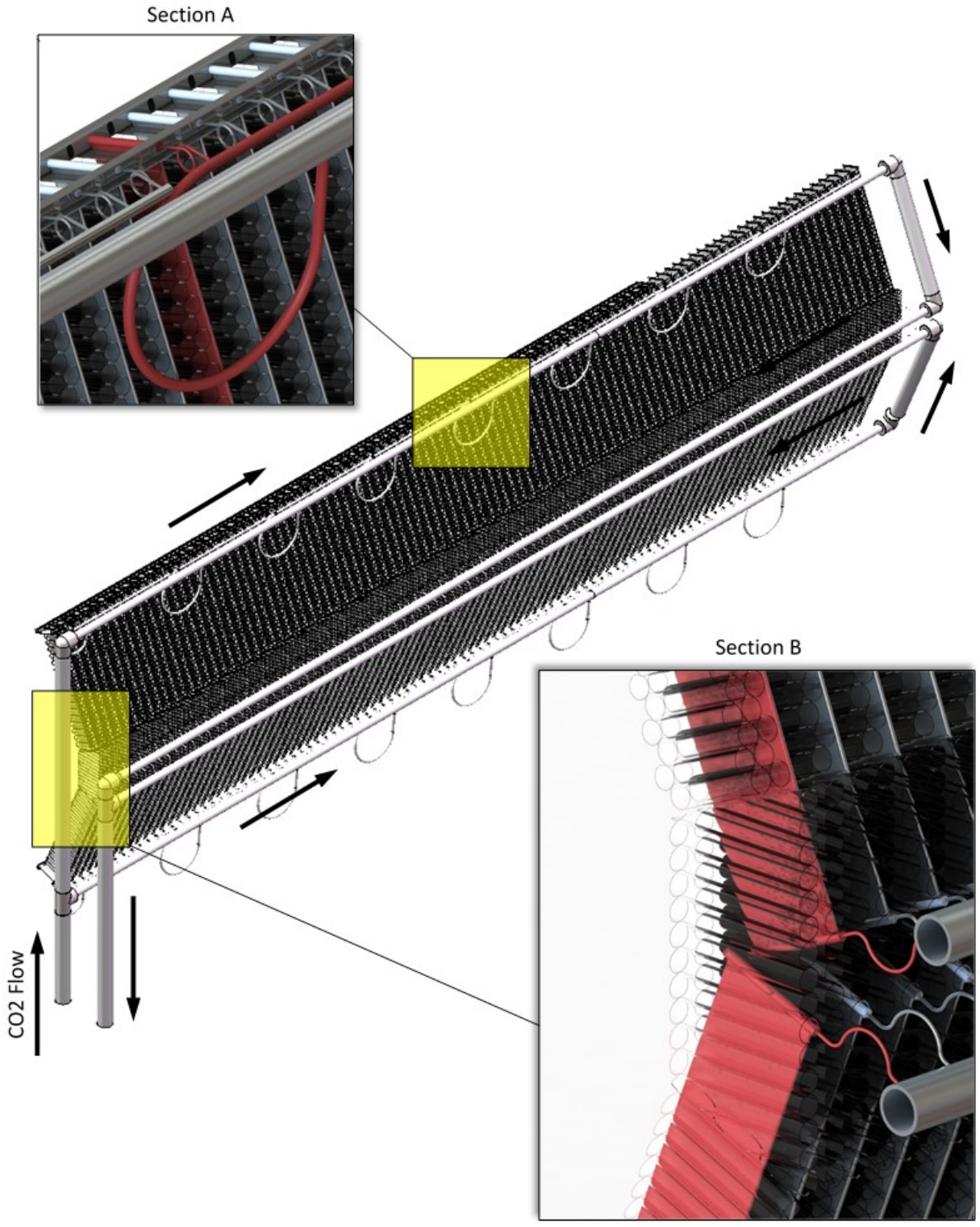

Figure 74 – Receiver Architecture highlighting flow distribution. Section A: Manifold strain relief. Section B: Heat exchanger pitch resulting in recessed and shielded header blocks.

Solar Field Design

Table 21 – Heliostat dimensions and properties.

PARAMETER	UNITS	VALUE
Width	m	2.00
Height	m	1.00
Aiming Error	mrad	1.00
Slope Error	mrad	1.00
Reflectivity	-	0.93

As introduced in Quarter 7, the system layout utilizing the RCBC engine as the heat transfer fluid circulator employs 3 receivers: 1 large 26.7MW$_t$ receiver and 2 smaller 5.4MW$_t$ cavity receivers. The two cavity receivers employ center-aiming at the aperture, while the open receiver requires a unique aim-strategy to yield an approximately linear flux distribution along the length of the receiver cells. In order to design a solar field capable of meeting the power and flux distribution requirements on all receivers, the latest version of NREL's SolarPILOT™, which was modified for the Gen3 project in Quarter 1, was employed. A complete description of the multi-receiver field design methodology and unique flux profile implementation can be found in the Gen3 Q1 report.

SolarPILOT was used to create an optimized system layout at design point by varying the receiver elevation angles, the tower height, the vertical offset between receivers, and the dimensions of the cavity apertures. The open receiver dimensions were specified by the receiver modeling effort (described in a subsequent section), based on the fluxes tolerable to maintain reasonable metal temperatures. Heat losses from both the cavity receivers and the open receiver were approximated and used to more accurately size the solar field. The heat losses from the open receiver were specified by the receiver modeling effort. The cavity radiation losses were approximated using blackbody emission through the aperture area at the average cavity temperature of approximately 770°C. The cavity convective losses were approximated using the correlation presented by Stine & McDonald[43] and verified using SolidWorks Flow Simulation. A conduction loss of 1% was also applied. Since only the cavity apertures could be evaluated using SolarPILOT, an iterative process using SolarPILOT and SolTrace was employed. The field layout and heliostat aimpoints were exported from SolarPILOT and imported into SolTrace to determine the placement of the receiver panels behind the aperture of the cavity receivers, such that the desired peak flux was maintained. Since the convective losses depend on the overall surface area of the cavity, the SolarPILOT model was then updated using a refined convective heat loss and the process repeated. The

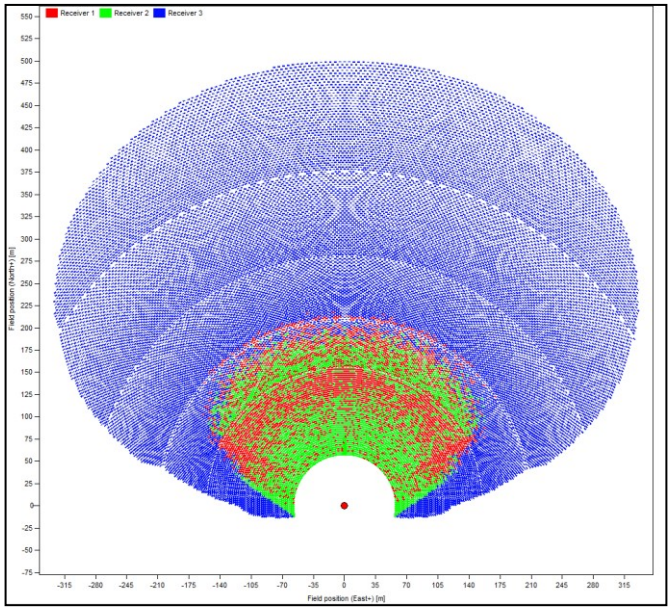

Figure 75 – Solar field layout for 3-receiver tower. Colors indicate at which receiver each heliostat aims. *Receiver 1* and *Receiver 2* correspond to the cavity receivers, which are lower on the tower than the open receiver (*Receiver 3*).

resulting field layout can be seen in Figure 75, with the different colors corresponding to the receiver to which each heliostat aims. In order to decrease the aperture size of the cavity receivers, thereby decreasing the heat losses, the closest heliostats are allocated to the cavity receivers. The resulting flux profiles on all three receivers are displayed in Figure 76, and the corresponding system dimensions are displayed in Table 23.

a)

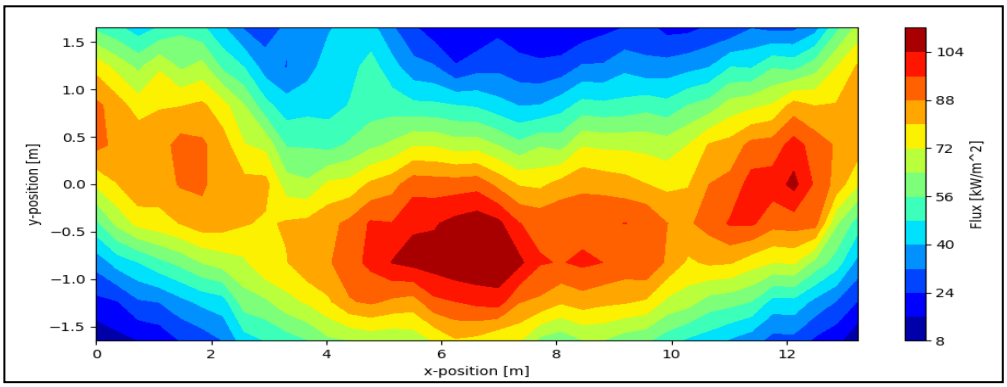

b)

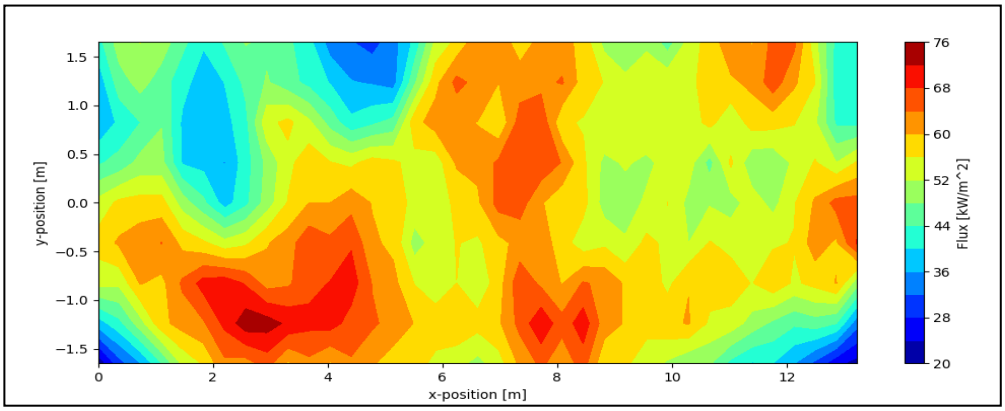

c)

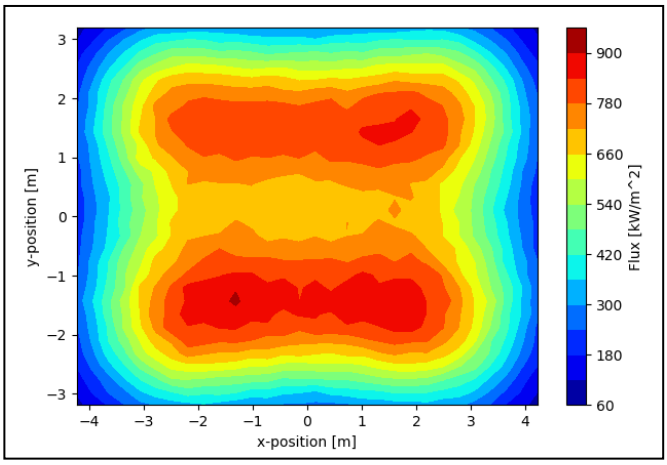

Figure 76 – Flux profiles calculated for a) Receiver 1 (cavity), b) Receiver 2 (cavity), and c) Receiver 3 (open). Note that Receiver 3 has rows of receiver cells stacked.

As seen in Figure 75, the acceptance angle of the two cavity receivers is large (~120°); as a result, many reflected rays strike the aperture at steep angles. This results in approximately 40-50% of the total power incident on the aperture spilling onto the cavity walls. Assuming the cavity walls will be made of a material similar to RSLE-57 (used in cavity receivers by other researchers), it is reasonable to assume that the majority of the power incident on the cavity walls will eventually strike the receiver panels due to reflection and re-emission from the cavity walls. Ideally, the peak flux modeled on the receiver panels should be less than the desired peak flux (~100kW/m^2 per the receiver modeling), to accommodate re-radiation from the cavity walls. The flux values reported in Figure 76 approximately meet the desired peak flux (within uncertainty) but do not account for reflection from the cavity walls. With modifications to the cavity/receiver, such as surface contouring and/or varying the cavity dimensions (ex. increasing the width), the flux levels can be brought to required levels.

Table 22 – Receiver specifications.

PARAMETER	UNITS	VALUE
Tower Height	m	101
Cavity Receiver 1		
Aperture Dimensions (WxH)	m	2.00 x 2.00
Receiver Dimensions (WxH)	m	13.20 x 1.65
Elevation Angle	°	28
Vertical Position	m	67.5
Cavity Receiver 2		
Aperture Dimensions (WxH)	m	2.00 x 2.00
Receiver Dimensions (WxH)	m	13.20 x 1.65
Elevation Angle	°	34
Vertical Position	m	77
Open Receiver		
Dimensions (WxH)	m	8.76 x 6.60
Elevation Angle	°	16
Vertical Position	m	101

Receiver Design

The receiver for the power cycle is to be made of Brayton's brazed internally finned heat exchanger cells. A thin walled pressure boundary can be used because of the support provided by the fins. To account for the high flux experienced by the nose of the cell, a nose channel is created that allows for direct cooling via CO_2. A rendering of the cross section of a part of a single cell is shown in Figure 77.

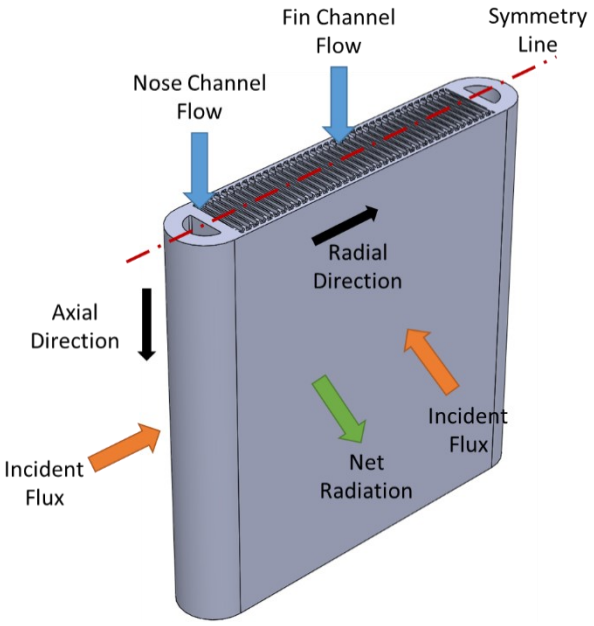

Figure 77 – Cross section of internally finned cell showing fin and nose channels.

The cells are low cost, and can withstand the temperatures (790 °C) and pressures (25 MPa) experienced by the receiver. Many cells are arranged parallel to the incoming sunlight, and together make up the receiver. Critical to the design of the receiver is the pressure drop, the maximum metal temperature, and the reradiation losses experienced by the receiver. Current specifications call for a 750 kPa maximum pressure drop, a max metal temperature of 790 °C, and reradiaiton losses less than 10 percent. A model is needed that can quickly and accurately calculate these output parameters for various receiver geometries. A finite difference model was created in EES that discretizes one side of one cell in

the receiver into 5 nodes in width, and 20 nodes in length [11]. Since the nose sees a significant flux, it too is discretized into 5 nodes radially and 20 nodes in length. The flux experienced by the cell changes with location because of shading, and significantly more flux is incident on the front of the cell compared to the back. Based on the location of all the heliostats in the field, the power each provides to the receiver, the cell spacing, cell width, and cell thickness; a flux profile can be created for the cell. At each location a resistance is calculated for conduction from one metal node to the adjacent metal nodes and from the metal to the fluid. There are two resistances in parallel for the heat going into the fluid, the heat can be directly convected, or it can be conducted down the fin, then convected into the fluid. A fin efficiency is calculated for the latter, and is used to calculate the total resistance between the surface metal and the fluid. The nodes in the nose are allowed to conduct radially, and are linked to the first column of nodes in the cell. Because of the high flux on the nose, up to 20 percent of the total energy into the receiver, the nose is assumed to be constructed around a D shaped tube that allows CO_2 to flow down the nose, keeping the temperature low. Heat from the CO_2 in the nose is allowed to flow into the CO_2 in the cell. It is assumed that a passive flow distribution device will be used in the cell to maintain constant exit temperatures. This device will force more flow down the nose and front of the cell where the flux is higher.

Radiation is also an important consideration because it serves to levelize the temperature profile, but also contributes to losses from the receiver. To calculate the radiation losses, a view factor is needed from each element to its surroundings. For the face of the cell, each element can see the opposite cell, the back insulation, and the environment. Determining the target radiation temperature each element sees is difficult because the surface temperature of the cell is not constant. If the average temperature of the cell is used, an overestimation of the temperature flattening effect will be experienced. So the other, more conservative extreme was assumed, where no radiation heat transfer occurs from the cell to its neighbor. It is not possible to assume no radiation heat transfer with the insulation because the insulation is adiabatic. Because there is flux incident on the insulation, it must be reradiated out either to the cell or the environment. An energy balance is conducted on the insulation and the temperature of the insulation is allowed to change so it is adiabatic, i.e. the amount of flux incident on the insulation is equal to the heat transfer from the insulation to the environment and the cell. The insulation must be modeled as isothermal as the number of radiation resistances grows with the product of the number of elements in the cell, and number of elements in the insulation. Discretizing the insulation into even 10 elements would increase the number of equations by 2000. Because EES limits the number of equations in a problem, adding 2000 more equations causes EES to run out of memory. Modeling the insulation as isothermal means that temperature smoothing is overestimated, however, this mostly occurs at the back of the cell where fluxes are lower, and metal temperature is less of a concern.

Pressure drop is determined through each element using friction factors calculated for square fin channels. By calculating pressure drop for each element, local properties can be used for the calculation of pressure drop and heat transfer coefficients. Because the fin channels do not allow flow in the radial direction, the total pressure drop in the cell is determined by the column of elements that has the lowest outlet pressure. The high flux on the nose necessitates extra flow to keep the nose cool which also means the highest pressure drop is in the nose channel. Using

all of the resistance equations calculated and the boundary conditions of flow and radiation, an energy balance can be added for each node including conduction, convection, and radiation to the appropriate elements. EES will iterate the temperatures of each element to solve all of the coupled energy balance equations simultaneously. The finite difference model returns the metal temperature, fluid temperature, and the fluid pressure at each element. An energy balance can be run on the cell to ensure the system of equations has been properly defined. Without radiation the amount of energy incident on the cell is equal to the amount of energy transferred to the fluid. When radiation is added energy does not balance due to the fact that average temperatures must be used for the back insulation (because radiation is the difference between T^4 a small difference in temperature can result in a large difference in heat transfer). The only solution to this problem is discretizing the back insulation which cannot be done due to the limitations of EES. An energy imbalance of about 3% is experienced when radiation is added, which is considered acceptable for this level of modeling.

Using the finite difference model, an initial receiver cell design can be specified that meets all of the design conditions. To keep the pressure drop under the allowable value, while maximizing the flow per cell, the thickness of the cell was specified as 8 mm which is more than twice as thick as typical internally finned designs. The upper limit for cell thickness is determined by the temperature drop through the metal of the nose where the flux is highest. The thickness of the D shaped nose tube is determined using B31.1 assuming the fin height is the outer diameter, and calculating the required inner diameter. 740H is specified for the nose tube material because of its high strength. The allowable stress of 740H is calculated in the same way as for the piping, 2/3rds of the 100,000 hour rupture life at the operating temperature (790 °C). Thicknesses greater than 8mm resulted in nose temperatures greater than 790 °C because of the increased thermal resistance caused by the nose tube. Cell costs are much less dependent on the fin thickness compared to the number of cells. For this reason, it is beneficial to have fewer large cells than many small cells. A width of 200 mm was chosen as it is near the upper limit possible for the manufacturing process. The results for the receiver are summarized in Table 23.

Table 23 – Receiver specifications.

PARAMETER	UNITS	VALUE
Inlet Temperature	°C	560
Outlet Temp.	°C	760
Inlet Pressure	MPa	25
Fin Height	mm	8
Width	mm	200
Length	m	1.65
Mass Flow / Cell	kg/s	0.36
Max. Metal Temp.	°C	783.5
Number of Cells	#	290

A more detailed write-up of the finite difference model is available as a separate memo that describes the model in more depth. From the model temperature plots of both the material and fluid can be obtained as shown in Figure 78 and Figure 79. The dimensions shown (Theta, X, and Y) refers to those indicated in Figure 77.

The temperature plots show that the areas of maximum metal temperature do not correspond to the maximum fluid temperature. Metal temperature is driven by flux the relationship between flux and the resistance to the fluid that removes heat. Areas with high metal temperatures have more flux compared to resistance of the fluid. Flux profiles on the cells in the radial directions are defined by the geometry of the cell, and in the axial direction they are defined by the aim point strategy of the heliostats. By applying more flux at the inlet of the fluid, where fluid temperatures

are lower, more flux can be applied while keeping metal temperatures within allowable limits. As the fluid heats up, the flux

		Nose Location (deg)					x Location (mm)				
		5.625	22.5	45	67.5	84.38	0.0125	0.05	0.1	0.15	0.1875
y Location (m)	0.02171	718.2	714.9	704.6	693.4	688.8	610.1	605.8	598.7	593.8	592.6
	0.08684	737.6	734.4	724.3	713.4	708.8	622.3	617.4	610.2	605.3	603.7
	0.1737	742.1	739	729.6	719.5	715.2	644	638.3	631.4	626.5	624.6
	0.2605	753.1	750.3	741.4	731.8	727.7	659.7	653.5	646.9	642.3	640.3
	0.3474	759	756.3	747.9	738.9	735.2	675.6	669	662.7	658.1	656
	0.4342	766.2	763.7	755.9	747.5	744	689.7	682.8	676.8	672.5	670.3
	0.5211	771.1	768.8	761.5	753.7	750.5	702.7	695.6	690	685.8	683.5
	0.6079	775.8	773.7	766.9	759.7	756.7	714.4	707.3	702	698	695.6
	0.6947	779.1	777.1	770.9	764.2	761.5	724.9	717.9	713	709.1	706.7
	0.7816	781.6	779.8	774.1	768	765.6	734.2	727.3	722.8	719.1	716.7
	0.8684	783	781.3	776.2	770.7	768.5	742.3	735.7	731.5	728.1	725.6
	0.9553	783.5	782	777.3	772.4	770.5	749.2	742.9	739.2	736	733.5
	1.042	782.9	781.6	777.5	773.1	771.4	754.9	749.1	745.8	742.8	740.4
	1.129	781.4	780.2	776.6	772.8	771.4	759.5	754.1	751.3	748.6	746.2
	1.216	778.8	777.8	774.8	771.5	770.3	762.9	758.1	755.8	753.4	751.1
	1.303	775.3	774.5	771.9	769.3	768.3	765.2	761	759.2	757.1	755
	1.389	770.7	770	768	765.9	765.2	766.3	762.8	761.5	759.8	757.9
	1.476	765.2	764.7	763.2	761.7	761.2	766.2	763.5	762.6	761.3	759.7
	1.563	758.5	758.2	757.2	756.2	755.9	764.5	762.6	762	761	760
	1.628	751.1	750.9	750.3	749.8	749.7	761.6	759.8	759	757.8	757.6

Figure 78 – Metal temperature in °C for design receiver meeting all design specifications, 0° is front of nose and 90° is at joint with cell.

must be reduced to maintain the maximum metal temperature. Study of several different flux shapes (linear, cosine, exponential) has shown that the linear temperature profile gives the lowest metal temperature. For the design receiver case presented above, the flux profile is shown in Figure 80.

		Nose	x Location (mm)				
			0.0125	0.05	0.1	0.15	0.1875
y Location (m)	0	563	563	563	563	563	563
	0.04342	573	574.8	574.2	574.2	574.4	574.7
	0.1303	592.1	595.8	594	593.8	593.7	593.9
	0.2171	610.1	615.4	612.7	612.2	611.9	611.8
	0.3039	627.1	634	630.5	629.9	629.5	629.2
	0.3908	643.1	651.2	647.1	646.4	645.8	645.3
	0.4776	658	667.2	662.5	661.7	661.1	660.3
	0.5645	671.8	681.8	676.8	676	675.2	674.3
	0.6513	684.5	695.2	690	689.1	688.2	687.1
	0.7382	696.2	707.4	702	701.1	700.1	698.8
	0.825	706.8	718.3	712.9	712	710.9	709.5
	0.9118	716.3	728	722.7	721.8	720.7	719.1
	0.9987	724.8	736.6	731.4	730.5	729.3	727.7
	1.086	732.2	743.9	739	738.1	736.9	735.2
	1.172	738.5	750.1	745.5	744.7	743.5	741.7
	1.259	743.8	755.1	750.9	750.2	749	747.3
	1.346	748	758.9	755.2	754.6	753.5	751.8
	1.433	751.2	761.7	758.4	757.9	756.9	755.3
	1.52	753.3	763.2	760.4	760.1	759.2	757.8
	1.607	754.3	763.4	761.2	760.8	759.8	758.7
	1.65	754.4	763	761	760.5	759.4	758.5

Figure 79 – Fluid temperature in °C for design receiver meeting all specifications.

Numerical Receiver Modeling

The next step in modeling the receiver is creating a numerical model in a CFD package. CFD allows for direct calculation of the heat transfer between the receiver cell and the fluid. In the finite difference model, the tall skinny channels are assumed to convect to the bulk temperature of the fluid. Results from the finite difference model has shown that the fin efficiency is relatively low, only about 30%, which means the majority of the fin is isothermal with the fluid and not participating in heat transfer. So the effective temperature the fluid sees may actually be much higher than the bulk

temperature of the fluid, which acts to decrease the effective heat transfer coefficient. A CFD model will be able to identify any inconsistencies. To use existing correlations, the fins were assumed to be square instead of the actual compacted fin shape. Past testing has shown the

		Nose Location (deg)					x Location (mm)				
		5.625	22.5	45	67.5	84.38	0.0125	0.05	0.1	0.15	0.1875
y Location (m)	0.02171	879.8	802.6	649.8	475.7	366.3	391.1	344.4	237.8	162.8	130.4
	0.08684	846.5	772.2	625.2	457.7	352.5	376.3	331.4	228.8	156.7	125.5
	0.1737	802.1	731.7	592.4	433.7	334	356.5	314	216.8	148.5	118.9
	0.2605	757.6	691.2	559.6	409.7	315.5	336.8	296.6	204.8	140.2	112.3
	0.3474	713.2	650.6	526.8	385.7	297	317	279.2	192.8	132	105.7
	0.4342	668.8	610.1	494	361.6	278.5	297.3	261.8	180.8	123.8	99.13
	0.5211	624.4	569.6	461.2	337.6	260	277.6	244.4	168.8	115.6	92.54
	0.6079	580	529.1	428.4	313.6	241.5	257.8	227	156.8	107.3	85.96
	0.6947	535.5	488.5	395.5	289.6	223	238.1	209.6	144.8	99.12	79.38
	0.7816	491.1	448	362.7	265.6	204.5	218.3	192.2	132.7	90.9	72.79
	0.8684	446.7	407.5	329.9	241.5	186	198.6	174.9	120.7	82.68	66.21
	0.9553	402.3	367	297.1	217.5	167.5	178.8	157.5	108.7	74.46	59.62
	1.042	357.8	326.4	264.3	193.5	149	159.1	140.1	96.73	66.24	53.04
	1.129	313.4	285.9	231.5	169.5	130.5	139.3	122.7	84.72	58.01	46.45
	1.216	269	245.4	198.7	145.5	112	119.6	105.3	72.71	49.79	39.87
	1.303	224.6	204.9	165.9	121.4	93.51	99.83	87.91	60.7	41.57	33.29
	1.389	180.2	164.3	133.1	97.42	75.01	80.08	70.52	48.7	33.35	26.7
	1.476	135.7	123.8	100.3	73.4	56.52	60.34	53.13	36.69	25.12	20.12
	1.563	91.31	83.3	67.44	49.38	38.02	40.59	35.74	24.68	16.9	13.53
	1.628	58	52.91	42.84	31.36	24.15	25.78	22.7	15.68	10.73	8.596

Figure 80 – Flux in kW/m² for each element in design receiver, 0° is front of nose and 90° is at joint with cell.

square fins to be a good approximation for pressure drop of the compacted fin, however the CFD model will be able to confirm this assumption. Future iterations of CFD testing will more accurately calculate radiation by including the effect of the quartz tube window.

An initial model has been created to confirm the analytical model. Two separate models are needed of the receiver geometry in order to represent the entire cell. One is the unit cell of one fin channel, and the other is the nose channel with several fin channels attached. A picture of the two sections to be modeled is shown in Figure 81.

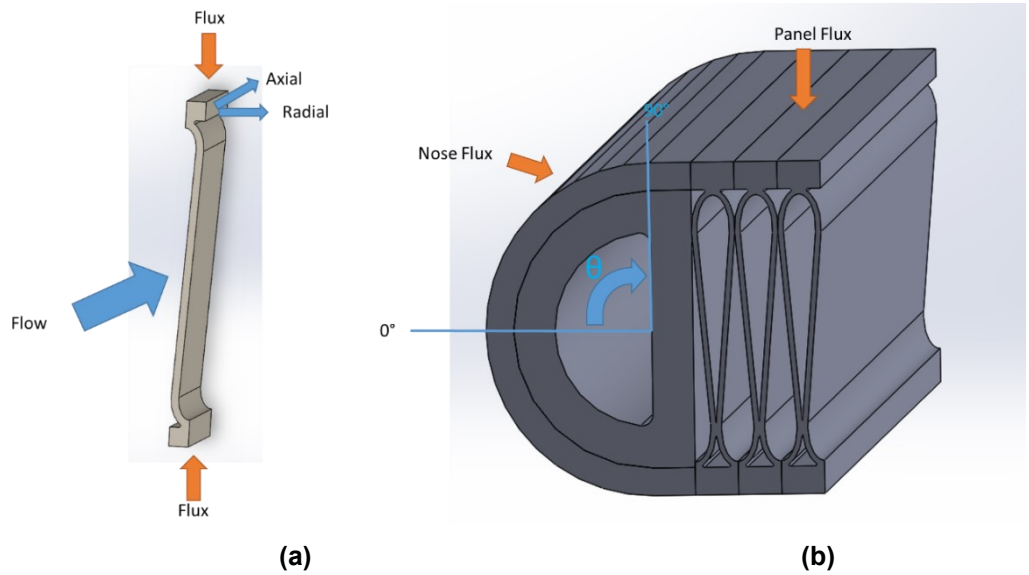

Figure 81 – (a) unit cell of one fin channel, (b) nose channel plus several fin channels.

Because the temperature profile of the fluid is not constant over the entrance to the fin channel, care must be taken when modeling to ensure accurate results. Because of this the entire length of the fin channel should be modeled at one time to ensure the temperature profiles are correct. However, modeling the entire length of fin can result in meshes that are excessively large and take too long to solve. An alternative method would be to model a short length of the fin and take the exit conditions from one section and use them as the entrance conditions to the next. This allows the mesh to be much smaller but adds complexity in the problem set up that SolidWorks Flow Simulation cannot handle.

Using SolidWorks Flow Simulation the one fluid channel cell was modeled using the conditions for the fin channel closest to the nose, as this channel experiences the highest temperatures. The results of the model are shown in Figure 82.

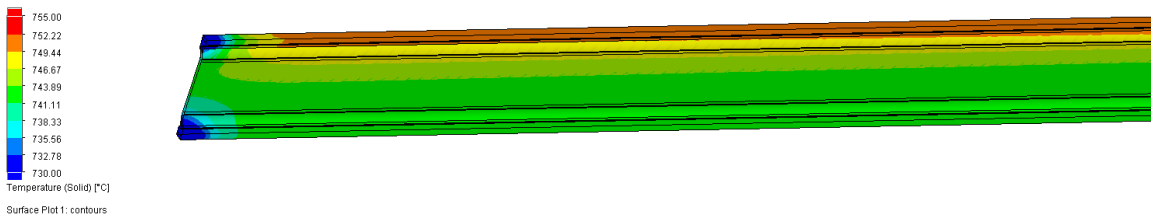

Figure 82 – Surface temperature of metal at discharge end of receiver.

The nose channel is more difficult to model because of its large size and more complex geometry. Only a short section of the nose has been modeled in ANSYS Fluent. A plot of the result is shown in Figure 83.

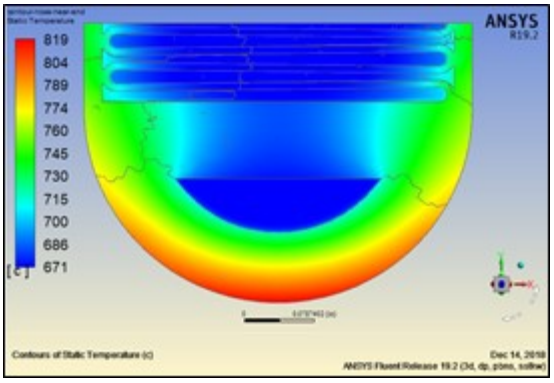

Figure 83 – Cross section of nose channel 2" from fluid inlet for 10 mm fin height.

As discussed before the maximum allowable temperature of the metal is 790 °C, while this model shows a maximum metal temperature of 819 °C. The geometry modeled here uses a 10 mm fin height, it is clear that the temperature gradient through the nose results in the metal exceeding the allowable temperature. For this reason, the thickness of the fin has been reduced, which reduces the thickness of the nose. A thinner cell means less flow can pass through at the same pressure drop so the amount of flow must be reduced as well. Because the amount of flow is reduced, the flux on the cell also must be reduced to account for the reduced flow. This model was able to identify an issue in the analytical model, where the resistance in the metal was neglected, meaning this model cannot be used to verify the final design. However, this model can still be used to verify the finite difference model. Under the same conditions the finite difference model predicts a temperature of 808 °C which is only 11 °C away from the modeled temperature. Because the finite difference model includes radiation and the ANSYS model does not, it was assumed that the error between the two was small enough to consider the model verified. Further modeling will be conducted to ensure the new design also matches the finite difference model. The finite difference model is not assumed to be the final design tool for the receiver, rather it is an important tool that can quickly hone in on a workable receiver design. After determining a receiver design using the finite difference model further modeling will be conducted in ANSYS to verify the design. NREL has developed an ANSYS model that can be used to verify the design of the receiver. As the project progresses so too can the model adding more of the cell to the model and including radiation.

Milestone 3.1.1:

The full scale system is predicted to have an annualized system energetic efficiency ≥ 99%.

A roll up of all losses was conducted for the thermal energy storage system. This included thermal losses from the HTMH vessel, transport pipe, regenerator vessel, regenerator ineffectiveness, and regenerator thermocline. These losses equated to almost exactly 1% of the total heat transfer into or out of the HTMH, leading to a 99% round trip efficiency which meets the milestone goal. The results are summarized in Table 20.

Milestone 3.1.2:

The full scale system is predicted to have an annualized system exergetic efficiency ≥ 95%. The specified goal of 95% complies with the DoE programmatic requirement. For the proposed

integrated system and in compliance with the DOE definition, the total TES exergetic efficiency (ψ), including not only the chemical exergy of the MH system, but also the thermal exergy associated with the heat transfer fluid and the power plant working fluid (i.e. sCO_2), is defined as:

$$\psi_{TES} = \frac{E_{HTMH\ to\ sCO_2\ (TES\ discharing)}}{E_{sCO_2\ to\ HTMH\ (TES\ charging)}} \geq 95\%$$

Using the temperature of the supplied heat, and the temperature of the rejected heat, and thermal efficiency of the TES system. An exergetic efficiency of 97.7% is reported with an uncertainty of ±2% which meets the milestone requirement.

Task 3.2:

Further characterize the selected HTMH and LTMH metal hydride media properties, specifically with respect to their internal thermal transport properties – how effectively thermal energy can be conveyed through the media and the resulting intermedia temperature gradients – and any performance degradation or material breakdown over time. The system analysis will be carried out, examining the performance with varying HTMH properties.

SubTask 3.2.1:

Perform an analysis to identify the relative impact of metal hydride material properties (thermal conductivity, gravimetric density, cost, operating temperature, kinetic rate, temperature variation) on the potential to improve the LCOE of the overall system. Particular attention will also be paid to the HTMH material durability. A possible modification of the initial TES layout (e.g. inclusion of extra MH material in the initial configuration) will be examined accounting for the possible material capacity degradation (if any) and durability. This will be included in the economic estimation, evaluating the influence on the overall LCOE.

SubTask 3.2.2:

Evaluate variations on the additives and formulations for the MH media to modify the greatest-effect material property(-ies) identified in SubTask 4.1. Demonstrate that the modified formulation or additive matches the predicted improvement in system LCOE within 10% as compared to the original formulation identified in Budget Period 1. Fully characterize the selected HTMH and LTMH formulations based on their inter-material thermal transport rates and their operational degradation and life Part of the subtask work will be relative to availability and scale up of the new enhanced material formulation. The enhanced material (e.g. with inclusion of Expanded Natural Graphite [ENG], nanostructures, etc) is anticipated to be easily available and scalable. The possibility of inclusion of ENG, with compaction of the material was demonstrated during Phase 1 of the project with 5, 10, 20wt% ENG, with no problem to scale the material up.

The possible (alternative) inclusion of nanostructures in the Ca based material is being examined for application at large scale level.

HTMH Formulation Investigation

Various additives were explored to enhance the thermal conductivity and desorption kinetics of Ca_2Si. Our previous work with $CaAl_2$ gave insight into the advantages of utilizing aluminum within the crystal structure of high temperature thermal energy storage materials. [30] These advantages include increased rates of reactions due to the higher mobility of aluminum and the shifted thermodynamics as well as significantly increased thermal conductivities compared to Ca_2Si. Unfortunately, the hydrogenation products of $CaAl_2$ are CaH_2 and Al, which limit the operational temperature to ~ 600 °C due to aluminum melting at ~ 660 ºC. It was realized that the presence of silicon may prevent aluminum from melting and phase segregating due to the formation of a solid solution as evidence by the phase diagram shown in Figure 84. In order to maintain a solid solution, the ratio of aluminum to silicon would have to be maintained at a point were aluminum was less than ~ 30 mole percent. In the dehydrogenated state, ternary phases between Ca, Si, and Al would prevent the melting of aluminum. A mismatch in pressure conditions required for the reversibility of some of the potential ternary phases prompted an experimental focus on the ternary phases themselves as the preferred method of aluminum doping.

To take advantage of the enhanced thermal conductivity of aluminum incorporation within the crystal structure while maintaining high operational temperatures, a variety of ternary phases were investigated. In the hydrogenated state a solid solution Al_xSi_y while the Ca would then become CaH_2. Preliminary tests with a variety of compositions revealed low capacities or very high equilibrium pressures for ternary phases which were high enough in silicon to keep aluminum is a solid solution at 750 °C. While evaluating several different $Ca_xSi_yAl_z$ compositions, it was found that the phase $CaSi_2Al_2$ had an equilibrium pressure greater than 80 bar H_2 at 750 °C. This inspired another mechanism to ensure aluminum incorporation without phase segregation. The concept of the ternary phase mechanism which prevents aluminum phase segregation (from melting) is described by the following overall equation.

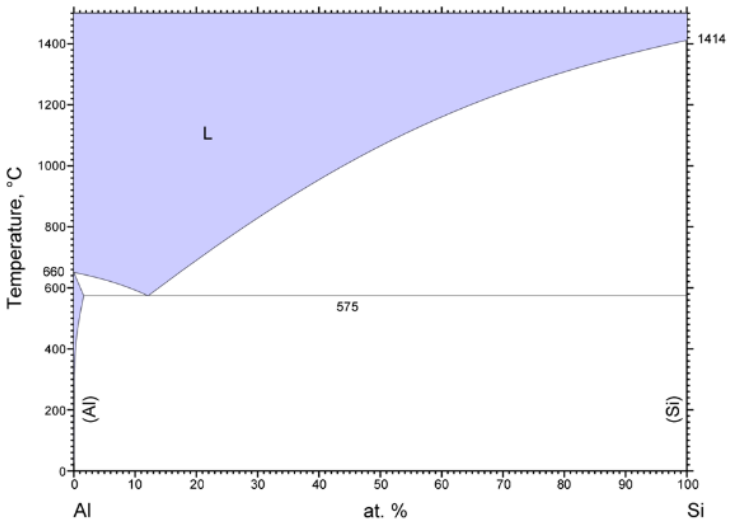

Figure 84 – Phase diagram for Al-Si.

$$Ca_3Si_2Al_2 + 2\ H_2 \rightarrow CaSi_2Al_2 + 2\ CaH_2$$ Equation 8

The degree of hydrogenation of $Ca_3Si_2Al_2$ can be controlled by controlling the pressure of hydrogen at temperature. To avoid aluminum segregation, the pressure simply must remain under 80 bar at 750 °C. This allows for a modified material which includes aluminum to speed up the reaction kinetics and enhance thermal transport properties. Figure 85 displays the XRD pattern for $Ca_3Al_2Si_2$ hydrogenated at 40 bar H_2 which confirms the products to be CaH_2 and $CaAl_2Si_2$.

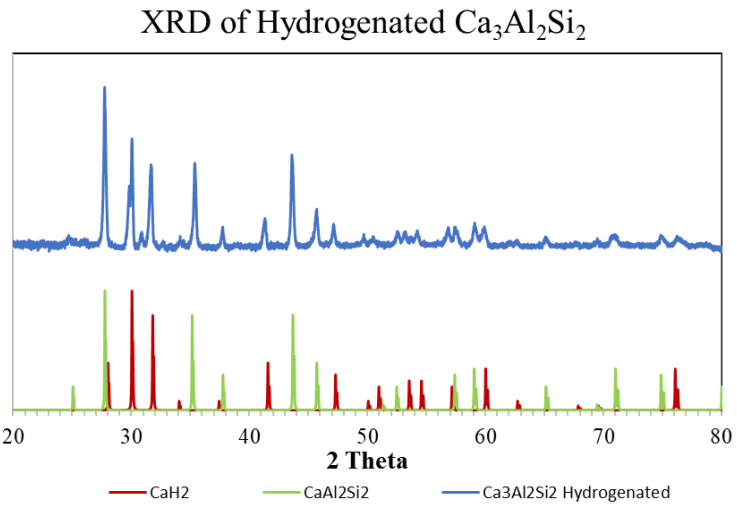

Figure 85 – XRD pattern of Hydrogenated $Ca_3Al_2Si_2$.

Although the recently developed high temperature metal hydride material is composed of low-cost elements, these elements obtained in high purity reagents can still have higher than desired costs. To demonstrate the production of the material from lower purity regents, the use of 98% CaH_2 was demonstrated to produce the same phase, $Ca_3Al_2Si_2$, as shown below in Figure 86. This reduction in purity reduces the cost of small-scale calcium hydride by over seven times. Furthermore, the cost of calcium hydride is significantly more expensive than calcium metal. We demonstrated complete conversion of calcium metal to calcium hydride by hydrogenating the metal at 850 °C and 10 bar of hydrogen pressure. The 98% purity CaH_2 is represents a lower bound of the expected purity of CaH_2 if the metal were purchase and converted to the hydride as part of the material production process. Additional reductions in the price come from using calcium metal instead of calcium hydride. Further realization in cost reduction can be achieved from the use of $CaSi_2$ as a starting material since the cost of this material is cheaper than calcium and silicone. The production of $Ca_3Al_2Si_2$ material from $CaSi_2$ was demonstrated after 3 annealing steps was demonstrated to justify the lower cost synthetic methodology.

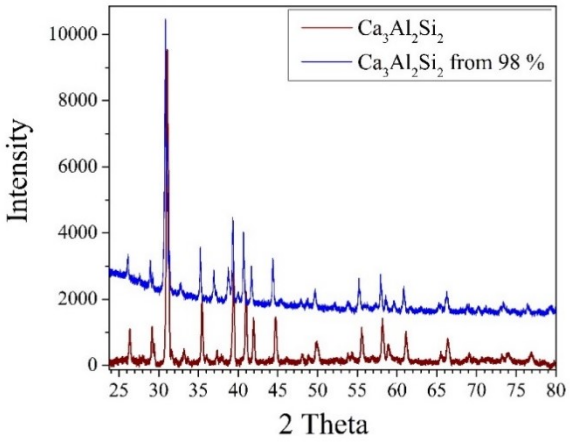

Figure 86 – a XRD pattern of $Ca_3Al_2Si_2$ produced from 99.9% purity CaH_2 (red) and 98% purity CaH_2 (blue).

Figure 87 illustrates the rapid rate of material hydrogenation at 700 °C and 39 bar H2. At this pressure and temperature equilibria are achieved in less than 1.5 hours.

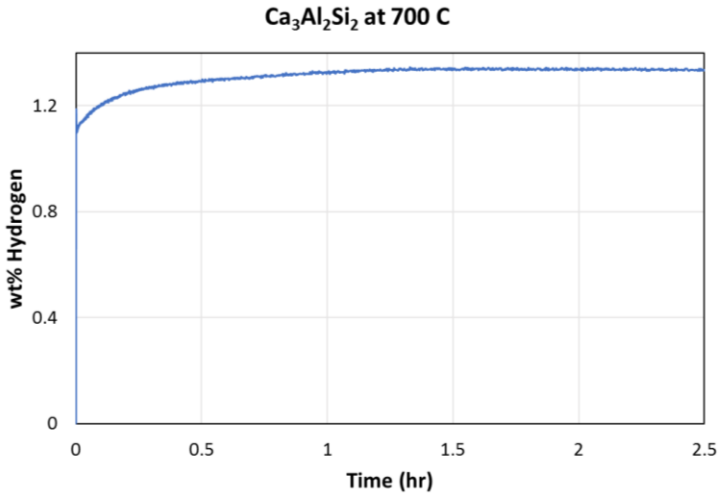

Figure 87 – Isothermal absorption curve of $Ca_3Al_2Si_2$ at 700 °C and 39 bar H_2.

To verify cycle stability, the material was cycled at 750 ºC and ~ 60 bar H_2 over 4 hours absorption/desorption cycles as shown in Figure 88. Commercial grade material was simulated as using 98% purity CaH_2 since this is lower in purity than expected if calcium metal was purchased and hydrogenated as part of the production process. Full theoretical capacity of the material was achieved (1.7 wt. %) at the starting pressure of 60 bar. A reduced pressure can be used at the expense of hydrogen capacity.

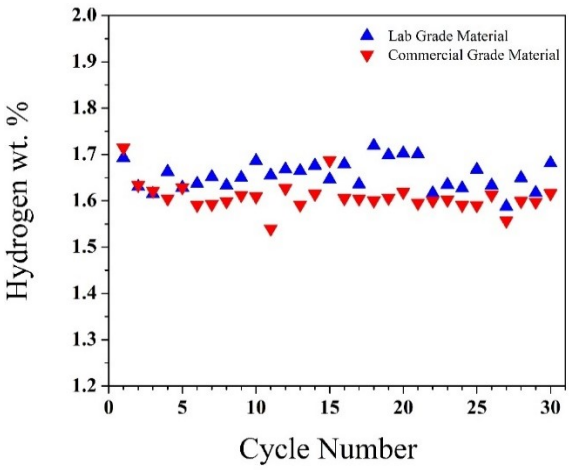

Figure 88 – Cycle stability of laboratory grade (blue) and commercial grade (red) $Ca_3Al_2Si_2$ over 30 cycles at 750 °C with a starting hydrogenation pressure of 60 bar.

Figure 89 below highlights the significant improvements in thermal conductivity which can be achieved by the incorporation of aluminum and ENG. A thermal conductivity of ~3.0 W/m*K and ~5.6 W/m*K can be achieved at 600 °C with the addition of ENG to Ca_2Si in ratios of 10 wt. % and 20 wt. % respectively. Although significant enhancements in the thermal conductivity with ENG are possible, it should be noted that reproducibility is highly dependent of the method in which the ENG is incorporated. This is due to the orientation of graphite within the pellet and efficiency of its dispersion within the material. As shown below, the addition of aluminum in the $Ca_3Al_2Si_2$ system provides thermal conductivities comparable to the addition of 10 wt. % ENG to the Ca_2Si system. The addition of 20 wt. % ENG to the aluminum incorporated materials allows for thermal conductivities greater than 8 W/m*K at operational conditions.

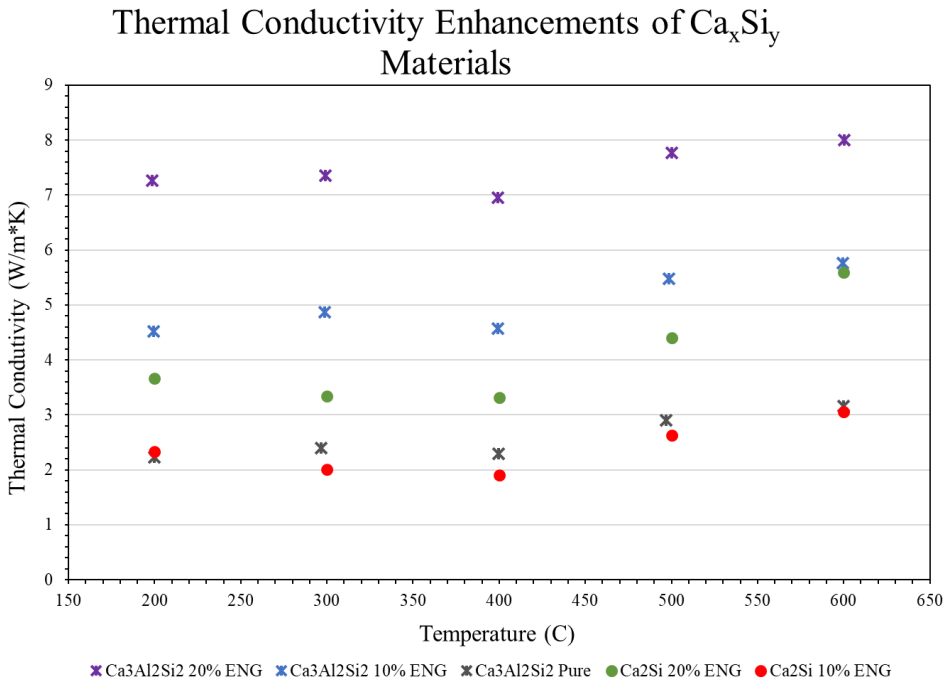

Figure 89 – Thermal conductivity of various high temperature metal hydride compositions.

LTMH Media Formulation

The LTMH to be coupled with the HTMH is based on a Ti-based MH formulation. During Phase 1 and Phase 2 several formulations were examined and two main formulations were selected as baseline materials.

The two materials are $TiMn_{1.5}$ (referred to as LTMH1) and TiFe (referred to as LTMH2). The LTMH1 material represents the baseline candidate to be paired with the HTMH, while the LTMH2 is the main alternative. The thermodynamic, thermal, physical and chemical properties of the candidate hydrides are shown in Table 24.

Table 24 – Thermodynamic and thermo-physical properties of LTMH1 (TiMn1.5) and LTMH2 (TiFe).

	UNITS	LTMH1: $TiMn_{1.5}$	LTMH2: TiFe	COMMENT
ΔH	$kJ/molH_2$	28.7	28	Literature data [1,2,4,5]
ΔS	$J/molH_2$-K	114	106	Literature data [1,2,4,5]
Bulk density	kg/m^3	3129	2900	Estimated, with void fraction of about 50%
Thermal conductivity, bare	W/m-K	0.35 - 0.70	0.35 - 0.70	Assumed values based on conservative assumptions for less conductive materials [3]
Thermal cond. enhanced, 8-10 wt% ENG added	W/m-K	7	7	Typical values achieved with ENG inclusion range between 7 W/mK to 10 W/mK [3]
Weight capacity	$kgH_2/kgMH$	0.0153	0.019	Literature data [1,2,4,5]
Specific heat	J/kg-K	500	500	Assumed, typical Ti based LTMH values

The equilibrium pressure-temperature profile of the LTMHs are shown in Figure 90, based on their thermodynamic values reported in Table 24. The two materials can also be possibly used in a parallel LTMH layout, working at the same temperatures but at slightly different operating pressures. The kinetics of both materials are very fast kinetics as reported in the above.

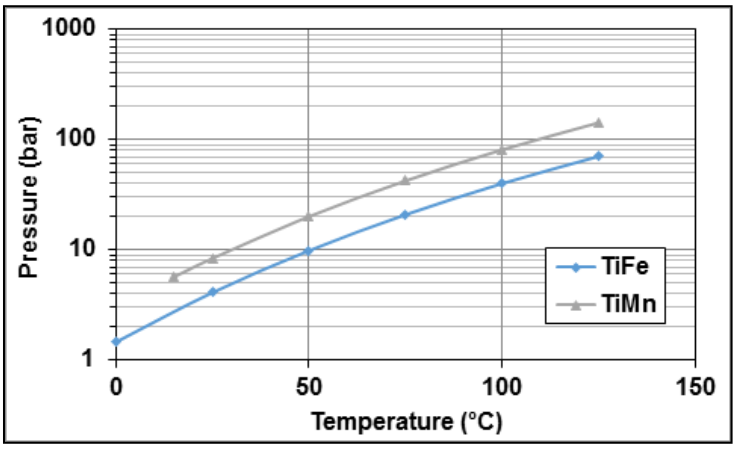

Figure 90 – Equilibrium temperature-pressure profiles for the LTMH1 (TiMn-material) and the LTMH2 (TiFe-material).

Metal Hydride Commercial Production and Costing

The baseline methodology identified to synthesize the Ca-based MH formulation ($Ca_3Al_2Si_2$) on large scale is based on the use of $CaSi_2$ as a precursor, along with Al and Ca. This has two main benefits: (1) $CaSi_2$ material is currently available at industrial quantities and at different levels of purity, (2) generally the material ($CaSi_2$) is inexpensive compared to other possible compounds (precursors), such as Ca or CaH_2.

The raw material cost of the high temperature metal hydride (HTMH) has been assessed assuming three levels of purity for Ca and $CaSi_2$. The assumed levels of purity of Ca and $CaSi_2$, with their raw material costs are shown in Table 25.

Table 25 – Raw material costs of Ca and CaSi2 at different levels of purity. Data from [44]–[46].

	Ca RAW MAT'L COST ($/kg)	$CaSi_2$ RAW MAT'L COST ($/kg)	COMMENT
Low purity	2	1.3 - 1.5	• Ca (purity <95%) available in industrial quantities • $CaSi_2$ (presence of impurities of C, Al, P, S) available in industrial quantities
Average purity	3	-	• Ca (purity = [95%,98%]) available in industrial quantities
High purity	4.5 - 6.0	10.0-15.0	• Ca (purity = [98%,99%]) available in industrial quantities • $CaSi_2$ (presence of small impurities of C, Al, P, S) available in industrial quantities
Very high purity	50.0 - 200.0	25.0 - 40.0	• Ca (purity >99%) available in industrial quantities • $CaSi_2$ available in industrial quantities and very high purity

The raw material cost for Al, equal to 0.9 $/lb, has been assumed based on prices currently available. Large companies (e.g. Alcoa) can sell quantities of Al at industrial scale in the form required to synthesize our material. The cost of Si was also examined as another possible precursor if a different synthesis procedure is considered[47].

Raw $Ca_3Al_2Si_2$ material cost results are shown in the following figures. Figure 91 shows the results for the low purity Ca and with the $CaSi_2$ three levels of purity.

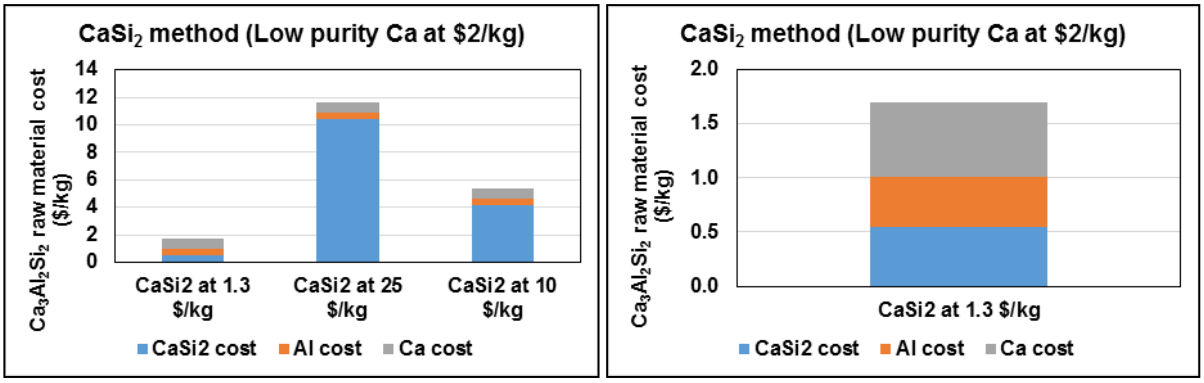

Figure 91 – Raw cost of $Ca_3Al_2Si_2$ for low purity Ca material (raw material cost of 1.7 $/kg achieved for low purity Ca and low purity $CaSi_2$).

Figure 92 shows the results for the average purity Ca with the $CaSi_2$ three levels of purity.

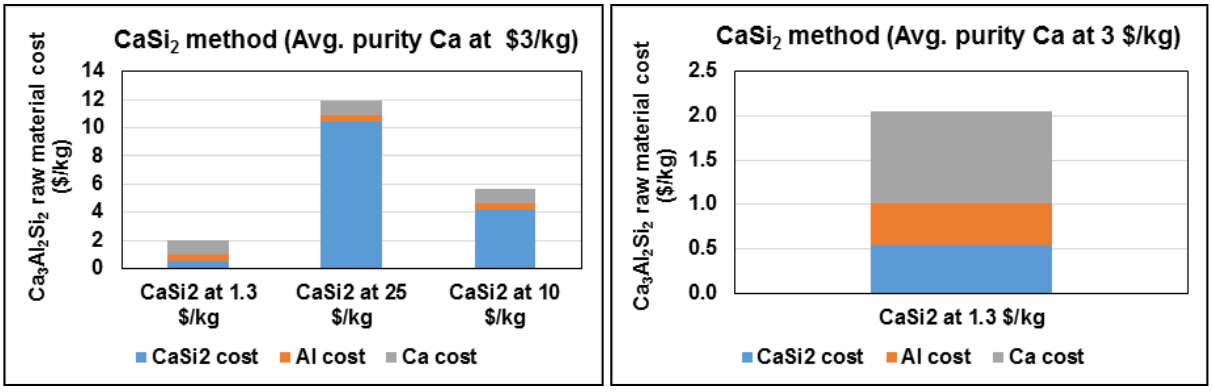

Figure 92 – Raw cost of $Ca_3Al_2Si_2$ for average purity Ca material (raw material cost of approximately 2.0 $/kg achieved for average purity Ca and low purity $CaSi_2$.

Figure 93 shows the results for the high purity Ca with the $CaSi_2$ three levels of purity.

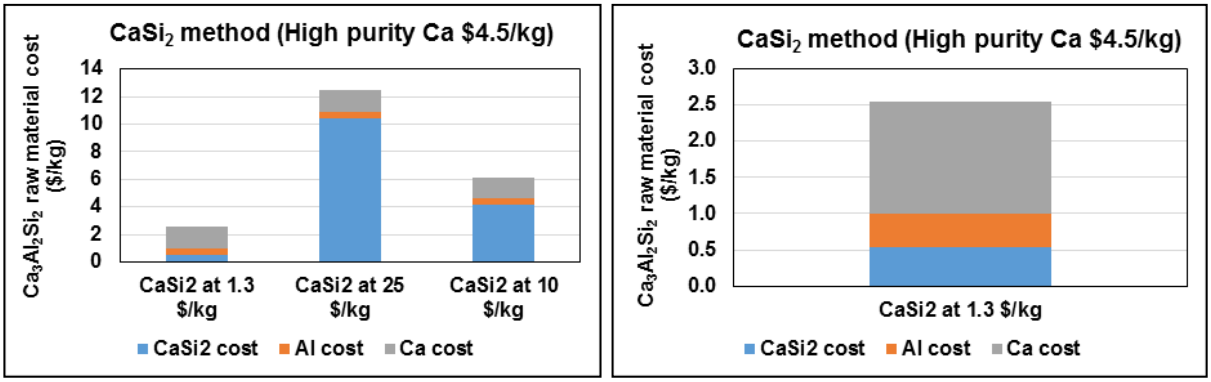

Figure 93 – Raw cost of $Ca_3Al_2Si_2$ for high purity Ca material (raw material cost of approximately 2.5 $/kg achieved for high purity Ca and low purity $CaSi_2$).

JMC Company has been selected as one company that can potentially provide large quantities of the materials. Greenway Energy has a long-term relationship with JMC, which provided quantities > 10 kg of Ti-based metal hydrides for different DOE-funded projects. The discussions with JMC are currently ongoing and the company can provide the $CaSi_2$ material in large scale quantities (e.g. 10 tons) and at different levels of purity.

The current baseline low temperature metal hydride material to be paired with the Ca-based metal hydride, is the $TiMn_{1.5}$ formulation. The presence of small amounts of Fe in the formulation can be used to fine tune the operating pressures and temperatures. Different formulations of Ti-Fe-Mn have been used in the past by SRNL and GWE to store hydrogen for vehicular applications and, varying the amount of Fe, the operating P and T can be slightly modified. Two cases have been considered for the current application: (1) Pure Ti, with different levels of Ti purity, (2) Ti-Fe ore, with different levels of other impurities. The raw material cost of the two Ti materials is shown in Table 26.

Table 26 – Raw material costs of Ti and TiFe ore at different levels of purity. From [48]

	Ti RAW MAT'L COST ($/kg)	Ti-Fe ORE RAW MAT'L COST ($/kg)	COMMENT
Low purity	6	2.5	• Low purity Ti with presence of mainly Fe, Mn, Al, Si • Ti-Fe minimum price (lower purity) found at $2/kg
Average purity	7	4	• Average purity of both Ti and Ti-Fe with traces of Al, Si, Mn, C, P, S (documented in the Ti-Fe ore)
High purity	15	5	• Cost of pure Ti very variable in time • Ti-Fe with reduced presence of the impurities, price found at $5/kg

The cost of the Mn has been assumed (cost of pure Mn for year 2017 and 2018) equal to $1.875/kg based on the market cost. Raw low temperature material (TiMn1.5) cost results are

shown in the following figures. Figure 94 shows the results using Ti at different purity levels. Figure 95 shows the results using Ti-Fe ore material at different purity levels.

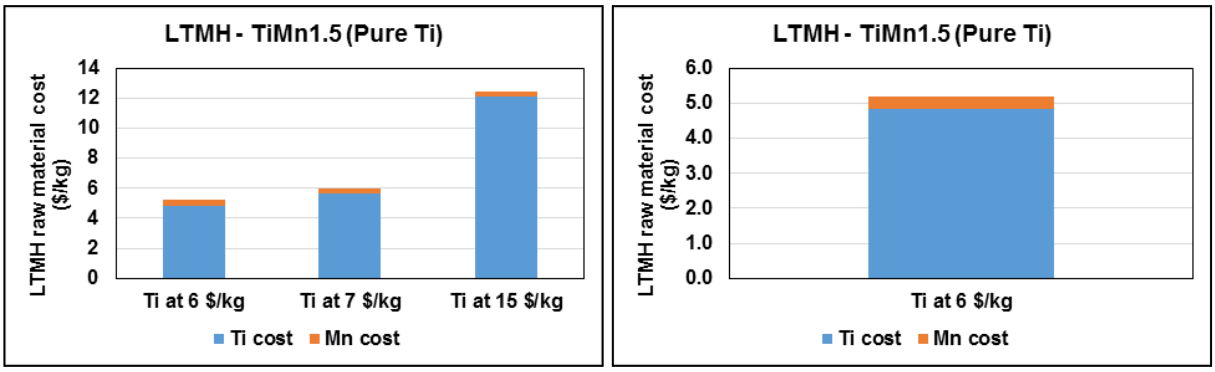

Figure 94 – Raw cost of TiMn1.5 using Ti element (raw material cost of approximately $5.2/kg achieved for low purity Ti and cost of Mn at $1.875/kg).

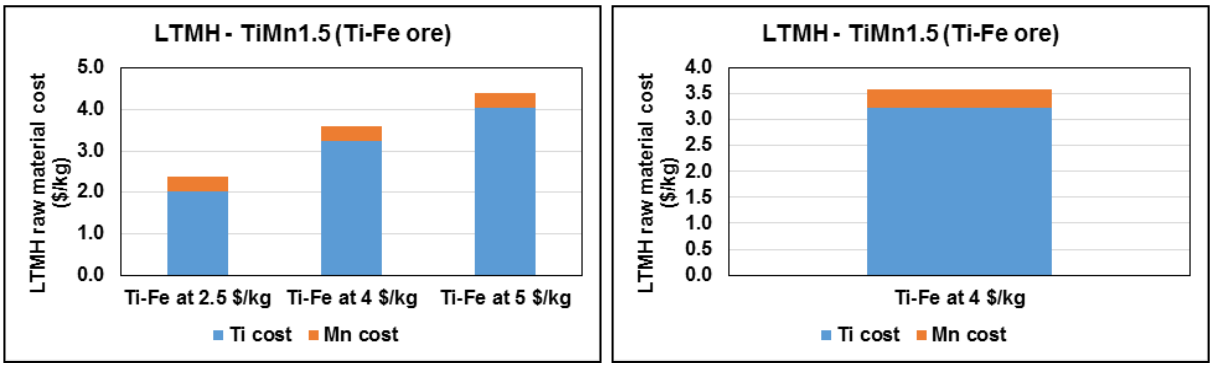

Figure 95 – Raw cost of TiMn1.5 using Ti-Fe ore element (raw material cost of approximately $3.6/kg achieved for average purity Ti-Fe material and cost of Mn at $1.875/kg).

Milestone 3.2.2.1:

The enhanced HTMH and/or LTMH formulations applicable for scale up to commercial production, will reduce the calculated LCOE by >$0.01/kWh. The revised HTMH formulation will be available at a price at or below $1.10/kg in quantities of 40,725,000 kg annually, while the revised LTMH formulation will be available at a price at or below $5.20/kg in quantities of 52,575,000 kg annually.

- The high temperature material, assuming the $CaSi_2$ precursor synthesis methodology, can achieve materials costs on the order of $1.7-2.0/kg, thus higher than the milestone target of $1.1/kg.
- However, the low temperature metal hydride material can be easily synthesized (already demonstrated in multiple applications) from Ti-Fe ore, rather than pure Ti material, mixed with Mn. The cost of this material is in the range $2.5-3.5/kg, which is below the $5.2/kg targets.

- The two materials have comparable weight capacities, so overall the system can meet the material cost targets. The high temperature material cost is about 60% higher than the target ($1.1/kg), while the LTMH material cost has a reduction of about 60% compared to the target ($5.2/kg). Thus there will be no change in LCOE.

Milestone 3.2.2.2:

Material properties for commercial versions of the HTMH and LTMH formulations identified in Milestone 3.2.2.1 will be experimentally measured at a commercial level. The thermodynamic and cycling properties of the material will be tested and compared with the lab scale material properties.

Cyclic testing was performed on the laboratory grade vs commercial grade material, and the results are shown in Figure 88. These results showed a slightly reduced hydrogen capacity of 96%, likely due to a reduction in the amount of HMHT due to impurities in the material. However, the commercial scale HTMH material did not experience any worse declines in hydrogen capacity compared to the laboratory material in cyclic testing. LTMH materials were not tested, as it was determined that sufficient testing had been completed on commercial LTMH material and the data was readily available in publications.

Task 3.3:

The system layout will be specified, capital costs (detailed for the engineered components, generalized for the balance of the system) will be calculated, and the results will be used to generate a full Power Plant LCOE. Detailed capital costs for the full scale system will be generated for the absorber cells, metal hydride TES system, and the LTMH thermal communication heat exchanger cells. Work will be performed to specify the receiver and thermal energy storage layouts within the tower, specifically focusing on the optimal means of conveying thermal energy from the absorber cells into the HTMH media. The suitability of this layout will be demonstrated by showing that thermo-mechanical considerations (strain, expansion, fatigue, etc.) are appropriately addressed, as is protection from concentrated solar spillage. Once the layout has been identified, overall capital cost estimates can be made for the balance of the receiver/tower/thermal energy system plant. The weights for the receiver/storage subsystem will determine the specifications for the tower. A structural analysis of the tower will be performed to define its design and cost and identify any required enhancements to its capacity. These capital costs and the annualized performance predictions generated in Task 2.1 will then be used to calculate the overall plant LCOE. An analysis will be performed to determine the optimal system thermal storage capacity to minimize LCOE based on the design variables (e.g. MH media storage capacity, cost to reinforce tower to increase its weight capacity, etc.)

SubTask 3.3.1:

Define the layout of the system components and address any identified thermo-mechanical concerns.

Materials

Candidate alloys for HTMH HX construction featuring the Brayton unit-cell heat exchanger include Inconel® 617 and 625 (annealed and solution-annealed) due to commercial availability, workability, and demonstrated creep properties of the sheet and foil form factors needed. Qualification of alloy 617 has been heavily investigated for nuclear and boiler applications, primarily in tube form, but nonetheless shown 100,000 hour life promise at and above 750 C in the stress regime of this application [49], [50]. Alloy 625 have been investigated and utilized previously with Brayton recuperators and creep properties are well understood [51]. One concern with both of these materials is loss of ductility as a result of aging at 750C [49]. The aging and embrittlement of the 617's microstructure is accompanied by gamma-prime precipitation resulting in additional strength and creep resistance making it the front runner for this application [49]. Material failure after 100,000 hours of aging for both alloys as a result of the embrittlement is application specific, particularly in regard to transients. Previous testing at Brayton has shown promising creep-fatigue behavior of alloy 625 base material and corresponding brazed joints, however this remains a concern.

Candidate alloys for tubular receiver construction include Inconel® 617, 740H, and Haynes® 230. Alloys 617 and 230 are often lumped into the same category, however, 230 has been shown to maintain a larger percentage of ductility with aging. In tube form factor, 740H has demonstrated superior strength and creep resistance to all candidate alloys listed here and is considered the front runner for the tubular receiver [50]. Primary concerns with 740H are the economics and manufacturing of the desired tube sizes.

Approach

Rupture life and minimum creep rate material property data have been collected from a variety of sources [50], [52]–[55] and used to model receiver life of both the cell and tubular geometries. Correlation between the life data and life expectancy of the geometry specific thermal/stress profiles is modeled with both the Larson-Miller Parameter (LMP) and the secondary creep rate Norton power-law [56]. For all following cases minus-3-sigma material properties are used to quantify life expectations in an effort to arrive at a bulletproof 100,000 hour design. Figure 96 outlines the LMP and relative superiority of the candidate materials; the LMP is related to stress through a power-law and thus even a small increment to the parameter has significant return on life.

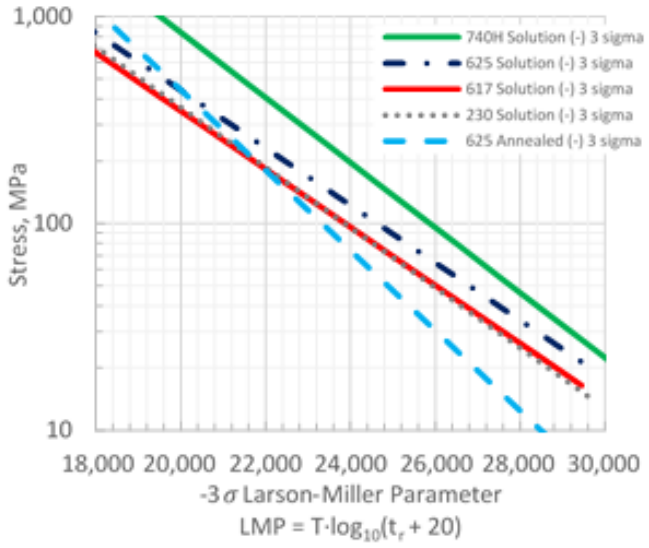

Figure 96 – (-3σ) Larson-Miller Parameter for candidate alloys.

Brayton Cell

The Brayton cell was analyzed at a maximum metal temperature of approximately 750°C. In this temperature range, the maximum allowable stress for the candidate materials to meet the 100,000 hour life requirement is approximately 60MPa. Analysis shows that the thermal stresses account for a mere 12 percent of this value and that the more significant contributors are the cell's radial and axial pressure loads. Figure 97 illustrates a 2D deformed FEA stress profile at 25 times scale for the cell. Thermal boundary conditions include a flux profile, convection to a bulk sCO_2 temperature, radiation/convection to ambient and symmetry at the right-most plane. Structural boundary conditions include pressurized sCO_2 and symmetry at the right most plane. Arrows identified with label "*A*" indicate a net force acting on the cell that is primarily reacted by the top and bottom parting plates. At 25 times scale, repercussions of this reaction are observed in the plates and fin ligaments that ultimately lead to cell failure. To quantify life in these regions, average temperature and stress values at a number of ligament and parting-plate bisections are recorded and used to calculate rupture life with the LMP. Norton creep model simulations confirm these as regions of failure. Figure 97 Section B exemplifies a few bisections observed as most critical from prior testing results as well as patterns in more recent simulations, these regions are of primary concern in life calculation.

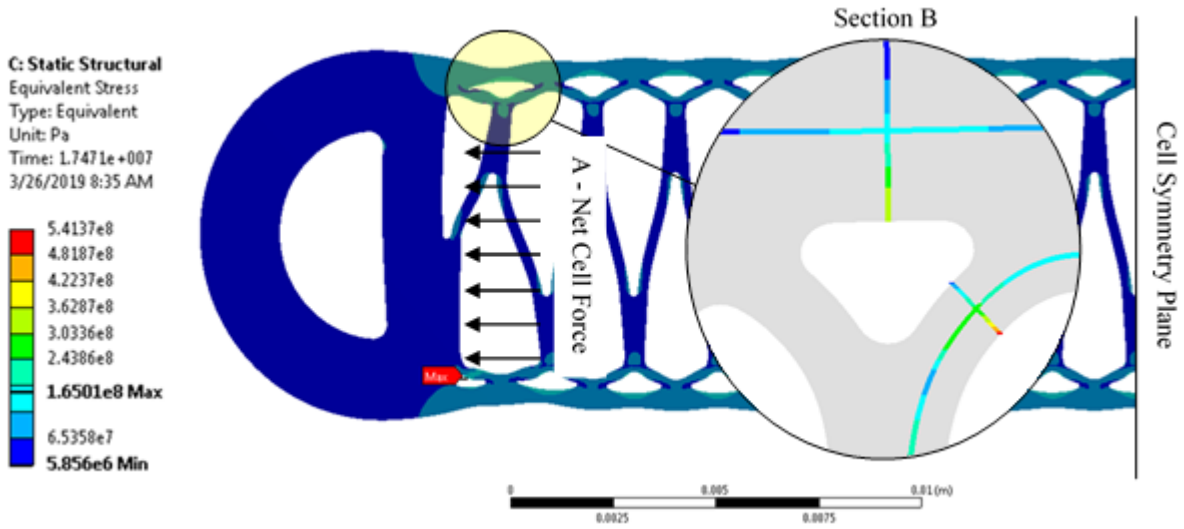

Figure 97 – Cell 25-times-scale stress profile. Arrows identified with label "A" indicate nef force acting on cell geoemtry. Section B: Exemplified stress profile bisection used in LMP life calculation

With a nearly set thermal profile, the cell net-reaction force magnitude and therefore stress profile is mitigated with fin height as this is the most direct method to reduce the carried force in the plate. Increasing plate thickness has inferior mitigation. A relationship between fin height and life has been developed through parametric analysis and is discussed shortly.

Along with the radial stress field outlined in Figure 97, a plug-load exhibits additional force that is to be carried axially by the cell. This plug load is proportional to projected area over material cross sectional area. Therefore, a relationship with fin height but also fin density exists. Using optimized results from the 2D study to narrow geometric combinations, a 3D model is used to characterize the plug-load effects and further define life expectancy.

Parametric analysis with fin height, parting plate thickness, and fin density were conducted to arrive at an optimal cell geometry; one meeting life criteria and resulting the largest possible receiver efficiency (i.e. smallest pressure drop). Fin height was found to have the largest main effect on life, results from this study are shown in Figure 98(a). For each geometric combination and material, a power-law relationship between life and fin height is observed. Variance on fin density and parting plate thickness have been omitted for readability but relationships with life align with the expected; higher fin densities and thicker parting plates lead to overall stiffer cells, each resulting in hydraulic and thermal complications for system level considerations. Critical take-aways from the figure include: long cells require an-open or tall cell to minimize pressure drop but life requires a short cell, the difference in life between materials stemming from the LMP (625 vs 617), the significance between nominal and -3σ material properties, and effects of the axial plug load (2D vs 3D). Uncertainty in the life model is to be determined as a small perturbation from the selected 100,000 hour geometry could be detrimental to cell life.

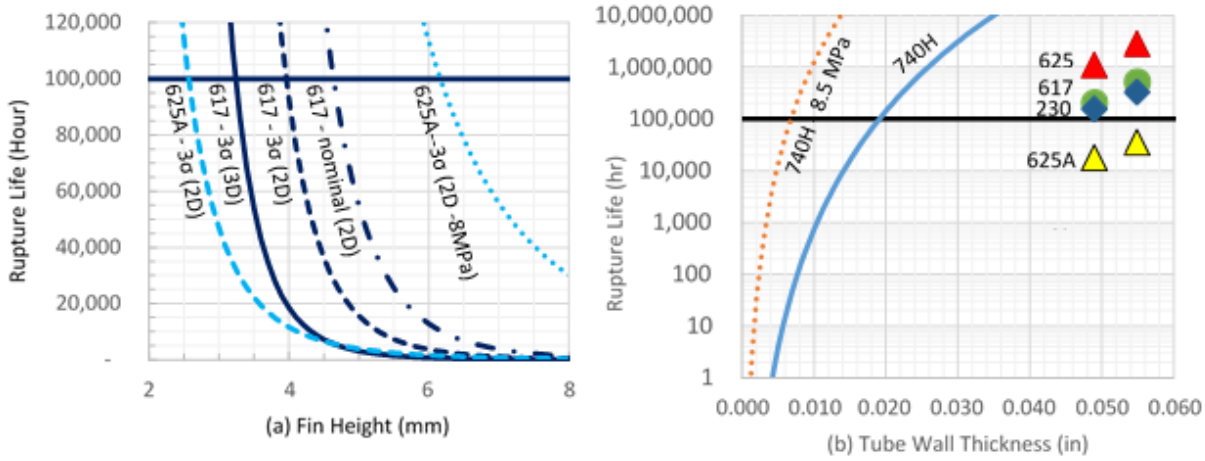

Figure 98 – (Left) Cell rupture life as a function of fin height. (Right) Tube rupture life as a function of wall thickness. All results at 25MPa unless otherwise noted.

Similar analysis were conducted on a 3D tube model. The uniform pressure loading exhibited with the tubes is advantageous for creep life considerations, specifically with decreasing diameter. Analysis and manufacturing considerations have arrived at ¼" tubing. With the prospective quasi-cavity receiver architecture, a disadvantage is the thru-wall and circumferential thermal gradients as a result of flux incident 180 degrees of the tube. Thus optimal tube thickness are thin to minimize these gradients and limited by material creep considerations; i.e.the number of grains in through wall cross section. It is standard practice to allow for 6 to 10 grains to maintain creep resistance [57]. For leading material candidate 740H, this requires thickness greater than 0.028 inches. At these thicknesses, analysis again show that again thermal stresses are dominated by the radial and, more pertinently for the thin walls, the plug load. Results from tubular parametric analysis are shown in Figure 98(b). The figure shows ¼" tube life as a function wall thickness for the various candidate materials. 740H quickly

identifies itself as a front runner bargaining for a large factor of safety under current operating conditions.

Speculation exists on which ASME code or section such CSP receiver technology is to be designed to given the rather unique diurnal operation and creep-fatigue interactions. Further investigation of these interactions are to be conducted. Analysis include uncertainty in life model inputs as well as the established and trusted linear summation of the creep and fatigue damage to understand the life factor of safety on these designs.

Milestone 3.3.1.1:

An integrated receiver and thermal energy storage system layout that is shown to have a predicted operation life of 90,000 hours considering creep, fatigue, corrosion, strength, and appropriate environmental factors (wind loads, etc.).

The methodology for determining the life of the receiver has been outlined above. It was determined that the receiver and HTMH HX design proposed would both exceed the 90,000 hour life requirement when considering normal temperature and pressure perturbations. The riser and downcomer have been designed using B31.1, which greatly exceeds the 90,000 hour life.

SubTask 3.3.2:

Generate detailed costs for the engineered components in the system (e.g., absorber cells and the metal hydride TES), and general costs for the balance of the system

HTMH Heat Exchanger Manufacturing Process and Cost Estimates

HTMH, LTMH, and Receiver cost estimates are based on an extensive manufacturing development plan that leverages Brayton Energy's long history, experience, and expertise in manufacturing robust, high performance heat exchangers for gas turbine applications, and the learnings from the past 7 years of working with sCO_2-capable designs. The findings are summarized in Figure 99, which shows the cost per kW_t of heat transfer capacity (for the HTMH system) as a function of total capacity produced. The data points shown on the curves represent periodic injections of capital equipment and/or tooling that enable the next trajectory of cost reduction with further production.

Note that the provided numbers are for the heat exchanger core only, and do not include the packaging and flow guide structure on the particle side; these design elements are expected to be a relatively modest overall adder to the total cost.

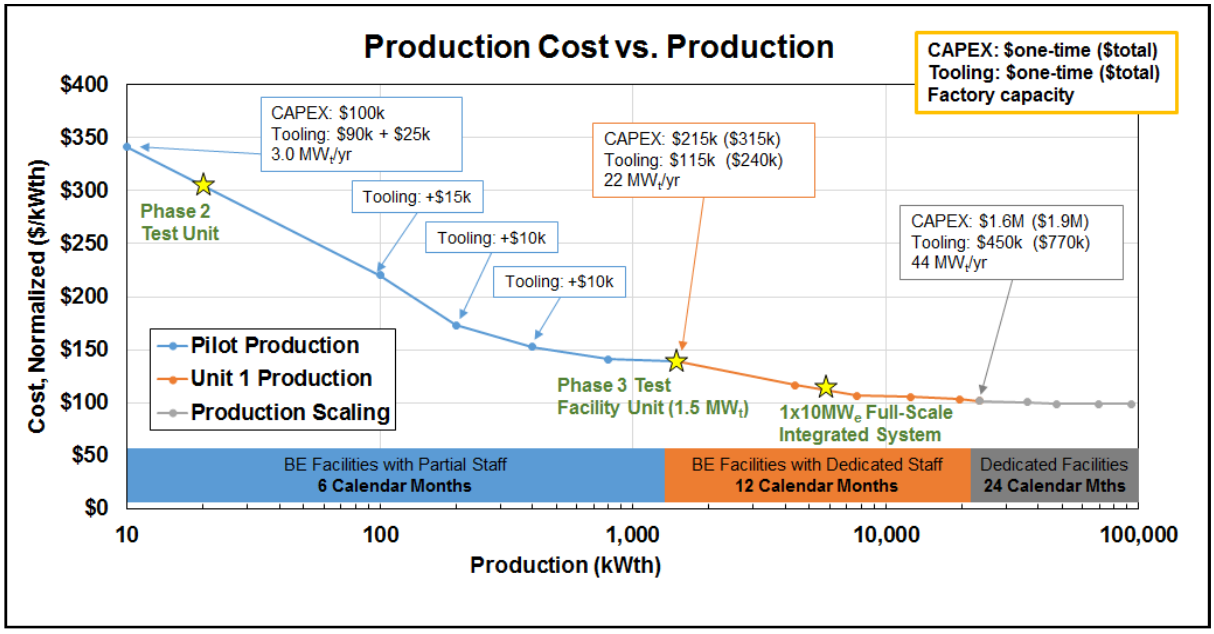

Figure 99 – Cost curve for the production of sCO2-to-particle heat exchanger cores, utilizing a manufacturing plan that incorporates periodic tooling upgrades and capital expenditures to achieve ongoing cost reductions.

Piping Design

Because of the high temperatures and pressures that the CO_2 cycle must experience, thick walled, expensive piping must be used which has a large impact on the economics of the cycle. The standard for sizing piping for power plants is B31.1, which was used for this analysis. Assumed conditions for the riser and downcomer are listed in Table 27.

Table 27 – Riser and downcomer design conditions.

PARAMETER	UNITS	RISER	DOWNCOMER
Temperature	°C	560	760
Pressure	MPa	25	25
Flow	kg/s	104.5	104.5

760 °C and 25 MPa is at the extremes of what can be economically produced for a power plant. An often proposed solution to high piping costs is an engineered pipe, where the pipe is internally insulated, allowing for lower metal temperatures, lower cost materials, and thinner walls. In conversations with Special Metals, EPRI, and Burns & McDonnell it was decided that an engineered pipe solution would not be used. There is no demonstrated engineered pipe design available for these temperatures, pressures, and fluid. Using an engineered pipe would be a significant risk to any investor, and was not proposed for this design.

Though CO_2 is relatively inert, at high temperatures significant corrosion can occur in low alloy steels. Stainless steels generally perform well in high temperature CO_2, and are the lowest cost option for the riser [58]. 347H stainless steel was chosen because of its good corrosion resistance, and high allowable stress. Since the conditions of the riser falls within the design space of current steam power plants, a standard pipe size was specified. The downcomer has much more extreme conditions and as such requires a nickel alloy in order to meet B31.1 wall thickness requirements. 740H is not yet listed in B31.1, but is listed in ASME Boiler and Pressure

Vessel Code, so creating a code case for B31.1 would not be exceedingly difficult. More important is the allowable stress to use in the B31.1 wall thickness equations. At high temperatures the allowable stress is determined almost solely on the creep rupture stress at 100,000 hours, which is highly dependent on the temperature of the material [59]. Figure 100 shows a plot of average 100,000 hour life rupture stress as a function of metal temperature.

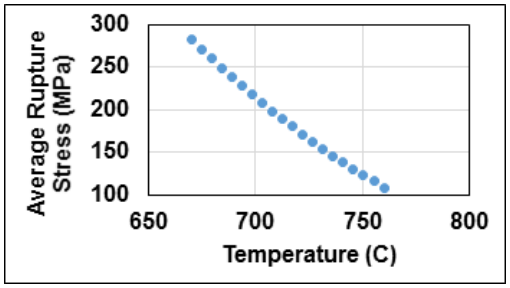

Figure 100 – Average rupture stress as a function of temperature for 100,000 hour life.

Choosing the operating temperature as 730 °C compared to 760 °C will increase the average rupture stress by 44% which can significantly reduce the mass of piping needed. In conversations with Special Metals, it was determined that the diameter and wall thickness of 740H should not be limited to standard sizes since piping for a commercial product would be made to order. As such optimizing between piping cost and cycle performance can be done much more easily.

Choosing pipe sizes is not as easy as choosing a diameter and wall thickness to meet the initial specifications. An important trade-off between pipe diameter (cost), and pressure drop (thermal efficiency) exist which must be taken into account. A cycle model is created in EES which includes the CO_2 engine, receivers, thermal energy storage heat exchangers, and piping. Pressure is specified at the exit of the main compressor, and pressure drops through the engine components, receivers, and thermal energy storage heat exchangers are calculated as a percentage of the absolute pressure according to the specifications document. Pressure drop through the piping and valves is calculated based on their chosen size. Thermal losses in the system are also calculated, but are secondary in importance. It is simple and inexpensive to insulate pipes to reduce thermal losses to a negligible amount. Piping costs are estimated using the mass of pipe required. For stainless steels a cost of $7/lb was used, while 740H was costed at $40/lb [60].

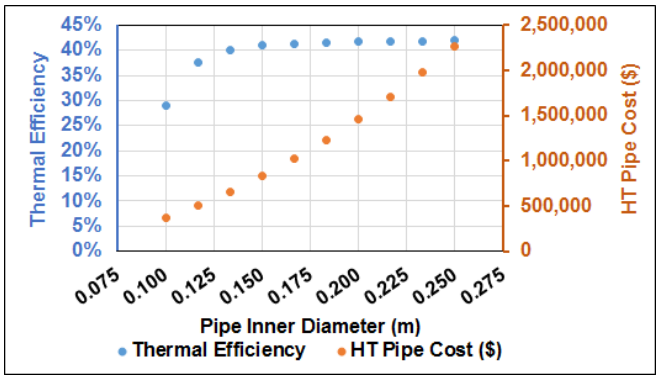

Figure 101 – Downcomer (high temperature) cost and thermal efficiency as a function of pipe inner diameter.

Figure 101 shows the thermal efficiency and cost of high temperature piping for different pipe inner diameters. Once the diameter is increased to 150 mm there is very little increase in thermal efficiency by making the pipe larger, which would only increase costs. Ideally, optimization would try to optimize LCoE, however without a much more detailed cost information this is impossible. Instead the knee of the thermal efficiency plot was chosen,

where making the pipe size larger will result in a small increase thermal efficiency but making the pipe smaller results in significantly lower thermal efficiency. The knee of the plot is a good estimate for the optimal LCoE point; for the high temperature pipe this corresponds to an inner diameter of 150 mm.

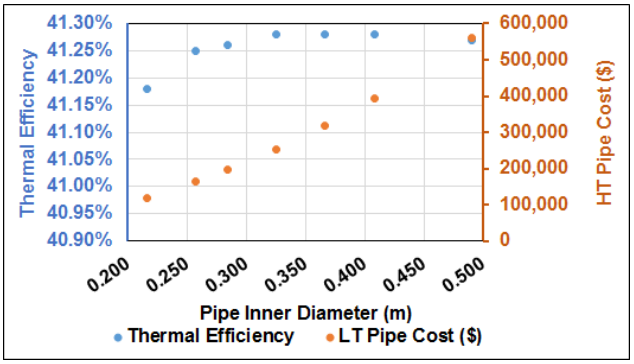

Figure 102 – Low temperature piping cost and thermal efficiency as a function of pipe inner diameter.

A similar plot for the low temperature pipe size is provided in Figure 102. As with the high temperature piping, a drastic fall off also occurs for the low temperature piping. However, costs for the low temperature pipe are approximately 10 times less than for the high temperature pipe. This means that it may be more economical to choose a slightly larger pipe to benefit from the higher thermal efficiency. A more detailed LCoE analysis is needed to choose the perfectly optimized result, however a pipe with an inner diameter of 216 mm will be close to the optimal value.

Table 28 – Summary of riser/downcomer design.

PARAMETER	UNITS	LT PIPE	HT PIPE
Material	-	347H	740H
Inner Diameter	mm	216	175
Wall Thickness	mm	28.6	34.9
Standard Size	-	10" Sch. 160	Custom
Length Req'd	m	44	69
Cost	k$	77	1,122

The results for the pipe optimization are given in Table 28. The method for calculating the pipe size is described above in the riser/downcomer section. Costing is done on a per mass basis, where the length and weight of all pipe sections needed is considered. The results for the pipe optimization are given in Table 28, the total cost for the riser piping is $209,000 while the downcomer is projected to cost $1,226,000.

The H_2 regenerator recovers heat that would otherwise be lost during charging when the hot H_2 is cooled in the LTMH. Without the regenerator an additional 3.4MW of heat would be needed during discharge just to bring the hydrogen to the proper temperature. Sizing of the regenerator is completed using a model defined in [61]. The model calculates an NTU and matrix capacity ratio based on fluid flows and bed dimensions and returns regenerator effectiveness. Table 29 lists regenerator input parameters and model results.

To reduce losses in the system, the regenerator must be specified with fairly high effectiveness. An aspect ratio of 3 was specified as a compromise between a very long bed which has thinner walls, and a very short bed which has lower losses. Because of the low flow rate and large cross-sectional area, the pressure drop in the bed is essentially negligible. Shell costs are calculated in the same way as for the HTMH shell, using a correlation for cost as a function of shell weight and correcting for inflation and material [62]–[64]. Packing costs are calculated using costs associated with stainless steel packing from the chemical processing industry and corrected for inflation [62], [63]. It is assumed that these costs will give a good approximation for the cost of stainless steel spheres.

Valves

Initial layouts planned on using the same MH HX cells for both charging and discharging. Using the same cells would require valves on both the hot and cold size of the TES. At the operating temperatures of the TES (760 °C) there is only one good choice for material, 740H. 740H has the highest allowable stress at 760 °C of any material approved by ASME BPVC and is the obvious choice for the valve and piping material. However, 740H is a forged material, so all 740H components must be forged in order for the material to maintain its properties. Even a relatively small 10 MW_e sCO_2 engine will require valves on the order of 6" which is a fairly large valve. FlowServe, an expert in the valve industry has indicated that a butteryfly valve is the best option for this application because of its relatively small forging size compared to other valve types. However, in conversations with forging shops, FlowServe was unable to obtain a quote for a butterfly valve over a size 4. The forge shops were concerned that they would not be able to maintain the material properties through the thick sections of the valve.

Table 29 – Input parameters and results from regenerator model.

PARAMETER	UNITS	VALUE
Hydrogen Flow Rate	kg/s	0.339
Hydrogen Pressure	MPa	1.5
H_2 Hot Inlet Temp	°C	730
H_2 Cold Inlet Temp	°C	60
Switching Time	hr	8
Regen. Effectiveness	%	98.40%
Sphere Size	mm	3
Packing Material	-	316
Shell Material	-	316
Shell Design Temp.	C	760
Shell Aspect Ratio	L/D	3
Shell Inner Diameter	m	1.8
Shell Thickness	mm	80
Shell Length	m	5.41
Packing Mass	kg	68,348
Shell Mass	kg	27,758
Packing Cost	$	$ 97,814
Shell Cost	$	$ 432,063

An alternative layout was proposed that eliminates all of the hot valves and instead uses valves at 560 °C, the turbine outlet temperature. Valves at this temperature are readily available at an acceptable cost. Four valves are needed to control of flow through the system. Research efforts in another Apollo program have looked at the optimal valves for these exact conditions, and results from that project have been used in this project. The valves specified are a Y-pattern globe valve made of 316. A 10" valve is specified, the same size as the piping, which has a cost of $283,000 each. A large portion of the costs are from actuation, a consequence of the high pressure in the system. Pressure drop through these valves is calculated and is only 40 kPa. A smaller size valve could be used, however there is not a large difference in cost, and the increase in efficiency due to lower pressure drop is more important than the cost savings.

SubTask 3.3.3:

Apply the capital costs and annualized receiver/TES performance profile to generate a system LCOE.

LCOE

Costs for the system are divided into four major categories; solar field, tower and receivers, TES, and power block. Solar field costs are determined by the surface area of heliostats required. A cost of \$75 per m^2 of heliostat area is specified for the heliostats as well as an additional \$8/m^2 for site improvement. These cost numbers are based on the DOE's long term goals for CSP technology. A wind turbine tower is targeted for this application because of the similar sizes and the ability to leverage the existing supply chain which reduces cost. When the project was initiated, the cost for an 80 m tower was quoted as 1 million dollars. Current system design calls for a tower that is 100 m tall, which is within the range of newer higher capacity wind turbines [65]. A scaling factor of 0.7 is used to calculate the cost of a 100 m tower from the 80 m tower quote.

Costing of the receivers is done by modifying the cost estimates for the HTMH and LTMH HX cells. First the required number of cells in each receiver can be calculated based on the known mass flow rate through the entire system as well as the maximum flow rate through each component. The manufacturing schedule for the cells shows that when the technology has reached maturity, 61% of the cost is in materials. This material cost was scaled to take into account the size difference between the receivers and HTMH/LTMH cells. It is assumed labor and processing costs are similar for both designs.

Table 30 – Capital costs by subsystem for the LCOE = 9.75¢/kWh_e case

CATEGORY	ROLLUP
Solar Field	**$ 4,974,854**
Heliostats	$ 4,495,350
Site Improvement	$ 479,504
Tower, Receivers	**$ 4,344,630**
Receivers	$ 970,390
Tower	$ 1,169,000
Piping	$ 1,199,240
Valves	$ 1,006,000
TES	**$ 19,246,869**
HTMH TES HX	$ 13,855,870
Shell	*$ 1,199,000*
Insulation	*$ 321,582*
HTMH	*$ 671,288*
Cells	*$ 11,664,000*
LTMH TES HX	$ 4,821,227
Shell	*$ 1,521,000*
LTMH	*$ 989,264*
Cells	*$ 2,310,963*
Regenerator	$ 569,772
Shell	*$ 432,063*
Insulation	*$ 39,895*
Packing	*$ 97,814*
Power Block	**$ 6,000,000**
TOTAL	**$ 34,566,353**

The costing for the TES components are described elsewhere in the report. Costs for the power block are assumed to be \$600/kW_e with the power block fixed at a constant 10MW_e of power output. A cost roll up of these components can be seen in Table 30.

Using the total system costs, System Advisor Model (SAM) can be used to calculate the resulting LCOE [66]. A parametric study is conducted showing the effect of engine efficiency on LCOE. In this analysis only the engine power is allowed to vary, while the total system costs, solar field size, and amount of storage are all kept constant. The purpose of the study is not to find the optimal cost vs efficiency point for the system, but rather to show the potential operating points of the system. There is significant uncertainty in the performance of the CO_2 engine that will be used as both a circulator and the power block, as such there is a wide range of potential operating efficiencies. The study is conducted for two different system costs which corresponds to different number of cells in the HTMH HX. The high-cost case assumes a maximum temperature drop of 30°C is allowed over the HTMH while the lower cost case assumes a maximum temperature drop of 60°C. Limiting the maximum

temperature drop to 30°C may be too conservative and could result in excessive capital costs. Figure 103 shows LCOE as a function of cycle efficiency for both cases. Under the high cost case the best LCOE possible is 9.18 ¢/kWh$_e$, while the lower cost case has a cost of 8.38 ¢/kWh$_e$.

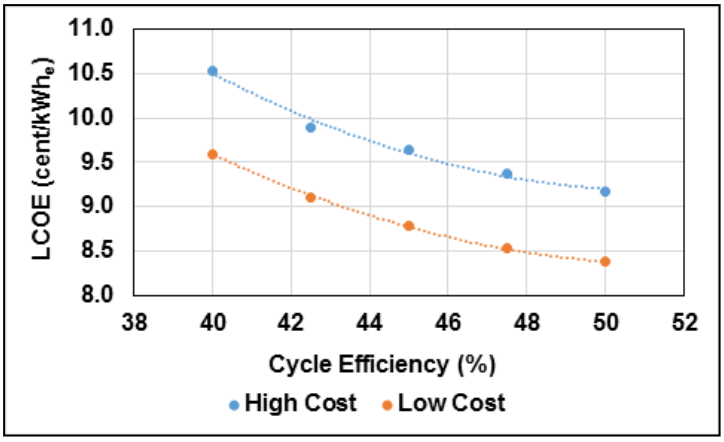

Figure 103 – LCOE as a function of cycle efficiency for a high and low system cost.

Milestone 3.3.3:

An integrated receiver, tower, and thermal energy storage system designed for a 10 MW$_e$ modular tower-based CSP sCO$_2$ Brayton Power Plant with Integrated TES that has a capital cost of $210/kW$_{th}$ or less (corresponding to the DoE goal of $150/kW$_{th}$ for the receiver/tower system + [$15/kWhr$_{th}$ x4 hrs. storage] for the TES), within an uncertainty of ±35%, over the full range of input variability.

A total cost of $1179.6/kW$_{th}$ is obtained for the system. Which is broken down into a cost of $114/kW$_{th}$ for the tower plus receiver and $260/kWh$_{th}$ for the TES system. While the tower and receiver costs meet the milestone, the TES system does not which is driven by the high costs of cells required for the HTMH HX. Material costs for the HTMH and LTMH alone exceed the DOE goal for TES system cost. However, there are scenarios where the LCOE of a CSP plant with MH TES would be competitive in the market. Further refinement in cost models puts the uncertainty at a ±35% level.

Task 3.4:

Design a prototype article to evaluate its performance and validate the predictions for the full-scale system. A sub-scale test article will be specified which captures all of the important operational characteristics of the full-scale system and incorporates all of the engineered innovations in this proposal. Suitable manufacturing trials will be constructed to demonstrate the feasibility and practicality of the proposed design. A test loop will be designed for the purpose of evaluating the test article, and a detailed test plan will be submitted.

SubTask 3.4.1:

A prototype article that embodies the innovative and functional elements of the proposed receiver and thermal energy storage system will be designed. The test article will be designed so as to capture all of the phenomena necessary to adequately simulate the full-scale design, with particular attention being paid to minimum test article size, critical dimensions, edge and boundary effects, and other critical considerations as may be identified by the Commercialization Advisory Board.

The HTMH HX is constructed to represent the full scale HX as closely as possible. At small scale the pressure vessel efficiency (useable volume of MH divided by the total volume of the pressure vessel) is low. In this case, only 27% of the pressure vessel is filled with MH, a full sized system is predicted to have a pressure vessel efficiency of greater than 75%. A stainless steel shell is used to contain the pressure of the hydrogen. MH is held in a rectangular grid around the cells using a sheet metal enclosure which approximates the geometry at the center of the PV. The HX is designed to be filled and sealed in the inert atmosphere of a glove box because exposure of the HTMH to air results in degradation. Designing for 10 kWh of storage would require 45 kg of HTMH alone, and with the surrounding PV shell, the total weight would be greater than 400 kg, too much to be filled in a glove box. A more realistic goal of 2 kWh of storage was chosen, as this resulted in a total weight of 170 kg. This is still very heavy, but using a hoist it should be possible to fit the PV in the glove box for filling. A rendering of the HTMH HX is shown in Figure 104.

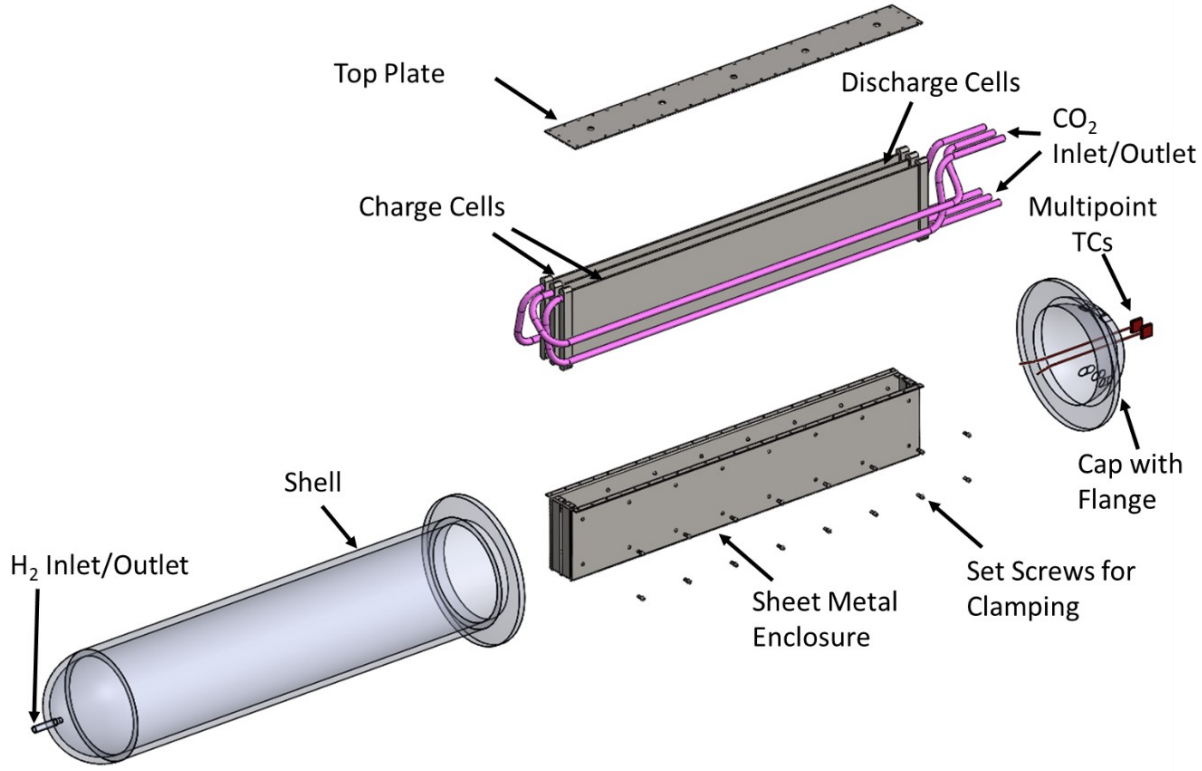

(a)

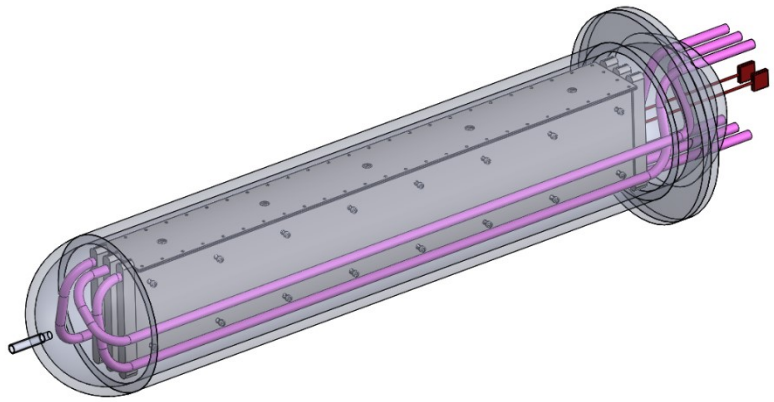

(b)

Figure 104 – (a) HTMH HX exploded view showing outer shell, sheet metal liner, instrumentation, and CO_2 cells. (b) assembled HTMH HX showing how the components fit together.

A flange is used to allow access to the cells in the glovebox so the PV can be filled and sealed in the inert environment. Three cells are used, two charge cells, and one discharge cell. In the full scale system there would be approximately the same number of charge and discharge cells, however in order to balance the flow with the MH distribution, 3 cells are used. Two cells would have a poor pressure vessel efficiency, and more than three cells would result in the fraction of flow to each cell not matching the amount of energy the cell would collect or release. To fill the sheet metal enclosure with MH, first the cells are placed in the correct position in the sheet metal enclosure and headered properly. The inlet and outlet CO_2 tubes should then be fed through the end cap and swaged into position. Any TCs that are used to instrument the bed can then be fed through the Swagelok pass through. Next, the entire HX unit can be placed in the glovebox. The HTMH powder requires significant force to reach its maximum density, and will be compressed into pucks before filling. These pucks will be the proper thickness to tightly fit between the cells. As the pucks are being inserted into the shell, the TCs should be located in the proper location and secured. After the pucks are inserted into the sheet metal shell, the top plate can be bolted into place. Screws in the sheet metal shell can then be tightened down to compress the cells into the MH pucks. This compression will ensure that there is good thermal contact between the cells and the MH. Specifications for the HX are given in Table 31.

Table 31 – HTMH CO_2 cell dimensions.

PARAMETER	UNITS	VALUE
Length	mm	821
Pipe	in.	8
Pipe Schedule	-	80
No. of Cells	#	3
Cell Width	mm	150
HTMH	kg	4.2

While this test article does not meet the goals set out in milestone 3.4.3.1, it does do a good job at being representative of the full scale system. A sensitivity study was conducted on the test section to see the resulting storage time when the parameters were changed by 10%, the design storage time of 1 hour was also reduced by 10%. This still gives a sufficient amount of storage to get valid results.

Test Uncertainty

It is important to quantify the uncertainty in the system before construction to determine if the test will provide meaningful results. Total uncertainty for each measurement is calculated using the Root Sum Squares (RSS) method as shown in Equation 9 [67].

$$u_{Total} = \sqrt{\sum_{i=i}^{k} u_i} \qquad \text{Equation 9}$$

where *k* is the number of sources of uncertainty and u_i is the uncertainty of each source. When multiple measurements are taken of the same parameter, the uncertainty of the measurement is reduced according to Equation 10

$$u_{eq} = \frac{u_{Total}}{\sqrt{N}} \qquad \text{Equation 10}$$

where u_{eq} is the equivalent uncertainty, and *N* is the number of measurements taken. The only location in the system where multiple measurements will be taken is the inlet and outlet of the HTMH HX where a small temperature difference mean small uncertainties in the measurements are needed. Uncertainty by measurement type is shown in Table 32.

Table 32 – Uncertainty of each measurement in test facility.

MEASUREMENT	DAQ RESOLUTION	DAQ UNCERTAINTY	INSTRUMENT UNCERTAINTY	TOTAL UNCERTAINTY
R Type TC	±0.015°C	±0.57°C	±0.7°C	±0.90°C
Dual Element R Type TC	-	-	-	±0.64°C
K type TC	±0.005°C	±0.52°C	±2.8°C	±2.85°C
Absolute Pressure	±2.98E-6%	±0.87%	±0.08%	±0.88%
Mass Flow	±2.98E-6%	±0.87%	±0.1%	±0.88%

Heat transfer into and out the HTMH HX is calculated using Equation 11.

$$\dot{Q}_{HTMH} = \dot{m}(h_{out} - h_{in}) \qquad \text{Equation 11}$$

Where h_{out} and h_{in} are calculated based on the measured temperature and pressure. One of the goals of the project is also the measure the energetic efficiency of the cycle. An exergy transfer rate is needed into and out of the HTMH HX, as shown in Equation 12.

$$\dot{X}_{HTMH} = \dot{Q}_{HTMH}\left(1 - \frac{T_0}{T}\right) \qquad \text{Equation 12}$$

where $\dot{Q}_{HTMH}$ is the heat transfer rate calculated in Equation 11, T_0 is the ambient temperature (assumed to be known with 100% certainty at 32°C), and T is the temperature at the heat transfer boundary. T the temperature at the boundary is taken as an average between the inlet and exit temperature. If heat transfer surface measurements prove to be reliable, they will be used instead. Using the EES uncertainty propagation tool and projected operating conditions, a measurement uncertainty for heat transfer and exergy transfer can be calculated as shown in Table 33 [68].

Table 33 – Calculated uncertainty for essential heat transfer measurements.

MEASUREMENT	UNITS	HTMH HEX HEAT TRANSFER	HTMH HEX EXERGY TRANSFER	RECEIVER HEAT TRANSFER
Nominal Value	kW	2	1.38	8.95
Uncertainty	kW	0.049	0.034	0.202
	%	2.46	2.46	2.26

Measurements for the receiver heat transfer have a low uncertainty, but the small temperature rise over the HTMH HX leads to higher uncertainty in the measurements. Over 85% of the uncertainty in the measurement comes from the uncertainty in the thermocouples. Since a high accuracy dual element TC is already being using, it will be next to impossible to decrease the uncertainty of the measurement. However, this uncertainty measurement is very conservative. It only considers the situation where the bed is charging and there is a very small temperature difference. When the system is discharging the temperature difference will be much lower and uncertainty will also drop. The P&ID diagram does not have any pressure drop measurements over the HTMH HX and the receiver, the reasons are two-fold. First, the circulator pump cannot provide a larger pressure drop, so the components will need to be low pressure drop in order to meet the flow requirements. Second, uncertainty analysis shows that the heat transfer measurements are not sensitive to pressure, a change of 200 kPa yields a change of 0.01%, which is insignificant.

SubTask 3.4.2:

Successfully demonstrate the manufacture of any new, untested, innovative, or different design elements critical to the operation of the proposed integrated receiver design. Any novel absorber brazed-cell architectures will be manufactured and quality tested to ensure adequate strength and performance in accordance with program requirements.

As outlined above, the optimal receiver for this project was specified as the Brayton tubular sCO_2 receiver that was primarily developed under the Gen 3 program. Because the Gen 3 project had its own derisk plan, it was determined that it would not be necessary to manufacture and test a separate receiver under the Apollo program. However, information about the Gen 3 receiver testing program is included below in order to satisfy the task.

The design of the phase 2 article was chosen to derisk the commercial design to the fullest extent possible. An illuminated length of 1.3m has been chosen which is approximately ¼ of the commercial design length. This shorter length allows us to achieve a more uniform flux profile with the limited number of heliostats available as well as reduces the number of heliostats required to meet the desired operating conditions. Because the receiver optimization was an ongoing effort in phase 2, test receiver geometry was designed to the optimal receiver geometry

as of the start of phase 2. This ended up being fairly close to the final optimal design which is specified in Table 34, which makes the results of testing useful for derisking the phase 3 receiver. Two design point tests are specified for phase 2, the match flux case which matches the absolute fluxes of the commercial receiver but scaled down to fit on the 1.3m receiver length. To approximate the stresses the commercial receiver would see, the maximum metal temperature was matched between the two receivers by adjusting the flow rate of the phase 2 receiver. The match exit temperature run matches the commercial receiver exit temperature while limiting the max temperature of the receiver to 790°C. As a result, the mass flow through the receiver must be decreased significantly. A comparison of the phase 2 receiver test cases to the current optimal commercial receiver design is given in Table 34 .

Table 34 Phase 2 receiver operating conditions compared to commercial receiver operating conditions

Parameter	Units	740H Commercial Design	P2-Match Flux	P2-Match Exit Temp.
Outer Diameter	in	3/8	3/8	3/8
Wall Thickness	in	0.07	0.08	0.08
Length	m	4.32	1.3	1.3
Receiver Efficiency	%	83.73	80.26	72.54
Pressure Drop	kPa	345.7	229.7	59.0
Coating Absorptivity	-	0.975	0.97	0.97
Coating Emissivity	-	0.6	0.85	0.85
Maximum Metal Temperature	°C	761.9	761.9	790
Mass Flow Per Tube	g/s	69.41	23.02	11.28
Total Mass Flow	kg/s	733.1	0.276	0.135
Inlet Temperature	°C	577.2	540	540
Exit Temperature	°C	730	673.7	730
Number of Tubes	-	10,562	12	12
Receiver Width	m	21.15	0.11	0.11
Receiver Aspect Ratio (L/W)	-	0.69	11.37	11.37

Flux Profile	-	Sinusoidal	Sinusoidal	Sinusoidal
Max Flux	kW/m2	668.7	672.3	519.7
Average Flux	kW/m2	388.6	390.7	302.0
Average HTC	W/m2-K	6933	3184	1787
Max dT Wall	°C	49.1	46.3	30.0
Power Per Tube	kW	13.5	3.88	2.71
Total Power	kW	142.6E3	46.56	32.54
Front to back dT - Top	°C	132.2	166	147.9
Front to back dT - Bottom	°C	31.0	39.4	28.8

Other off-design tests were also planned, where performance would be measured over a range of inlet conditions allowing for the performance model to be verified throughout its operating range.

Instrumentation was added to the receiver to meet the objectives listed above. Thermocouples are inserted into the flow which allow inlet and exit temperatures to be measured. Pressure sensors at the inlet and exit measure pressure, while a Coriolis flow meter measures flow through the receiver. These instruments can be used to calculate the enthalpy at the inlet and exit of the receiver which can be used along with mass flow rate to determine heat transfer to the CO_2. Pressure drop measurements are made with a differential pressure transducer which is plumbed into the inlet and exit headers of the receiver article. Back wall tube temperatures are measured directly by thermocouples welded to the back wall. Receiver efficiency requires a measurement of incident flux. For this a calorimeter was used which is the same size as the receiver test article and is located directly adjacent to the receiver. By switching the aim point of the heliostat field from the receiver to the calorimeter, the flux incident on the receiver can be determined.

One other compromise that needed to be made on the phase 2 receiver was placing the receiver tubes within a cavity. At high temperature and flux, the tubes experience differential thermal growth where the tube tends to grow towards the field. Without a cavity this would cause the tubes on the edge to be exposed to more flux than their neighbors which are shaded which in turn would lead to premature failure. As a result the receiver test article experiences more shading and lower power. For phase 2 testing a coating from Brightsource was used which is similar to those used on the Ashalim CSP plant, though slightly modified for the test article conditions. While the higher emissivity of the Brightsource coating results in lower performance, it can still provide a valuable derisk of the receiver performance. Brightsource has a long history of reliable coating performance which made it a good choice for the phase 2 test article. An image of the phase 2 receiver test article is given in Figure 105.

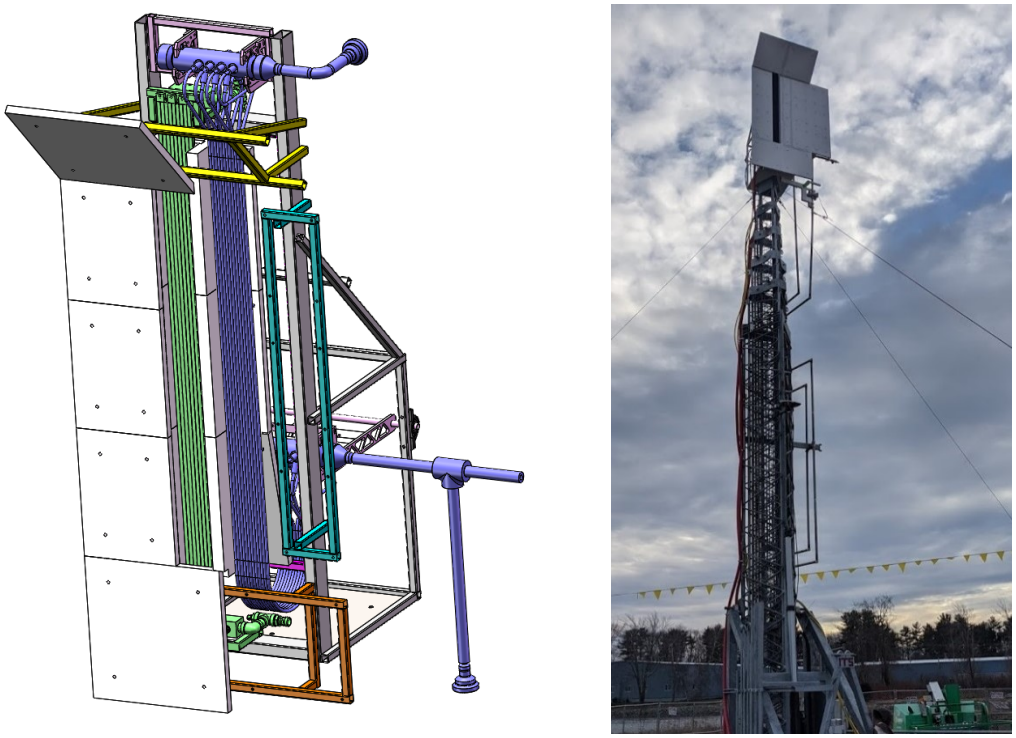

(a) (b)

Figure 105 Phase 2 receiver test article (a) cutaway showing receiver and calorimeter, (b) receiver mounted on tower.

While the complete range of testing was not able to be completed before the deadline, through great effort two tests were completed. The first was a heat loss test where hot CO_2 was flowed through the receiver with no flux applied. Time constraints dictated that insulation could not be added to the pipes which resulted in significant heat loss in the pipes running to the receiver and from the receiver to the recuperator. As a result, the maximum inlet temperature achievable was 168.2°C. Consequently, the low operating temperatures meant that the expansion valve in the circulator skid was not able to build pressure properly so the maximum pressure attainable was 10.4MPa. Heat loss testing was conducted by using the heater to heat the CO_2 at the inlet of the receiver and measuring the temperature lost over the receiver test section. Because the receiver was uninsulated the results did not match the model well with significantly more heat loss than the model predicted. At the low operating temperatures, almost all of the heat loss is due to convection. The heat transfer coefficient to the air is a function of the geometry and windspeed and direction which was unknown at the time of the test as the anemometer had not yet been deployed. Without the time to fully understand and correct the losses seen in the subscale test article it is impossible to determine if the receiver has met the performance targets at this time.

The second test put the maximum amount of flux on the receiver possible from our partial strength solar field. Because the control computer for the heliostat field has not yet been completed, each of the 12 heliostats needed to be moved on target individually. This made it difficult to maintain a constant flux input to the receiver article and made measuring incident flux out of the question. At solar noon, the period of highest irradiation, the calorimeter received

15kW of power. Because of the low operating temperature of the calorimeter (only 5°C hotter than ambient) the losses can be assumed to be negligible. At the point of highest solar flux, the heat transfer to the CO_2 was measured to be 5.6kW at a CO_2 inlet temperature of 143.1°C. After testing was completed, the receiver was brought down and inspected, there was no visible damage to the tubes or the coating. While far from design point, this test proved the ability of the receiver to operate with CO_2 and handle at least some amount of flux. Though the objectives laid out at the start of the project were not met, significant progress was made towards them culminating in a successful on-sun test. Some pictures from the on-sun testing are shown in Figure 106.

(a) (b)

Figure 106 (a) receiver testing with applied flux, (b) solar field while testing receiver

SubTask 3.4.3:

A test loop will be designed for use of prototype testing.

The full scale design calls for a high temperature of 760 °C at 25 MPa CO_2 pressure. These temperatures are very difficult to design for at smaller scales. A full scale system can be designed to use custom extruded 740H pipe, which has a significant allowable

stress at these temperature; however, 740H is not available in the small tube sizes needed for testing. 625 is widely available in tube sizes, however there are still issues with meeting the temperature and pressure requirements. Figure 107 shows the allowable pressure according to B31.1 as a function of temperature for potential tubing sizes and materials.

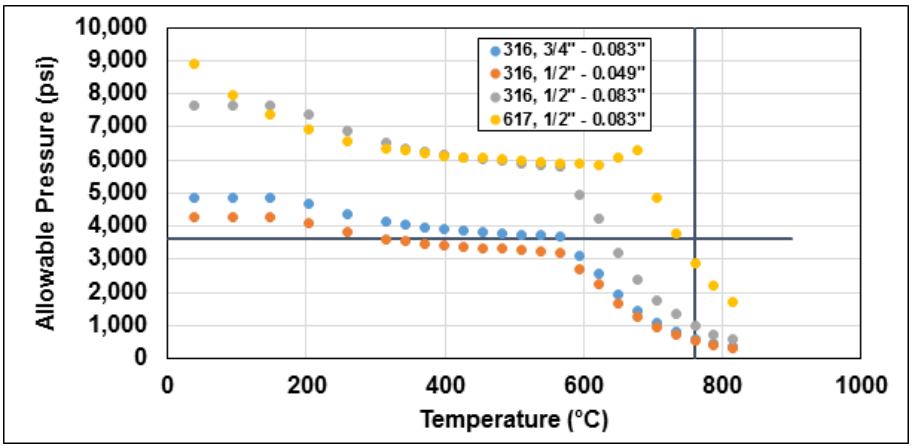

Figure 107 – Tube allowable pressure as a function of material temperature for different tube sizes and materials.

The vertical line on the plot indicates the desired operating temperature (760 °C), while the horizontal line indicates the desired operating pressure (3600 psi). After 600 °C the allowable stress of 316 starts to fall rapidly, and at the 76 0°C desired operating temperature, the allowable pressure for ½" - 0.083" tubing is only 1000 psi. Using 625 tubing in the same size increases the allowable pressure significantly, to almost 3000 psi. However, this is still less than the desired operating temperature. If pipe or medium pressure tubing were used it is possible to reach the desired operating conditions, but these options are much higher cost and more difficult to implement. For either case there is no good way for the CO_2 tubing to penetrate the H_2 shell. Using ½" tubing allows a standard Swagelok tube fitting to be used as a pass through, greatly simplifying construction. So it was decided that instead of running at the full 760 °C, we would instead run at 732 °C for the maximum temperature, which means the full system pressure can be used. The performance of the HTMH also needs to be analyzed to ensure that the hydration reaction still takes place at lower temperature. Figure 108 shows the operating pressure of the LTMH and HTMH as a function of temperature. Decreasing the operating temperature of the HTMH to 730 °C will decrease the operating pressure of the H_2, but will not

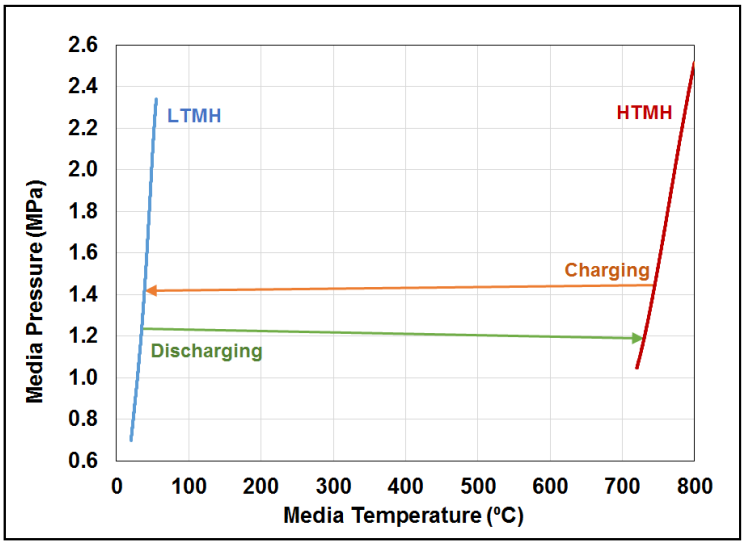

Figure 108 – Operating pressure as a function of temperature for LTMH and HTMH.

prevent the reaction of continuing. Dropping the operating pressure of the hydrogen is also advantageous as it allows the use of a schedule 80 pipe instead of a costlier schedule 100 pipe.

The regenerator in the TES system is used to recover the thermal energy that would otherwise be lost as hot H_2 flows out of the HTMH during charging. Without the regenerator, during discharge, an additional heat load would be needed to heat the hydrogen from the temperature of the LTMH to the temperature of the HTMH. A regenerator effectiveness of 98% was specified, which corresponds to a 0.4% loss in heat transfer rate in the HTMH HX. Specifications for the test hydrogen regenerator are given in Table 35.

Table 35 – Specifications for hydrogen regenerator.

PARAMETER	UNITS	VALUE
Length	mm	200
Pipe Size	in.	3
Pipe Schedule	-	80
Packing Mat'l	-	SS Spheres
Packing Mass	kg	4.2

To save costs, the LTMH HX was specified as a modified commercially available shell and tube heat exchanger. A two pass U tube heat exchanger was specified with an additional blind flange on the back side which can be removed to allow filling of the LTMH. A water-glycol mixture is passed through the tube side which is used to keep the LTMH at the desired operating temperature (60 °C).

The water loop is used to maintain the temperature of the LTMH. A heater and cooler are needed to maintain the LTMH temperature. The heater and cooler are sized to provide 3 kW of heat/heat rejection which is approximately five times as much power as is required, which will ensure the system can maintain temperature even with losses.

Figure 109 shows a P&ID layout of the test facility and indicates the location of the required instrumentation.

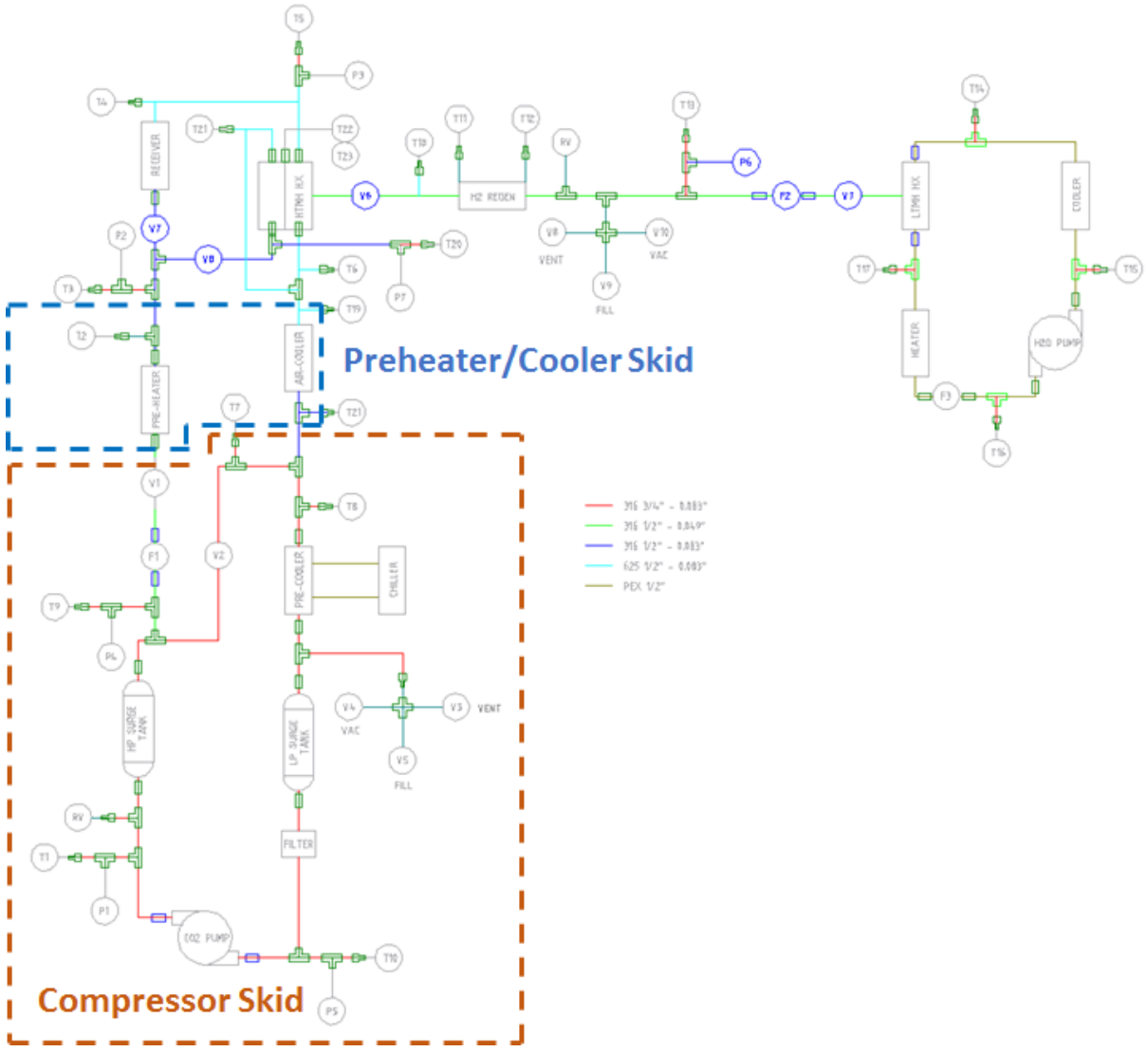

Figure 109 – P&ID of metal hydride test facility.

The test facility must survive at least 1,000 hours at the desired operating conditions. To this end, all of the tubing and pressure vessels were designed to either ASME BPVC or using B31.1. Components specified using BPVC and B31.1 will have lives in excess of 30 years [20], [21]. Using these conservative codes means the test facility components can be reused for future testing without worrying about past damage. The receiver and HTMH cells are built using the same design as the full scale system components at a smaller length. This means that these components can withstand at least 100,000 hours of operating time, the same length as the full scale system would experience. Because none of the components are designed to 1,000 hour life, it was determined that a parametric analysis of life of the components would not be needed to ensure all test data can be taken.

Test Cost

A significant amount of equipment is needed in order to test the TES system under representative conditions. A detailed parts list has been assembled for this project. It divides the test facility into 3 separate skids that are integrated together to form the total test system.

A compressor skid, pre-heating/pre-cooling skid, and test section skid are specified. Separating the compressor from the other components allow it to be used in other DOE sponsored projects where sCO_2 is required; there it is anticipated that the cost of the "pump skid", and possibly the "Pre-Heating/Cooling Skid", will be shared among multiple programs to the mutual benefit of each. Table 36 lists the main subsystem costs, and a full parts list is available upon request.

Table 36 – Test setup subsystem costs.

PARAMETER	COST
Pump Skid Costs	$ 128,582
Pre-Heating/Cooling Skid	$ 7,250
Test Section Skid	$ 196,491
Total Costs	$ 332,323

Milestone 3.4.3.1:

Design of a 5 kW_{th} test article and test setup – with a 10 kWh_{th} storage capacity – to be used for simulated on-sun operation, the article itself consisting the absorber architecture, flowing working fluid, and integrated thermal energy storage.

Due to size constraints of the outer shell, a maximum of 2kWh of metal hydride could fit in the outer shell. The heat exchange cells were designed to be able to provide a maximum of 2kWth of heat transfer, allowing for 1 hour of storage. The on-sun test article was not tested under the Apollo program as the Brayton Gen 3 program was testing an almost identical design.

Milestone 3.4.3.2:

Analytically supported predictions that the test setup has a creep life of at least 1,000 hours in order to ensure safe operation throughout the testing program.

Life modeling was completed using the same methodology used for the cells and receiver. It was found that the test article would exceed the 1,000 hour rating required for this milestone.

SubTask 3.4.4:

A test plan will be generated to document the equipment, procedures, and calculations needed to operate a prototype system to demonstrate that the proposed receiver/TES system will meet the performance predictions.

The purpose of this testing is to prove the operation of the TES system, the long term performance of the TES module, the ability to store thermal energy for extended periods of time with minimal losses, and the ability of the system to match the modeled results. The different tests that will be conducted are laid out below.

Loss Testing – The goal of the loss testing is to quantify the losses in the test article under steady state conditions so the losses can be used to correct data gathered in the future. Starting at low temperatures, fluid will be passed through the test article and the heat loss will be measured once steady state has been reached. At higher temperatures it will take some time to reach steady state because of the reaction with the HTMH.

1 Hour Testing – This test will determine the performance of the test article while fully charging and discharging. The test article will start from a fully charged state, because the fully charged state can be fairly easily determined. Next the test article will be fully discharged. The definition

of fully discharged depends greatly on the goals for the system, but initially the test article will be defined as fully discharged when the exit temperature of the CO2 drops below 670°C. The test can then be repeated as many times as desired to obtain repeatable results.

20 Minute Cyclic Testing – This test consists of the bed being rapidly cycled between charge and discharge, and will determine the ability of the TES system to maintain its performance after many cycles. Starting from a fully charged bed, the test article will be discharged for 40 minutes, leaving it at 1/3rd charged. Next the test article will be recharged for 20 minutes, bringing it to 2/3rds charged. After, the test article will be switched between discharge for 20 minutes, and charge for 20 minutes. The ability of the HTMH to maintain its performance after many cycles will be determined. This test will also give an insight into differences between the HTMH charge and discharge rates.

1 Hour Dwell testing – The purpose of this test is to determine the ability of the TES to store energy over long periods of time. The system will start from a fully charged condition, then all flow turned off and the system allowed to dwell for one hour. Then the flow is turned back on and the HTMH bed is allowed to discharge. At small scale it is difficult to get accurate measurements because of the high heat loss. However, using the losses calculated earlier, the thermal losses can be quantified and separated from losses associated with the HTMH.

As testing progresses it is expected that other tests will want to be explored, and time has been allotted for those tests to occur.

Milestone 3.4.4.1:

A test plan describing the full range of tests to be performed, and demonstrating an experimental uncertainty for the TES energetic efficiency that will be ≤ 0.5 pts.

As stated in Table 34 the uncertainty for the energetic efficiency is 2.46%. This is due to the large uncertainty in temperature measurements which cannot be reduced by changing instruments.

Milestone 3.4.4.2:

A test plan describing the full range of tests to be performed, and demonstrating an experimental uncertainty for the TES exergetic efficiency that will be ≤ 0.5 pts.

As stated in Table 34 the uncertainty for the exergetic efficiency is 2.46%. This is due to the large uncertainty in temperature measurements which cannot be reduced by changing instruments.

Budget Period 3

Problem Statement: The predicted performance of the full integrated (receiver+thermal transport+HTMH+LTMH+low temperature heat rejection) system needs to be demonstrated in order to establish the practicability of the proposed solution.

Task 4.1:

Build and test a prototype article to evaluate its performance and validate the predictions for the full scale system. The test article and rig will then be assembled and tested, and the prototype article will undergo testing. The results of this testing will be used to verify the performance predictions for the full-scale system, and to further refine the LCOE of the overall system.

There are two major technology pieces that need to be demonstrated the solar receiver and the TES HX. As a cost saving measure, the solar receiver will not be tested in this project as it has already been demonstrated in the Gen 3 program. Results from the completed Gen 3 testing are listed above. This leaves the TES HX, which was originally designed to be 10kWh but was later resized to 2kWh due to cost and size constraints.

SubTask 4.1.1:

Sourcing, Purchasing, Fabrication, and Assembly of Test System

A significant redesign to the HTMH test article was made in the final budget period to account for challenges identified in design reviews. A summary of changes compared to the design presented in budget period 2 is given below.

- It was found that the flanged connection for the vessel would be too heavy and exceed the budget for the project. As an alternative, the vessel was broken into two separate pressure vessels. An inner vessel which is used to protect the HTMH from atmosphere when being transported, and an outer vessel which can contain the hydrogen pressure at temperature. The inner vessel needs to be installed in a glove box, so a threaded connection was used. A 316L 6” sch 10 pipe was used for the inner vessel and a 316 threaded insert was welded into the Haynes 230 cap. A pressure boundary is made in the glove box by threading the inner vessel into the cap. Once pressurized with Argon, the vessel can be transported without fear of degradation of the material. When the vessel arrives a Brayton, the outer pressure vessel can be completed by welding a 8” sch 80 Haynes 230 pipe to the cap. This pipe is required to meet the temperature and pressure (730°C at 650 psi) requirements of the hydrogen. A welded connection means the vessel cannot be inspected during testing without ruining the HTMH. An image of this change is shown in Figure 110.

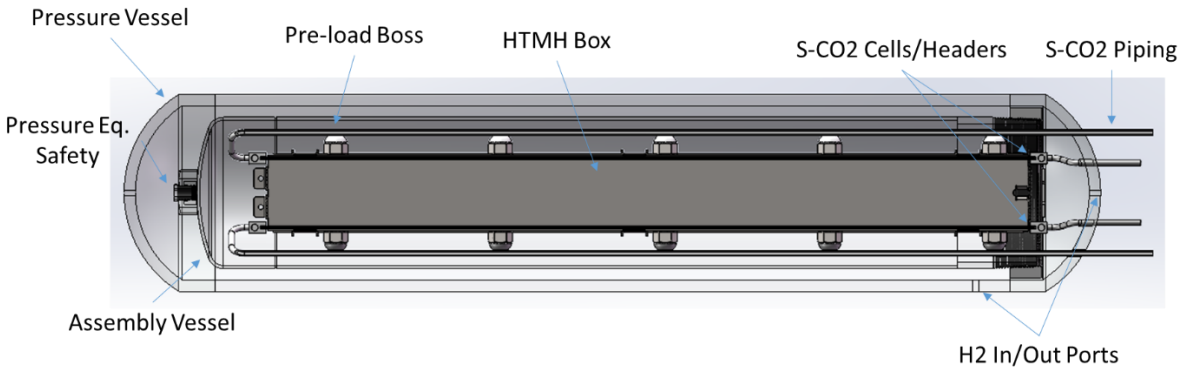

Figure 110 HTMH vessel overview

- The original design called for three heat transfer cells, which was reduced to two cells in the final design. Initially the cells were designed so two cells were permanently charging while the other cell was permanently discharging. While operating the CO2 skid, it was observed that using valves to switch flow between these two different flow paths would risk failure of the piping. The final design has two cells with flow traveling in the same direction, temperature is changed by controlling the heater power.
- The sheet metal retainer within the vessel which is used to hold the compressed pucks of HTMH next to the heat exchange cells was modified to provide a clamping force on the HTMH pucks. Belleville washers were used to provide a clamping force to the cells forcing them to compress the pucks between the cells even at high temperature. This compression allows for good thermal contact between the cells and the pucks even with the differential thermal expansion of the pucks, cells, and sheet metal retainer. Belleville washers are preinstalled into the HX vessel and are tightened down to the proper spec after all the pucks have been installed. A rendering of the sheet metal retainer is given in Figure 111.

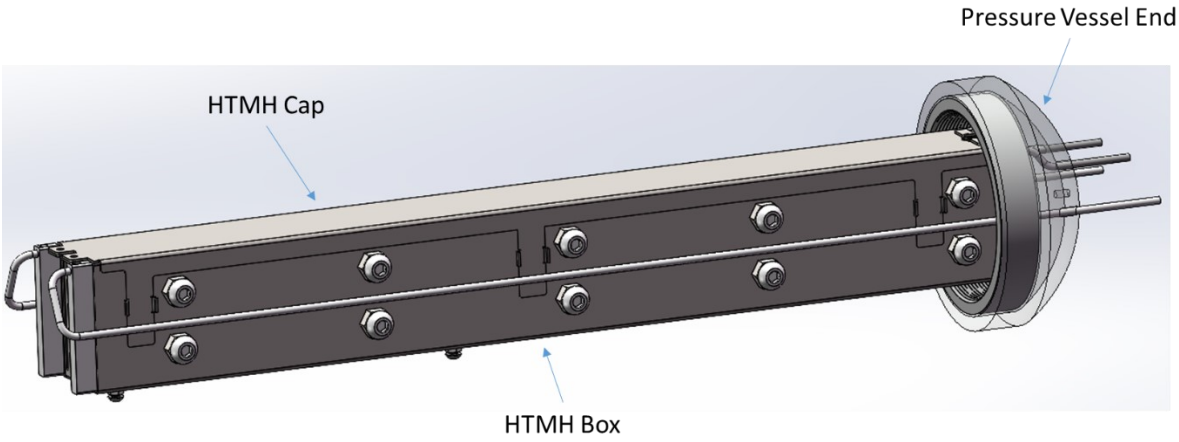

(a)

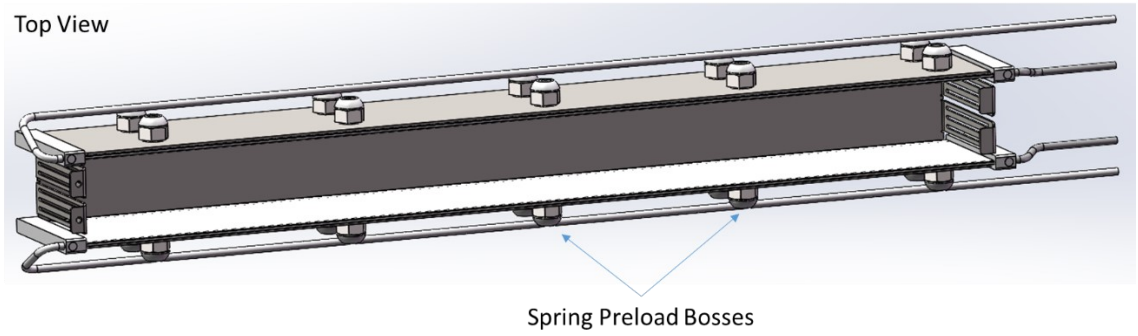

(b)

Figure 111 HTMH sheet metal retainer (a) fully assembled, (b) showing opening for HTMH pucks

The HTMH HX is designed for the following conditions listed in the table below. These are compared to the design for a single module of the commercial system.

Table 37 HTMH HX Design Point Specifications for test article and single module (of 3) of the commercial scale system

Parameter	Units	Test Article	Phase 2 Commercial Single Module
Storage Rate	kW	2	6,600
Storage Amount	Hr	1	3.7
MH Mass	kg	10.8	111,881
Number of Cells	-	2	2210
Cell Length	mm	800	2,000
Cell Width	mm	114	150
MH Contact Area	m^2	0.18	1326
Specific Flux	kW/m^2	10.93	4.98
Plate Spacing	mm	74.5	84.4
CO_2 Flow Rate	g/s	52.1	105
Charging Inlet Temp	°C	730	730
Discharging Inlet Temp	°C	565	565

The test article was designed to match a commercial module as closely as possible, however some changes needed to be made in order to accommodate the test. This can be seen in the specific flux parameter which is a measure of how much energy each unit area of cell must absorb. The test article is about two times higher than the commercial module. This leads to a higher required temperature difference in order to drive the heat flux in the test article compared to the commercial module. Ideally, the test article would have more cells in order to match the specific

flux, however these cells would not fit into the vessel. Alternatively, the test article can be run at a lower heat release rate for a longer duration, where the specific flux would match the commercial system. Inlet and exit temperatures are design to match, while the plate spacing is adjusted to maximize the amount of HTMH that can fit in the test article vessel.

HTMH HX Assembly

The first task in assembling the HTMH HX was to assemble the sheet metal box which holds the HTMH in place next to the cells. Next the cells were inserted and the headered together. The sheet metal box was welded into the cap, along with the NPT threaded insert which was used to create a seal with the inner vessel. Before being shipped to SRNL, the inner vessel was fabricated, threaded into the cap, and pressure tested to ensure an airtight seal could be made.

(a)

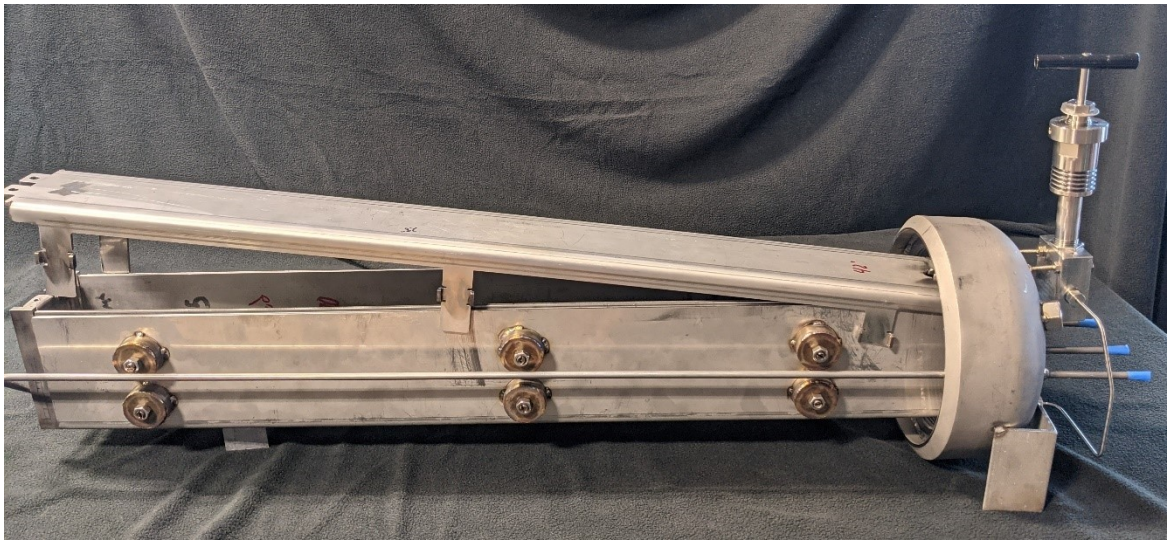

(b)

Figure 112 HTMH HX (a) inner sheet metal box with cells showing cap partially installed, (b) vessel with inner shell threaded into cap.

Figure 113 HTMH outer shell with one cap welded on

At SRNL, the HMTH was loaded in the vessel and the inner vessel sealed. When the vessel arrived at Brayton, the pressure in the vessel was confirmed to be positive, indicating the HTMH had not been exposed to air. The outer shell was welded in place around the inner vessel and the vessel was leak checked. We were unable to perform a hydro test, as water would have ruined the metal hydride, Brayton Energy does not have the facilities to safely conduct a pneumatic test, so only a leak test was performed with low pressure (15psi) nitrogen on the outer vessel welds, these were found to be free of leaks.

Once the outer shell was assembled, the CO2 tubing was fabricated and welded to the vessel. These cannot be attached by fittings as the temperature is too high for any off the shelf products, so all the tubing was 625 tubing welded into position. Machined socket weld connectors were used to join the tubes, and custom machined fittings were used to header the CO_2 tubes together.

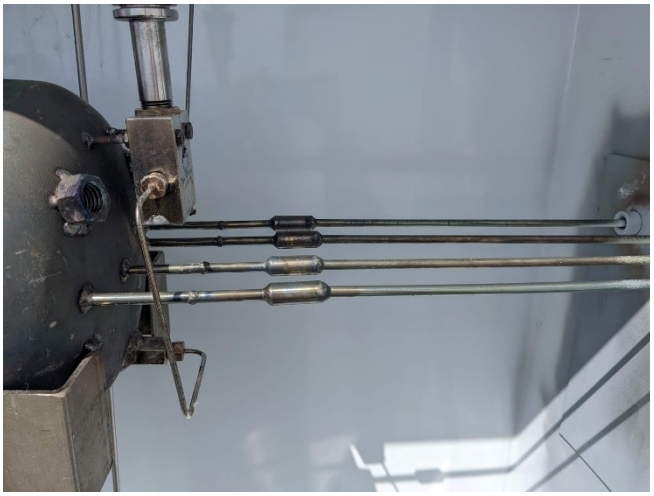

(a)

(b)

Figure 114 CO2 tubes welded to vessel. (a) tube stubs welded to inlet/outlet tubes. (b) Tube heading showing union crosses and dP transmitter

From here the HTMH HX was mounted into the box along with the other heat exchange components. Mounted on the box was a box pressurizer, which was designed to be used to pressurize the box full of nitrogen while the test was running. Thus, any hydrogen leaking from the vessel would have no oxygen to combust with. It was assumed that the pressurizer would provide a constant flow of nitrogen through the box, in actuality the pressurizer only maintained a low pressure in the box but did not provide constant flow beyond the initial purge. A risk was identified that a small hydrogen leak could displace all of the nitrogen in the box, resulting in a dangerous amount of hydrogen building up in the box. Thus, if the box was opened with an ignition source present, an explosion could occur. Research into the hazards of hydrogen indicated that keeping the box open and allowing sufficient air flow around the test article would be the safest method of operation. A picture of all the components mounted in the box is shown below.

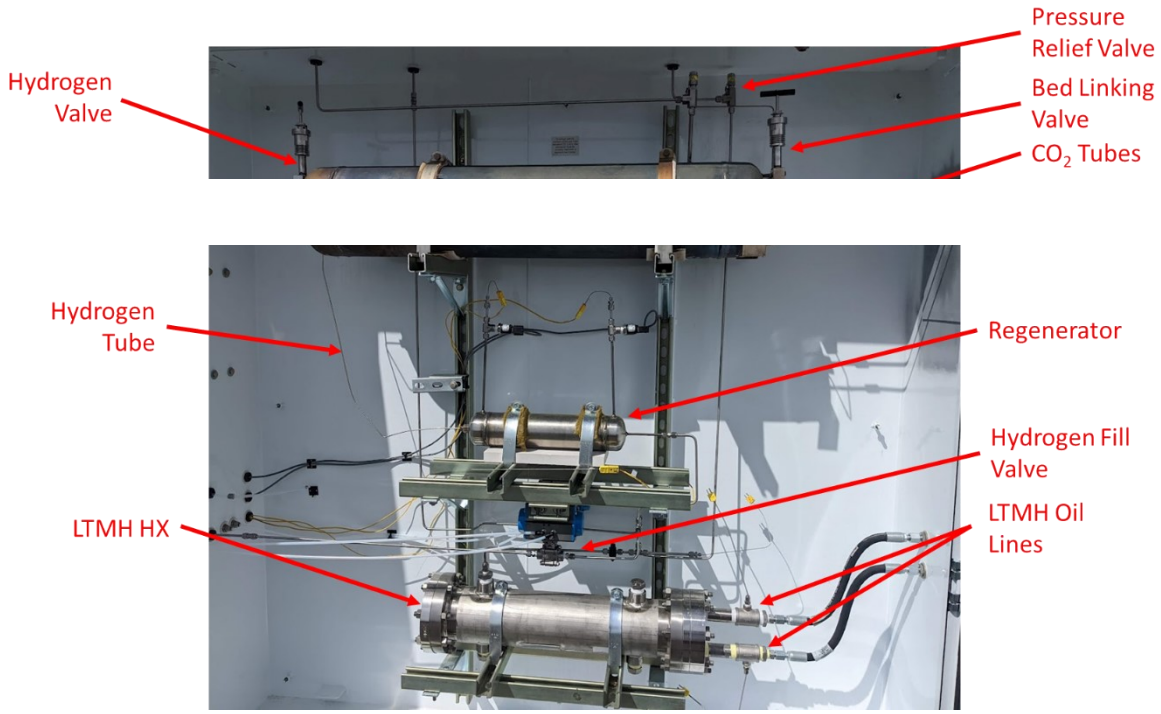

Figure 115 Heat exchange components mounted in box, showing HTMH HX, regenerator, LTMH HX, and associated components

Mounting in Box

With all the components mounted, the CO_2 plumbing can be completed. Tubes were connected from the high temperature heater to the HTMH HX, this line operates at the highest temperatures (up to 730°C) and because of that is specified as Inconel 625. All connections on this run must also be welded. The CO_2 return line and attemperation lines are also added, both of these are

316 stainless as they operate below 550°C as such, Swagelok fittings were used. All lines were insulated as much as possible to minimize heat loss to and from the system. The attemperation line is used to reduce the temperature from the exit of the test article to below 550°C which is the safe temperature for both the downstream tubing and the CO2 skid recuperator. CO_2 for the attemperation line is siphoned off from the exit of the pump to be used in the mixing tee. While the quality of the returning heat is degraded, the total heat available is not, meaning the system does not suffer significant performance losses.

Hydrogen was stored on the opposite side of the box from the inlet/exit CO_2 tubes and consisted of a size 300 bottle with a regulator. The regulator was manually set to the maximum desired hydrogen pressure and used to fill into the vessel. A remotely operated ball valve is used to fill and vent hydrogen into and out of the HTMH system.

Figure 116 Outside of support box showing hydrogen cylinders and box pressurizer.

HTMH Fabrication

During the development phase of new metal hydride thermochemical energy storage materials, high purity reagents were utilized to reduce uncertainties in the material property measurements and identify suitable materials for high temperature operation. In order to demonstrate low-cost production of the newly developed HTMH material, synthesis methodologies using $CaSi_2$ were sought due to the low cost of the precursor. Our team initially synthesized the $Ca_3Al_2Si_2$ material using a synthesis methodology developed at SRNL as described in the equation below.

$$3\ CaH_2 + 2\ Al + 2\ Si \rightarrow Ca_3Al_2Si_2 + 3\ H_2 \uparrow$$ Equation 13

The highest cost precursor from this synthetic methodology was the CaH_2 in high purity (99.9%). Previous work demonstrated the synthesis of the material and cycle stability using a lower purity (98%) CaH_2, which is significantly cheaper than the higher purity CaH_2 as shown in Figure 110. To further reduce the cost of production, synthetic methodologies have been developed to utilize $CaSi_2$. Figure 117, below illustrates the feasibility of using this precursor to produce the material. The materials were intermittently mixed and heated to 900 °C for 12 hours for each annealing step. After the 2nd annealing step at 900 °C, the primary phase of the material is $Ca_3Al_2Si_2$ with only minor impurities.

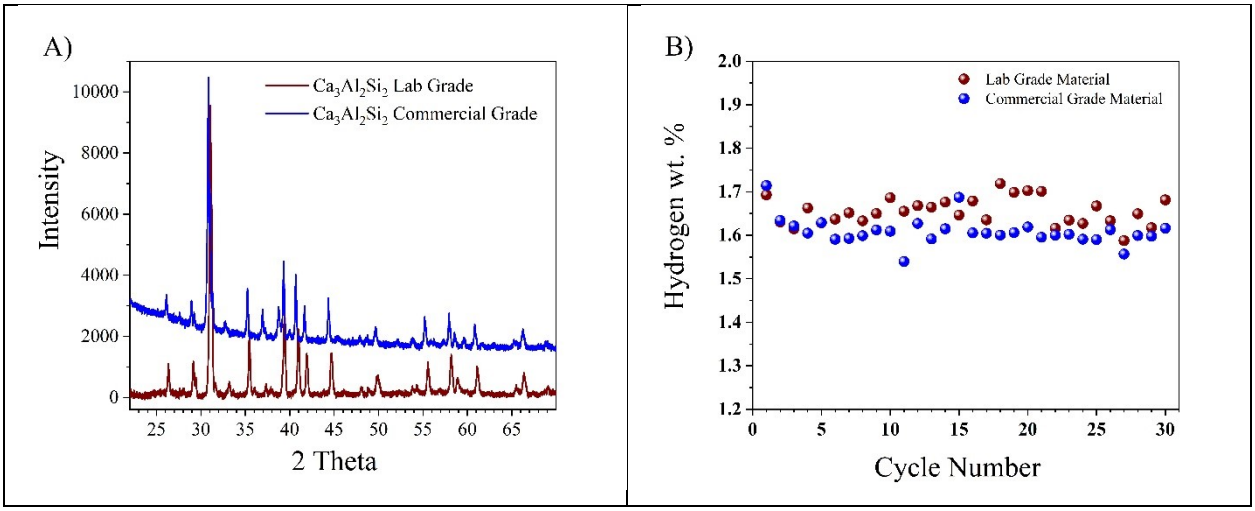

Figure 117 A) XRD patterns of Ca3Al2Si2 produced from 99.9% CaH2 (red) and 98% purity CaH2 (blue) B) Cycling stability comparison of laboratory grade (red) and commercial grade (blue) HTMH

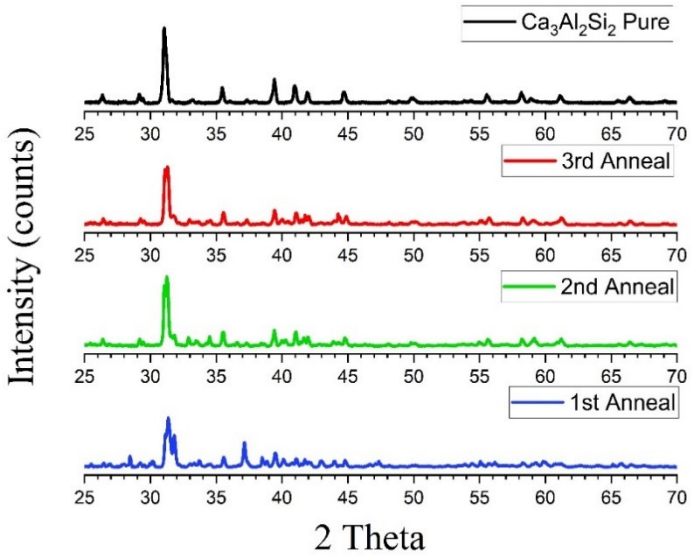

Figure 118 XRD patterns of Ca3Al2Si2 produced from 97% purity CaSi2 after various annealing steps.

The synthetic pathway chosen for kilogram quantity scale up was the pathway using commercial grade CaH_2, as shown in Equation 13. This methodology was chosen due to its effectiveness in

producing the desired phase with a reduced number of annealing steps and a reduced cost compared to the lab grade CaH_2.

Two reaction vessels were fabricated at SRNL to produce multi kilogram quantities of the HTMH material. Figure 119 displays the vessels fabricated for the annealing process used to synthesize the material and the corresponding furnaces used for this step. The synthesis methodology employed involved the homogenization of reactants following by high temperature annealing under vacuum to produce the desired $Ca_3Al_2Si_2$ phase. Initial homogenization and subsequent homogenizations between annealing steps were carried out by rotary ball milling under inert conditions. Figure 120, left, shows the kilogram quantity rotary milling apparatus acquired for scale up of the HTMH material for this project. Once the HTMH was synthesized, 10 wt. % of dried ENG was added via rotary milling to enhance thermal conductivity. A dual length argon filled glovebox was evacuated to facilitate the material scale up and addition of dried expanded natural graphite (Figure 120, right).

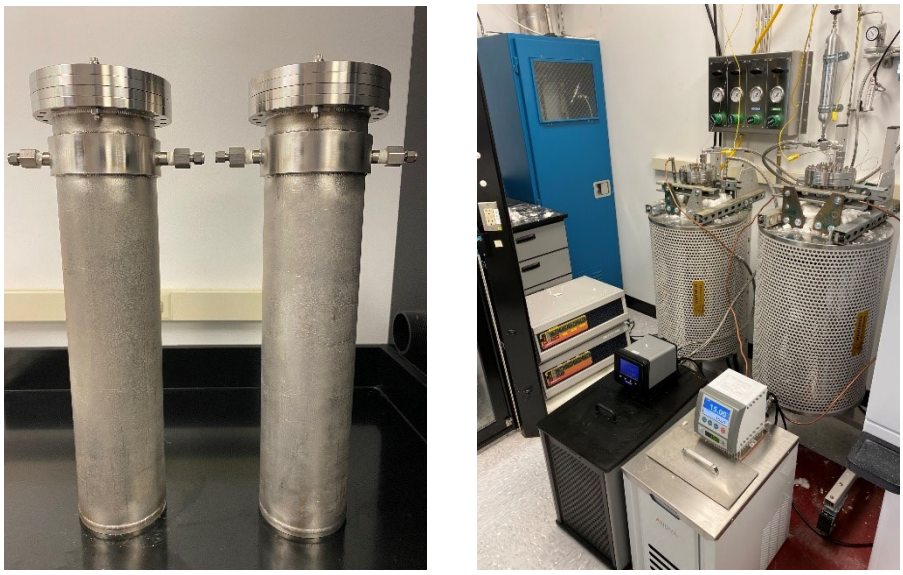

Figure 119 HTMH synthesis vessels fabricated at SRNL for material scale up (left) and the furnaces used for synthesis (right)

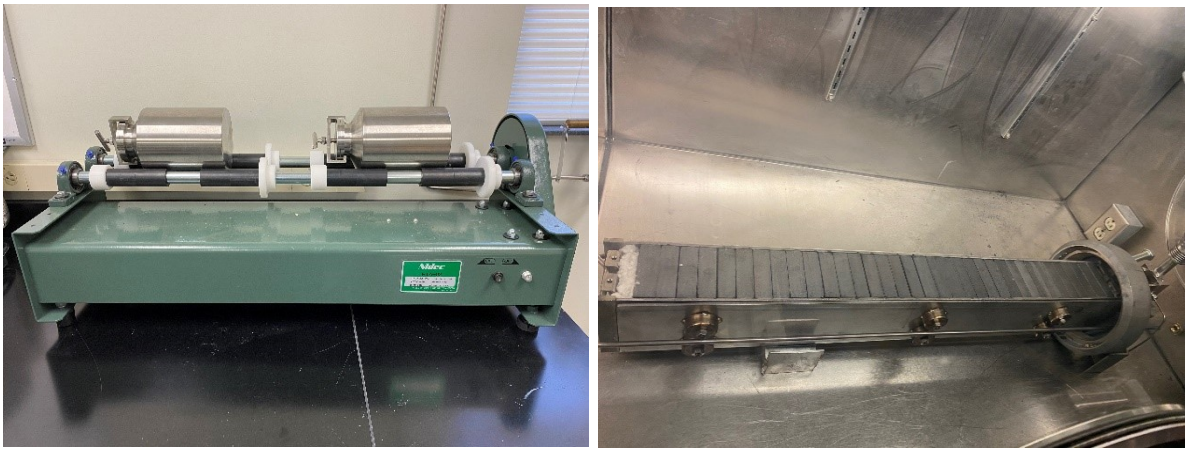

Figure 120 (Left) Rotary mill for the production of kilogram quantities of HTMH. (Right) **Fully loaded heat exchanger in dual length glovebox under argon**

To facilitate the pelletization of multi-kilogram quantities of HTMH, an environmental box was constructed to house a 300-ton hydraulic press, as shown in Figure 121. Atmospheric conditions were monitored and controlled during pelletization of the HTMH material by oxygen sensors and drying agents contained within the glovebag under a continuous purge of argon gas. Using a custom die set, the fully homogenized composite material was compressed to 150,000 lbs under inert conditions to form regular, rectangular pellets. The dye set and a characteristic pellet are shown in Figure 122.

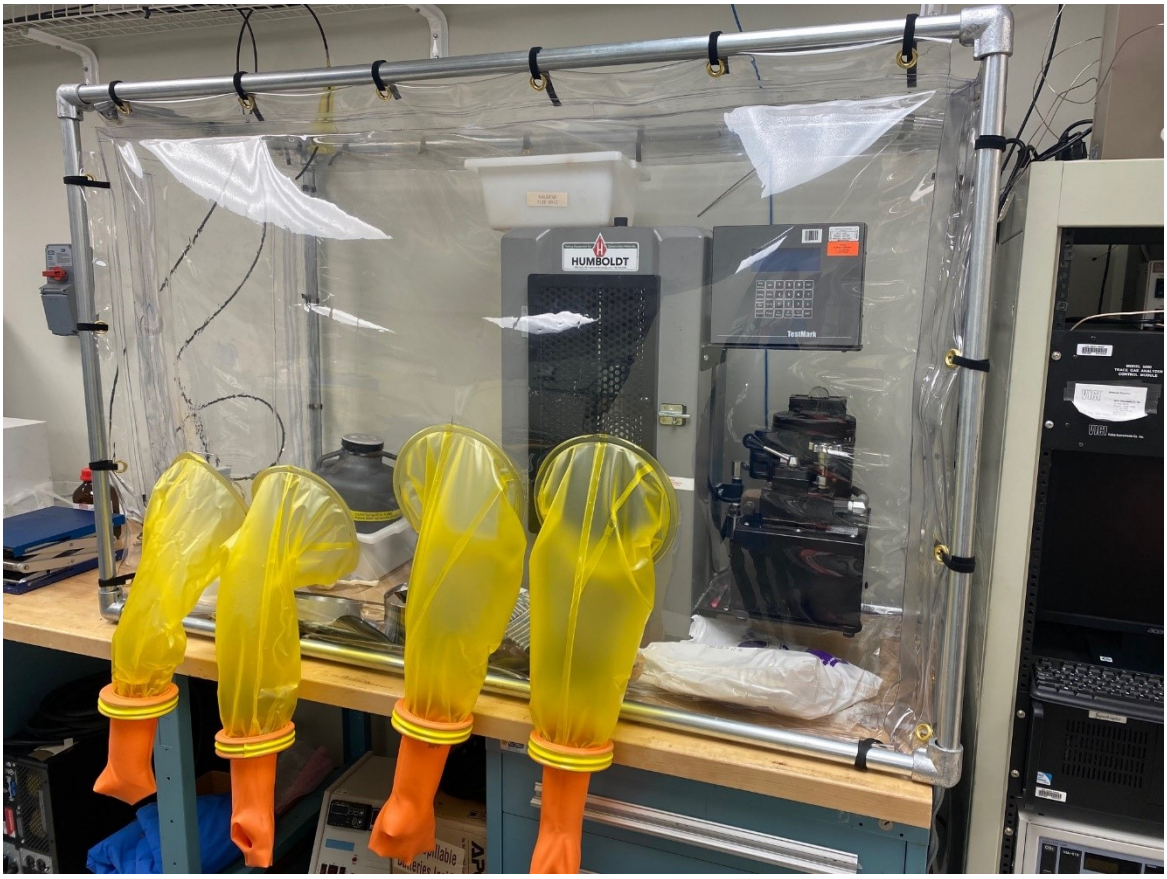

Figure 121 Containment glovebag produced for HTMH pelletization

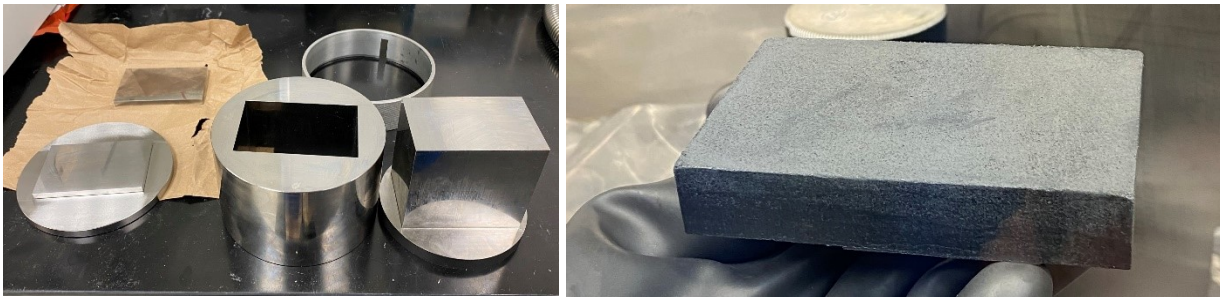

Figure 122 (Left) Die set for compression of HTMH pellets and (Right) pelletized HTMH material.

Once pressed, the pellets were transferred to the evacuated dual length argon filled glovebox, which housed the heat exchanger from Brayton Energy. Thirty-nine pellets with an average density of 1.40 g/cm^3 and weighing a total of 9.621 kg (8.6589 kg HTMH, 0.9621 kg dried expanded natural graphite) were individually inserted into the heat exchanger (Figure 113). Once loaded, the heat exchanger was sealed in the inert environment under argon. The sealed heat exchanger was leak checked and brought to a slight positive pressure of 1400 torr of argon for shipment to Brayton Energy for full system testing.

SubTask 4.1.2:

The prototype article will be tested in accordance with the test plan, with the data being used to validate the predicted performance of the full-scale system. The system performance will be demonstrated in each of the operational modes and at the operational limits identified in Milestone 1.1.8.3.

Numerous delays were experienced during the construction of the test facility. Funding issues caused many stoppages in work, and changes to the design as a result of learnings durign construction further delayed completion. As a result the test plan was not able to be completed in its entirety. However tests were completed with the goal of measuring the amount of heat released from the high temperature metal hydride when hydrogen is introduced. Each test consisted of the following three steps:

1. Flow hot CO_2 through system and allow exit CO_2 temperature to reach a steady state
    a. System was considered steady state when the inlet and exit temperature remained within 5C for approximately 15 minutes without a noticable increasing or decreasing trend.
2. Introduce hydrogen to the bed and record temperature rise of CO_2 at exit
    a. Inlet CO_2 temperature is held constant
    b. Introduction of hydrogen causes a spike in CO_2 exit temperature as hydrogen bonds with the metal hydride releasing energy.
    c. Bonding is allowed to continue until CO_2 exit temperature has reached a steady state at which point it is assumed the metal hydride is fully discharged of energy.
3. Vent hydrogen while heating to remove remaining hydrogen from bed.
    a. This occurs more favorably at high temperature and low pressure, vacuum is prefered.

This test was run at several different inlet temperatures. A plot showing the CO_2 temperature and hydrogen pressure for one of these runs is given in Figure 123.

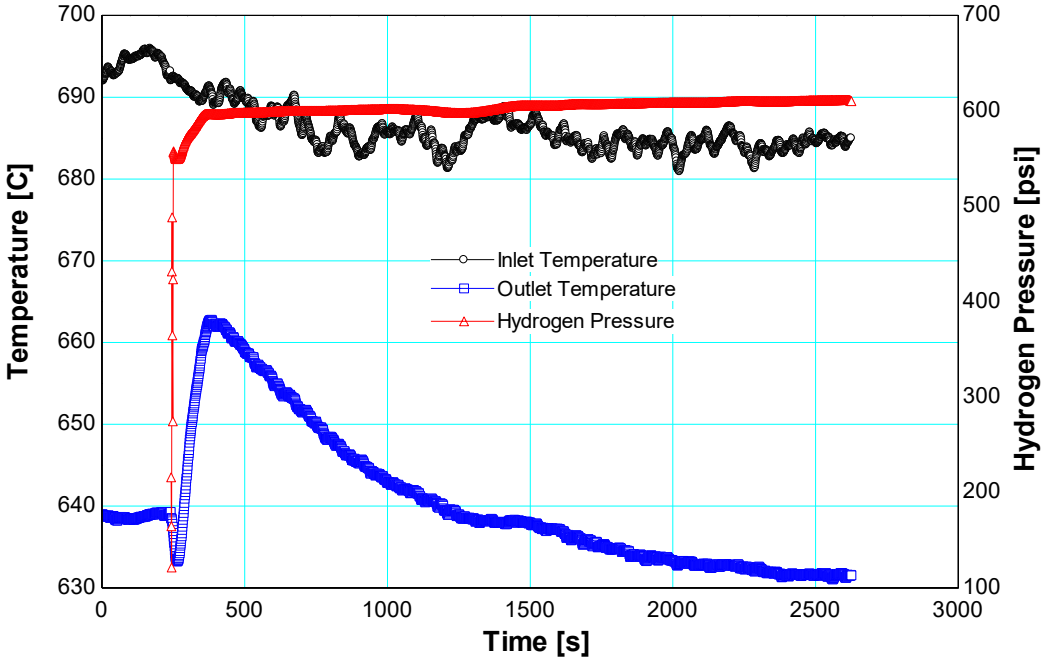

Figure 123 Temperature and Hydrogen pressure vs time for a sample run

In this run, the steady state data is shown as the first part of the plot where there is no hydrogen pressure. A heat loss term was calculated according to Equation 14.

$$\dot{Q}_{loss,spec} = \frac{\dot{Q}_{loss}}{\left(T_{CO_2,avg} - T_{amb}\right)} \qquad \text{Equation 14}$$

Where $T_{CO_2,avg}$ is the average of the inlet and exit CO_2 temperatures to vessel, T_{amb} is the ambient temperature, and $\dot{Q}_{loss}$ is as defined below.

$$\dot{Q}_{loss} = \dot{m}_{CO_2}(h_{in} - h_{out}) \qquad \text{Equation 15}$$

Where $\dot{m}_{CO_2}$ is the mass flow rate of CO_2, and h_{in} and h_{out} are the enthalpy at the inlet and outlet of the vessel respectively. When hydrogen is introduced, the temperature initially drops because of the large volume of cold hydrogen filled into the vessel. It quickly recovers and the temperature starts to spike, reaching a peak about 5 minutes after initially being introduced. By integrating this spike over the period of time with which it was observed, the total heat release from the hydrogen-MH bond can be determined as given in Equation 16. The specific loss term was used to correct the data for the heat loss experienced.

$$Q_{HTMH} = \int_0^{t_{end}} \dot{m}_{CO_2}(h_{out} - h_{in}) - \dot{Q}_{loss,spec}\left(T_{CO_2,avg} - T_{amb}\right)dt \qquad \text{Equation 16}$$

Where t_{end} is the time at the end of the heat release process and other terms are as defined above. The $\dot{Q}_{loss,spec}$ term is determined by the steady state run that immediately preceeds each

test run to match the loss conditions as closely as possible. Because of the small design heat transfer rate (2kW) and large size of equipment, it becomes difficult to measure the response of the hydrogen reaction. During steady state, with no hydrogen being added, a temperature drop between 60 to 100°C in the CO_2 temperatures was measured, while the response from adding hydrogen only caused a rise in exit temperature of about 25°C. Additionally, the inlet temperature is noisy as a result of long tube runs to the test facility (required to ensure safety) and sensitivity to heat loss changes, particularly wind which causes further uncertainty in the measurment. Second there is a lower average inlet temperature to the HTMH HX during the hydrogen pressurization due to the difficulty of heater control. However despite these challenges, some useable data was gathered. Table 38 summarizes the heat release from all of the completed runs.

Table 38 Results summary for energy release testing

Run #	Average CO_2 Inlet Temp [C]	Average CO_2 Outlet Temp [C]	Ambient Temp [C]	Heat Loss Rate [kW]	Expected Heat Loss Rate [kW]	Average H_2 Heat Release [kW]	Test Time [s]	Total Heat Release [kWh]
1	472.4	410.5	12.1	3.627	3.298	-0.329	3239	-0.296
2	548.5	497.6	9.8	2.935	4.103	1.168	2059	0.668
3	623.7	540.6	11.1	5.444	5.348	-0.096	2114	-0.056
4	698.9	614.6	8.5	5.632	6.500	0.868	3961	0.955
5	699.1	641.3	22.0	3.856	4.396	0.540	2411	0.362
6	685.8	640.6	12.6	2.971	3.672	0.701	2384	0.464

While some of the runs produced good results, others did not produce the expected response. Particularly runs 1 and 3 produced a small negative average heat release rate. For run 1, this is likely because the temperature of the metal hydride was too low, where the reaction kinetics of the hydration reaction was too slow to overcome the heat loss and produce a noticeable heat release. It was hypothesized that the bed was not fully discharged of hydrogen before run 3, resulting in a lack of heat release.

For the remaining runs which did experience a good response, the total energy released from the bed varied widely throughout the tests. The most likely reason for this result is that the metal hydride was again not fully discharged of hydrogen before charging started. This discharging step is difficult to achieve to completion as it occurs more favorably at high temperatures and low hydrogen pressures. Because of how the system operates, it is difficult to keep the system at high temperatures for extended periods of time as reaching temperature is a timely proposition, and the system needs to be constantly monitored while under operation for abnormal readings.

Ideally, low hydrogen pressure would mean operating the system under a vacuum, however this ability was not forseen, and not included in the system. Also adding to the difficulty in achieving low hydrogen pressures was the small diameter (1/16" ID) tube that connected the hydrogen source to the test article which provided a major flow restriction to filling or discharging the test article of hydrogen. Once it was determined that the bed not being fully discharged may be causing an issue, a proceedure was developed to try to achieve, if not a fully discharged state, an equally discharged state for two consecutive runs. Runs 5 and 6 both where allowed to dwell at ~700°C inlet temperatures while continuously venting down the hydrogen whenever it exceeded 5 psig. For these runs, a fully discharged bed was considered to be a run where the time between venting was 15 seconds. Even trying to standarize the discharge in this way did not result in even results, the total discharged eneregy differed between runs 5 and 6 by ~20%. Other factors could have affected this measurement as well; differing heat loss rates compared to the steady state measured value, or not charging the bed with hydrogen to completion.

The estimate of steady state heat loss is another large source of error. This was empiricaly measured at the start of each test, however each test lasts about 45 minutes where changing conditions could cause changes to the loss rate. The clearest way this was seen, was in the temperature into the heat exchanger, where large wind gusts would cause a dip in inlet temperature. Better insulation would help to mitigate these effects, however it is unlikely they would be eliminated. The other factor resulting in unsteady temperature was the unsteady mass flow which varies by about 20% on a sub-second basis. This is likely due to the design of the pump, which features three pistons operating out of phase with each other. At high speeds, the pulses from each stroke are indistinguishable, however at the slow speeds the pump was operating at for this test, the pulses seem to be significant. A smaller pump would have a more uniform flow, or using a higher bypass, however these options were not available for this test.

Higher temperature may also have allowed a higher heat release of the metal hydride, or at least faster reaction kinentics. The original design called for a temperature of 730°C while testing only achieved 700°C. This is due to the temperature drop between the exit of the heater and the inlet to the heat exchanger. A limit of 730°C is imposed on the heater, which in turn results in lower than 730°C temperatures to the heat exchanger. Higher than expected heat loss resulted in the max temperature to be 700°C which was pushing the capabilities of the heater.

During testing, the maximum pressure of the hydrogen was approximatly 615psi which is less than the MAWP for the vessel of 650psi. However the pressure relief valve for the vessel was set to 650 psi and it has a 90% operating ratio, meaning the operating pressure should be 585psi, so the vessel was already exceeding the limits of its pressure relief valve. It would have been difficult to design a vessel to have a higher rating, thicker walls are a solution, but would not fit within the available budget. Internal insulation would also be an option to keep wall temperatures lower and allow a lower cost material to be used. However, this presents another risk with local failure of the insulation resulting in failure of the vessel and was not persued.

While there were many issues with the charging and discharging process, in the best run 0.955 kWh of thermal energy was released from the bed, which corresponds to 59.1% of the expected value. There are many reasons for this discrepency which have been covered above. At a larger

scale the total energy recovery would be closer to the theoretical value as the signal to noise ratio would be much better.

As mentioned above, the low temperature metal hydride loop which would have been used in the place of the hydrogen bottles to store and release hydrogen durign the test was not implemented due to time constraints. However, this side of the technology is well understood and has been proposed many times as a stable way to store hydrogen. While it would have been interesting to test both at the same time, the concept of the HTMH TES system was demonstrated with the tests completed.

Milestone 4.1.2.1:

A difference between experimental data and numerical operating data of ≤ 15% will be shown at the selected measurement points.

An uncertainty analysis was conducted on both the steady state heat loss, and the energy released from the HTMH to determine the measurement uncertainty. The first step in that analysis is to determine the uncertainty in each of the measurements. There are several uncertainty components that go into each measurement, a summary of those inputs, and their values is given in Table 39.

Table 39 Measured variables uncertainty values at manufacturer listed limits

Measurement	Instrument Type	DAQ Resolution	DAQ Uncertainty	Instrument Uncertainty	Total Uncertainty
Temperature	K-Type TC	±0.005°C	±0.9°C	±2.2°C or 0.75% whichever is greater	±5.327°C at 700°C
Pressure	Diaphragm	±2.98E-6%	±0.04%	±1%	1.001%
Mass Flow	Coriolis	±2.98E-6%	±0.04%	±0.1%	0.1077%

Each uncertainty contribution is added together using a root sum of squares method to obtain the total uncertainty according to Equation 17.

$$u_{Total} = \sqrt{\sum_{i=i}^{k} u_i^2} \qquad \text{Equation 17}$$

The uncertainties listed above use the uncertainties listed by the manufacturer. These limits are often given as maximal values, and are not associated with a confidence interval, meaning that they can be taken to include all possible outcomes (i.e. 100% confidence interval). However, this

is not as useful when looking at data where a lower confidence interval may be more appropriate. It was found that manufacturer listed uncertainty bands can be approximated as a three sigma (99.7%) confidence interval [69]. From this, a new table can be made using the one sigma (68%) confidence interval as shown in Table 40.

Table 40 Measured variables uncertainty values at one sigma uncertainty limits

Measurement	Instrument Type	DAQ Resolution	DAQ Uncertainty	Instrument Uncertainty	Total Uncertainty
Temperature	K-Type TC	±0.005°C	±0.3°C	±0.73°C or 0.25% whichever is greater	±1.776°C at 700°C
Pressure	Diaphragm	±2.98E-6%	±0.013%	±0.33%	0.3336%
Mass Flow	Coriolis	±2.98E-6%	±0.013%	±0.03%	0.036%

An uncertainty propagation was conducted using EES on the steady state heat loss data [70]. Data was recorded every second and for each data point, a steady state heat loss term was calculated (Equation 14) along with an uncertainty for that measurement. The average heat loss term was used in the heat release calculations and the uncertainty in that value was also propagated through to the heat release calculations. The standard deviation of the average heat loss term was also propagated through to the heat release calculation; however the standard deviation was a much smaller contribution compared to the other components. A summary of the heat release for each run, and its associated uncertainty is given in Table 41. These uncertainties are specified with a 95% confidence interval, corresponding to a two-sigma variation.

Table 41 Heat release uncertainty for 95% confidence interval for all 6 runs

Run #	Total Heat Release [kWh]	Total Heat Release Uncertainty [kWh]	Uncertainty Percent [%]
1	-0.26095	0.333689	127.9%
2	0.680018	0.3666	53.9%
3	-0.05622	0.420615	748.2%
4	0.957747	1.027743	107.3%
5	0.36005	0.445486	123.7%
6	0.464034	0.427099	92.0%

As the table shows, the uncertainty in the heat release is much greater than the 15% difference specified in the milestone. An uncertainty contribution table is provided for a single time step in run 6 to understand where the uncertainty is coming from.

(700C H2 V2, Run 2384)		
Variable±Uncertainty	**Partial derivative**	**% of uncertainty**
$\dot{Q}_{H2}$ = 0.1373±0.2263		
$\dot{m}_{gram}$ = 54.73±0.0285 [g/s]	$\partial\dot{Q}_{H2}/\partial\dot{m}_{gram}$ = -0.0641	0.01 %
T_{in} = 685±1.739 [C]	$\partial\dot{Q}_{H2}/\partial T_{in}$ = -0.06513	25.04 %
T_{out} = 631.5±1.607 [C]	$\partial\dot{Q}_{H2}/\partial T_{out}$ = 0.06963	24.45 %
T_{box} = 12.37±0.4738 [C]	$\partial\dot{Q}_{H2}/\partial T_{box}$ = -0.005644	0.01 %
$P_{in,psig}$ = 1211±4.066 [psi]	$\partial\dot{Q}_{H2}/\partial P_{in,psig}$ = 0.0001973	0.00 %
$P_{out,psig}$ = 788±2.646 [psi]	$\partial\dot{Q}_{H2}/\partial P_{out,psig}$ = -0.0002594	0.00 %
$\dot{Q}_{loss,spec}$ = 0.005644±0.000249	$\partial\dot{Q}_{H2}/\partial\dot{Q}_{loss,spec}$ = 645.9	50.49 %

Figure 124 Uncertainty contribution for a single time step of run 6 hydrogen heat release data

About half of the uncertainty comes from the inlet and exit temperature measurements, while the other half comes from the specific heat loss term. The heat loss term itself has an uncertainty propagation associated with it, as shown in Figure 125.

(700C SS V2, Run 241)		
Variable±Uncertainty	**Partial derivative**	**% of uncertainty**
$\dot{Q}_{loss,spec}$ = 0.00496±0.0002253		
$\dot{m}_{gram}$ = 49.84±0.02595 [g/s]	$\partial\dot{Q}_{loss,spec}/\partial\dot{m}_{gram}$ = 0.00009953	0.01 %
T_{in} = 693.2±1.759 [C]	$\partial\dot{Q}_{loss,spec}/\partial T_{in}$ = 0.00009121	50.69 %
T_{out} = 639.3±1.626 [C]	$\partial\dot{Q}_{loss,spec}/\partial T_{out}$ = -0.00009726	49.27 %
T_{box} = 13.69±0.4738	$\partial\dot{Q}_{loss,spec}/\partial T_{box}$ = 0.000007601	0.03 %
$P_{in,psig}$ = 1243±4.175	$\partial\dot{Q}_{loss,spec}/\partial P_{in,psig}$ = -2.646E-07	0.00 %
$P_{out,psig}$ = 843.3±2.831	$\partial\dot{Q}_{loss,spec}/\partial P_{out,psig}$ = 3.488E-07	0.00 %

Figure 125 Uncertainty contribution for a single time step of run 6 steady state heat loss data

Again, the uncertainty in the data is almost entirely due to the uncertainty in the temperature measurements. This also propagates through to the heat release data which also has almost all its uncertainty in the temperature measurement.

Original plans called for a calibrated thermocouple to be used, however the calibration curve for the thermocouple received ends at 400°C which is well below the 700°C measurement temperature. If used, the calibrated thermocouple would have provided a maximum uncertainty of ±0.55°C at the 99.7% confidence interval corresponding to a 10-fold decrease compared to the standard thermocouple error that was used instead. Thermocouples could also have been calibrated to each other using an oven. Since the temperature difference is of most importance in these calculations, this would have greatly reduced the thermocouple error. However, time did not allow for such calibration before testing began.

Larger temperature rises would also have caused a large reduction in measured uncertainty. Initial uncertainty analysis assumed a temperature rise of ~140°C compared to the ~30°C seen in the test. Because almost all of the uncertainties of the heat release measurement are in the temperature differences, a four time increase in the temperature difference would lead to an approximately 4x reduction in measured uncertainty. This effect can be seen in runs one and three, where the lack of temperature increase results in a very high measured uncertainty.

Milestone 4.1.2.2:

Applying the data and learnings from the test article testing, the full-scale system is predicted to have an annualized system energetic efficiency ≥ 99%.

The round-trip efficiency calculation method was reported in Subtask 3.1. After the experimental testing, a new capacity factor for the HTMH was calculated, which is defined as the best case experimental measured capacity compared to the laboratory measured capacity which was determined to be 59.1%. From there the commercial scale HTMH HX must be resized to hold the increased amount of HTMH. This in turn will increase the thermal losses from the vessel as the vessel must be larger. A summary of the updated thermal losses and a comparison to the previously reported thermal losses is given in Table 42.

Table 42 Updated System Energetic Efficiency

Parameter	Units	Original Value	Updated Value
Heat Transfer Rate	MW	19.8	19.8
Vessel Thermal Losses	kWth	81.0	121.8
H2 Pipe Thermal Loss	kWth	32	32
H2 Regenerator Thermal Loss	kWth	17.6	17.6
H2 Regenerator ineffecitiveness	kWth	55.5	55.5
H2 Regenerator Thermocline	kWth	6.6	6.6
Total TES Loss	kWth	192.7	233.5
Energetic Round Trip Efficiency	%	99.03%	98.82%

In this table, the only value that has been updated is the vessel thermal losses due to the larger vessel required. The hydrogen piping and regenerator are all the same size as the only change discovered through testing was the decreased hydrogen content of the HTMH, not the required hydrogen amount. The relatively small increase in thermal losses is due to the linear relationship between surface area to volume ratio and vessel diameter. At large vessel sizes (as this is) an increase in volume only results in a small increase in surface area, which in turn minimizes additional losses. Still, the result from the experimental testing show that the milestone is not met, however, it is only 0.02% away from meeting the result, and changes to the insulation on the vessel or the hydrogen system would result in the system exceeding the milestone requirement. However, the modified design was not reported as it would not be the lowest LCOE solution.

Milestone 4.1.2.3:

Applying the data and learnings from the test article testing, the full scale system is predicted to have an annualized system exergetic efficiency ≥ 95%.

Again, exergetic efficiency is calculated in the same way as in Subtask 3.1. The only changes made to the exergetic efficiency calculation is the input of the energetic efficiency from above. Using the updated parameters, the updated exergetic efficiency is 97.65% which meets the milestone requirement of 95%

SubTask 4.1.3:

Apply the capital costs and annualized receiver/TES performance profile to generate a system LCOE.

The goal of this task is to update the LCOE calculation by applying the knowledge learned in the experimental testing. In this case only data about the HTMH HX was taken, and as a result, only the HTMH HX will be updated. There was no data taken about the round trip energetic efficiency of the metal hydride as time constraints limited test time. However, there were several runs completed where the energy released from the metal hydride was measured. All runs had differing amount of heat release for reasons discussed above, the run with the highest heat release was used as the baseline here, as it was assumed that with better knowledge over the process, the heat release could be maximized for every run in a commercial system. The highest heat release run had 59.1% of the expected energy release compared to previous assumptions which was used to redesign the HTMH HX compared to phase 2 as shown in Table 43.

Table 43 Updated HTMH HX design summary

Parameter	Units	Phase 2 HTMH HX	Phase 3 HTMH HX
MH Mass Req'd (per module)	kg	111,881	223,592
MH Conductivity	W/m-K	7	7
Number of Cells (per module)	#	2210	3,049
Pressure Vessel Qty. (per module)	#	2	4
PV Outer Diameter	m	4.882	3.5
PV Thickness	mm	25.8	47.18
PV Length	m	4	4
PV Material	N/A	P91	P91
Number of Modules	#	3	3
Cost per PV	$	$ 186,500	$ 155,230
Total PV Cost	$	$ 1,119,000	$ 1,863,000

Total Insulation Cost	$	$ 322,000	$ 754,236
Total Cell Cost	$	$ 5,689,000	$ 7,848,761
Total Cost	$	$ 7,316,500	$ 10,621,227

While the metal hydride material is increased, so is the number of cells required to keep the temperature drop in the metal hydride section to 30°C maximum during the charging or discharging process. Because the material has a lower capacity under the phase 3 assumptions, more cells are required in order to maintain that same temperature drop as the conduction lengths are longer. Other changes were made to the pressure vessel such as increasing the temperature at the wall, which increases the required wall thickness, but reduces insulation cost. The end result is the entire heat exchanger costs about 45% more under the new assumptions. These modified heat exchanger costs were rolled into the total system costs as shown in Table 44.

Table 44 Cost roll up of all components in metal hydride CSP plant

Parameter	Cost Metric	Phase 2 Value	Phase 3 Value
Solar Field		*$ 4,974,854*	*$ 5,046,234*
Heliostats	$75/m2	*$ 4,495,350*	*$ 4,559,850*
Site Improvement	$8/m2	*$ 479,504*	*$ 486,384*
Tower + Receiver(s)		$ 4,344,630	$ 4,344,630
Receivers		$ 970,390	$ 970,390
Tower		$ 1,169,000	$ 1,169,000
Piping		*$ 1,199,240*	*$ 1,199,240*
Valves		*$ 1,006,000*	*$ 1,006,000*
Thermal Energy Storage		*$ 11,921,515*	*$ 15,466,546*
HTMH TES HX		*$ 7,881,288*	*$ 11,807,549*
Shell		*$ 1,199,000*	*$ 1,863,000*
Insulation		*$ 322,000*	*$ 754,236*
HTMH		*$ 671,288*	*$ 1,341,552*
Cells		*$ 5,689,000*	*$ 7,848,761*
LTMH TES HX		*$ 3,665,504*	*$ 3,284,275*
Shell		*$ 1,521,000*	*$ 1,521,000*
LTMH		*$ 989,264*	$ 989,264

Cells		*$1,155,240*	$ 774,010
Regenerator		*$ 374,723*	$ 374,723
Shell		*$ 161,433*	$ 161,433
Insulation		*$ 61,657*	$ 61,657
Packing		*$ 151,633.00*	$ 151,633
Power Block	$600/kW$_e$	$ 6,000,000	$ 6,000,000
TOTAL		$ 27,240,999	$ 30,786,030

Costs for phase 3 track very closely to those used in phase 2. The largest increase came from the increase in the HTMH HX, while a smaller increase was due to increasing the size of the solar field. An increased solar field size was needed to better match the heat input to the system to the amount of storage available, it was recognized that the phase 2 solar field was too small to fully utilize the storage capacity specified. SAM was used to calculate the LCOE for the overall power plant, the following assumptions were used in the calculation.

Table 45 Input parameters and outputs from SAM LCOE calculations

Parameter	Units	Value
INPUTS		
Location	N/A	Daggett, CA
Solar Multiple	N/A	2
Solar Resource at Design	W/m^2	950
Power Block Output	MWe	10
Nominal Conversion Efficiency	%	50
Thermal Energy Storage Capacity	MWhr	74
Analysis Period	Yr	30
Discount rate	%	7
OUTPUTS		
LCOE	¢/kWh	8.56
Capacity Factor	%	42.8
Net Electric to Grid	MWh	37,514

The overall LCOE of 8.56 ¢/kWh is very similar to the phase 2 reported value of 8.4 ¢/kWh. These values are still quite a bit higher than the DOE goal of 5 ¢/kWh for base load CSP plants. In the end, the compact nature of metal hydride thermal energy storage does not prove an advantage to conventional salt, or next generation particle thermal energy storage systems in terms of cost. Significant extra equipment is required to contain the hydrogen, and the storage media itself on

a per kWh basis is not much cheaper than particles. Adding that to the fact that the particles cannot be easily moved, makes it near impossible to be cost competitive. However, metal hydrides may find applications in areas where compact thermal energy storage at high temperature is more important than cost such as space or mobile applications.

Milestone 4.1.3.1:

An integrated receiver, tower, and thermal energy storage system designed for a 10 MW_e modular tower-based CSP sCO_2 Brayton Power Plant with Integrated TES that has a capital cost of \$210/kW_{th} or less (corresponding to the DoE goal of \$150/kW_{th} for the receiver/tower system + [\$15/$kWhr_{th}$ x 4 hrs. storage] for the TES), within an uncertainty of ±10%, over the full range of input variability.

As outlined in Table 44 the total cost of a 74MWh metal hydride thermal energy storage system plus tower, receiver, and transport system is \$19.8 million. Normalizing this to \$/kWh_{th} results in a cost of \$268/kWh_{th}. Which is 27% higher than the milestone value. Even when including a 10 percent uncertainty value to all the cost estimates, the lower limit would still exceed the milestone goal. The main contributor to not hitting this goal is the TES system, which has a normalized cost of \$209/kWh_{th} which greatly exceeds the goal of \$15/kWh_{th}. The largest contributor to this cost is the HTMH cells, however the HTMH material itself normalized to a cost of \$18.13/kWh meaning that even if everything else in the system is free, it would still exceed the DOE goal. Phase 1 and 2 did not reveal this problem because the properties of the metal hydride were not fully known. If the metal hydrides can be improved to have a larger heat capacity per unit mass while maintaining a similar cost this might prove to be a better option.

Large numbers of cells are also required in the system to remove the heat from the metal hydride, which is driven by the poor conductivity of the metal hydride. Even with ENG (Expanded Natural Graphite) added as a conductivity enhancer, the conductivity was only increased to 7 W/m-K. This means that in order to avoid very large temperature gradients (which have the potential to over temp and damage portions of the metal hydride) a large number of cells are required to remove heat. A particle heat exchanger avoids these costs by moving particles over a much smaller heat exchange surface with closely spaced plates. This was not possible with the metal hydride as the entire storage and transport system would need to be not only sealed to air, but also pressurized up to 4.5MPa. This system would not be too dissimilar to redox thermal energy storage projects proposed previously [71]. Those systems also proposed a chemical reaction between the particle and a gas (in their case oxygen) however complexities in their design also caused them to fall out of favor. Again, while the metal hydrides may not be a good fit for CSP thermal energy storage, other applications may be able to better take advantage of their high energy density.

References

[1] U.S. Department of Energy, “SunShot Vision Study,” 2010.

[2] N. R. E. Laboratory, “System Advisor Model Version 2019.11.11.” Golden, CO (United States), 2019.

[3] L. Rapp, “Sandia National Laboratories Brayton Lab - sCO2 Testing Facilities,” 2019. https://www.osti.gov/servlets/purl/1646164 (accessed Apr. 29, 2021).

[4] National Energy Technology Laboratory, “SUPERCRITICAL CO2 TURBOMACHINERY.”

[5] NREL, “Concentrating Solar Power Projects - Power Tower Projects.” https://www.nrel.gov/csp/solarpaces/power_tower.cfm (accessed Nov. 05, 2017).

[6] Z. Ma and C. S. Turchi, “Advanced Supercritical Carbon Dioxide Power Cycle Configurations for Use in Concentrating Solar Power Systems: Preprint,” 2011, Accessed: Apr. 26, 2022. [Online]. Available: http://www.osti.gov/bridge

[7] Electric Power Research Institute (EPRI), “A Report from EPRI’s Innovation Scouts.”

[8] B. Egan, H. Q. Tech, V. Rajgopal, and D. Bobo, “Final report for project 7120 Project Title: Advanced supercritical carbon dioxide cycles.” [Online]. Available: www.wisc.edu

[9] R. K. Shaltens, “Advanced Stirling Conversion Systems for Terrestrial Applications Work performed for”.

[10] “Project Profile: High-Temperature Thermal Array for Next-Generation Solar Thermal Power Production | Department of Energy.” https://www.energy.gov/eere/solar/project-profile-high-temperature-thermal-array-next-generation-solar-thermal-power (accessed Apr. 26, 2022).

[11] J. H. Boo, S. M. Kim, and Y. H. Kang, “An Experimental Study on a Sodium Loop-type Heat Pipe for Thermal Transport from a High-temperature Solar Receiver,” in *Energy Procedia*, May 2015, vol. 69, pp. 608–617. doi: 10.1016/j.egypro.2015.03.070.

[12] J. Kesseli, “Brayton Power Conversion System,” 2011.

[13] S. Sullivan, J. Kesseli, J. Nash, J. Faris, D. Kesseli, and W. Caruso, “High-Efficiency Low-Cost Solar Receiver for use in a Supercritical CO2 Recompression Cycle.”

[14] C. Bing, D. Tech, M. Lausten, and A. Prescod, “DE-EE00025832 Direct s-CO 2 Receiver Development National Renewable Energy Laboratory Final Report for Public Release Project Title: Direct s-CO 2 Receiver Development.”

[15] T. W. Neises, M. J. Wagner, and A. K. Gray, “Structural Design Considerations for Tubular Power Tower Receivers Operating at 650°C,” Jun. 2014. [Online]. Available: www.nrel.gov/publications.

[16] J. D. Ortega, S. D. Khivsara, J. M. Christian, J. E. Yellowhair, and C. K. Ho, “Coupled Optical-Thermal-Fluid Modeling of a Directly Heated Tubular Solar Receiver for Supercritical CO2 Brayton Cycle,” *ASME 2015 9th International Conference on Energy Sustainability, ES 2015, collocated with the ASME 2015 Power Conference, the ASME 2015 13th International Conference on Fuel Cell Science, Engineering and Technology, and the ASME 2015 Nuclear Forum*, vol. 1, Oct. 2015, doi: 10.1115/ES2015-49474.

[17] D. A. Sheppard, M. Paskevicius, and C. E. Buckley, “Thermodynamics of hydrogen desorption from NaMgH3 and its application as a solar heat storage medium,” *Chemistry*

of Materials, vol. 23, no. 19, pp. 4298–4300, Oct. 2011, doi: 10.1021/CM202056S/SUPPL_FILE/CM202056S_SI_001.PDF.

[18] D. Harries, "A novel thermochemical energy storage technology," 2010.

[19] R. Zidan, "Storing High Exergetic Thermal Energy Based on Reversible Alloying and High Enthalpy Hydrides," 62/087,939, 2014

[20] C. Corgnale, B. Hardy, T. Motyka, R. Zidan, J. Teprovich, and B. Peters, "Screening analysis of metal hydride based thermal energy storage systems for concentrating solar power plants," *Renewable and Sustainable Energy Reviews*, vol. 38, pp. 821–833, 2014, doi: 10.1016/J.RSER.2014.07.049.

[21] C. Corgnale, B. Hardy, T. Motyka, and R. Zidan, "Metal hydride based thermal energy storage system requirements for high performance concentrating solar power plants," *International Journal of Hydrogen Energy*, vol. 41, no. 44, pp. 20217–20230, Nov. 2016, doi: 10.1016/J.IJHYDENE.2016.09.108.

[22] P. A. Ward *et al.*, "High performance metal hydride based thermal energy storage systems for concentrating solar power applications," *Journal of Alloys and Compounds*, vol. 645, no. S1, pp. S374–S378, Oct. 2015, doi: 10.1016/J.JALLCOM.2014.12.106.

[23] X. Guo *et al.*, "Laves phase hydrogen storage alloys for super-high-pressure metal hydride hydrogen compressors," *Rare Metals*, vol. 30, no. 3, pp. 227–231, 2011.

[24] Z. Cao *et al.*, "Development of ZrFeV alloys for hybrid hydrogen storage system," *International Journal of Hydrogen Energy*, vol. 41, no. 26, pp. 11242–11253, Jul. 2016, doi: 10.1016/J.IJHYDENE.2016.04.083.

[25] C. Corgnale, B. J. Hardy, D. A. Tamburello, S. L. Garrison, and D. L. Anton, "Acceptability envelope for metal hydride-based hydrogen storage systems," *Int J Hydrogen Energy*, vol. 37, no. 3, pp. 2812–2824, 2012.

[26] T. Gamo, Y. Moriwaki, N. Yanagihara, T. Yamashita, and T. Iwaki, "Formation and properties of titanium-manganese alloy hydrides," *International Journal of Hydrogen Energy*, vol. 10, no. 1, pp. 39–47, Jan. 1985, doi: 10.1016/0360-3199(85)90134-X.

[27] X. Guo *et al.*, "Laves phase hydrogen storage alloys for super-high-pressure metal hydride hydrogen compressors," *Rare Metals*, vol. 30, no. 3, pp. 227–231, 2011.

[28] J. R. Johnson and J. Reilly, "The Use of Manganese Substituted Ferrotitanium Alloys for Energy Storage," Dec. 1977, doi: 10.2172/1004984.

[29] G. Friedlmeier, A. Manthey, M. Wanner, and M. Groll, "Cyclic stability of various application-relevant metal hydrides," *J Alloys Compd*, vol. 231, no. 1–2, pp. 880–887, 1995.

[30] P. A. Ward, J. A. Teprovich, Y. Liu, J. He, and R. Zidan, "High temperature thermal energy storage in the CaAl2 system," *Journal of Alloys and Compounds*, vol. 735, pp. 2611–2615, Feb. 2018, doi: 10.1016/J.JALLCOM.2017.10.191.

[31] V. Dostal, “A Supercritical Carbon Dioxide Cycle for Next Generation Nuclear Reactors,” Massachusetts Institute of Technology, 2004. [Online]. Available: http://dspace.mit.edu/handle/1721.1/17746#files-area

[32] A. S. of M. Engineers, “Section VIII Rules for Construction of Pressure Vessels,” in *ASME Boiler and Pressure Vessel Code*, B. and P. V. C. American Society of Mechanical Engineers, Ed. New York, 2007.

[33] R. K. Sinnott and Gavin. Towler, *Chemical engineering design.* Butterworth-Heinemamn, 2009. Accessed: Feb. 05, 2019. [Online]. Available: https://books.google.com/books?hl=en&lr=&id=Fq7xhZjPuLEC&oi=fnd&pg=PP1&dq=chemical+engineering+design&ots=fulgAu2dEY&sig=Q1MBCZygnrYWYqrwm057gUg5MCQ#v=onepage&q=chemical%20engineering%20design&f=false

[34] Oil and Gas Journal, “Nelson-Farrar Cost Indexes - Oil & Gas Journal,” 2017. https://www.ogj.com/articles/print/volume-115/issue-8/processing/nelson-farrar-cost-indexes.html (accessed Feb. 05, 2019).

[35] Steel Tank, “Relative Cost Ratio.” https://www.steeltank.com/Portals/0/Pressure%20Vessels/SSWseminarOct2012/Relative%20Cost%204%2015%202012.pdf (accessed Feb. 05, 2019).

[36] HarbisonWalker International, “Hydrogen Gas Plants,” 2019. https://thinkhwi.com/industries/refineries-petrochemicals/hydrogen-gas-plants/ (accessed Feb. 12, 2019).

[37] R. K. Sinnott and Gavin. Towler, *Chemical engineering design.* Butterworth-Heinemamn, 2009.

[38] Oil and Gas Journal, “Nelson-Farrar Cost Indexes - Oil & Gas Journal,” 2017. https://www.ogj.com/articles/print/volume-115/issue-8/processing/nelson-farrar-cost-indexes.html (accessed Feb. 06, 2019).

[39] G. F. (Geoffrey F. Hewitt, *Hemisphere handbook of heat exchanger design*. New York: Hemisphere Pub. Corp, 1990.

[40] PMC Supplies, “GREENTHERM 23 LI Medium-Duty Brick (2300^{o}F Firebrick).” https://pmcsupplies.com/greentherm-23-li-medium-duty-brick-2300-f-firebrick.html (accessed Feb. 12, 2019).

[41] Microtherm Thermal Insulation Solutions, “Microtherm Product Performanec.”

[42] M. Bahrami, M. M. Yovanovich, and J. R. Culham, “Effective thermal conductivity of rough spherical packed beds,” 2006, doi: 10.1016/j.ijheatmasstransfer.2006.02.021.

[43] W. B. Stine, “Cavity receiver convection heat loss,” *ci.nii.ac.jp*, Accessed: Apr. 27, 2022. [Online]. Available: https://ci.nii.ac.jp/naid/10003312772/

[44] “Commodity Statistics and Information | U.S. Geological Survey.” https://www.usgs.gov/centers/national-minerals-information-center/commodity-statistics-and-information (accessed Apr. 27, 2022).

[45] "Calcium prices, news and research - Asian Metal." https://www.asianmetal.com/CalciumPrice/Calcium.html (accessed Apr. 27, 2022).

[46] "Calcium." https://www.chemicool.com/elements/calcium.html (accessed Apr. 27, 2022).

[47] "• Silicon price by type U.S. 2021 | Statista." https://www.statista.com/statistics/301564/us-silicon-price-by-type/ (accessed Apr. 27, 2022).

[48] "Made-in-China.com - Manufacturers, Suppliers & Products in China." https://www.made-in-china.com/ (accessed Apr. 27, 2022).

[49] J. Benz and T. L. Richardwright, "Aging of Alloy 617 at 650 and 750°C," 2013, Accessed: May 10, 2022. [Online]. Available: http://www.inl.gov

[50] R. Purgert *et al.*, "BOILER MATERIALS FOR ULTRA SUPERCRITICAL COAL POWER PLANTS," 2015.

[51] P. J. Maziasz and R. W. Swindeman, "Selecting and Developing Advanced Alloys for Creep-Resistance for Microturbine Recuperator Applications," *Proceedings of the ASME Turbo Expo*, vol. 1, Jul. 2014, doi: 10.1115/2001-GT-0541.

[52] F. Gustavo, L. Pereira, J. M. Lourenço, R. Maribondo Do Nascimento, and A. Castro, "Fracture Behavior and Fatigue Performance of Inconel 625," *Materials Research*, vol. 21, no. 4, p. 20171089, 2018, doi: 10.1590/1980-5373-MR-2017-1089.

[53] J. K. Wright, "Draft ASME Boiler and Pressure Vessel Code Case for Use of Alloy 617 for Class A Elevated Temperature Service Construction," 2015. Accessed: Sep. 15, 2019. [Online]. Available: https://inldigitallibrary.inl.gov/sites/sti/sti/6799575.pdf

[54] High Temp Metals, "Haynes 230 Tech Data." http://www.hightempmetals.com/techdata/hitempHaynes230data.php (accessed Dec. 07, 2016).

[55] PCC Energy Group, "Inconel Alloy 740H." [Online]. Available: http://www.pccenergy.com/assets/files/740H-White-Paper.pdf

[56] D. L. May and A. P. Gordon, "THE APPLICATION OF THE NORTON-BAILEY LAW FOR CREEP PREDICTION THROUGH POWER LAW REGRESSION," 2013, Accessed: May 10, 2022. [Online]. Available: http://www.asme.org/about-asme/terms-of-use

[57] J. P. Shingledecker, "Metallurgical Effects on Long-Term Creep-Rupture in a New Nickel-Based Alloy," University of Tennessee, Knoxville, 2012. Accessed: May 10, 2022. [Online]. Available: https://trace.tennessee.edu/utk_graddiss/1348

[58] J. D. Tucker *et al.*, "Supercritical CO2 round robin test program," in *The 6th International Symposium - Supercritical CO2 Power Cycles*, 2018, pp. 1–12.

[59] J. P. Shingledecker, N. D. Evans, and G. M. Pharr, "Influences of composition and grain size on creep–rupture behavior of Inconel® alloy 740," *Materials Science and Engineering: A*, vol. 578, pp. 277–286, Aug. 2013, doi: 10.1016/J.MSEA.2013.04.087.

[60] A. K. Kalra, “Piping materials for supercritical carbon dioxide Brayton cycle,” University of Wisconsin-Madison, 2015.

[61] G. Nellis and S. A. Klein, *Heat Transfer*. New York: Cambridge University Press, 2009.

[62] R. K. Sinnott and Gavin. Towler, *Chemical engineering design.* Butterworth-Heinemamn, 2009.

[63] Oil and Gas Journal, “Nelson-Farrar Cost Indexes - Oil & Gas Journal,” 2017.

[64] Steel Tank, “Relative Cost Ratio.”

[65] Clean Technica, “GE Renewable Energy Unveils Largest Onshore Wind Turbine | CleanTechnica.” https://cleantechnica.com/2017/09/13/ge-renewable-energy-unveils-largest-onshore-wind-turbine/ (accessed Feb. 15, 2019).

[66] N. R. E. Laboratory, “System Advisor Model Version 2019.11.11.” Golden, CO (United States), 2019.

[67] R. S. Figliola and D. E. Beasley, *Theory and Design for Mechanical Measurements*, 5th ed. John Wiley & Sons, Inc., 2011.

[68] F-Chart, “EES Engineering Equation Solver.” 2015.

[69] J. T. Nakos, “Uncertainty Analysis of Thermocouple Measurements Used in Normal and Abnormal Thermal Environment Experiments at Sandia’s Radiant Heat Facility and Lurance Canyon Burn Site,” 2004. [Online]. Available: http://www.doe.gov/bridge

[70] F-Chart, “EES Engineering Equation Solver.” 2015.

[71] L. Imponenti, K. J. Albrecht, R. J. Braun, and G. S. Jackson, “Measuring Thermochemical Energy Storage Capacity with Redox Cycles of Doped-CaMnO3,” *ECS Transactions*, vol. 72, no. 7, pp. 11–22, 2016, doi: 10.1149/07207.0011ecst.